



# Synthesis of Tungsten Oxide Thin Films for Photoelectrochemical Applications

**Author:**

Kwong, Wai Ling

**Publication Date:**

2014

**DOI:**

<https://doi.org/10.26190/unsworks/16694>

**License:**

<https://creativecommons.org/licenses/by-nc-nd/3.0/au/>

Link to license to see what you are allowed to do with this resource.

Downloaded from <http://hdl.handle.net/1959.4/53359> in <https://unsworks.unsw.edu.au> on 2024-05-01

**SYNTHESIS OF TUNGSTEN OXIDE THIN FILMS FOR  
PHOTOELECTROCHEMICAL APPLICATIONS**

**WAI LING KWONG**

**UNIVERSITY OF NEW SOUTH WALES**

**2014**

# **Synthesis of Tungsten Oxide Thin Films for Photoelectrochemical Applications**

A Thesis Submitted in Fulfilment of the Requirements for the Degree of

Doctor of Philosophy

in

Materials Science and Engineering

by

Wai Ling Kwong

School of Materials Science and Engineering

Faculty of Science

University of New South Wales

April 2014

<b>PLEASE TYPE</b>	<b>THE UNIVERSITY OF NEW SOUTH WALES</b>
<b>Thesis/Dissertation Sheet</b>	
Surname or Family name: <b>KWONG</b>	
First name: <b>WAI LING</b>	Other name/s: <b>N/A</b>
Abbreviation for degree as given in the University calendar: <b>Ph.D.</b>	
School: <b>MATERIALS SCIENCE AND ENGINEERING</b>	Faculty: <b>SCIENCE</b>
Title: <b>SYNTHESIS OF TUNGSTEN OXIDE THIN FILMS FOR PHOTOELECTROCHEMICAL APPLICATIONS</b>	

<b>Abstract 350 words maximum: (PLEASE TYPE)</b>
<p>WO<sub>3</sub> thin-film photoanodes were electrodeposited from peroxotungstic acid (PTA) solutions onto fluorine-doped tin oxide substrates and annealed at ≤500°C for times up to 18 h. The effects of processing parameters, including deposition potentials and times, compositions of the electrolyte solutions, and post-deposition annealing conditions, on the physical, mineralogical, optical, and photoelectrochemical properties of the films were studied.</p> <p>The amorphous films transformed to the polycrystalline monoclinic phase upon annealing ≥275°C. Higher deposition rates were obtained by increasing the deposition potential (−0.3 to −0.6 V <i>versus</i> Ag/AgCl) and W concentration of PTA (0.05-0.20 mol L<sup>−1</sup>), which determined the flux of PTA ions toward the working electrode. The deposition rates also depended on the types (oxalic, formic, and citric acids) and amounts (0.01-0.10 mol L<sup>−1</sup>) of carboxylic acids added to PTA as dispersing agents. The hydronium ions and conjugate bases formed upon dissolution of carboxylic acids participated in solute dispersion and separation, which altered the mechanisms of nucleation and grain growth. The deposition rates and times (≤3 h) resulted in films of varied thicknesses (168-1400 nm). The grain sizes of the films differed slightly (77-122 nm) with the W concentration in PTA and they differed significantly (42-132 nm) with the sizes of the conjugate bases of the carboxylic acids. Reduced optical indirect band gaps (E<sub>g</sub>; 2.5-3.3 eV) were obtained by increasing the thickness and grain (particle and/or agglomerate) size of the films, both of which affected the film crystallinity. The predominance of (002) and (200) X-ray diffraction peaks from planes parallel to the substrate of the films depended on the nucleation density and the thermally induced recrystallisation kinetics, which were controlled by the W concentration of PTA and the annealing conditions, respectively. This resulted in films with three types of preferred orientation: (002), both (002) and (200), and (200).</p> <p>Enhanced photoelectrochemical properties were obtained from (i) the lower E<sub>g</sub> and improved light absorption associated with films consisting of greater thickness; (ii) the beneficial balances of (a) surface reaction and recombination sites and (b) hole and electron transports in the film associated with small agglomerates (~93 nm); and (iii) the low E<sub>g</sub>, low valence band maximum, and suppressed charge-carrier recombination in films associated with (002) orientation.</p>

Declaration relating to disposition of project thesis/dissertation		
<p>I hereby grant to the University of New South Wales or its agents the right to archive and to make available my thesis or dissertation in whole or in part in the University libraries in all forms of media, now or here after known, subject to the provisions of the Copyright Act 1968. I retain all property rights, such as patent rights. I also retain the right to use in future works (such as articles or books) all or part of this thesis or dissertation.</p> <p>I also authorise University Microfilms to use the 350 word abstract of my thesis in Dissertation Abstracts International (this is applicable to doctoral theses only).</p>		
.....	.....	.....
<b>Signature</b>	<b>Witness</b>	<b>Date</b>
<b>The University recognises that there may be exceptional circumstances requiring restrictions on copying or conditions on use. Requests for restriction for a period of up to 2 years must be made in writing. Requests for a longer period of restriction may be considered in exceptional circumstances and require the approval of the Dean of Graduate Research.</b>		

FOR OFFICE USE ONLY	Date of completion of requirements for Award:
---------------------	---

**THIS SHEET IS TO BE GLUED TO THE INSIDE FRONT COVER OF THE THESIS**

**COPYRIGHT STATEMENT**

'I hereby grant the University of New South Wales or its agents the right to archive and to make available my thesis or dissertation in whole or part in the University libraries in all forms of media, now or here after known, subject to the provisions of the Copyright Act 1968. I retain all proprietary rights, such as patent rights. I also retain the right to use in future works (such as articles or books) all or part of this thesis or dissertation.

I also authorise University Microfilms to use the 350 word abstract of my thesis in Dissertation Abstract International (this is applicable to doctoral theses only).

I have either used no substantial portions of copyright material in my thesis or I have obtained permission to use copyright material; where permission has not been granted I have applied/will apply for a partial restriction of the digital copy of my thesis or dissertation.'

Signed .....

Date .....

**AUTHENTICITY STATEMENT**

'I certify that the Library deposit digital copy is a direct equivalent of the final officially approved version of my thesis. No emendation of content has occurred and if there are any minor variations in formatting, they are the result of the conversion to digital format.'

Signed .....

Date .....

**ORIGINALITY STATEMENT**

'I hereby declare that this submission is my own work and to the best of my knowledge it contains no materials previously published or written by another person, or substantial proportions of material which have been accepted for the award of any other degree or diploma at UNSW or any other educational institution, except where due acknowledgement is made in the thesis. Any contribution made to the research by others, with whom I have worked at UNSW or elsewhere, is explicitly acknowledged in the thesis. I also declare that the intellectual content of this thesis is the product of my own work, except to the extent that assistance from others in the project's design and conception or in style, presentation and linguistic expression is acknowledged.'

Signed .....

Date .....

# ACKNOWLEDGEMENT

My first and sincerest gratitude is dedicated to my supervisor, Professor Charles Christopher Sorrell, for his continuous guidance, encouragement, and inspiring advices throughout my Ph.D. journey. His vast knowledge and passion for science have greatly enlightened me in this field of research.

I am earnestly thankful to Professor Nicholas Savvides for his valuable discussion with me and his contributions in my research. My appreciations also are dedicated to Dr. Auppatham Nakaruk, Dr. Pramod Koshy, Dr. Wanqiang Martin Xu, and Dr. Judy Hart for their assistance in my experiments and helpful comments on my work.

I would like to thank the staff of the School of Materials Science and Engineering: Professor Sean Li and Dr. Owen Standard for their useful feedback on my work; Dr. George Yang, Dr. Jan Seidel, Dr. Rahmat Kartano, Mr. Anthony Zhang, Ms. Soo Woon Chong, Dr. Thiam Teck Tan, Dr. Dewei Chu, Mr. Thwin Htoo, Mr. Danny Kim, and Ms. Jane Gao for their technical assistance; Ms. Lana Strizhevsky, Ms. Courtenay Atwell, Ms. Lucy Zhang, Ms. Judy Lim, and Ms. Qing Xia for their administrative support. I also would like to thank the staff of Electron Microscopy Unit, Solid State & Elemental Analysis Unit, and Spectroscopy Laboratory for their technical support. Thank you to all of my fellow schoolmates for their kindness and consideration, which have created a very pleasant working environment in the School. A special thank goes to Dr. Kok Tee Lau for his help in setting up my workplace and useful advices on my work.

I am very grateful to the receipt of University International Postgraduate Award (UIPA) and Postgraduate Research Support Scheme (PRSS) from the University of New South Wales, which have provided the financial support throughout my Ph.D. research study program.

Last but not least, thank you to my family for their never-ending love and care throughout my life. To Nikki, for sharing all the good and bad moments, thank you for everything.

# ABSTRACT

WO<sub>3</sub> thin-film photoanodes were electrodeposited from peroxotungstic acid (PTA) solutions onto fluorine-doped tin oxide substrates and annealed at  $\leq 500^{\circ}\text{C}$  for times up to 18 h. The effects of processing parameters, including deposition potentials and times, compositions of the electrolyte solutions, and post-deposition annealing conditions, on the physical, mineralogical, optical, and photoelectrochemical properties of the films were studied.

The amorphous films transformed to the polycrystalline monoclinic phase upon annealing  $\geq 275^{\circ}\text{C}$ . Higher deposition rates were obtained by increasing the deposition potential ( $-0.3$  to  $-0.6$  V *versus* Ag/AgCl) and W concentration of PTA ( $0.05$ - $0.20$  mol L<sup>-1</sup>), which determined the flux of PTA ions toward the working electrode. The deposition rates also depended on the types (oxalic, formic, and citric acids) and amounts ( $0.01$ - $0.10$  mol L<sup>-1</sup>) of carboxylic acids added to PTA as dispersing agents. The hydronium ions and conjugate bases formed upon dissolution of carboxylic acids participated in solute dispersion and separation, which altered the mechanisms of nucleation and grain growth. The deposition rates and times ( $\leq 3$  h) resulted in films of varied thicknesses (168-1400 nm). The grain sizes of the films differed slightly (77-122 nm) with the W concentration in PTA and they differed significantly (42-132 nm) with the sizes of the conjugate bases of the carboxylic acids. Reduced optical indirect band gaps ( $E_g$ ; 2.5-3.3 eV) were obtained by increasing the thickness and grain (particle and/or agglomerate) size of the films, both of which affected the film crystallinity. The predominance of (002) and (200) X-ray diffraction peaks from planes parallel to the substrate of the films depended on the nucleation density and the thermally induced recrystallisation kinetics, which were controlled by the W concentration of PTA and the annealing conditions, respectively. This resulted in films with three types of preferred orientation: (002), both (002) and (200), and (200).

Enhanced photoelectrochemical properties were obtained from (i) the lower  $E_g$  and improved light absorption associated with films consisting of greater thickness; (ii) the beneficial balances of (a) surface reaction and recombination sites and (b) hole and electron transports in the film associated with small agglomerates ( $\sim 93$  nm); and (iii) the low  $E_g$ , low valence band maximum, and suppressed charge-carrier recombination in films associated with (002) orientation.

# TABLE OF CONTENTS

COPYRIGHT AND AUTHENTICITY STATEMENTS	i
CERTIFICATE OF ORIGINALITY	ii
ACKNOWLEDGEMENT	iii
ABSTRACT	iv
TABLE OF CONTENTS	v
LIST OF FIGURES	x
LIST OF TABLES	xvi
LIST OF APPENDICES	xvii
LIST OF JOURNAL AND CONFERENCE PUBLICATIONS	xviii
<b>1 INTRODUCTION</b>	<b>1</b>
1.1 PHOTOELECTROCHEMICAL WATER SPLITTING	1
1.2 RESEARCH OBJECTIVES	4
1.3 CHAPTER OUTLINE	4
<b>2 LITERATURE REVIEW</b>	<b>6</b>
2.1 PHOTOELECTROCHEMICAL WATER SPLITTING	6
2.1.1 PHOTOELECTRODE REQUIREMENTS	9
2.2 TUNGSTEN OXIDE THIN FILMS AS PHOTOANODES	12
2.2.1 NANOSTRUCTURED TUNGSTEN OXIDE PHOTOANODES	13
2.2.2 STRATEGIES TO IMPROVE THE PHOTOCONVERSION EFFICIENCY	19
2.2.3 PHASES AND CRYSTALLOGRAPHY – EFFECT ON PHOTOELECTROCHEMICAL PROPERTIES	24
2.3 SYNTHESIS OF NANOSTRUCTURED TUNGSTEN OXIDE THIN FILMS	26
2.3.1 SOL GEL	26
2.3.2 SPRAY PYROLYSIS DEPOSITION	27
2.3.3 REACTIVE MAGNETRON SPUTTERING	28
2.3.4 THERMAL VAPOUR DEPOSITION	29

2.3.5	THERMAL OXIDATION	30
2.3.6	HYDRO/SOLVOTHERMAL	31
2.3.7	ANODISATION	32
2.3.8	ELECTRODEPOSITION	34
2.3.8.1	OVERVIEW OF ELECTRODEPOSITION	34
2.3.8.2	ELECTRODEPOSITION OF TUNGSTEN OXIDE THIN FILMS	35
2.3.8.3	ELECTRODEPOSITED TUNGSTEN OXIDE THIN FILMS FOR PHOTOELECTROCHEMICAL APPLICATIONS	37
<b>3</b>	<b>EXPERIMENTAL PROCEDURES</b>	<b>39</b>
3.1	SYNTHESIS OF TUNGSTEN OXIDE THIN FILMS USING ELECTRODEPOSITION	39
3.1.1	CHEMICALS	39
3.1.2	PREPARATION OF PEROXOTUNGSTIC ACID ELECTROLYTE SOLUTIONS OF DIFFERENT TUNGSTEN CONCENTRATIONS	39
3.1.3	PREPARATION OF PEROXOTUNGSTIC ACID ELECTROLYTE SOLUTIONS CONTAINING CARBOXYLIC ACIDS	40
3.1.4	ELECTRODEPOSITION OF TUNGSTEN OXIDE THIN FILMS	41
3.1.5	POST-DEPOSITION ANNEALING	43
3.2	CHARACTERISATION TECHNIQUES	43
3.2.1	COMPUTATIONAL DETAILS	44
3.2.2	MEASUREMENT OF FILM THICKNESS BY FOCUSED ION BEAM MILLING AND SCANNING ELECTRON MICROSCOPY	44
3.2.3	TEM SAMPLE PREPARATION BY FOCUSED ION BEAM MILLING AND <i>EX-SITU</i> LIFT-OUT	46
3.3	PHOTOELECTROCHEMICAL MEASUREMENTS	47
3.3.1	PHOTOELECTROCHEMICAL CELL	47
3.3.2	MEASUREMENT PARAMETERS	48

3.4	PHOTOCATALYTIC DEGRADATION OF METHYLENE BLUE	50
<b>4</b>	<b>SYNTHESIS OF TUNGSTEN OXIDE THIN FILMS BY ELECTRODEPOSITION: EFFECT OF DEPOSITION POTENTIAL</b>	52
4.1	INTRODUCTION	52
4.2	RESULTS AND DISCUSSION	52
4.2.1	LINEAR VOLTAMMETRIC STUDY OF PEROXOTUNGSTIC ACID ELECTROLYTE SOLUTIONS	52
4.2.2	EFFECT OF DEPOSITION POTENTIAL ON THE MORPHOLOGICAL, MINERALOGICAL, OPTICAL, AND PHOTOELECTROCHEMICAL PROPERTIES OF ELECTRODEPOSITED TUNGSTEN OXIDE THIN FILMS	54
4.2.2.1	MORPHOLOGICAL PROPERTIES	54
4.2.2.2	MINERALOGICAL PROPERTIES	56
4.2.2.3	OPTICAL PROPERTIES	58
4.2.2.4	PHOTOELECTROCHEMICAL PROPERTIES	60
4.3	KEY RESULTS	62
<b>5</b>	<b>SYNTHESIS OF TUNGSTEN OXIDE THIN FILMS BY ELECTRODEPOSITION: EFFECTS OF TUNGSTEN CONCENTRATION OF PEROXOTUNGSTIC ACID AND DEPOSITION TIME</b>	63
5.1	INTRODUCTION	63
5.2	RESULTS AND DISCUSSION	63
5.2.1	POTENTIOSTATIC CURRENT TRANSIENT AS A FUNCTION OF TUNGSTEN CONCENTRATION OF PEROXOTUNGSTIC ACID – GROWTH MECHANISM OF TUNGSTEN OXIDE THIN FILMS	63
5.2.2	EFFECTS OF TUNGSTEN CONCENTRATION OF PEROXOTUNGSTIC ACID AND DEPOSITION TIME ON THE PROPERTIES OF TUNGSTEN OXIDE THIN FILMS	66
5.2.2.1	MORPHOLOGICAL AND MINERALOGICAL PROPERTIES	66

	5.2.2.2	OPTICAL PROPERTIES	70
	5.2.2.3	PHOTOELECTROCHEMICAL PROPERTIES	73
5.3		KEY RESULTS	80
<b>6</b>		<b>CRITICAL ROLE OF {002} PREFERRED ORIENTATIONS ON ELECTRONIC BAND STRUCTURES OF MONOCLINIC TUNGSTEN OXIDE THIN FILMS</b>	<b>81</b>
6.1		INTRODUCTION	81
6.2		RESULTS AND DISCUSSION	81
	6.2.1	FILM DEPOSITED FROM PTA SOLUTION OF HIGH TUNGSTEN CONCENTRATION (0.20 MOL L <sup>-1</sup> )	82
	6.2.2	FILM DEPOSITED FROM PTA SOLUTION OF LOW TUNGSTEN CONCENTRATION (0.05 MOL L <sup>-1</sup> )	87
	6.2.3	MECHANISM OF PREFERRED CRYSTALLOGRAPHY IN ELECTRODEPOSITED TUNGSTEN OXIDE THIN FILMS	91
	6.2.4	EFFECT OF PREFERRED ORIENTATION	95
		6.2.4.1 DEGREE OF CRYSTALLOGRAPHY	95
		6.2.4.2 MICROSTRUCTURE	96
		6.2.4.3 OPTICAL PROPERTIES	99
		6.2.4.4 CHEMICAL PROPERTIES	100
		6.2.4.5 CORRELATION BETWEEN CRYSTALLOGRAPHIC ORIENTATION, OXYGEN VACANCY CONCENTRATION, AND BAND GAP	103
		6.2.4.6 ELECTRONIC PROPERTIES	105
		6.2.4.7 PHOTOELECTROCHEMICAL PROPERTIES	107
		6.2.4.8 ELECTROCHEMICAL PROPERTIES	108
		6.2.4.9 PHOTOCATALYTIC PROPERTIES	109
6.3		KEY RESULTS	111
<b>7</b>		<b>CARBOXYLIC ACID-ASSISTED ELECTRODEPOSITION OF TUNGSTEN OXIDE THIN FILMS</b>	<b>113</b>
7.1		INTRODUCTION	113
7.2		RESULTS AND DISCUSSION	114

7.2.1	EFFECT OF THE TYPE OF CARBOXYLIC ACID	114
7.2.1.1	FILM THICKNESS	114
7.2.1.2	SURFACE MORPHOLOGY	118
7.2.1.3	MINERALOGY	122
7.2.1.4	OPTICAL PROPERTIES	124
7.2.1.5	PHOTOELECTROCHEMICAL PROPERTIES	125
7.2.2	EFFECT OF THE OXALIC ACID CONCENTRATIONS	129
7.2.2.1	FILM THICKNESS	129
7.2.2.2	SURFACE MORPHOLOGY	130
7.2.2.3	MINERALOGY	135
7.2.2.4	OPTICAL PROPERTIES	137
7.2.2.5	PHOTOELECTROCHEMICAL PROPERTIES	139
7.3	KEY RESULTS	143
<b>8</b>	<b>CONCLUSIONS</b>	145
8.1	CONCLUSIONS	145
8.2	RECOMMENDATIONS FOR FUTURE WORK	150
	<b>REFERENCES</b>	152
	<b>APPENDICES</b>	A1

# LIST OF FIGURES

FIGURE	CAPTION	PAGE
2.1	Schematic diagram of photoelectrochemical cell. $E_c$ = conduction band energy; $E_v$ = valence band energy; $e^-$ = photogenerated electron; $h^+$ = photogenerated hole.	7
2.2	Band diagram illustrating the hole retrieval length in a photoanode at the photoanode/electrolyte interface. $L_p$ = hole diffusion length; $W$ = depletion layer width; $E_c$ = conduction band energy; $E_v$ = valence band energy; $e^-$ = photogenerated electron; $h^+$ = photogenerated hole [5].	9
2.3	Maximal photoconversion efficiency as a function of band gap wavelength of a photoelectrode under the AM 1.5 global solar condition [42].	11
2.4	Band structure diagram of $WO_3/BiVO_4$ heterojunction film [93]. FTO = fluorine-doped tin oxide substrate; $e^-$ = photogenerated electron; $h^+$ = photogenerated hole.	24
2.5	Scanning electron microscopy images of $WO_3$ films deposited using sol-gel from precursor solutions containing (a) no acids, (b) HCl, (c) $HClO_4$ , (d) $H_2SO_4$ [105].	27
2.6	Scanning electron microscopy images of $WO_3$ films deposited using spray pyrolysis on (a) fluorine-doped tin oxide substrate (FTO) of high sheet resistance and (b) FTO of low sheet resistance [51].	28
2.7	Scanning electron microscopy image of $WO_3$ film deposited using reactive magnetron sputtering [87].	29
2.8	Scanning electron microscopy images of $WO_3$ film deposited using thermal vapour deposition and viewed at different magnifications [57].	30
2.9	Scanning electron microscopy image of $WO_3$ film deposited using thermal oxidation [119].	31
2.10	Scanning electron microscopy images of $WO_3$ film deposited using hydrothermal method and viewed at different magnifications [123].	32
2.11	Scanning electron microscopy images of $WO_3$ films prepared by anodisation at (a) 20 V, (b) 40 V, and (c) 60 V [44].	33
2.12	Scanning electron microscopy images of $WO_3$ films prepared using electrodeposition by (a) continuous mode, (b) pulsed mode at 100 ms pulses, and (c) pulsed mode at 5 ms pulses [40].	36
3.1	Solutions obtained during the preparation of PTA solutions.	40
3.2	Schematic diagram (left) and photograph (right) of the experimental setup of the electrodeposition system. WE, RE, and CE are the working, reference, and counter electrodes, respectively.	42
3.3	Photographs of the as-deposited (left) and annealed (right) films.	43
3.4	FIB images of the milling steps for acquisition of cross-sectional views of the films. (a) Deposition of platinum strip on the surface of the film, (b) regular milling, (c) clean milling, and (d) cross-sectional view at $45^\circ$ tilt.	45
3.5	FIB images on the milling steps for the preparation of TEM samples. (a) Milling of X labels on the surface of the film, (b) deposition of the	47

	platinum strip, (c,d) regular milling on both sides of the platinum strip, (e) regular milling at the bottom part of the sample at 45° tilt, (f,g) clean milling at 1.5° tilt on both sides of the sample with one side released, and (h) regular milling on the remaining side of the sample.	
3.6	TEM sample (a) picked up by a sharp glass tip, (b) adhered to the tip by electrostatic force, and (c) laid flat on the copper grid coated with Formvar.	47
4.1	Linear sweep voltammogram for PTA of 0.05-0.20 mol L <sup>-1</sup> tungsten concentrations measured at a scan rate of 5 mV s <sup>-1</sup> and a step size of 1 mV.	53
4.2	SEM images of WO <sub>3</sub> thin films deposited at potentials of (a) -0.3 V to -0.6 V and (b) -0.7 V to -0.9 V from PTA of 0.05 mol L <sup>-1</sup> tungsten concentration and annealed at 450°C for 2 h. Inset SEM images are the cross-sectional views of the films at 45° tilting.	55
4.3	Representative XRD spectrum of the as-deposited films deposited at -0.4 V from PTA of 0.05 mol L <sup>-1</sup> tungsten concentration (* indicates peaks of FTO substrate).	57
4.4	XRD spectra of WO <sub>3</sub> thin films deposited at various deposition potentials from PTA of 0.05 mol L <sup>-1</sup> tungsten concentration (* indicates peaks of FTO substrate) and annealed at 450°C for 2 h.	58
4.5	Optical transmittance spectra as a function of wavelength of WO <sub>3</sub> thin films deposited at various deposition potentials from PTA of 0.05 mol L <sup>-1</sup> tungsten concentration and annealed at 450°C for 2 h.	59
4.6	Potentiostatic photocurrent densities of WO <sub>3</sub> thin films(deposited from PTA of 0.05 mol L <sup>-1</sup> tungsten concentration and annealed at 450°C for 2 h) measured under chopped illumination (50 W tungsten-halogen lamp; light source-to-sample distances of ~45 cm; intensity of ~30 mW m <sup>-2</sup> ) at 0.7 V <i>versus</i> Ag/AgCl in 0.5 mol L <sup>-1</sup> NaCl aqueous electrolyte.	61
5.1	Deposition current densities as a function of time and tungsten concentration of WO <sub>3</sub> thin films deposited at -0.4 V <i>vs</i> Ag/AgCl for 30 min (PTA electrolyte solution conductivities before electrodeposition also given).	64
5.2	SEM images of WO <sub>3</sub> thin films deposited from PTA of tungsten concentrations of: (a) 0.05-0.20 mol L <sup>-1</sup> for 30 min, (b) 0.05 mol L <sup>-1</sup> for 30-120 min, (c) 0.10 mol L <sup>-1</sup> for 30-60 min and annealed at 450°C for 2 h (insets: cross-sectional views).	68
5.3	XRD spectra of WO <sub>3</sub> thin films deposited from PTA of tungsten concentrations of 0.05 mol L <sup>-1</sup> for 30-120 min (a-d), 0.10 mol L <sup>-1</sup> for 30-60 min (e-f), and 0.20 mol L <sup>-1</sup> for 30 min (g) and annealed at 450°C for 2 h. XRD spectra of FTO substrate of the present work and the reference data for tetragonal SnO <sub>2</sub> [155] also given (* indicates peak from FTO substrate).	69
5.4	Transmittance spectra of WO <sub>3</sub> thin films deposited from PTA of tungsten concentrations of: 0.05 mol L <sup>-1</sup> for 30-120 min (a-d), 0.10 mol L <sup>-1</sup> for 30-60 min (e-f), and 0.20 mol L <sup>-1</sup> for 30 min (g) and annealed at 450°C for 2 h. Transmittance spectrum of FTO substrate also is shown for reference.	70
5.5	Tauc plots of WO <sub>3</sub> thin films deposited from PTA of 0.05-0.20 mol L <sup>-1</sup>	72

	tungsten concentration for 30 min and annealed at 450°C for 2 h.	
5.6	Optical indirect band gaps $E_g$ of $WO_3$ thin films as a function of film thickness $d$ . These films were deposited from PTA of 0.05-0.20 mol $L^{-1}$ tungsten concentration for 30-120 min and annealed at 450°C for 2 h.	72
5.7	Linear potentiodynamic voltammograms (photocurrent density $J_{ph}$ vs applied potential $E$ ), under chopped illumination (50 W tungsten-halogen lamp; light source-to-sample distances of ~45 cm; intensity of ~30 $mW m^{-2}$ ), in aqueous 0.5 mol $L^{-1}$ NaCl (pH 6.27), of $WO_3$ thin films deposited from 0.05-0.20 mol $L^{-1}$ tungsten concentration for 30-120 min and annealed at 450°C for 2 h. The scan rate and step size were 5 $mV s^{-1}$ and 1 mV, respectively.	74
5.8	Plots of $J_{ph}^2$ as a function of applied potential $E$ of $WO_3$ thin films deposited from PTA of 0.05-0.20 mol $L^{-1}$ tungsten concentration for 30 min and annealed at 450°C for 2 h.	76
5.9	Photoconversion efficiencies of $WO_3$ thin films as a function of applied potential $E$ . These films were deposited from PTA of 0.05-0.20 mol $L^{-1}$ tungsten concentration for 30-120 min and annealed at 450°C for 2 h.	77
5.10	Photoconversion efficiencies of $WO_3$ thin films as a function of film thickness $d$ . These films were deposited from PTA of 0.05-0.20 mol $L^{-1}$ tungsten concentration for 30-120 min and annealed at 450°C for 2 h.	78
6.1	XRD spectra of the films deposited from PTA of 0.20 mol $L^{-1}$ tungsten and annealed for 0.5 h at temperatures 25°-500°C; F denotes peaks for FTO.	83
6.2	Relative XRD intensities $R_x = (I_x / (I_{002} + I_{020} + I_{200}))$ (where $x = 002, 020, \text{ or } 200$ ) as a function of annealing time for the films deposited from PTA of 0.20 mol $L^{-1}$ tungsten and annealed at fixed temperatures in the range 275°-500°C.	85
6.3	Relative XRD intensities $R_x = (I_x / (I_{002} + I_{020} + I_{200}))$ (where $x = 002, 020, \text{ or } 200$ ) as a function of annealing temperature for the films deposited from PTA of 0.20 mol $L^{-1}$ tungsten and annealed for (a) 0.5 h and (b) 8 h.	86
6.4	XRD spectra of the films deposited from PTA of 0.05 mol $L^{-1}$ tungsten and annealed for 0.5 h at 25°-500°C; F denotes peaks for FTO.	88
6.5	Relative XRD intensities $R_x = (I_x / (I_{002} + I_{020} + I_{200}))$ (where $x = 002, 020, \text{ or } 200$ ) as a function of annealing time for the films deposited from PTA of 0.05 mol $L^{-1}$ tungsten and annealed at fixed temperatures in the range 350°-500°C.	89
6.6	Relative XRD intensities $R_x = (I_x / (I_{002} + I_{020} + I_{200}))$ (where $x = 002, 020, \text{ or } 200$ ) as a function of annealing temperature for the films deposited from PTA of 0.05 mol $L^{-1}$ tungsten and annealed for (a) 0.5 h and (b) 8 h.	90
6.7	Schematic diagram of the (a) unit cell and (b) three major crystal planes (002), (020), and (200) of monoclinic $WO_3$ .	93
6.8	XRD spectra of films $T_{002}$ , $T_{002+200}$ , and $T_{200}$ ; reference data for monoclinic $WO_3$ [97] also are shown; F denotes peaks for FTO substrate.	96

6.9	SEM secondary electron images of the surface morphologies (a-c) and corresponding TEM cross-sectional images (d-f) of films T <sub>002</sub> , T <sub>002+200</sub> , and T <sub>200</sub> .	97
6.10	Optical transmittance spectra of films T <sub>002</sub> , T <sub>002+200</sub> , and T <sub>200</sub> .	99
6.11	XPS spectra of (a) W(4f) and (b) O(1s) for films T <sub>002</sub> , T <sub>002+200</sub> , and T <sub>200</sub> .	101
6.12	Threefold correlation between crystallographic orientation, oxygen vacancy concentration, and optical indirect band gap.	104
6.13	(a) XPS valence band and (b) electronic band structure of films T <sub>002</sub> , T <sub>002+200</sub> , and T <sub>200</sub> ; E <sub>g</sub> , CB, VB, and ΔVBM are optical indirect band gap, conduction band, valence band, and energy difference in valence band maxima, respectively.	106
6.14	Linear potentiodynamic photocurrent densities of films T <sub>002</sub> , T <sub>002+200</sub> , and T <sub>200</sub> measured in 0.5 mol L <sup>-1</sup> NaCl aqueous solution under the chopped illumination from a 300 W Xe lamp (~280 mW cm <sup>-2</sup> ) coupled with air mass 1.5 global and UV (<305 nm) blocking filters.	107
6.15	Cyclic voltammograms of films T <sub>002</sub> , T <sub>002+200</sub> , and T <sub>200</sub> measured in 0.5 mol L <sup>-1</sup> NaCl aqueous solution in dark environment.	109
6.16	Photocatalytic degradation of methylene blue as a function of irradiation time <i>t</i> . C <sub><i>t</i></sub> and C <sub>0</sub> are the concentrations of methylene blue at irradiation time <i>t</i> and <i>t</i> = 0, respectively.	110
7.1	Thicknesses of WO <sub>3</sub> thin films as a function of deposition times. Dashed line indicates film thickness ~700 nm. These films were deposited from pure PTA of 0.20 mol L <sup>-1</sup> tungsten concentration and PTA containing 0.03 mol L <sup>-1</sup> carboxylic acids and annealed at 450°C for 2 h.	115
7.2	Schematic diagram of the effects of hydronium ions and conjugate bases on deflocculation and dispersion of PTA ions.	118
7.3	SEM images of WO <sub>3</sub> thin films of similar thicknesses ~700 nm deposited from (a) pure PTA of 0.20 mol L <sup>-1</sup> tungsten concentration and PTA containing 0.03 mol L <sup>-1</sup> (b) formic acid, (c) oxalic acid, and (d) citric acid and annealed at 450°C for 2 h.	119
7.4	XRD patterns of WO <sub>3</sub> thin films of similar thicknesses ~700 nm deposited from pure PTA of 0.20 mol L <sup>-1</sup> tungsten concentration and PTA containing 0.03 mol L <sup>-1</sup> carboxylic acids and annealed at 450°C for 2 h. * marks the FTO peaks.	122
7.5	Representative Williamson-Hall plot ( $\beta\cos\theta = 2\varepsilon\sin\theta + 0.9\lambda/r$ ) [211] of WO <sub>3</sub> thin films deposited from pure PTA of 0.20 mol L <sup>-1</sup> tungsten concentration and annealed at 450°C for 2 h. $\beta$ is the full-width-half-maximum of the XRD peak while $\varepsilon$ , <i>r</i> , and $\lambda$ are the sample strain and crystallite size and the X-ray wavelength, respectively. $\varepsilon$ and <i>r</i> can be obtained respectively from the gradient and the extrapolation of the plot to the abscissa.	124
7.6	Optical transmittance spectra of WO <sub>3</sub> thin films of similar thicknesses ~700 nm deposited from pure PTA of 0.20 mol L <sup>-1</sup> tungsten concentration and PTA containing 0.03 mol L <sup>-1</sup> carboxylic acids and annealed at 450°C for 2 h.	125
7.7	Transient open-circuit photopotential measurements of WO <sub>3</sub> thin films of similar thicknesses ~700 nm deposited from pure PTA of 0.20 mol	127

	$L^{-1}$ tungsten concentration and PTA containing $0.03 \text{ mol L}^{-1}$ carboxylic acids and annealed at $450^{\circ}\text{C}$ for 2 h. The light source used was a 50 W tungsten-halogen lamp with intensity of $\sim 100 \text{ mW m}^{-2}$ (light source-to-sample distance of $\sim 25 \text{ cm}$ ).	
7.8	Transient photocurrent measurements of $\text{WO}_3$ thin films of similar thicknesses $\sim 700 \text{ nm}$ deposited from pure PTA of $0.20 \text{ mol L}^{-1}$ tungsten concentration and PTA containing $0.03 \text{ mol L}^{-1}$ carboxylic acids and annealed at $450^{\circ}\text{C}$ for 2 h. Measurements were taken under a chopped illumination (50 W tungsten-halogen lamp; light source-to-sample distances of $\sim 25 \text{ cm}$ ; intensity of $\sim 100 \text{ mW m}^{-2}$ ) at an applied potential of 0.7 V.	128
7.9	Transient photocurrent measurements of $\text{WO}_3$ thin films of similar thicknesses $\sim 700 \text{ nm}$ deposited from pure PTA of $0.20 \text{ mol L}^{-1}$ tungsten concentration and PTA containing $0.03 \text{ mol L}^{-1}$ carboxylic acids and annealed at $450^{\circ}\text{C}$ for 2 h. Measurements were taken under the illumination from a 50 W tungsten-halogen lamp (light source-to-sample distances of $\sim 25 \text{ cm}$ ; intensity of $\sim 100 \text{ mW m}^{-2}$ ) at an applied potential of 0.7 V.	129
7.10	SEM images of $\text{WO}_3$ thin films of similar thicknesses $\sim 400 \text{ nm}$ deposited from (a) pure PTA of $0.20 \text{ mol L}^{-1}$ tungsten concentration and PTA containing oxalic acid of concentrations (b) $0.01 \text{ mol L}^{-1}$ , (c) $0.03 \text{ mol L}^{-1}$ , (d) $0.05 \text{ mol L}^{-1}$ , and (e) $0.10 \text{ mol L}^{-1}$ and annealed at $450^{\circ}\text{C}$ for 2 h. Insets in (a) and (e) are at lower magnification.	131
7.11	AFM images of $\text{WO}_3$ thin films of similar thicknesses $\sim 400 \text{ nm}$ deposited from (a) pure PTA of $0.20 \text{ mol L}^{-1}$ tungsten concentration and PTA containing oxalic acid of concentrations (b) $0.01 \text{ mol L}^{-1}$ , (c) $0.03 \text{ mol L}^{-1}$ , (d) $0.05 \text{ mol L}^{-1}$ , and (e) $0.10 \text{ mol L}^{-1}$ and annealed at $450^{\circ}\text{C}$ for 2 h.	132
7.12	RMS surface roughnesses ( $\diamond$ ) and surface area ratios ( $\blacksquare$ ) as a function of grain size of $\text{WO}_3$ thin films of similar thicknesses $\sim 400 \text{ nm}$ deposited from (a) pure PTA of $0.20 \text{ mol L}^{-1}$ tungsten concentration and PTA containing oxalic acid of concentrations (b) $0.01 \text{ mol L}^{-1}$ , (c) $0.03 \text{ mol L}^{-1}$ , (d) $0.05 \text{ mol L}^{-1}$ , and (e) $0.10 \text{ mol L}^{-1}$ and annealed at $450^{\circ}\text{C}$ for 2 h.	134
7.13	XRD spectra of monoclinic $\text{WO}_3$ thin films of similar thicknesses $\sim 400 \text{ nm}$ deposited from (a) pure PTA of $0.20 \text{ mol L}^{-1}$ tungsten concentration and PTA containing oxalic acid of concentrations (b) $0.01 \text{ mol L}^{-1}$ , (c) $0.03 \text{ mol L}^{-1}$ , (d) $0.05 \text{ mol L}^{-1}$ , and (e) $0.10 \text{ mol L}^{-1}$ (* FTO peaks) and annealed at $450^{\circ}\text{C}$ for 2 h.	136
7.14	Transmittance spectra of $\text{WO}_3$ thin films of similar thicknesses $\sim 400 \text{ nm}$ deposited from (a) pure PTA of $0.20 \text{ mol L}^{-1}$ tungsten concentration and PTA containing oxalic acid of concentrations (b) $0.01 \text{ mol L}^{-1}$ , (c) $0.03 \text{ mol L}^{-1}$ , (d) $0.05 \text{ mol L}^{-1}$ , and (e) $0.10 \text{ mol L}^{-1}$ and annealed at $450^{\circ}\text{C}$ for 2 h.	137
7.15	Linear potentiodynamic photocurrent densities of $\text{WO}_3$ thin films deposited from (a) pure PTA of $0.20 \text{ mol L}^{-1}$ tungsten concentration and PTA containing oxalic acid of concentrations (b) $0.01 \text{ mol L}^{-1}$ , (c) $0.03 \text{ mol L}^{-1}$ , (d) $0.05 \text{ mol L}^{-1}$ , and (e) $0.10 \text{ mol L}^{-1}$ and annealed at $450^{\circ}\text{C}$ for 2 h. Illumination was from a 50 W tungsten-halogen lamp	140

	(light source-to-sample distances of ~25 cm; intensity of ~100 mW m <sup>-2</sup> ). Dark currents (measured without illumination) also are shown.	
7.16	Schematic of trend of size effect on photocurrent density, where arrows indicate effect of fundamental microstructural feature (below arrows) on the photoelectrochemical performance factor (above arrows) (→ indicates increase in performance factor; ← indicates decrease in performance factor). Solid line (–) indicates experimental data; dotted line (···) indicates extrapolation; GB = grain boundaries.	143
A-1	Spectral output of the 300 W ozone free Xe lamp (Newport; part number 6258).	A1
A-2	Spectral output of the 8 W Hg lamp (UVP; major spectral output at 254 nm).	A2
A-3	Spectral output of the tungsten-halogen and Xe arc lamps [A1].	A3
A-4	XRD stick pattern of monoclinic $\gamma$ -WO <sub>3</sub> (space group: P2 <sub>1</sub> /n).	A4
A-5	XRD stick pattern of tetragonal SnO <sub>2</sub> (space group: P4 <sub>2</sub> /mnm).	A5

# LIST OF TABLES

TABLE	CAPTION	PAGE
2.1	Properties of nanostructured WO <sub>3</sub> photoanodes prepared by different techniques.	15
5.1	Summary of analytical data (photoconversion efficiencies measured using tungsten-halogen lamp).	65
6.1	Surface properties of crystal planes of monoclinic WO <sub>3</sub> ; E is the energy of the W-O bond.	94
6.2	Analytical data for films T <sub>002</sub> , T <sub>002+200</sub> , and T <sub>200</sub> .	96
7.1	Analytical data obtained for all the samples from the different tests.	116
7.2	Analytical data obtained from the different tests on the films deposited from pure PTA of 0.20 mol L <sup>-1</sup> tungsten concentration and PTA containing 0.01-0.10 mol L <sup>-1</sup> oxalic acid.	133
7.3	Effect of decreasing grain size on photoelectrochemical (PEC) performance factors and associated photocurrent densities of WO <sub>3</sub> thin films.	142

# LIST OF APPENDICES

APPENDIX	TITLE	PAGE
1	Spectral output of the 300 W ozone free Xe lamp (Newport; part number 6258).	A1
2	Spectral output of the 8 W Hg lamp (UVP; major spectral output at 254 nm).	A2
3	Ratio of the integrated light intensities of tungsten-halogen to Xe lamps.	A3
4	XRD stick pattern of monoclinic $\gamma$ -WO <sub>3</sub> (space group: P2 <sub>1</sub> /n).	A4
5	XRD stick pattern of tetragonal SnO <sub>2</sub> (space group: P4 <sub>2</sub> /mnm).	A5
6	“Photoelectrochemical properties of WO <sub>3</sub> thin films prepared by electrodeposition”, <i>Energy Procedia</i> , <b>34</b> , 617-626 (2013).	A6
7	“Electrodeposited nanostructured WO <sub>3</sub> thin films for photoelectrochemical applications”, <i>Electrochim. Acta</i> , <b>75</b> , 371-380 (2012).	A7
8	“Tunable photoelectrochemical properties by nanostructural control in WO <sub>3</sub> thin films prepared by carboxylic acid-assisted electrodeposition”, <i>J. Phys. Chem. C</i> , <b>117</b> , 17766-17776 (2013).	A8
9	“Photoelectrochemical properties of WO <sub>3</sub> nanoparticulate thin films prepared by carboxylic acid-assisted electrodeposition”, <i>Thin Solid Films</i> , <b>544</b> , 191-196 (2013).	A9

# LIST OF JOURNAL AND CONFERENCE PUBLICATIONS

## JOURNAL PUBLICATIONS

1. **W.L. Kwong**, W. Xu, P. Koshy, J. Hart, M. Ferry, C.C. Sorrell, “Critical Role of {002} Preferred Orientations on Electronic Band Structures of Electrodeposited Monoclinic WO<sub>3</sub>Thin Films”, in preparation.
2. **W.L. Kwong**, A. Nakaruk, P. Koshy, C.C. Sorrell, “Tunable Photoelectrochemical Properties by Nanostructural Control in WO<sub>3</sub>Thin Films Prepared by Carboxylic Acid-Assisted Electrodeposition”, *J. Phys. Chem. C*, **117**, 17766–17776 (2013).
3. **W.L. Kwong**, N. Savvides, C.C. Sorrell, “Electrodeposited Nanostructured WO<sub>3</sub> Thin Films for Photoelectrochemical Applications”, *Electrochim. Acta*, **75**, 371–380 (2012).

## REFEREED CONFERENCE PUBLICATIONS

4. **W.L. Kwong**, A. Nakaruk, P. Koshy, C.C. Sorrell, “Photoelectrochemical Properties of WO<sub>3</sub> Nanoparticulate Thin Films Prepared by Carboxylic Acid-Assisted Electrodeposition”, *Thin Solid Films*, **544**, 191–196 (2013).

## UNREFEREED CONFERENCE PUBLICATIONS

5. **W.L. Kwong**, H. Qiu, A. Nakaruk, P. Koshy, C.C. Sorrell, “Photoelectrochemical Properties of WO<sub>3</sub> Thin Films Prepared by Electrodeposition”, *Energy Procedia*, **34**, 617–626 (2013).

## CONFERENCE PRESENTATIONS

6. “Photoelectrochemical Properties of WO<sub>3</sub>Nanoparticulate Thin Films Prepared by Carboxylic Acid-Assisted Electrodeposition”, Oral presentation at 6<sup>th</sup> International Conference on Technological Advances of Thin Films & Surface Coatings (Thin Films 2012), Singapore, 14-17 July 2012.

# CHAPTER 1

## Introduction

This chapter provides the research background on photoelectrochemical water splitting and the materials used as the photoelectrodes in a photoelectrochemical cell. Research problems related to the photoelectrode materials for photoelectrochemical application are stated. Subsequently, the research objectives and the thesis structure are presented.

### 1.1 Photoelectrochemical Water Splitting

Methods to produce hydrogen are being pursued actively due to the potential of hydrogen to supplement or possibly replace fossil fuels for energy applications. As much as  $\sim 140 \text{ kJ g}^{-1}$  of energy are generated by hydrogen upon its oxidation in a fuel cell, with water being the only by-product [1]. In contrast, conventional combustion of gasoline generates only  $\sim 43 \text{ kJ g}^{-1}$  [2] with  $\text{CO}_2$  as the by-product. Compared to fossil fuels, the utilisation of hydrogen by combustion in fuel cells produces no pollutants or greenhouse gases, which allows hydrogen to be viewed as the fuel of the future [3].

At present, hydrogen is produced principally by conventional electrolysis of water and steam reforming of methane, both of which are associated with greenhouse gas generation [1]. In order to develop an environmentally neutral process for hydrogen production, renewable processes such as photoelectrochemical water splitting[4] must be used. This involves the absorption and conversion of solar energy by a photoelectrode into electrical and subsequently chemical energies, which are finally stored in the form of hydrogen gas. The photoelectrochemical mechanism is detailed in Chapter 2. The scope of current research on photoelectrochemical hydrogen production is large, which includes the design of photoelectrochemical cells, the fabrication of photoelectrodes, the transport and storage of hydrogen fuel, and the design of hydrogen fuel cells. The present work focused on research on the fabrication of photoelectrode materials for photoelectrochemical applications.

Photoelectrodes in photoelectrochemical cells are made of semiconductor materials that require the following mandatory characteristics [3]:

- (i) Optical band gap  $\geq 2$  eV;
- (ii) High stability in aqueous environments;
- (iii) High resistance against photocorrosion.

Since the irradiance of the solar spectrum is high in the visible region (400-800 nm), efficient photoelectrodes should have small optical band gaps (ideally  $\sim 2$  eV) in order to be photosensitive in the visible region [3, 4]. It is equally important to have the conduction and valence band edge positions of the photoelectrodes to be higher and lower than the reduction and oxidation potentials of water, respectively, so that the photogenerated electrons and holes have sufficient energies to activate the water photolysis reactions [1, 4]. Furthermore, the photoelectrodes should have large minority charge diffusion lengths in order to reduce the energy losses due to recombination of the photogenerated excitons (electron-hole pairs) [5]. Additionally, the photoelectrodes should be made of abundant and environmentally friendly materials using economical synthesis techniques in order to allow large-scale implementation.

Various metal oxide and non-oxide semiconductors have been studied as photoelectrode materials. However, compared to oxides, non-oxide materials, which include InP [6], GaP [7], CdSe [8], and CdTe [9], are mostly unstable against photocorrosion [3]. Metal oxides have shown great promises as candidates for photoelectrodes due to their stability in aqueous environments [3, 10]. Since Fujishima and Honda [11] first demonstrated in 1972 hydrogen production by photoelectrochemical water splitting using  $\text{TiO}_2$  as the photoanode, research activities in this area intensified on improving the photoelectrochemical performance of  $\text{TiO}_2$  [12] and investigating the photoelectrochemical performances of other metal oxides, including  $\alpha\text{-Fe}_2\text{O}_3$  [13],  $\text{WO}_3$  [14],  $\text{ZnO}$  [15],  $\text{Cu}_2\text{O}$  [16], and titanate compounds including  $\text{SrTiO}_3$  [17] and  $\text{BaTiO}_3$  [18].  $\text{TiO}_2$  and titanate compounds are stable against corrosion and photocorrosion [10]. However, they suffer low photoelectrochemical efficiencies due to their large optical band gaps ( $>3$  eV) [19], which result in low optical absorptions.  $\text{Fe}_2\text{O}_3$  has small optical band gap of  $\sim 2$  eV [20], which enables absorption of a

significant portion of the visible light. However, it has small hole diffusion length ( $\sim 2\text{-}4$  nm) [21], which causes a high recombination rate of the photogenerated excitons.  $\text{Cu}_2\text{O}$  also has band gap similar to that of  $\text{Fe}_2\text{O}_3$ [22]. However, it is unstable against photocorrosion, where it is reduced from  $\text{Cu}^+$  to  $\text{Cu}^0$  by the photogenerated electrons [23].  $\text{ZnO}$  has similar band gap as that of  $\text{TiO}_2$ , which is too large ( $>3$  eV) to absorb light effectively in the visible region [15].

Among the metal oxides studied as photoelectrode materials,  $\text{WO}_3$  has shown good promise owing to advantages such as low optical band gap [24] ( $\sim 2.7$  eV, compared to that of  $\text{TiO}_2$ , which is  $>3$  eV), high resistance against corrosion and photocorrosion [10], and low-cost fabrication [25-28]. Recently, nanostructured  $\text{WO}_3$  thin films [29] have attracted great attention in photoelectrochemical water splitting applications owing to their large specific area-to-volume ratios, compared to bulk and flat thin films, and this enhances the number of reaction sites on their surfaces for water photolysis [30]. Nanostructured  $\text{WO}_3$  also has shown low photogenerated exciton recombination rates owing to its small dimensions compared to the hole diffusion length of  $\sim 150$  nm [31]. It has been found that the physical, mineralogical, and optical properties of nanostructured  $\text{WO}_3$  are dependent on the synthesis techniques and variable via control of the synthesis parameters [25, 27, 28, 32, 33].

Among the synthesis techniques used to fabricate nanostructured  $\text{WO}_3$  thin films, electrodeposition has the advantages of low processing cost and feasibility in producing large deposition areas. This method is capable of direct deposition of  $\text{WO}_3$  thin films from solution onto transparent conducting substrates, where the physical, mineralogical, and optical properties of the films can be controlled by varying the processing parameters, particularly the composition of the electrolyte solution, deposition parameters, and post-deposition annealing conditions. While nanostructured  $\text{WO}_3$  thin films prepared by electrodeposition have been studied extensively in electrochromic applications [34-38], reports of their photoelectrochemical properties are scarce [39, 40].

## 1.2 Research Objectives

The present work aimed to synthesise electrodeposited  $\text{WO}_3$  thin films and to evaluate their photoelectrochemical properties. The investigation focused on the effects of varying the processing parameters, such as the deposition potential and time, composition of the precursor electrolyte solutions, and post-deposition annealing conditions, on the physical, mineralogical, and optical properties of the films. The work aimed to optimise the preceding properties by controlling the processing parameters in order to maximise the photoelectrochemical performances of the films.

## 1.3 Chapter Outline

An overview of the chapters of the thesis is as follows:

- Chapter 2: This chapter outlines the principles of photoelectrochemical water splitting and discusses the requirements of photoelectrode materials. It includes a review on the application of  $\text{WO}_3$  as a photoelectrode material, with particular focus on nanostructured  $\text{WO}_3$  thin films and strategies to improve their photoelectrochemical efficiencies. The review further expands on the influence of the phases and crystallography on the photoelectrochemical properties of  $\text{WO}_3$ . Subsequently, a literature review on the techniques employed in the synthesis of  $\text{WO}_3$  nanostructures is presented.
- Chapter 3: This chapter describes the experimental procedures employed in the preparation of electrolyte solutions, thin film processing, and characterisation of the films.
- Chapter 4: This chapter presents the investigation of the effect of the deposition potential on the morphological, mineralogical, optical, and photoelectrochemical properties of electrodeposited  $\text{WO}_3$  thin films. The results obtained in this chapter provided the optimal value of deposition potential, which was then employed to synthesise the films in subsequent work.

- Chapter 5: This chapter examines the effects of varying the composition of the precursor electrolyte solutions and the deposition time on the morphological, mineralogical, optical, and photoelectrochemical properties of electrodeposited  $\text{WO}_3$  thin films.
- Chapter 6: This chapter focuses on the effect of crystallographic orientations on the photoelectrochemical performance of electrodeposited  $\text{WO}_3$  thin films. The crystallographic orientations of the films were manipulated through control of the composition of the precursor electrolyte solutions and post-deposition annealing conditions.
- Chapter 7: This chapter describes methods to control the grain sizes of electrodeposited nanocrystalline  $\text{WO}_3$  thin films by using carboxylic acids as dispersing agents in the precursor electrolyte solutions. The effect of variation in the grain sizes on the mineralogical, optical, and photoelectrochemical properties of the films are discussed.
- Chapter 8: This chapter presents the conclusions of the thesis.

# CHAPTER 2

## Literature Review

This chapter provides a review of literature on the use of metal oxides as the photoelectrodes for photoelectrochemical water splitting applications. Because of the broad nature of the research topic, the literature survey has been focused on the synthesis and properties characterisation of  $\text{WO}_3$  thin films for photoelectrochemical applications. In the first part, the principles for photoelectrochemical water splitting and the photoelectrode requirements are discussed. In the second part, the photoelectrochemical performances of nanostructured  $\text{WO}_3$  photoanodes are reviewed. In the last part of the chapter, different methods for synthesising nanostructured  $\text{WO}_3$  thin films are presented.

### 2.1 Photoelectrochemical Water Splitting

In principle, a photoelectrochemical cell consists of at least a photosensitive electrode, *viz.*, photoanode, which is made of *n*-type semiconductor, and a counter electrode [3, 4]. These electrodes are immersed in an aqueous electrolyte and subjected to solar irradiation. Alternatively, the photosensitive electrode can be made of *p*-type semiconductor, which is known as the photocathode. Figure 2.1 shows the schematic diagram of a typical photoelectrochemical cell. The Fermi levels of the photoanode and electrolyte in contact align themselves to achieve thermal equilibrium, in which the majority charge carriers (*i.e.*, electrons) in the photoanode diffuse to the photoanode/electrolyte interface, thereby resulting in band-bending where a region of immobilised positively-charged donor sites and a layer of accumulated negative charges is formed at the surface of the photoanode. The opposite charge accrual gives rise to an intrinsic localised electric field in this region, which is known as the conventional *depletion layer*.

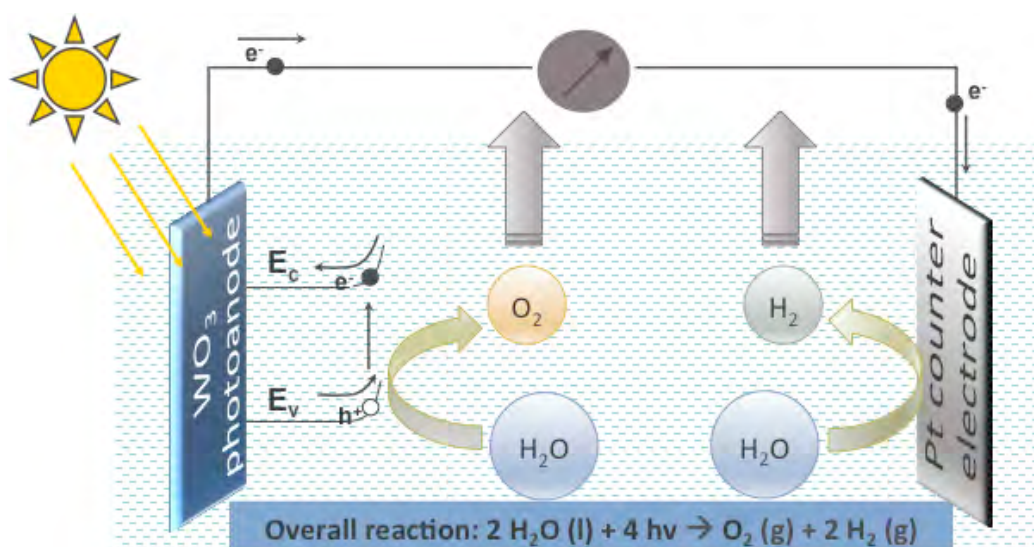
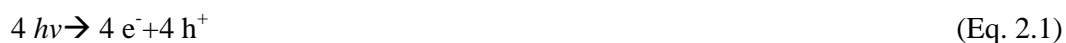


**Figure 2.1:** Schematic diagram of photoelectrochemical cell.  $E_c$  = conduction band energy;  $E_v$  = valence band energy;  $e^-$  = photogenerated electron;  $h^+$  = photogenerated hole.

The photoanode absorbs photons of sufficient energy and generates excitons (*i.e.*, electron-hole pairs) where the electrons are excited from the valence band to the conduction band, thereby creating holes (*i.e.*, vacancies) in the valence band (see Equation 2.1). These photogenerated excitons are separated by the electric field in the depletion layer where the holes are transferred to the photoanode/electrolyte interface for water oxidation. This generates oxygen gas and hydrogen ions at the photoanode (see Equation 2.2) while the electrons travel to the back electrical contact of the photoanode and subsequently to the cathode through the external circuit for water reduction (see Equation 2.3). The production of oxygen and hydrogen gases individually at separate electrodes is advantageous for ease of collection without the need for purification.

Photogeneration of excitons:



where  $h$ ,  $\nu$ ,  $e^-$ , and  $h^+$  are the planck's constant, photon frequency, photogenerated electron and hole, respectively.

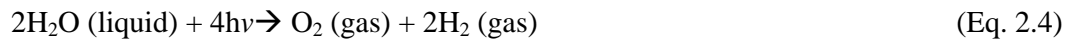
At photoanode:



At cathode:



Overall water splitting reaction:



Critically, photogenerated excitons can be separated immediately outside the depletion layer within the bulk [5]. The distance that a photogenerated hole can diffuse from the location where it is photogenerated, to the edge of the depletion layer without recombining with a photogenerated electron is known as the *hole diffusion length*  $L_p$ . The sum of the hole diffusion length and the depletion layer width  $W$  is known as the *hole retrieval length*, which represents the region over which the photogenerated excitons will contribute to the photocurrent without recombining. In contrast, in the bulk of the photoanode, there is no equivalent mechanism to enhance charge separation and therefore the photogenerated excitons recombine readily and rapidly and hence do not contribute to the photocurrent. The preceding comments apply to individual and multiple grains in solids, such as thin films, provided that each grain is subjected to irradiation and is in contact with the electrolyte. The band diagram illustrating the hole retrieval length in a photoanode is shown in Figure 2.2. It is important to note that the  $L_p$  is a key component in all photocatalytic grains because this distance must be traversed by the photogenerated hole in order to reach the intrinsic charge-separating field of the depletion layer or the surface.

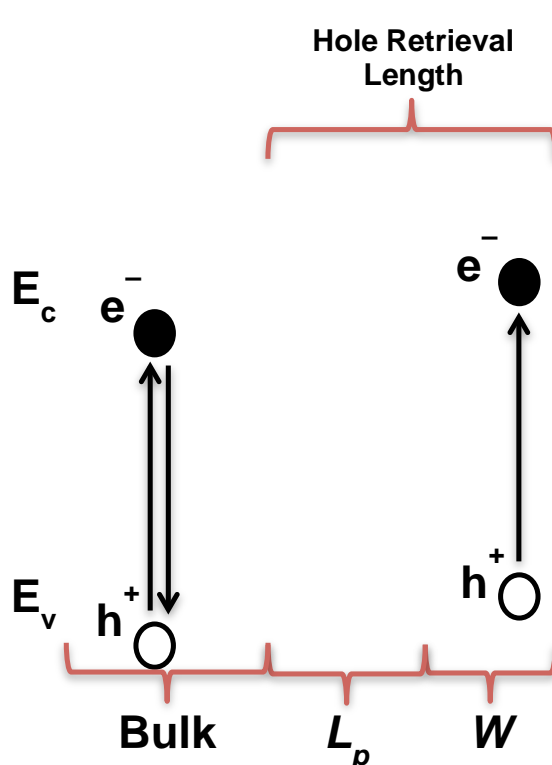


**Figure 2.2:** Band diagram illustrating the hole retrieval length in a photoanode at the photoanode/electrolyte interface.  $L_p$  = hole diffusion length;  $W$  = depletion layer width;  $E_c$  = conduction band energy;  $E_v$  = valence band energy;  $e^-$  = photogenerated electron;  $h^+$  = photogenerated hole [5].

### 2.1.1 Photoelectrode Requirements

The photoelectrode is an important component of a photoelectrochemical cell. It must satisfy the following criteria in order to achieve high photoconversion efficiency (*i.e.*, ratio of the energy attainable from water splitting to the incident solar energy – details on the measurement of photoconversion efficiency are provided in Section 3.3):

(i) *Stable in aqueous environment:*

The photoelectrode should not dissolve in the aqueous electrolyte.

(ii) *Stable against photocorrosion:*

The photoelectrode should be highly stable against photocorrosion, where it has been reported to show reversible oxidation state in order to accommodate

photogenerated holes without decomposition [41]. For example, for  $\text{TiO}_2$ , the reversible oxidation state is  $\text{Ti}^{3+} \rightleftharpoons \text{Ti}^{4+}$ ; for  $\text{WO}_3$ , the reversible oxidation state is  $\text{W}^{4+} \rightleftharpoons \text{W}^{6+}$ . Another consideration for the photostability of a photoelectrode material is based on the determination of the critical decomposition potential of the material [10].

(iii) *Energy band gap of ~2 eV:*

The theoretical water splitting occurs according to Equation 2.4 when the absorbed photon energy  $\geq$  the threshold energy  $E_t = \frac{\Delta G^0(\text{H}_2\text{O})}{nF}$  [1]. The standard Gibbs free energy ( $\Delta G^0(\text{H}_2\text{O})$ ) for the formation of 1 mol of water at 25°C and 1 bar is 237.2 kJmol<sup>-1</sup>; the number of moles of holes (n) required to oxidise 1 mol of water is 2; the Faraday constant (F) is 96485.34 C mol<sup>-1</sup>. Therefore,  $E_t = 1.23$  eV. This corresponds to the minimal electromotive force (emf) required for water splitting, which also corresponds to the threshold optical band gap of the photoanode (or photocathode). The preceding associated with an appropriate electronic band edge positions can photogenerate electrons (or holes) with energies  $\geq 1.23$  eV. However, this theoretical value is underestimated owing to the inevitable energy losses caused by the overpotential at the electrodes and the ionic conductivity of the electrolyte. Therefore, the practical threshold optical band gap of the photoelectrode should be ~2 eV [4]. That is, the photoelectrode with optical band gap <2 eV cannot photogenerate electrons and holes with sufficient energy for water splitting. On the other hand, the photoelectrode with large optical band gap  $\gg 2$  eV is not photosensitive in the visible region of solar spectrum. This compromise between the optical band gap and the photoconversion efficiency of a photoelectrode is shown in Figure 2.3. Provided that the optical band gap of a photoelectrode is  $\geq 2$  eV, the closer the optical band gap to 2 eV, the higher the photoconversion efficiency, owing to the increased optical absorption in the visible region of the solar spectrum.

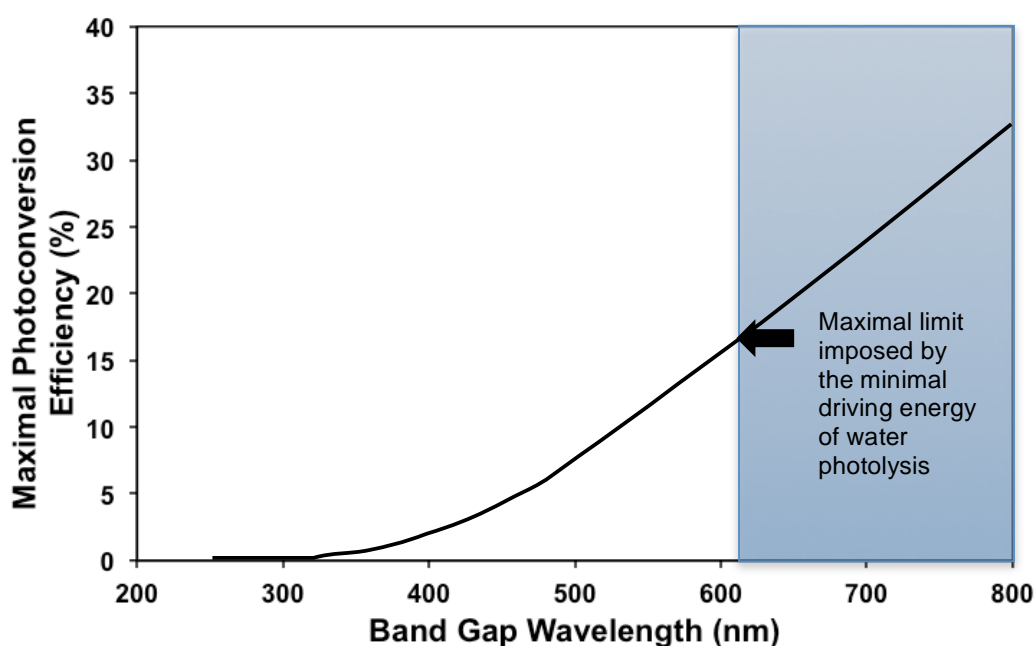


**Figure 2.3:** Maximal photoconversion efficiency as a function of band gap wavelength of a photoelectrode under the AM 1.5 global solar condition [42].

(iv) *Appropriate electronic band edge positions:*

In addition to the threshold optical band gap, the photoelectrode also should have appropriate electronic band edge positions where the conduction band minimum should be higher than the water reduction potential while the valence band maximum should be lower than the water oxidation potential, so as to photogenerate electrons and holes with sufficient energies for water splitting [3, 4]. Inappropriate electronic band edge positions result in the need to apply an external bias in order to create sufficient band bending for water splitting, which reduces the photoconversion efficiency.

(v) *Low electrical resistivity:*

The photoelectrode should have low electrical resistivity to facilitate charge carrier transport at minimal recombination rates.

To date, there is no single material that satisfies all the above-mentioned requirements. The development of new photosensitive semiconductor materials with sufficiently low optical band gaps, high stability in aqueous environment, resistance against photocorrosion, and the capability to perform spontaneous water splitting remains a

challenge, which must be overcome to ensure an efficient photoelectrochemical hydrogen production to meet the global energy demands.

## 2.2 Tungsten Oxide Thin Films as Photoanodes

Among the metal oxides discussed in Section 1.1,  $\text{WO}_3$  was chosen as the photoelectrode material for the present work.  $\text{WO}_3$  is an *n*-type semiconductor, which has been studied in the form of nanostructured thin films for a wide range of applications, including solar energy generation [43], photocatalysis [44], gas and biosensing [45, 46], and electrochromism [36]. It has been considered as an alternative to  $\text{TiO}_2$  (a wide band-gap semiconductor, 3.0-3.2 eV [19]) owing to the advantages of being stable against corrosion and photocorrosion and photosensitive in the visible region of solar spectrum due to its relatively small indirect optical band gap of 2.7-3.0 eV [41].

Early investigation of the photoelectrochemical properties of  $\text{WO}_3$  photoanodes showed that the charge mobility was small ( $\sim 10 \text{ cm}^2 \text{ V}^{-1} \text{ sec}^{-1}$ ) and the hole diffusion length was short ( $\sim 150 \text{ nm}$ ), which implied that the photocurrent mainly arose from the excitons photogenerated within the depletion layer [31]. Therefore, increasing the photocurrents of  $\text{WO}_3$  photoanodes would require the expansion of the depletion layer width, which could be achieved by reducing the donor concentration. However, this would lead to depreciated electrical conductivity/charge transport properties and thus increased energy losses due to the recombination of excitons [47]. The more positive or the lower conduction band minimum of  $\text{WO}_3$  than the water reduction potential makes an external bias a necessity for water splitting to occur [48]. The amorphous tungsten oxide films recrystallised after annealing and demonstrated a decreased band gap (from 3.05 eV in the amorphous phase to 2.75 eV in the monoclinic phase), an increased donor concentration, and consequently a higher photoconversion efficiency [43, 49]. The amorphous tungsten oxide showed rapidly decreasing and inferior photocurrents compared to that of crystalline  $\text{WO}_3$  owing to the presence of lattice defects, which caused recombination of the photogenerated excitons [50]. The intrinsic band gap of  $\sim 2.7 \text{ eV}$  allows the light absorption of  $\text{WO}_3$  in the visible light region up to  $\sim 440 \text{ nm}$  [15].

### 2.2.1 Nanostructured Tungsten Oxide Photoanodes

In the last decade, the development of nanomaterials has attracted wide interest due to their distinctive semiconducting properties, which has led to increased potential for various applications [30]. Nanomaterials offer feasibility in the control of electronic and optical properties by modification of their structures and sizes. Growing nanostructured films by the bottom-up approach minimises the problem of lattice mismatch at the film/substrate interface and hence reduces the defect-trapping of charge carriers. There are various  $\text{WO}_3$  nanostructures described in the literature, which include 0-D nanostructures (nanoparticles) [51], 1-D nanostructures (nanotips, nanorods, nanowires) [52-57], 2-D nanostructures (nanosheets, nanoplates, nanobelts) [25, 58, 59], and 3-D nanostructures (nanocubes, nanospheres, nanopores) [28, 44, 60-63].

There is a growing interest in nanostructured metal oxide thin films as photoelectrodes [30, 64] for photoelectrochemical applications. Nanostructured materials are advantageous in this regard owing to the following [5, 30]:

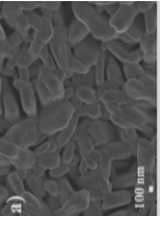
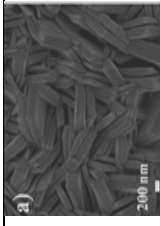
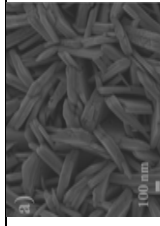
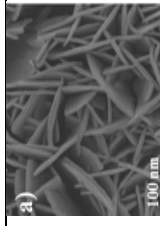
- (i) In nanostructured *n*-type photoanode, there is a high probability that the grain is small relative to the hole diffusion length and thus the photogenerated holes have high probability to diffuse to the photoanode/electrolyte interface to oxidise water before recombining with photogenerated electrons.
- (ii) The high surface areas of nanostructured materials act as active water splitting reaction sites.
- (iii) The grain sizes of nanostructured materials are of the same order as the wavelength of incident light. This causes the incident light to be scattered maximally at the grain boundaries, thereby increasing the optical path length and consequently, the optical absorption is enhanced.

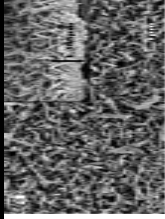
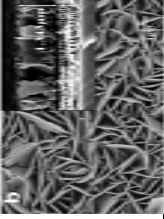
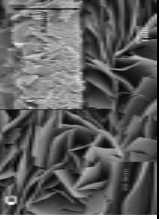
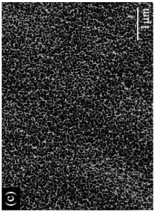
It has been demonstrated that nanostructured  $\text{WO}_3$  thin films show superior photoelectrochemical properties compared to that of bulk  $\text{WO}_3$ [47, 65]. The photoelectrochemical efficiencies of bulk  $\text{WO}_3$  photoanodes are limited by the

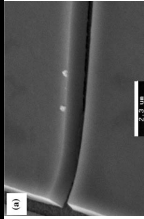
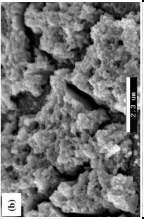
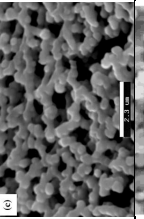
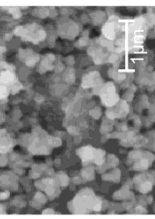
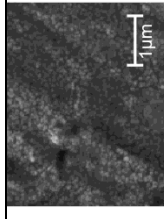
absorption of light with wavelength near the intrinsic band gap wavelength. However, the preceding does not occur in nanostructured  $\text{WO}_3$  photoanodes, where the photoelectrochemical efficiencies near the band gap wavelength increase with increasing film thickness due to increased optical absorption. Moreover, nanostructured  $\text{WO}_3$  photoanodes also show greater efficiency in separating excitons and thus suppressed recombination owing to the *non-conventional depletion layer* formed by a concentration gradient in the solid when it was in contact with the aqueous electrolyte solution. The preceding may be attributed to the exciton separation mechanism that occurs in  $\text{WO}_3$  nanostructures with dimensions smaller than the hole diffusion length of  $\sim 150$  nm. That is, in principle, grains of this size or smaller can suppress exciton recombination since the photogenerated holes can reach the surface and oxidise the water molecule at the photoanode/electrolyte interface before they can recombine with the photogenerated electrons.

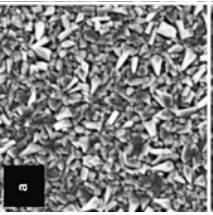
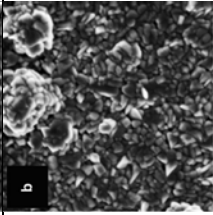
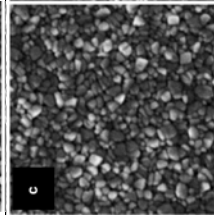
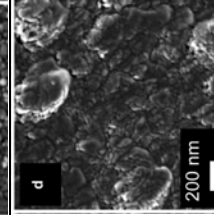
Table 2.1 summarises the properties of nanostructured  $\text{WO}_3$  photoanodes prepared by different techniques. Due to different measurement settings, it is difficult to make direct comparison of the photoelectrochemical performances of the photoanodes synthesised by various techniques. Nonetheless, it can be seen clearly that different growth mechanisms as well as the synthesis parameters associated with various synthesis techniques have resulted in photoanodes with various morphological, mineralogical, optical, and photoelectrochemical properties. A literature survey on the  $\text{WO}_3$  nanostructures prepared by different techniques is presented in Section 2.3.

**Table 2.1:** Properties of nanostructured WO<sub>3</sub> photoanodes prepared by different techniques.

Synthesis technique	Sample / Morphology	Mineralogy	Optical band gap (eV)	Photoelectrochemical measurement setting (Electrolyte / Light source)	Photocurrent density (mA cm <sup>-2</sup> )	Ref.
Hydrothermal	Reaction 17 h–annealed 700°C 	Monoclinic	2.65	0.1 mol L <sup>-1</sup> Na <sub>2</sub> SO <sub>4</sub> / 1.5 G solar simulator of 100 mW cm <sup>-2</sup>	2.25 at 1.1 V vs. Ag/AgCl	[66]
	Reaction 17 h–annealed 500°C 		-		1.4 at 1.1 V vs. Ag/AgCl	
	Reaction 8 h–annealed 500°C 		-		0.5 at 1.1 V vs. Ag/AgCl	
	Reaction 2 h–annealed 500°C 		-		0.4 at 1.1 V vs. Ag/AgCl	

Synthesis technique	Sample / Morphology	Mineralogy	Optical band gap (eV)	Photoelectrochemical measurement setting (Electrolyte / Light source)	Photocurrent density (mA cm <sup>-2</sup> )	Ref.
Solvothermal	WO <sub>3</sub> nanowire array film 	Hexagonal	2.92	0.1 mol L <sup>-1</sup> Na <sub>2</sub> SO <sub>4</sub> / AM 1.5 solar simulator of 100 mW cm <sup>-2</sup>	0.25 at 1.2 V vs. Pt	[67]
	WO <sub>3</sub> nanoflake array film-Type 1 	Monoclinic	2.61		0.75 at 1.2 V vs. Pt	
	WO <sub>3</sub> nanoflake array film-Type 2 	Monoclinic	2.51		1.43 at 1.2 V vs. Pt	
Anodisation	WO <sub>3</sub> nanoporous thin film (anodised at 60 V for 1.0 h+40 V for 0.5 h) 	Monoclinic	2.94	H <sub>2</sub> SO <sub>4</sub> (pH 0) / 300 W Hg lamp (principal wavelength 365 nm) of 2.0 mW cm <sup>-2</sup>	2.5 at 1.5 V vs. SCE	[68]
	WO <sub>3</sub> planar thin film (anodised at 20 V for 0.5 h)		3.25		0.25 at 1.5 V vs. SCE	

Synthesis technique	Sample / Morphology	Mineralogy	Optical band gap (eV)	Photoelectrochemical measurement setting (Electrolyte / Light source)	Photocurrent density ( $\text{mA cm}^{-2}$ )	Ref.
Sol-gel	Pure PTA 	Monoclinic	2.6	1 mol L <sup>-1</sup> H <sub>2</sub> SO <sub>4</sub> / 1 kW Xe lamp of 86 mW cm <sup>-2</sup>	0.7 at 1.6 V vs. SCE	[69]
	PTA+HCl 				2.4 at 1.6 V vs. SCE	
	PTA+HClO <sub>4</sub> 				1.6 at 1.6 V vs. SCE	
Electrodeposition	Continuous deposition 	-	-	0.1 mol L <sup>-1</sup> NaOAc / 150 W Xe lamp of 25 mW cm <sup>-2</sup>	0.0124 at 0 V vs. Pt	[40]
	Pulsed deposition 				0.0086 at 0 V vs. Pt	

Synthesis technique	Sample / Morphology	Mineralogy	Optical band gap (eV)	Photoelectrochemical measurement setting (Electrolyte / Light source)	Photocurrent density ( $\text{mA cm}^{-2}$ )	Ref.
Reactive magnetron sputtering	Sputter pressure 30 mTorr-film thickness 470 nm 	Monoclinic / Orthorhombic	-	0.5 mol L <sup>-1</sup> NaClO <sub>4</sub> (pH 4.6) / Hg-Xe lamp	2.000 at 1 V <sub>vs.</sub> Ag/AgCl	[70]
	Sputter pressure 20 mTorr-film thickness 395 nm 				2.500 at 1 V <sub>vs.</sub> Ag/AgCl	
	Sputter pressure 10 mTorr-film thickness 435 nm 				0.250 at 1 V <sub>vs.</sub> Ag/AgCl	
	Sputter pressure 2 mTorr-film thickness 450 nm 				0.125 at 1 V <sub>vs.</sub> Ag/AgCl	

### 2.2.2 Strategies To Improve The Photoconversion Efficiency

In brief, the efficiency of a photoelectrode is mainly dependent on its excellence in solar absorptivity, photogenerated charge separation, and charge transport properties. That is, an efficient photoanode absorbs light in the visible region for the photogeneration of excitons, effectively separate them to avoid losses due to recombination, and effectively transfer them to the respective water splitting reaction sites at the photoanode/electrolyte and cathode/electrolyte interfaces. There is a number of strategies to improve the photoconversion efficiency of a photoelectrode and this is summarised as follows:

(i) *Nanostructural control:*

Nanostructuring a material increases the specific surface area to volume ratio and the associated number of reaction sites [30]. Furthermore, the photogenerated minority charge carriers in a nanostructured photoelectrode stand higher chances to diffuse to the surface of the photoelectrode to participate in water splitting reaction provided that the dimension of the nanostructure is smaller than the typical minority charge carrier diffusion length [5]. In addition, it has been reported that vectorial charge transport can be developed in 1-D nanostructures, which enhances the photoconversion efficiency by reducing the exciton recombination rate [71, 72].

Nonetheless, decreasing the dimensions of a material also is likely to increase its structural defects owing to the increased structural termination [60, 73]. The nature of a defect in the charge transport properties of a photoelectrode is dependent on its location in the photoelectrode [74, 75]. Defects located on the surface of a photoanode may act as reaction sites by facilitating the trapping of photogenerated holes and adsorption of water molecules. On the other hand, defects located within the bulk of the photoanode, such as grain boundary areas, may trap photogenerated electrons and thereby increases their recombination rate during the transport to the back contact (substrate). It also has been observed that when the dimensions of a material is less than or equal to its exciton Bohr radius (*i.e.*, characteristic exciton distance at the lowest energy

state), quantum size effect occurs where the optical band gap increases due to the spatial confinement of the photogenerated excitons [1, 75, 76]. The grain size optimisation of a photoelectrode, which can be done by controlling the synthesis parameters [60, 73, 77-79], is important for optimisation of the above-mentioned properties in order to maximise the photoelectrochemical performance.

(ii) *Dye-sensitisation:*

The improved photosensitivity of a photoelectrode in the visible light region has been achieved by dye-sensitisation, in which the concept is inspired by the optical absorption of chlorophyll in plants in natural photosynthesis [75]. The dye can be incorporated onto the photoelectrode by soaking it in the solution containing the dye for an extended period of time [80]. These small-band-gap dye molecules absorb visible light and photogenerate excitons. Provided that the conduction band edge of the dye is more negative than that of the photoanode, the photogenerated electrons can be transferred to the conduction band of the photoanodes whereas the photogenerated holes are consumed by redox mediators such as the iodide/tri-iodide( $I/I_3^-$ ) couple. The typically insufficient oxidation potential of the photogenerated holes fail to activate the water oxidation reaction and thus results in only single water reduction reaction, which is unattractive for photoelectrochemical application [81]. Recent research focuses on the implementation of dye-sensitised photoelectrodes incorporated with water-oxidation/reduction co-catalysts such that the dual processes of water oxidation and reduction can be facilitated [82].

(iii) *Doping:*

The optical band gap engineering of a material is viable through the doping of metal and/or non metal elements [75, 83]. Depending on the radii of the dopants, the dopants may replace the atoms of the material (substitutional doping) or be incorporated into the interstitial spacing of the crystal structure of the material (interstitial doping). These dopants impose mid-gap band into the band structure of the material, thereby forming a narrower effective band gap. The mid-gap

band position and the conductivity of a doped material is dependent on the type and amount of the dopants [84, 85].

In the case of heavy doping, Burstein-Moss effect may occur where degenerate materials that behave like a metal is formed [1, 86]. Degenerate materials demonstrate larger optical band gaps as compared to that of pure materials. For example, in an *n*-type heavily doped material, the high donor concentration causes up-shifting of Fermi level into the conduction band. In this case, electrons in the valence band are photoexcited into the energy levels located above the Fermi level, which also is now located well above the conduction band minimum. Therefore, the apparent optical band gap is measured as the sum of the band gap (between valence band maximum and conduction band minimum) and the Burstein-Moss shift (between conduction band minimum and Fermi level). While doping may be employed for optical band gap engineering, it often leads to the formation of defect sites attributed to damaged crystal structures caused by the introduction of dopants, which trap and recombine excitons [87].

(iv) *Co-catalysts:*

The photoelectrochemical performance of a photoelectrode often is limited by the slow charge carrier transfer at the interfaces of the photoelectrode/electrolyte and photoelectrode/substrate, which increases the probability of recombination of the excitons [83]. The slow charge carrier transfer, which also is the main cause of overpotential, may be due to the (i) charge carrier trapping at defect sites on the surface and within the bulk of photoelectrode and (ii) insufficient energies of the photogenerated electrons and holes to drive the water splitting reactions. Consequently, an external bias usually is necessary for the initiation of the water splitting reactions.

This issue may be resolved by depositing co-catalysts on the photoelectrode [75]. The excitons photogenerated in the photoelectrode are separated where the photogenerated electrons (or holes) are transferred to the oxygen (or hydrogen) evolving co-catalysts for water reduction (or oxidation). The high conductivity and the electrochemical properties of the co-catalysts facilitate swift interfacial

transfer of the photogenerated charge carriers from the photoelectrodes to the co-catalysts to the surface-adsorbed water molecules and thereby reduces the overpotential for water splitting reactions, which lowers the external bias and improves the photoconversion efficiency. Examples of co-catalysts include Pt, Au, NiO<sub>x</sub>, RuO<sub>2</sub>, and IrO<sub>2</sub>. The high cost of noble metals, such as Pt and Au, reduces their practicability for implementation at commercial scales.

Recent research has focused on oxide-based co-catalysts. Of these, cobalt-based and manganese-based oxygen evolution co-catalysts have shown great promises owing to the similar crystal structures with that of the oxygen evolving complex (manganese-calcium cluster) in the photosystem II of plants[81]. In addition, the high abundance of these elements makes them favourable as low-cost catalysts. More recently, investigation of non-metallic co-catalysts such as carbon nanomaterials (carbon nanotubes, graphene *etc.*) has drawn great attention owing to their unique structures and the associated physical properties that can revolutionise the way that photogenerated charge carriers are transported within and at the interfaces of the carbon-incorporated photoelectrode, leading to an increase in the photoconversion efficiency[88].

(v) *Binary/ternary compounds:*

Photoelectrodes consisting of binary or ternary metal oxides, which usually are synthesised using solid state reaction method, have shown improved photocurrents owing to their enhanced optical absorption [75]. This is due to the hybridisation of the atomic orbitals of the new metal ions with the metal oxides, which results in a new band structure of the binary/ternary metal oxide [89]. However, important attention needs to be paid to the choices of new metal ions to be inserted to form binary/ternary metal oxides because they affect the resultant crystal structures. It has been reported that the band structures of binary/ternary metal oxides are dependent on the crystal structures (or precisely the interatomic distance), where small band gaps are obtained due to the weak orbital interaction in the crystal structure with large interatomic distances [90, 91].

(vi) *Heterostructures:*

Heterojunction photoelectrodes have demonstrated higher photocurrents than that of the photoelectrodes consisting of a single material owing to the improvement in solar absorption and separation of the photogenerated excitons [75, 92]. These heterojunction films, which consist of layers of two or more metal oxides, exhibit combined properties of the multiple metal oxides that are not seen in the single metal oxides. The choices of the metal oxides are based on the stability against corrosion and photocorrosion, the photosensitivity in different regions of the solar spectrum, and the appropriate conduction and valence band edge positions that aid in the separation of photogenerated excitons.

Figure 2.4 shows the schematic diagram of an example of bi-layered  $\text{WO}_3/\text{BiVO}_4$  heterojunction thin film photoanode [93]. Inspired by the Z-scheme two-step photoexcitation in natural photosynthesis [94], the photons of lower energies are absorbed by the small-band-gap  $\text{BiVO}_4$  while photons of higher energies are absorbed by large-band-gap  $\text{WO}_3$ . To ensure swift transfer of the photogenerated charge carriers, the conduction band minimum of the large-band-gap  $\text{WO}_3$  should be more positive than that of the small-band-gap  $\text{BiVO}_4$  but more negative than the water reduction potential (0 V *versus* NHE). In this case, the photogenerated excitons are separated spatially where the electrons are transferred from the conduction band of  $\text{BiVO}_4$  to the conduction band of  $\text{WO}_3$  and migrate to the back contact while the holes are transferred from the valence band of  $\text{WO}_3$  to the valence band of  $\text{BiVO}_4$  and oxidise water molecules at the photoanode/electrolyte interface. However, the design of a heterojunction photoelectrode is complex compared to a single-material photoelectrode, in which rapid transfer kinetics of the charge carriers must be ensured at the heterojunctions as well as at the interfaces of back contact/photoelectrode/electrolyte.

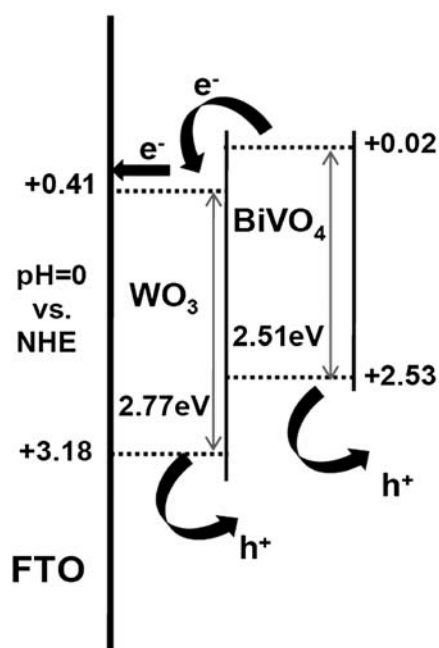


**Figure 2.4:** Band structure diagram of  $\text{WO}_3/\text{BiVO}_4$  heterojunction film [93]. FTO = fluorine-doped tin oxide substrate;  $e^-$  = photogenerated electron;  $h^+$  = photogenerated hole.

### 2.2.3 Phases and Crystallography – Effect on Photoelectrochemical Properties

A number of tungsten oxide phases has been reported [95]. Some of these oxides are hypostoichiometric and unstable. The most stable  $\text{WO}_3$  has a tungsten oxidation state of +6. It has a high melting point of  $1472^\circ\text{C}$  and high stability in acidic solutions. The indirect optical band gap of  $\text{WO}_3$  is dependent on its crystallinity. Larger band gaps have been observed in  $\text{WO}_3$  of lower crystallinity [43].  $\text{WO}_3$  exhibits temperature-dependent crystal phases, where it exists in tetragonal form ( $\text{P4/nmm-D}_{4h}^7$ ) above  $740^\circ\text{C}$ ; orthorhombic form ( $\text{Pmnb-D}_{2h}^{16}$ ) at  $330^\circ\text{--}740^\circ\text{C}$ ; monoclinic form ( $\gamma\text{-WO}_3$ ;  $\text{P2}_1/\text{n}$ ) from  $17^\circ\text{--}330^\circ\text{C}$ ; triclinic form ( $\beta\text{-WO}_3$ ;  $\text{P1-C}_1^1$ ) from  $-50^\circ\text{C}$  to  $17^\circ\text{C}$ ; and monoclinic form ( $\alpha\text{-WO}_3$ ,  $\text{Pc-C}_2^2$ ) from  $-143^\circ\text{C}$  to  $-50^\circ\text{C}$ . The metastable oxides such as hexagonal  $\text{WO}_3$  ( $\text{h-WO}_3$ ) and pyrochlore  $\text{WO}_3$  ( $\text{p-WO}_3$ ) also have been reported, which transform to monoclinic  $\text{WO}_3$  above  $400^\circ\text{C}$  [95].

It has been shown that among the crystal phases, monoclinic  $\gamma$ - $\text{WO}_3$  demonstrates the best photoelectrochemical performance [96]. Randomly distributed monoclinic  $\text{WO}_3$  powders show equivalent intensities for the X-ray diffraction peaks of the three dominant planes (002), (020), and (200) [97], as shown in Appendix 4. Recent studies [63, 98, 99] have shown that the growth of  $\text{WO}_3$  grain facets could be controlled through the use of growth directing agents, which were preferentially adsorbed onto the crystal surfaces. The monoclinic  $\text{WO}_3$  quasi-cubic-like crystals, with equal proportions of (002), (020), and (200) facets, showed superior oxygen evolution from water compared to rectangular sheet-like samples with predominantly (002) facets owing to the lower valence band maximum and hence stronger oxidation power of the former [63]. Nonetheless, the latter was more capable in photocatalytic reduction of  $\text{CO}_2$  owing to the higher conduction band minimum, which resulted in a higher reduction potential of the photogenerated electrons. Zhang *et al.*[99] produced orthorhombic  $\text{WO}_3$  nanocrystals with tunable (001) facet surface area and observed that the (001) facet demonstrated the best photocatalytic activity of the orthogonal planes owing to its high surface energy, which enhanced the photoexcitation and suppression of recombination of excitons. The preceding examples showed that the performances of  $\text{WO}_3$  photoanodes were strongly dependent on the crystallographic orientations of the exposed surface, which ultimately determines their physical and electronic properties.

The surface state of a photoelectrode has a critical effect on the efficiency of a photoelectrochemical cell [1, 4]. It accommodates water oxidation (in the case of an *n*-type photoanode) at the photoanode/electrolyte interface. This interfacial reaction is influenced by the (i) surface configurations (numbers of reaction and recombination sites), which determine the efficiencies of photogenerated hole transport and the adsorption of reactants (water molecules) at the interface, and (ii) surface electronic states (valence and conduction band edges), which determine the reduction and oxidation energies of the photogenerated electrons and holes, respectively, and thus the feasibility of reduction and oxidation of water molecules by these charge carriers [63]. The anisotropic properties associated with different crystal planes of a material indicate that the crystallographic orientation of a photoelectrode surface can influence its photoelectrochemical performance. Therefore, it is important to understand and control

the crystallography of photoelectrodes for optimisation of their photoelectrochemical performances.

While most studies have focused on growth control of the typical exposed {001} crystal facets of  $\text{WO}_3$  powders, equivalent work in thin film forms for use in photoelectrochemical cells is uncommon. Another drawback is the use of growth directing agents, which has the potential to result in sample contamination. A novel approach to control the crystallographic orientations of electrodeposited  $\text{WO}_3$  thin films uncontaminated by growth directing agents through the manipulation of the deposition and annealing parameters is presented in Chapter 6.

### 2.3 Synthesis of Nanostructured Tungsten Oxide Thin Films

Many processing techniques have been used to produce  $\text{WO}_3$ , which include sol-gel, spray pyrolysis, reactive sputtering deposition, thermal vapour deposition, thermal oxidation, hydrothermal/solvothermal methods, anodisation, and electrodeposition. The photoelectrochemical performances of nanostructured  $\text{WO}_3$  films are greatly dependent on the synthesis techniques, in which various nanostructures with different physical and optical properties are produced. In general, meso- or nanoporous structures and nanoparticles can be obtained by sol-gel [18], anodisation [25, 43, 44, 100], and electrodeposition [14, 39, 40] while 1-D nanostructures such as nanorods, nanowires, and nanotips can be synthesised by hydrothermal/solvothermal [45, 101] and thermal oxidation [52, 102] methods. Anodisation at elevated temperatures also produces 2-D nanostructures such as nanoplatelets, nanodisks, and nanobelts [59]. This section reviews the techniques commonly employed for the synthesis of  $\text{WO}_3$  nanostructures.

#### 2.3.1 Sol Gel

Sol-gel produces precipitation of tungsten oxide from precursor solutions, which is followed by centrifugation and annealing to produce crystalline  $\text{WO}_3$  powders. The powders can be processed to form thin films using techniques such as spin-coating, doctor blade coating, and dip-coating. The properties of the films can be controlled by altering the solution chemistry, *i.e.*, precursor materials, solvents, solution pH, solution

concentration, and addition of organic dispersants. It has been reported that flat films with smooth surfaces resulted from pure precursor solutions whereas nanoparticulate and nanoporous films were produced from acidified precursor solutions [27, 32, 69, 103-105]. Examples of the microstructures of  $\text{WO}_3$  films produced using sol-gel method are provided in Figure 2.5 [105]. The synthesis of  $\text{WO}_3$  using this method is advantageous in terms of the low processing cost and the ease of subsequent large-area thin film coating. However, control of the properties of  $\text{WO}_3$  requires careful attention to the solution chemistry.

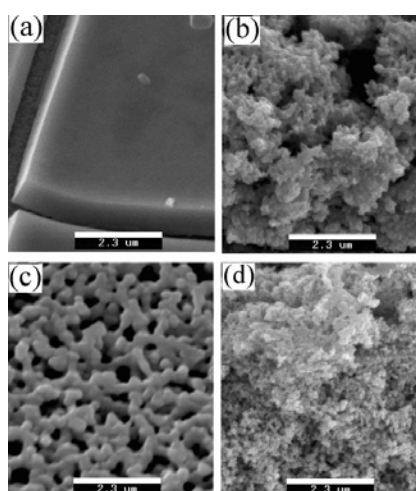


**Figure 2.5:** Scanning electron microscopy images of  $\text{WO}_3$  films deposited using sol-gel from precursor solutions containing (a) no acids, (b)  $\text{HCl}$ , (c)  $\text{HClO}_4$ , (d)  $\text{H}_2\text{SO}_4$  [105].

### 2.3.2 Spray Pyrolysis Deposition

In spray pyrolysis deposition, a fine mist of droplets containing tungsten precursor reactants are sprayed and carried by a compressed inert gas flow to a heated substrate where the reactants react to form tungsten oxide films. The droplet solution is prepared such that the reaction products other than tungsten oxide are volatile at the deposition temperature. Modifying the spray parameters, *i.e.*, nozzle-substrate distance, substrate temperature and type, carrier gas, droplet size, cooling rate after deposition, and composition of the precursor reactants can vary the deposition rate and properties of the films [51, 106-109]. The films deposited using this method have been reported to exhibit nanoparticulate structures. Examples of the microstructures of the films are

shown in Figure 2.6 [51]. This method is advantageous for its simplicity in apparatus setting and possibility for mass production [110]. However, the quality of the film is dependent on the droplet size, which has been reported as being difficult to control [111].

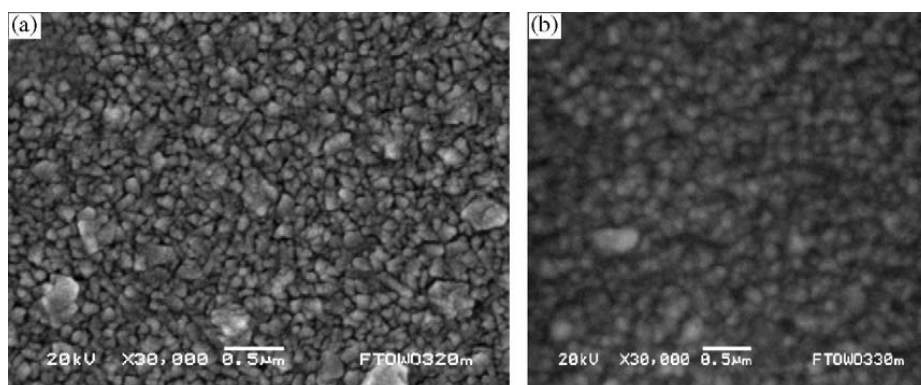


**Figure 2.6:** Scanning electron microscopy images of  $\text{WO}_3$  films deposited using spray pyrolysis on (a) fluorine-doped tin oxide substrate (FTO) of high sheet resistance and (b) FTO of low sheet resistance [51].

### 2.3.3 Reactive Magnetron Sputtering

Reactive magnetron sputtering deposits tungsten oxide films by reacting the sputtered tungsten target atoms with the reactive gas fed into a vacuum chamber. Typically, a tungsten metal, which serves as a source target, is placed in a vacuum chamber where it is subjected to negative electrical potential and thereby establishes an electric field in the chamber. Mixture of reactive and inert gases such as oxygen or nitrogen and argon gases are introduced into the chamber and are ionised through collisions with the fast-moving residual electrons that are accelerated by the electric field. These newly released electrons also are accelerated by the electric field and participate in collisions with other neutral gas molecules, thereby generating chain ionisation reaction and causing sustained plasma discharge. The positively charged gas ions are attracted by the negatively charged tungsten target where they bombard and eject the tungsten atoms from the target surface. These sputtered tungsten atoms reach the remote substrate and react with the reactive gases to form tungsten oxide films. The properties of the films can be manipulated by varying the process parameters such as the compositions and the partial pressures of reactive and inert gases, the substrate temperature and the plasma

power. The poly-nanocrystalline morphology have been reported in the films prepared using this technique [33, 87, 112-118]. An example of the microstructure of the film is shown in Figure 2.7 [87]. This technique presents itself as an attractive physical method in thin film deposition. However, it only facilitates limited deposition area and involves the use of expensive apparatus and complicated installation and setup.

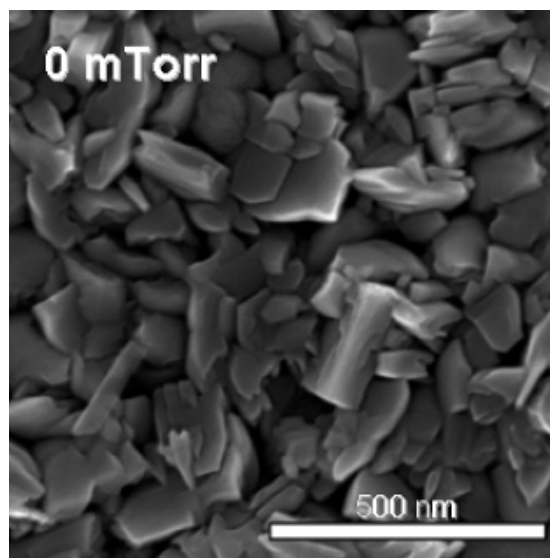


**Figure 2.7:** Scanning electron microscopy image of  $\text{WO}_3$  film deposited using reactive magnetron sputtering [87].

#### 2.3.4 Thermal Vapour Deposition

Thermal vapour deposition involves heating and vapourising the tungsten source (tungsten filament or  $\text{WO}_3$  powder) under the application of a high external electric power to  $\sim 1000^\circ\text{C}$  in an inert and/or oxygen gas-filled enclosed system, *e.g.*, furnace or vacuum chamber.  $\text{WO}_3$  film is grown on a substrate placed underneath the tungsten source. The processing parameters such as the distance between the filament and the substrate, the composition and flow rate ratio of the feeding gases, the heating duration and temperature of the tungsten source and substrate have been found to be capable of modifying the properties of  $\text{WO}_3$  films. One-dimensional  $\text{WO}_3$  nanostructured arrays including nanorods [52-54], nanotips [55], and nanowires [56, 57] can be synthesised using this method. An example of the microstructure of  $\text{WO}_3$  film produced using thermal vapour deposition is shown in Figure 2.8 [57]. This method is disadvantageous

in term of the processing costs, *i.e.*, necessity of high electric power and high temperatures.

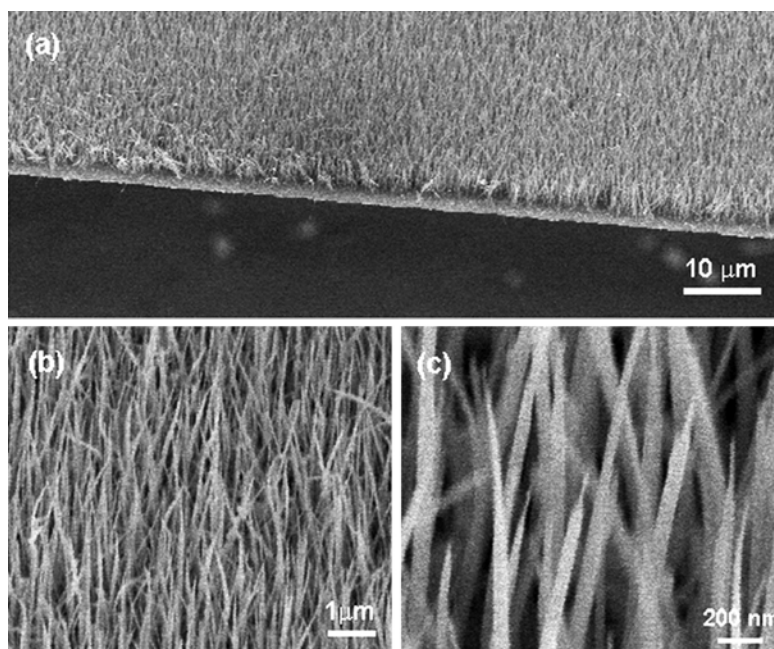


**Figure 2.8:** Scanning electron microscopy images of WO<sub>3</sub> film deposited using thermal vapour deposition and viewed at different magnifications [57].

### 2.3.5 Thermal Oxidation

Similar to thermal vapour deposition, thermal oxidation involves heating the tungsten sheet or wire to high temperatures in an enclosed system in order to oxidise the tungsten source. Tungsten oxide is grown on the tungsten source, which acts as a substrate. The enclosed system is introduced with inert gas such as Ar prior to heating. The oxygen source in the system originates from the residual O<sub>2</sub> and/or deionised water introduced in the enclosed system [102]. The properties of the films can be modified by varying the heating duration and temperature applied to the tungsten source and the type and composition of the gas introduced in the enclosed system. Nanostructures including nanobelts [119] and nanorods [102] can be produced using this method. An example of the morphology of the film is shown in Figure 2.9. This method is unfavourable in term of the processing costs arising from the high electricity consumption and high temperatures.

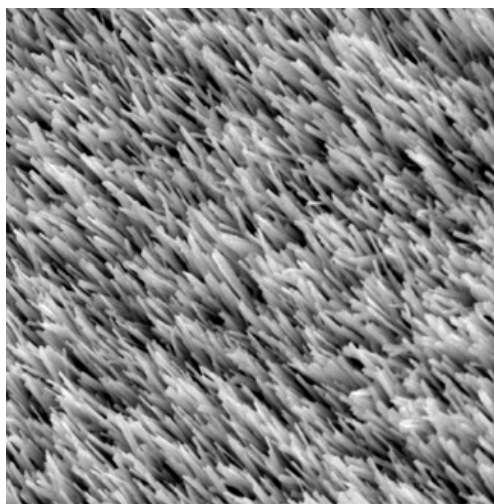


**Figure 2.9:** Scanning electron microscopy image of WO<sub>3</sub> film deposited using thermal oxidation [119].

### 2.3.6 Hydro/Solvothermal

In hydrothermal/solvothermal method, WO<sub>3</sub> precursor solution is prepared and subsequently transferred to a Teflon-coated autoclave reactor for processing at ~180°C for ~12 h to form WO<sub>3</sub> precipitate. The precipitate is filtered, cleaned with distilled water to remove the ion residues and finally dried in an oven and annealed in a furnace to form crystalline powder. The difference between hydrothermal and solvothermal synthesis lies in the non-aqueous precursors employed in the latter. To form WO<sub>3</sub> film, the powder is dispersed by surfactant solution such as poly(ethylene glycol) to form stable suspension and then casted onto a substrate by various techniques such as spin-coating, Langmuir-Blodgett technique, doctor blade method *etc.*, followed by thermal treatment to remove the surfactant. WO<sub>3</sub> film also can be fabricated using assembled coating method, which does not require the use of surfactants[120]. A direct one-step growth of WO<sub>3</sub> on conducting substrate has been reported where the substrate is put in the autoclave containing WO<sub>3</sub> sol for reaction. However, this method produced sparsely distributed WO<sub>3</sub> film of poor uniformity, which could be improved by growing a WO<sub>3</sub> seed layer on the substrate using spin-coating prior to the reaction in autoclave[121]. Recently, WO<sub>3</sub> nanowires have been synthesised by hydrothermal method using a microwave oven instead of the conventional autoclave [101]. This method took a relatively short reaction time of 3 h as compared to that of the

conventional autoclave (>10 h). Modification of the synthesis parameters, which include the composition of the precursor solutions, reaction time, and temperature, have been reported to vary the properties of  $\text{WO}_3$ . This method has been used to produce  $\text{WO}_3$  nanorods [45, 101, 120, 122], nanospheres [28, 60], and nanoplates [121]. An example of the microstructure of  $\text{WO}_3$  produced using hydrothermal is shown in Figure 2.10 [123]. Similar to sol-gel, control of the properties of  $\text{WO}_3$  prepared by hydro/solvothermal method requires careful attention to be given to solution chemistry. Furthermore, this method also is associated with disadvantages such as low yield of  $\text{WO}_3$  powders and long reaction times.

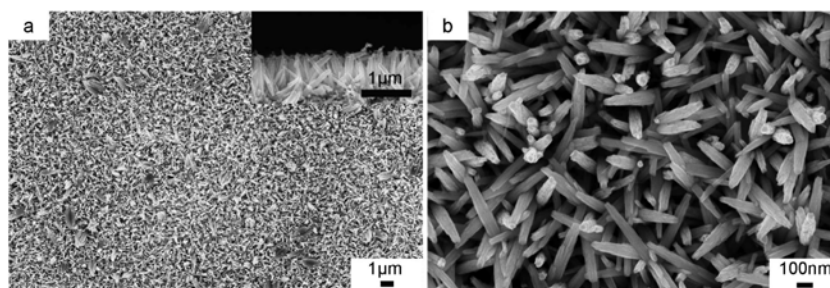


**Figure 2.10:** Scanning electron microscopy images of  $\text{WO}_3$  film deposited using hydrothermal method and viewed at different magnifications [123].

### 2.3.7 Anodisation

The anodisation system employed to synthesise  $\text{WO}_3$  films usually consists of a high-purity tungsten foil and a platinum foil as the working and counter electrodes, respectively, both of which are immersed in an electrolyte solution, which usually contains fluoride ions (*e.g.*, NaF, HF).  $\text{WO}_3$  films are grown by electrochemical oxidation of the tungsten foil at an applied potential of 20-60 V for 1-6 h. The properties of the films can be manipulated by varying the anodisation parameters and the composition and temperature of the electrolyte solutions. Nanoporous films have been produced using this technique [124-127]. The porous features of the films result from the competition between oxide formation and dissolution, where the latter is the result of the etching by the fluoride ions in the electrolyte. It also has been reported that higher anodisation potentials and longer reaction times lead to higher degrees of porosity in the films [44, 61, 62] while increasing the temperature of the electrolyte

solution produces films with nanoplatelet structures [25, 58, 59]. Examples of the microstructures of  $\text{WO}_3$  films produced by anodisation are shown in Figure 2.11 [44]. Anodisation presents an inexpensive method to produce self-organised nanostructured films without the need of template or catalyst. However, due to the rapid achievement in steady rates of both the oxide formation and etching, the films produced using this method were too thin to provide sufficient volume interaction for various solar applications.

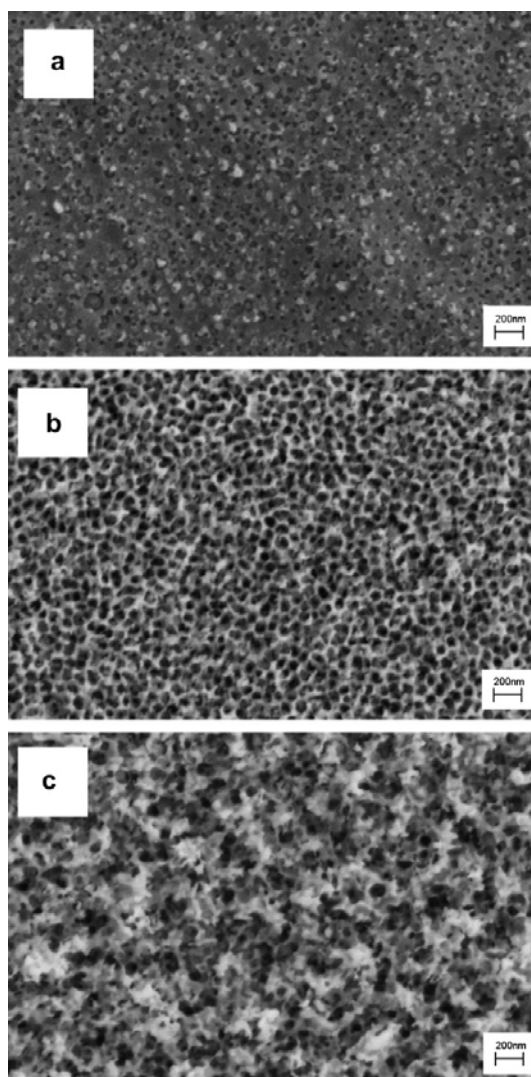


**Figure 2.11:** Scanning electron microscopy images of  $\text{WO}_3$  films prepared by anodisation at (a) 20 V, (b) 40 V, and (c) 60 V [44].

## 2.3.8 Electrodeposition

### 2.3.8.1 Overview of Electrodeposition

From a practical point of view, a low-cost nanostructural synthesis of thin films with large deposition area and high uniformity is desirable. The synthesis techniques that utilise vacuum systems are expensive. Thermal oxidation and anodisation require high input electric power and/or temperatures  $>1000^{\circ}\text{C}$ , whereas hydro/solvothermal method requires expensive autoclaves to create high vapour pressure and temperature conditions. Sol-gel offers a method for economical production of nanostructured powder. However, similar to the hydro/solvothermal method, subsequent film deposition (*i.e.*, spin coating, doctor-blade) is required to produce thin films. Moreover, careful attention needs to be paid to the solution chemistry in order to produce high quality oxides. Furthermore, post-deposition annealing is required to obtain well-adhered films as well as to remove any binder solutions used during the film deposition.

In this work, electrodeposition was used to synthesise  $\text{WO}_3$  thin films. This technique is advantageous owing to the following:

- (i) Direct and large-area coating of thin films on conductive substrates
- (ii) Economical and simple apparatus, which makes it viable for large-scale production
- (iii) Low processing cost of film deposition at room temperature and at atmospheric pressure
- (iv) Ease of control of the film thickness by monitoring the charge consumption during the deposition process

The electrodeposition setup consists of an electrochemical cell with at least two electrically conductive electrodes. The cell is connected to a potentiostat/galvanostat for control of its electrical potential/current. In a two-electrode cell, the working electrode, where film deposition occurs, and the counter electrode, which usually consists of chemically inert and conductive materials such as platinum, are used. In potentiostatic mode where the potential of the cell is controlled, a reference electrode

would usually be added. This is because the potential of an electrode is defined in relation to another constant-potential electrode. In a two-electrode cell, the potential of the working electrode cannot be measured/controlled precisely with respect to that of the counter electrode owing to the polarisation of the counter electrode. In contrast, in a three-electrode cell with reference electrode, constant potential of the reference electrode can be established regardless of the different electrolyte solutions used. The potential of the working electrode is controlled/measured with respect to the reference electrode while the current flows between the working and the counter electrodes. These electrodes are immersed in an electrolyte solution to complete the electrochemical circuit.

An electric field is created between the working and the counter electrodes upon the application of an external bias. The electric field drives the ionic species of interest in the electrolyte solution to the working electrode and they react (oxidation or reduction) to form a deposit at the working electrode. Due to the necessity to establish a closed electrochemical circuit, the working electrode must be electrically conductive and only electrically conductive materials, such as metals, semiconductors and electrically conductive polymers, can be synthesised. Electrodeposition has been employed in the synthesis of metal oxide thin films. Annealing usually is required to recrystallise the films that are deposited in the hydrate forms. Exceptions can be seen in the case of some metal oxides, such as  $\text{Cu}_2\text{O}$  and  $\text{ZnO}$ , where crystalline oxides are deposited and therefore annealing is not required to achieve crystallinity. The physical properties of the deposited films, such as thicknesses, morphologies, and mineralogies, can be modified by varying the properties of the electrolyte solutions (pH, concentration, and temperature) as well as the pre- and post-deposition parameters (deposition time, deposition potential/current, and annealing).

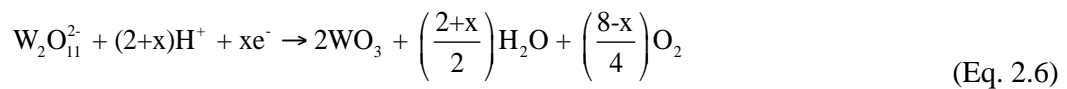
#### 2.3.8.2 Electrodeposition of Tungsten Oxide Thin Films

Peroxotungstic acid (PTA) usually is used as the precursor electrolyte solution for the electrodeposition of  $\text{WO}_3$ . The chemical formula of PTA is proposed as  $\text{H}_2[(\text{O}_2)_2\text{W}(\text{O})\text{O}(\text{O})_2] \cdot n\text{H}_2\text{O}$ , where  $(\text{O}_2)$  denotes a peroxide ligand. The tungsten oxidation state in PTA is +6 [128]. PTA can be prepared by dissolving metallic

tungsten, tungsten carbide, tungstic acid ( $\text{WO}_3 \cdot \text{H}_2\text{O}$ ) or alkaline salt of tungstic acid (e.g.,  $\text{K}_2\text{WO}_4$ ,  $\text{Na}_2\text{WO}_4$ ,  $\text{Li}_2\text{WO}_4$ ) in  $\text{H}_2\text{O}_2$  [129-132]. In the case of metallic tungsten, its dissolution in  $\text{H}_2\text{O}_2$  follows the reaction [128]:



The deposition of  $\text{WO}_3$  by cathodic reduction of PTA occurs as follows [128, 130]:



where  $x$  varies from 0 to 8, depending on the peroxide ligand content of the reducible peroxotungstate species.

Generally, electrodeposition can be done either potentiostatically (fixed deposition potential) or galvanostatically (fixed deposition current). There are two deposition modes, *viz.*, continuous and pulsed modes, which produced  $\text{WO}_3$  thin films of different morphologies [40]. The pulsed mode (periodically powered electrodeposition) produces thinner films consisting of smaller grain sizes compared to the continuous mode (continuously powered electrodeposition) owing to the shorter reaction time. The grain sizes decrease with decreasing pulse duration as shown in Figure 2.12 [40].

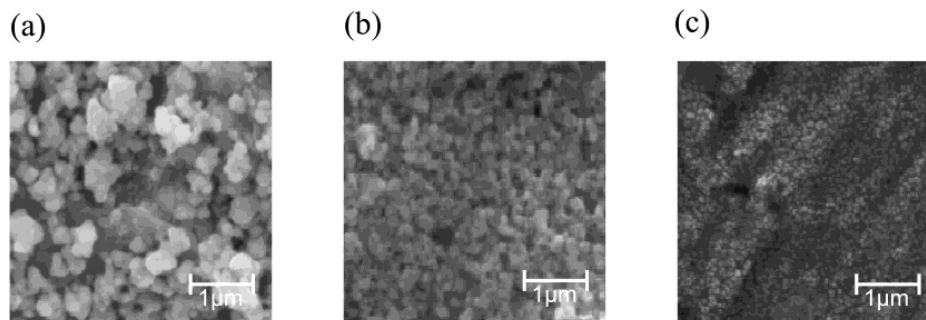


**Figure 2.12:** Scanning electron microscopy images of  $\text{WO}_3$  films prepared using electrodeposition by (a) continuous mode, (b) pulsed mode at 100 ms pulses, and (c) pulsed mode at 5 ms pulses [40].

### 2.3.8.3 Electrodeposited Tungsten Oxide Thin Films for Photoelectrochemical Applications

Electrodeposited  $\text{WO}_3$  nanostructured thin films have been studied previously for electrochromic applications [34-36] but there are only few reports on photoelectrochemical applications. Baeck *et al.*[40] prepared nanoparticulate  $\text{WO}_3$  thin films by pulsed electrodeposition and attributed the improved photocurrents to the decrease in the particle sizes associated with enhanced surface area, which facilitated light absorption, charge transport, and surface redox activity. Yang *et al.* [39] modified the morphology of electrodeposited  $\text{WO}_3$  through pH adjustment and found that the photoelectrochemical properties of mesoporous films were improved greatly compared to those of nonporous films due to the increased surface area of the former. These reports show that controlling the processing of  $\text{WO}_3$  is important because the resultant photoelectrochemical response is influenced strongly by the associated physical, optical, and electrical properties. Chapters 4 and 5 present detailed investigation on the tailoring of the preceding properties of the electrodeposited  $\text{WO}_3$  thin films through the control of the deposition parameters such as the deposition potential, the deposition time, and the composition of the PTA electrolyte solutions. These parameters represent important fundamental controlling agents to the growth mechanism and the resulting physical, optical, and photoelectrochemical properties of electrodeposited  $\text{WO}_3$  thin films.

As mentioned in Section 2.2.2, nanostructural control of the grain sizes of  $\text{WO}_3$  thin-film photoanodes is important to achieve a positive balance of (i) the numbers of reaction and recombination sites, (ii) the charge transport properties and (iii) the optical properties of the films. The size-controlled synthesis of  $\text{WO}_3$  nanostructures has been reported using various techniques such as hydrothermal[60], sol-gel[73, 133, 134], hot-wire chemical vapour deposition[135], arc discharge deposition[136], and radio-frequency magnetron sputtering[137, 138]. Most of these techniques require expensive instruments and/or vacuum systems, and the sizes of the nanostructures have been controlled principally by thermal treatments at high temperatures (400°-950°C). An alternative to these techniques is organic-compound-assisted wet chemical synthesis. This technique combines the benefits of eco-friendly organic compounds with

uncomplicated, economical, and large-area deposition methods. Sun *et al.*[78]used colloidal processing at high oxalic acid concentrations with tungstic acid to produce smaller grain sizes and lower crystallinities in WO<sub>3</sub> thin films. Meda *et al.*[77]reported the size tuning of WO<sub>3</sub> grains prepared by a proton exchange resin method through the addition of various organic dispersants, including ethylene glycol, poly(ethylene glycol), Igepal, Brij, and sugars, where the grain sizes decreased with increasing dispersant molecular weight. Naseri *et al.*[139]used poly(ethylene glycol) to control the topologies of WO<sub>3</sub> nanocrystalline thin films prepared by a sol–gel method. There is a limited number of investigations on size-controlled wet chemical synthesis of WO<sub>3</sub> thin films using organic compounds, and the understanding of the mechanisms associated with the growth of the nanoparticles remains tentative. In this regard, Chapter 7 presents the electrodeposition of WO<sub>3</sub> nanocrystalline thin film photoelectrodes where the grain sizes of the films are controlled and optimised by using carboxylic acids as the dispersing agents in the PTA electrolyte solutions.

## CHAPTER 3

### Experimental Procedures

This chapter describes the experimental procedures employed in the synthesis of  $\text{WO}_3$  thin films, which include the preparation of peroxotungstic acid (PTA) as the electrolyte solutions, the electrodeposition of  $\text{WO}_3$  thin films, and the post-deposition annealing of the films. This is followed by the description of the characterisation techniques used in the determination of the physical, mineralogical, optical, and photoelectrochemical properties of the films.

#### 3.1 Synthesis of Tungsten Oxide Thin Films Using Electrodeposition

##### 3.1.1 Chemicals

Tungsten foils (99.99%, Shanghai Leading Metal, China), 30% w/w hydrogen peroxide (analytical reagent, Univar), propan-2-ol (99.5% analytical reagent, Univar), and distilled water were used to prepare the PTA solutions. The carboxylic acids used were formic acid (99% analytical reagent, Asia Pacific Specialty Chemicals), oxalic acid dihydrate (99.5% Merck), and citric acid monohydrate ( $\geq 99\%$  ACS reagent, Sigma-Aldrich).

##### 3.1.2 Preparation of Peroxotungstic Acid Electrolyte Solutions of Different Tungsten Concentrations

Tungsten foil (1.8384 g) was dissolved in 20 mL 30% w/w  $\text{H}_2\text{O}_2$  aqueous solution in a Pyrex container to form the PTA solution. Upon complete dissolution, excess  $\text{H}_2\text{O}_2$  was eliminated by immersing a thin platinum foil (1.5 cm  $\times$  2.0 cm) into the PTA solution and heating to 60°C to catalyse the decomposition of  $\text{H}_2\text{O}_2$  until the gas evolution ceased. Figure 3.1 illustrates the solutions deriving from the main stages of the preparation of PTA solutions. The resultant PTA solutions were diluted by the

addition of propan-2-ol and distilled water in 1:1 volume ratio to give tungsten concentrations of  $0.05 \text{ mol L}^{-1}$ ,  $0.10 \text{ mol L}^{-1}$ , and  $0.20 \text{ mol L}^{-1}$ , which were used as the electrolytes for  $\text{WO}_3$  deposition. The mixing of the solutions was assisted by the use of an ultrasonicator. The pH values, measured using a pH/conductivity meter (Horiba F54, Japan), were 2.14, 1.81, and 1.68, respectively. PTA solutions without hydrogen peroxide were unstable [130, 140], where an insoluble precipitate of an amorphous  $\text{WO}_3$ -based hydrated phase would form easily when the PTA solutions were heated beyond the point at which gas evolution ceased and/or upon storage for  $>48 \text{ h}$ . The higher the tungsten concentration of PTA solutions, the shorter the storage time before precipitation occurred. The presence of propan-2-ol is known to extend the stability of the PTA solutions by preventing the formation of precipitates [140].

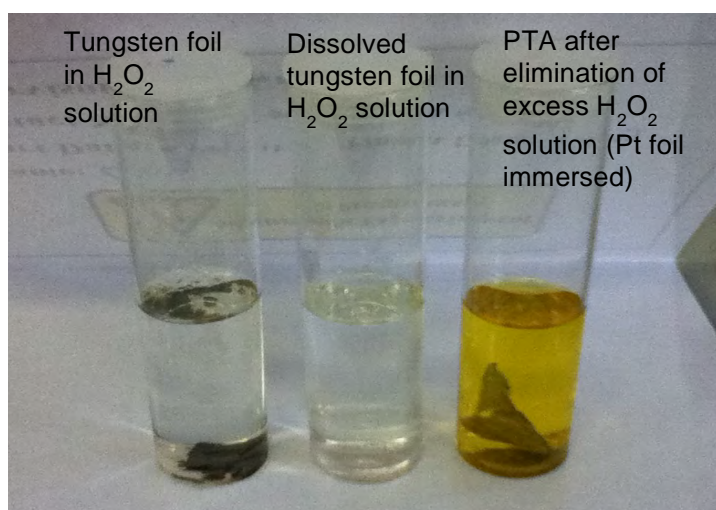


**Figure 3.1:** Solutions obtained during the preparation of PTA solutions.

### 3.1.3 Preparation of Peroxotungstic Acid Electrolyte Solutions Containing Carboxylic Acids

To study the effect of carboxylic acids on the electrodeposition of  $\text{WO}_3$  thin films,  $0.03 \text{ mol L}^{-1}$  carboxylic acid (*viz.*, formic, oxalic, or citric acid) was added to the PTA containing  $0.20 \text{ mol L}^{-1}$  tungsten concentration and these PTA solutions were used as the electrolytes for film deposition. The mixing of the acids in the PTA solutions was assisted by the use of an ultrasonicator. Since optimal results were obtained (discussed

in detail in Chapter 7) with the addition of oxalic acid, the effect of oxalic acid concentrations (0.01-0.10 mol L<sup>-1</sup>) was studied further.

#### 3.1.4 Electrodeposition of Tungsten Oxide Thin Films

WO<sub>3</sub> thin films were deposited at room temperature using a three-electrode electrochemical system with fluorine-doped tin oxide on glass (FTO; Wuhan Ge'ao Scientific Education Instrument, China; 15 Ω sq<sup>-1</sup>; 3.0 cm × 2.5 cm), thin platinum foil (Pt; 2.0 cm × 4.0 cm), and Ag/AgCl as the working (WE), counter (CE), and reference (RE) electrodes, respectively. These electrodes were connected to a computer-controlled potentiostat (EZstat Nuvant Systems, Inc.; resolution 300 μV and 3 nA at the ±100 μA range), as illustrated in Figure 3.2. All potentials reported were relative to the reference electrode. The immersed areas of the FTO and Pt electrodes were 1.5 cm × 1.0 cm and 2.0 cm × 2.0 cm, respectively. Linear potential sweeps were measured at a scan rate of 5 mV s<sup>-1</sup> and a step size of 1 mV from 0.1 V to -0.8 V in order to study the reduction peaks of the PTA containing different tungsten concentrations. These reduction peaks correspond to the chemical reaction of the PTA ions to form WO<sub>3</sub> according to Equation 2.6.

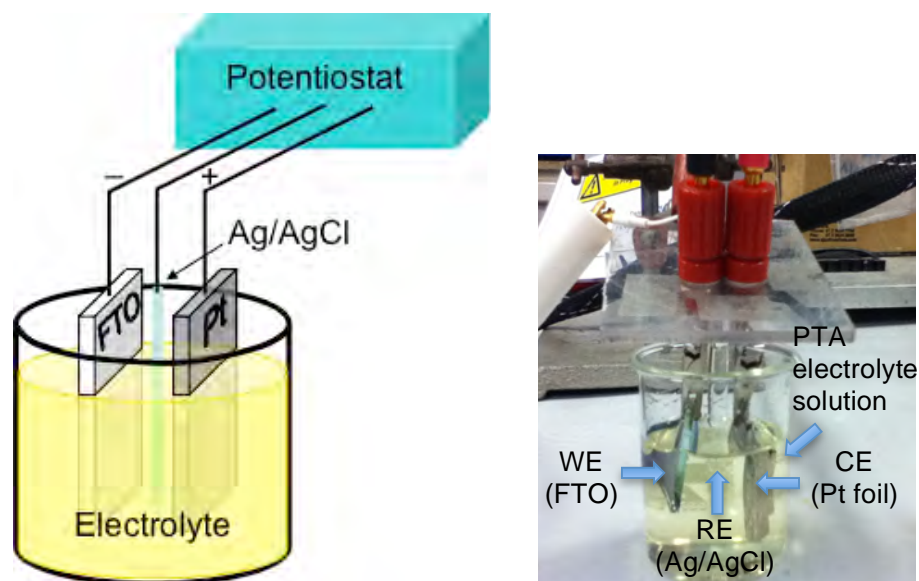


**Figure 3.2:** Schematic diagram (left) and photograph (right) of the experimental setup of the electrodeposition system. WE, RE, and CE are the working, reference, and counter electrodes, respectively.

For the investigation of the effect of deposition potentials,  $\text{WO}_3$  thin films were deposited at deposition potentials ranging from  $-0.3\text{ V}$  to  $-0.6\text{ V}$  for 90 min from the PTA containing  $0.05\text{ mol L}^{-1}$  tungsten concentration. Following the results obtained for the optimal deposition potential in the electrodeposition of  $\text{WO}_3$  thin films in Chapter 4, the following Chapters 5-7 adopted  $-0.4\text{ V}$  as the optimal deposition potential in the electrodeposition of  $\text{WO}_3$  thin films. In the investigation of the effect of tungsten concentrations of pure PTA solutions in Chapter 5, the films were deposited for 30-120 min from PTA containing  $0.05\text{-}0.20\text{ mol L}^{-1}$  tungsten concentrations in order to obtain films of various thicknesses. On the other hand, in Chapter 7, which presented the study of carboxylic acid-assisted electrodeposition, shorter deposition times ranging from 5 min to 60 min were used for PTA solutions that contained carboxylic acids in order to avoid resultant cracking and poorly adhered thick films.

In the study of crystallographic orientations in Chapter 6,  $\text{WO}_3$  films with similar thicknesses ( $\sim 650\text{ nm}$ ) were deposited for 30 min and 3 h from PTA containing  $0.20\text{ mol L}^{-1}$  and  $0.05\text{ mol L}^{-1}$  tungsten concentrations, respectively, owing to the lower deposition rates in PTA containing lower tungsten concentrations. This was to avoid

the potential influence of film thickness on the photoelectrochemical properties of the films. The as-deposited samples were flushed immediately with a wash bottle containing distilled water, placed on an open petri dish in a sample cupboard, and dried for  $\geq 1$  h at room temperature.

### 3.1.5 Post-Deposition Annealing

The as-deposited tungsten oxide films after air drying were placed on an aluminosilicate brick and annealed in air in a muffle furnace at heating and initial cooling rates of  $5^{\circ}\text{C min}^{-1}$ . To study the effect of annealing conditions, the films were annealed at temperatures up to  $500^{\circ}\text{C}$  for annealing times up to 18 h. Figure 3.3 shows photographs of the as-deposited and the annealed  $\text{WO}_3$  films. The blue colour of the as-deposited film was reported to be caused by the formation of tungsten bronze  $\text{H}_x\text{WO}_3$  whose oxidation state of tungsten is  $<+6$  [141].

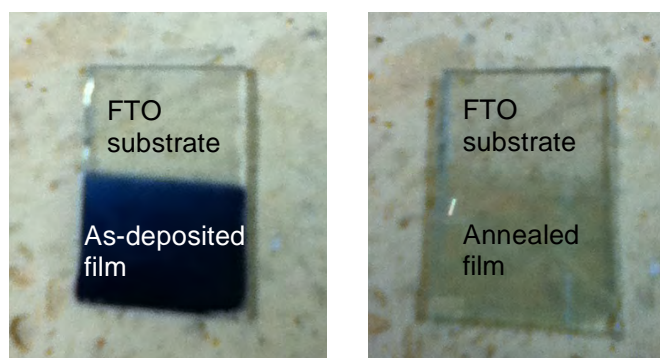


**Figure 3.3:** Photographs of the as-deposited (left) and annealed (right) films.

## 3.2 Characterisation Techniques

Prior to the examination of  $\text{WO}_3$  thin films using electron microscopy, sample preparations were done, which involved mounting the films onto stainless steel studs and grounding the films using copper tapes and silver paint. For sample milling as described in Section 3.2.3, a gold layer of  $\sim 50$  nm was sputter-coated onto the films to avoid surface charging.

The microstructures of WO<sub>3</sub> thin films were examined using scanning electron microscopy (SEM; FEI Nova NanoSEM; accelerating voltage 5 kV) and atomic force microscopy (AFM; Bruker Dimension Icon; tapping mode). The structural properties of the films were analysed using transmission electron microscopy (TEM; Phillips CM200; accelerating voltage 200 kV). True porosities of the films were investigated using image analysis software (*ImageJ*, National Institutes of Health). The mineralogies of the unaltered films were determined by X-ray diffraction (XRD; Philips X'pert Materials Powder Diffractometer; CuK $\alpha$  radiation; 45 kV; 40 mA; step size 0.026°; scan speed 0.22° s<sup>-1</sup>). The software *PANalytical X'pert HighScore Plus* was used to analyse the XRD spectra. Light transmissions were measured using a dual-beam ultraviolet-visible (UV-VIS) spectrophotometer (Pelkin-Elmer Lambda 35).

Surface elemental composition and electronic valence band spectra were examined using X-ray photoelectron spectroscopy (XPS; Thermo Scientific Escalab 250; 150 W monochromated AlK $\alpha$  X-ray source with spot size of 500  $\mu$ m), where the pass energies applied for survey and region scans were 100 eV and 20 eV, respectively; software *Advantage* was used to analyse the XPS spectra. The binding energies were referenced to C(1s) from the adventitious hydrocarbon at 285 eV.

### 3.2.1 Computational Details

The optimised lattice parameters of monoclinic  $\gamma$ -WO<sub>3</sub> (space group P2<sub>1</sub>/n [97]) were calculated using *CRYSTAL09* code with *B3LYP* hybrid functional. The resultant crystal structure was constructed using *VESTA* software.

### 3.2.2 Measurement of Film Thickness by Focused Ion Beam Milling and Scanning Electron Microscopy

The electrodeposited WO<sub>3</sub> film thicknesses were determined using focused ion beam milling (FIB; FEI XP200; 30 keV Ga ions) and subsequently viewed using SEM. These were done by the procedures as follows:

- (i) A platinum strip with dimensions  $17.0 \times 1.5 \times 1.0 \mu\text{m}$  (length  $\times$  width  $\times$  depth) was deposited at a beam current of 350 pA on the surface of the film as a protective layer to the subsequent ion beam milling (see Figure 3.4(a)).
- (ii) A regular milling volume of dimensions  $15.0 \times 2.5 \times 1.5 \mu\text{m}$  (length $\times$ width $\times$ depth) at a high beam current of 2700 pA was performed (see Figure 3.4(b)). This step milled away some of the platinum strip, the film, and the FTO glass substrate.
- (iii) A clean milling volume of dimensions  $15.0 \times 0.5 \times 1.0 \mu\text{m}$  (length $\times$ width $\times$ depth) at a low beam current of 150 pA was performed in order to mill away possible re-deposition on the cross-section of the film (see Figure 3.4(c)).
- (iv) The cross-section of the film was viewed using SEM (FEI Nova NanoSEM; accelerating voltage 5 kV) at  $45^\circ$  tilt(see Figure 3.4(d)).

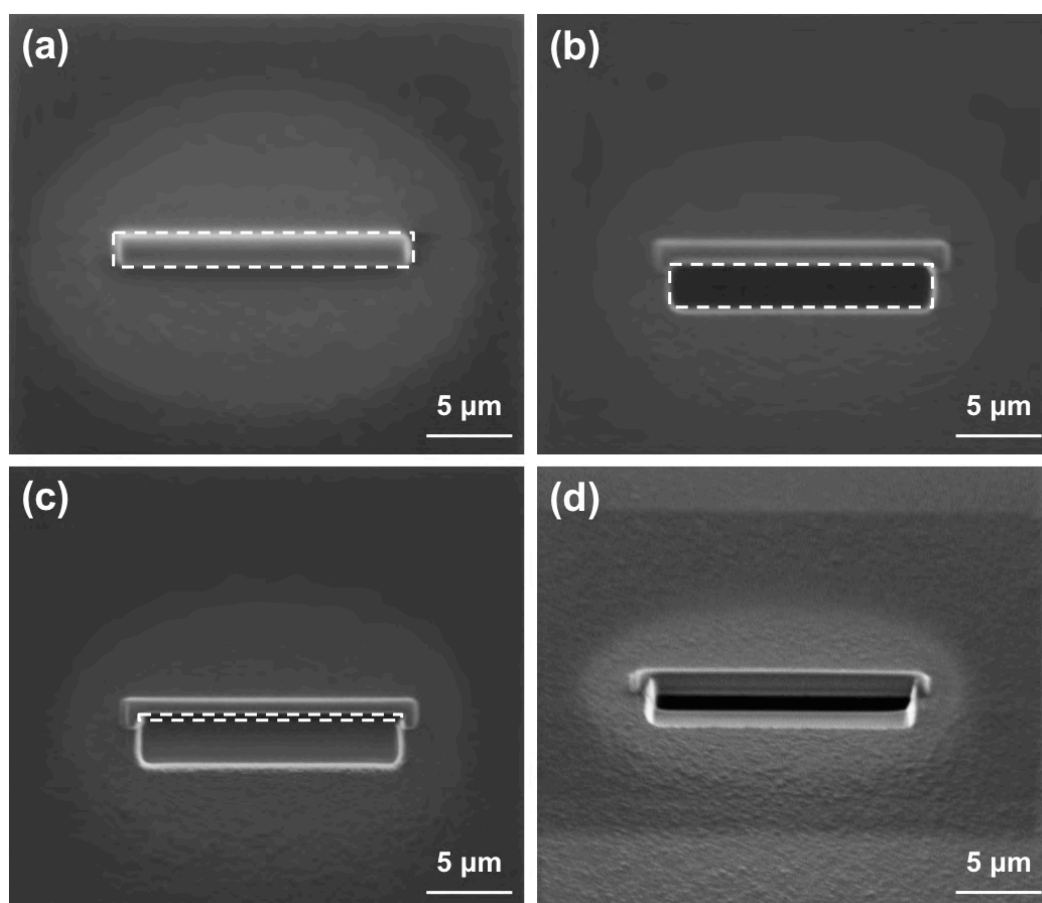


**Figure 3.4:** FIB images of the milling steps for acquisition of cross-sectional views of the films. (a) Deposition of platinum strip on the surface of the film, (b) regular milling, (c) clean milling, and (d) cross-sectional view at  $45^\circ$  tilt.

### 3.2.3 TEM Sample Preparation by Focused Ion Beam Milling and *Ex-Situ* Lift-Out

TEM samples were prepared using focused ion beam milling (dual-beam FIB-SEM; XT Nova Nanolab 200; 30 keV Ga ions) and *ex-situ* lift-out. These were done by the procedures as follows (see Figure 3.5):

- (i) A mask with labels *X* was milled for easy spotting of the sample location during *ex-situ* lift-out (see Figure 3.5(a)).
- (ii) A platinum strip was deposited on the surface of the film as a protective layer to the subsequent ion beam milling, as described above (see Figure 3.5(b)).
- (iii) Regular milling on both sides along the length of the platinum strip was performed, as described above (see Figure 3.5(c,d)). This step milled away some of the platinum strip, the film, and the FTO glass substrate.
- (iv) One side of the rectangular strip was milled at 45° tilt to release the bottom side of the wedge (see Figure 3.5(e)).
- (v) Clean milling was performed on both sides of the samples at 1.5° tilt in order to thin the samples into wedge shapes. One side of the sample was milled to prevent stress-induced bending (see Figure 3.5(f,g)).
- (vi) The clean milling continued until the sample thickness reached ~100 nm. Subsequently, the remaining side of the wedge was milled in readiness to be lifted out (see Figure 3.5(h)). The *ex-situ* lift-out procedures using an optical microscope equipped with a micromanipulator system are shown in Figure 3.6.

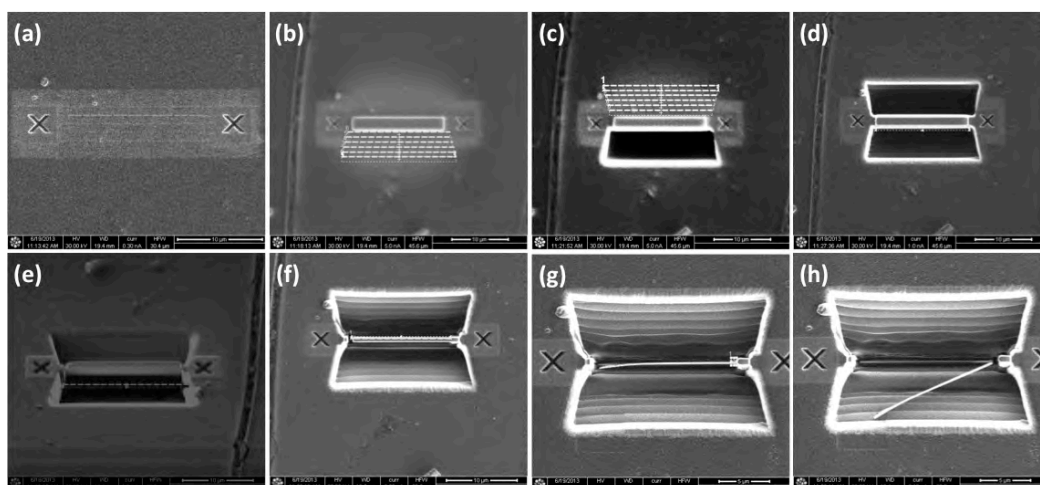


**Figure 3.5:** FIB images on the milling steps for the preparation of TEM samples. (a) Milling of X labels on the surface of the film, (b) deposition of the platinum strip, (c,d) regular milling on both sides of the platinum strip, (e) regular milling at the bottom part of the sample at 45° tilt, (f,g) clean milling at 1.5° tilt on both sides of the sample with one side released, and (h) regular milling on the remaining side of the sample.

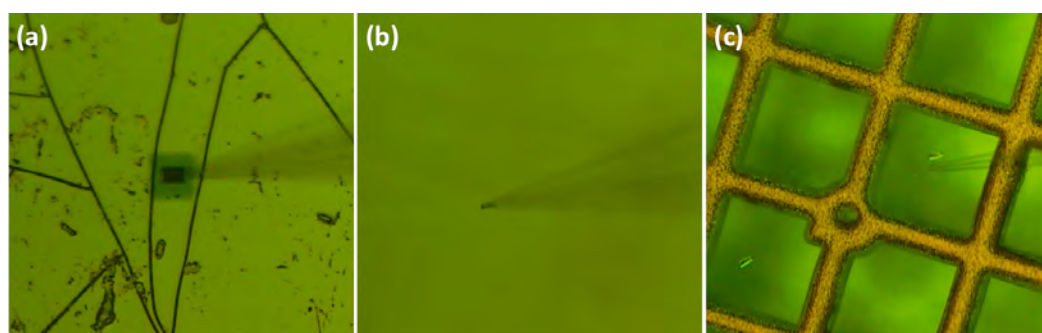


**Figure 3.6:** TEM sample (a) picked up by a sharp glass tip, (b) adhered to the tip by electrostatic force, and (c) laid flat on the copper grid coated with Formvar.

### 3.3 Photoelectrochemical Measurements

#### 3.3.1 Photoelectrochemical Cell

The photoelectrochemical properties of  $\text{WO}_3$  thin films were measured at room temperature using the same electrochemical system as described in Section 3.1.4 (see Figure 3.2). In this case, the films deposited on FTO substrates and  $0.5 \text{ mol L}^{-1}$  NaCl aqueous solutions (measured pH = 6.27) were used as the working electrodes and the

electrolyte solutions, respectively. Localised acidification by the formation of hypochlorous acid (HClO) during photoelectrolysis established a pH of ~2 in the proximity of the WO<sub>3</sub> photoanode [142] and thus it was not necessary to acidify the electrolyte; therefore an electrolyte pH approaching neutral was used. The relevant reactions are:



The films were illuminated using a 50 W tungsten-halogen lamp as the light source. The intensity of the incident light was measured using a light meter (Digitech QM1587) to be ~30 mW m<sup>-2</sup> or ~100 mW cm<sup>-2</sup> at light source-to-sample distances of ~45 cm or ~25 cm, respectively. It may be noted that the tungsten-halogen light source was used for comparative test purposes only and so the measured photoelectrochemical performances are not directly comparable with those using other light sources, such as Xe lamp. Nonetheless, the photoelectrochemical measurements of the films also were done using a solar simulator equipped with a 300 W Xe lamp (Newport; part number 6258) as the light source, which was available only in the final stage of the work. The information of the spectral output of the lamp is provided in Appendix 1. The solar simulator was coupled with air mass 1.5 global (Newport; part number 81094) and UV (<305 nm; Newport; part number 20CGA-305) blocking filters. The light intensity was measured using a light power meter (Thorlabs PM100USB) equipped with a thermal power sensor (Thorlabs S314C) to be ~280 mW m<sup>-2</sup> (light source-to-sample distance of ~9.5 cm). The light source was chopped at a frequency of 0.05 Hz.

### 3.3.2 Measurement Parameters

The linear potentiodynamic voltammeteries were scanned at a rate of 5mVs<sup>-1</sup> with a step size of 1mV. In order to measure the relaxation time of the open-circuit photopotential, the films were pre-treated by biasing at 0.7 V for 1 min under illumination (50 W tungsten-halogen lamp; light source-to-sample distances of ~25 cm; intensity of ~100 mW m<sup>-2</sup>) so as to achieve an equilibrium state (as shown by achievement of stable

photocurrents) and then left to reach a stationary potential under open-circuit (without bias) and dark conditions. Subsequently, illumination was switched on for the photopotential to reach a stationary value and then switched off again to measure the time taken for it to decay.

The photoconversion efficiency  $\eta$  of  $\text{WO}_3$  thin-film photoanode is defined as the ratio of the power output to the power input [1]. The power input is the incident light intensity  $J_{\text{light}}$  ( $\text{W m}^{-2}$ ) integrated over the illuminated area  $A$  ( $\text{m}^2$ ) whereas the power output is the power stored as hydrogen less the power contribution from the external bias potential  $I_{\text{ph}}E$  (W).

$$\text{Photoconversion efficiency, } \eta = \frac{\text{power}_{\text{output}}}{\text{power}_{\text{input}}} \times 100\% = \frac{\text{power}_{\text{hydrogen}} - I_{\text{ph}}E}{J_{\text{light}} \times A} \times 100\% \quad (\text{Eq. 3.4})$$

$I_{\text{ph}}$  and  $E$  are photocurrent and external bias potential, respectively. The power stored as hydrogen can be expressed as  $\text{power}_{\text{hydrogen}} = \Delta G^0(\text{H}_2\text{O})R_{\text{H}_2}$ , where  $\Delta G^0(\text{H}_2\text{O})$  is the standard Gibbs free energy of formation for 1 mol of water  $237.2 \text{ kJ mol}^{-1}$  at  $25^\circ\text{C}$  and 1 bar) and  $R_{\text{H}_2}$  is the rate of production of hydrogen ( $\text{mol s}^{-1}$ ). When  $I_{\text{ph}}$  is the photocurrent responsible for the generation of hydrogen at the rate of  $R_{\text{H}_2}$  and assuming

that all charge carriers participate in the generation of hydrogen/oxygen, then  $R_{\text{H}_2} = \frac{I_{\text{ph}}}{nF}$ ,

where  $n$  is the number of moles of electron needed to generate 1 mole of hydrogen and  $F$  is the Faraday constant. The value of  $n$  can be determined from Equation 2.3 to be 2. The photoconversion efficiencies of  $\text{WO}_3$  thin films were determined using Equation 3.5 as follows:

$$\begin{aligned}
\eta &= \frac{\Delta G^0(\text{H}_2\text{O})R_{\text{H}_2} - I_{\text{ph}}E}{J_{\text{light}} \times A} \times 100\% \\
&= \frac{(237.2 \text{ kJ mol}^{-1}) \left( \frac{I_{\text{ph}}}{2 \text{ mol} \times 96485.34 \text{ C mol}^{-1}} \right) - I_{\text{ph}}E}{J_{\text{light}} \times A} \times 100\% \\
&= \frac{I_{\text{ph}}(1.23 - E)}{J_{\text{light}} \times A} \times 100\% \\
&= \frac{J_{\text{ph}}(1.23 - E)}{J_{\text{light}}} \times 100\% \tag{Eq. 3.5}
\end{aligned}$$

where  $J_{\text{ph}}$  is the photocurrent density.

Transient potentiostatic photocurrent measurements were done at a bias potential of 0.7 V, which gave a maximal photoconversion efficiency at this value. Cyclic voltammetry of the films involved scanning from  $-0.5$  V to  $+0.5$  V at a rate and step size of  $5 \text{ mV s}^{-1}$  and  $1 \text{ mV}$ , respectively, in dark environment.

It has been shown that the use of sodium chloride can stabilise the photoelectrochemical performance of  $\text{WO}_3$  photoanodes by avoiding the formation of a passivating layer of peroxy (O-O) species on the surface of the photoanodes, which is favoured when commonly used acids are employed as supporting electrolytes to lower the electrolyte pH [142-144]. However, it may be noted that up to  $\sim 20\%$  of the dark currents may be provided by chlorine gas formation [142].

### 3.4 Photocatalytic Degradation of Methylene Blue

Prior to the start of the photocatalytic test,  $\text{WO}_3$  thin films (area  $1.5 \text{ cm} \times 1.5 \text{ cm}$ ) were immersed for  $\sim 24$  h in methylene blue aqueous solutions of concentration 1 ppm in order for the system to achieve surface absorption equilibrium. The films then were fully immersed in 20 mL methylene blue solutions, contained in a 50 mL Pyrex beaker, with initial concentration of 1 ppm and illuminated at a sample-lamp distance of 10 cm for 0-23 h using 8 W Hg lamp (UVP; major spectral output at 254 nm, as shown in Appendix 2). The resultant methylene blue solutions were taken at certain irradiation time intervals for measurement of optical absorption spectra using the UV-VIS

spectrophotometer (Pelkin-Elmer Lambda 35). The intensities of the characteristic absorption peaks of methylene blue at ~664 nm were recorded for the evaluation of the photodegradation performance using the following equation[145, 146]:

Beer-Lambert equation: 
$$A_t = \varepsilon \times \ell \times C_t \quad (\text{Eq. 3.6})$$

where  $\varepsilon$  and  $\ell$  are the molar absorptivity and optical path length of methylene blue solution, respectively;  $A_t$  and  $C_t$  are the optical absorbance and concentration of methylene blue solution at irradiation time  $t$ , respectively. Since  $\varepsilon$  and  $\ell$  are constant, the absorbance is linearly proportional to the concentration of methylene blue in the solution. The performances of the films in photocatalytic degradation of methylene blue were evaluated from the relative concentration of methylene blue with respect to initial concentration at  $t = 0$  ( $C_t/C_0$ ) as a function of irradiation time. A control sample (methylene blue solution containing no film) also was studied for comparative purposes.

## CHAPTER 4

### Synthesis of Tungsten Oxide Thin Films by Electrodeposition: Effect of Deposition Potential

#### 4.1 Introduction

This chapter presents the electrodeposition of  $\text{WO}_3$  thin-film photoanodes from peroxotungstic acid (PTA) solution. As mentioned in Chapter 2, previous reports [39, 40] showed that the photoelectrochemical properties of  $\text{WO}_3$  thin films were influenced strongly by their physical, optical, and electrical properties, which in turn were controlled by the processing parameters. Deposition potential is a critical parameter in electrodeposition because it controls the electric field generated between the working and counter electrodes and therefore influences the deposition mechanism [147]. This chapter details the investigation on the effect of deposition potential on the deposition mechanisms and the resultant morphological, mineralogical, and optical properties of electrodeposited  $\text{WO}_3$  thin films. The influence of these properties on the photoelectrochemical performance of the films was analysed. It was found that applying a suitable potential during electrodeposition resulted in physically homogeneous and strongly-adhered films. Part of the work presented in this chapter has been published in Energy Procedia, year 2013, volume 34, and pages 617-626. A copy of the publication is provided in Appendix 6.

#### 4.2 Results and Discussion

##### 4.2.1 Linear Voltammetric Study of Peroxotungstic Acid Electrolyte Solutions

Figure 4.1 shows the linear sweep voltammograms for the PTA solutions of tungsten concentrations ranging from 0.05-0.20 mol  $\text{L}^{-1}$  measured at a scan rate of 5  $\text{mV s}^{-1}$  and a step size of 1 mV. The dashed lines at approximately  $-0.38 \text{ V}$  and  $-0.68 \text{ V}$ ,

corresponding approximately to a change in the gradients of the curves, delineated the optimal potential range for the reduction of the PTA ions to tungsten oxide [148, 149], as indicated by the consistently homogeneous microstructures of the films. The minimal deposition potentials required to reduce PTA ions to tungsten oxides were observed to be approximately  $-0.4$  V for the PTA of  $0.05$ - $0.20$  mol L<sup>-1</sup> tungsten concentrations. This shows that the minimal reduction potential of the PTA ions was not affected by the amounts present in the electrolyte solutions. The study of the effect of tungsten concentrations of the PTA solutions on the properties of the electrodeposited WO<sub>3</sub> thin films is discussed in detail in Chapter 5. The following sections of this chapter present the effect of the deposition potential on the properties of the films deposited from PTA of  $0.05$  mol L<sup>-1</sup> tungsten concentration for 90 min. This tungsten concentration was chosen because deposition at increasing potentials from PTA of higher tungsten concentrations led to thick films, which cracked owing to drying stresses. The dried as-deposited films were annealed at  $450^{\circ}\text{C}$  for 2 h. These annealing parameters were commonly used to transform the amorphous films to monoclinic phase [26, 39, 68], which was reported as the most efficient phase in photoelectrochemical application [96]. A detailed investigation of the effect of annealing condition on the formation of preferred crystallographic orientations of WO<sub>3</sub> thin films had been reported in Chapter 6.

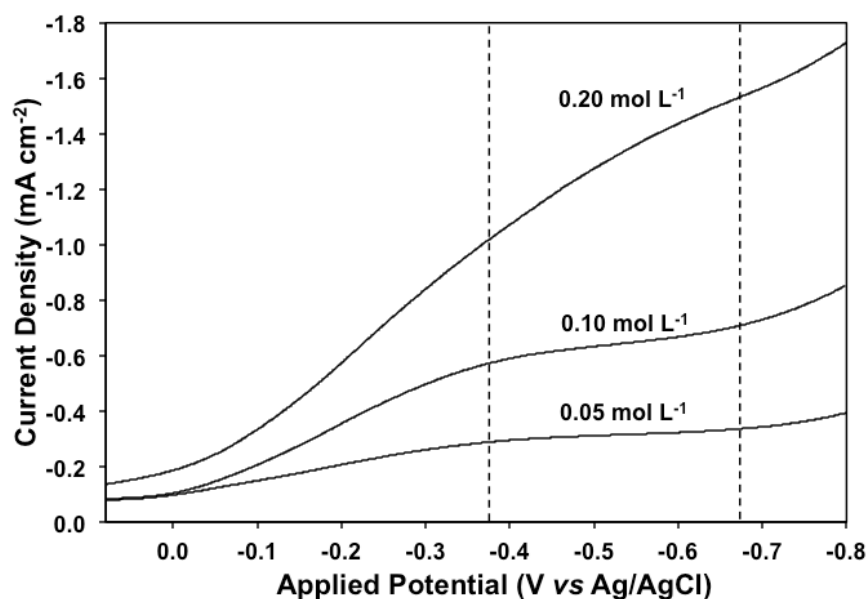


**Figure 4.1:** Linear sweep voltammogram for PTA of  $0.05$ - $0.20$  mol L<sup>-1</sup> tungsten concentrations measured at a scan rate of  $5$  mV s<sup>-1</sup> and a step size of  $1$  mV.

## 4.2.2 Effect of Deposition Potential on The Morphological, Mineralogical, Optical, and Photoelectrochemical Properties of Electrodeposited Tungsten Oxide Thin Films

### 4.2.2.1 Morphological Properties

Figure 4.2(a) shows the SEM images of the surfaces and cross-sections (insets) of the annealed films deposited at different potentials. The films consisted of irregularly shaped particles that formed a porous network. The film thicknesses (and hence the deposition rates) increased from 168 nm to 431 nm with increasing deposition potential for a fixed deposition time of 90 min. The average particle sizes of the matrix grains were in the range ~80-90 nm, which varied insignificantly at different deposition potentials, which indicated that the nucleation and growth mechanism were not influenced significantly by the deposition potential. However, the sample deposited at  $-0.60$  V, which was the thickest among the investigated films, exhibited some exaggerated grain growth. This deposition potential lies at the upper limit of the range for stable film growth, as shown in Figure 4.1.

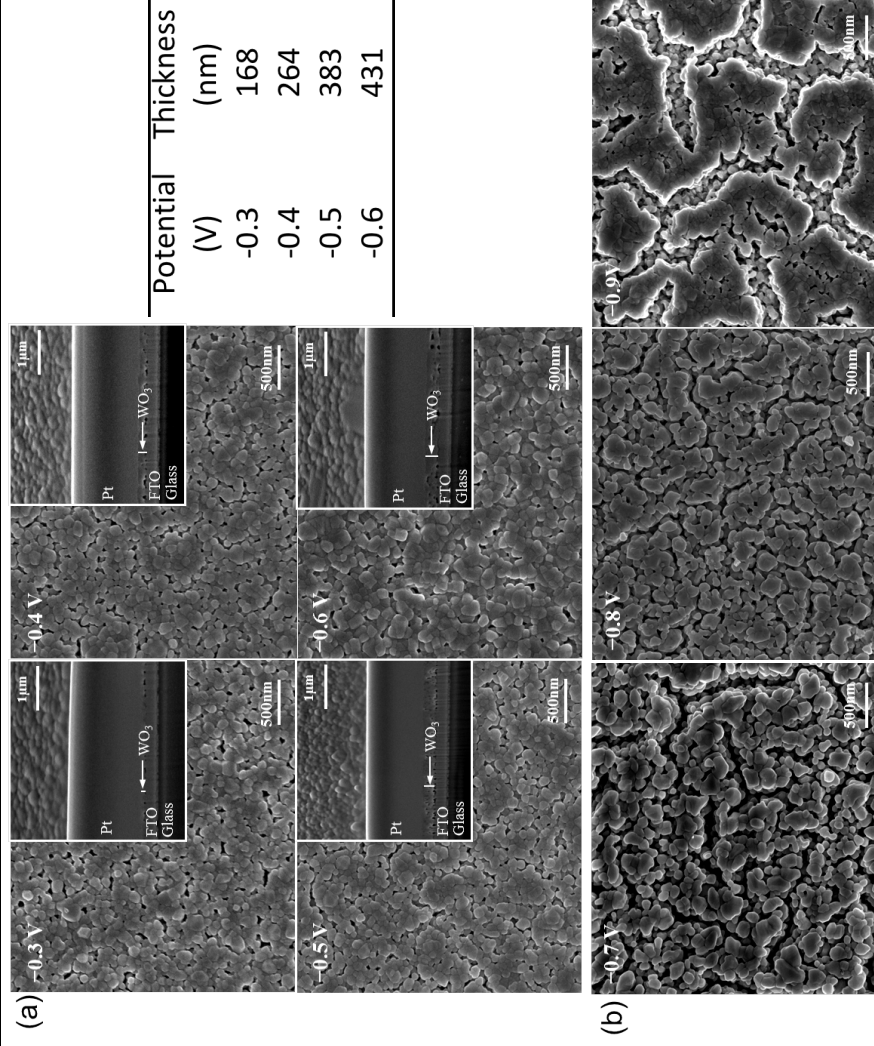


**Figure 4.2:** SEM images of  $\text{WO}_3$  thin films deposited at potentials of (a)  $-0.3$  V to  $-0.6$  V and (b)  $-0.7$  V to  $-0.9$  V from PTA of  $0.05 \text{ mol L}^{-1}$  tungsten concentration and annealed at  $450^\circ\text{C}$  for 2 h. Inset SEM images are the cross-sectional views of the films at  $45^\circ$  tilting.

Increasing the deposition potential enhanced the strength of the electric field between the working electrode (FTO substrate) and the counter electrode (Pt foil) and this accelerated the transport of the PTA ions (increased ionic flux) for deposition on the FTO substrates, as evidenced by the overall increasing current density shown in Figure 4.1. The rapid increase in current density above  $-0.60$  V owing to the extremely strong electric field across the working and counter electrodes resulted in films of thickness  $>634$  nm, without significant difference in matrix particle size, and this resulted in excessive drying shrinkage and potential cracking, as shown in Figure 4.2(b). Hence, the potential of  $-0.60$  V represented the upper limit to produce films of sufficient thinness to avoid drying shrinkage stresses. It should be noted that the upper limit for the deposition potential lowered for the deposition from PTA of higher tungsten concentrations owing to the extremely high ionic flux, which was influenced by both the deposition potential and the tungsten concentration.

#### 4.2.2.2 Mineralogical Properties

According to Woodward *et al.*[97], from which the standard XRD pattern is derived (see Appendix 4), monoclinic  $\text{WO}_3$  shows three major peaks (all  $\sim 95$ -100% intensity) at  $\sim 23.1^\circ$ ,  $23.6^\circ$ , and  $24.3^\circ$   $2\theta$ , which are indexed to the (002), (020), and (200) planes, respectively. The crystallographic parameters are  $a = 0.730$  nm,  $b = 0.754$  nm,  $c = 0.769$  nm,  $\alpha = 90.0^\circ$ ,  $\beta = 90.9^\circ$ , and  $\gamma = 90.0^\circ$ . The as-deposited tungsten oxide films were amorphous, as seen from the characteristic broad hump at  $20^\circ$ - $26^\circ$   $2\theta$  of the XRD spectra (see Figure 4.3 for the representative spectrum). Only FTO peaks were detected, which were indexed according to the XRD pattern of tetragonal  $\text{SnO}_2$  shown in Appendix 5. Annealing of the films at  $450^\circ\text{C}$  for 2 h resulted in recrystallisation of the films in monoclinic phase as confirmed from the XRD spectra shown in Figure 4.4. The crystallite sizes of the films, which were estimated by averaging those of the three major XRD reflections (002), (020), and (200) using Debye-Scherrer equation [150], varied in the range of 34-45 nm without trend with increasing deposition potential. This showed that each  $\text{WO}_3$  particle consisted of 2-3 crystallites. Some preferred orientations of the (002) and (200) planes parallel to the substrate can be seen (all three peaks are of approximately equal intensities in randomly distributed monoclinic  $\text{WO}_3$ ), as has been observed by others [39, 151]. It is likely that the preferred

orientations resulted from the easier growth of the orthogonal (002) and (200) planes relative to the non-orthogonal (020) plane. A detailed discussion of the mechanisms related to the crystal growth in non-random orientations of the films is presented in Chapter 6. The general increase in peak intensities with deposition potentials were attributed to improved crystal lattice symmetry as a result of the relief of physical mismatch stresses at the film/substrate interface with increasing film thickness, which was shown in Figure 4.2(a).

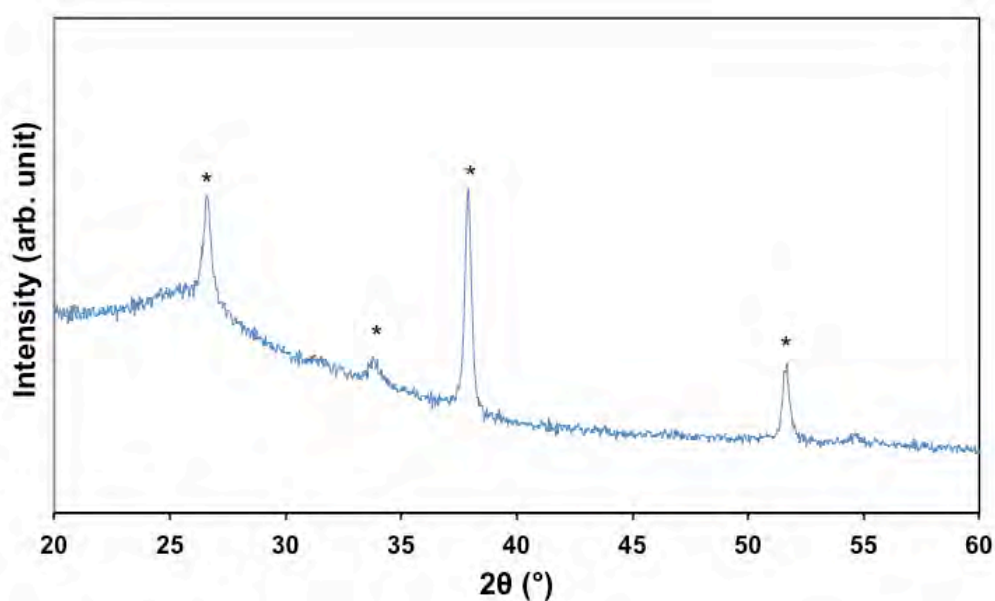


**Figure 4.3:** Representative XRD spectrum of the as-deposited films deposited at -0.4 V from PTA of 0.05 mol L<sup>-1</sup> tungsten concentration (\* indicates peaks of FTO substrate).

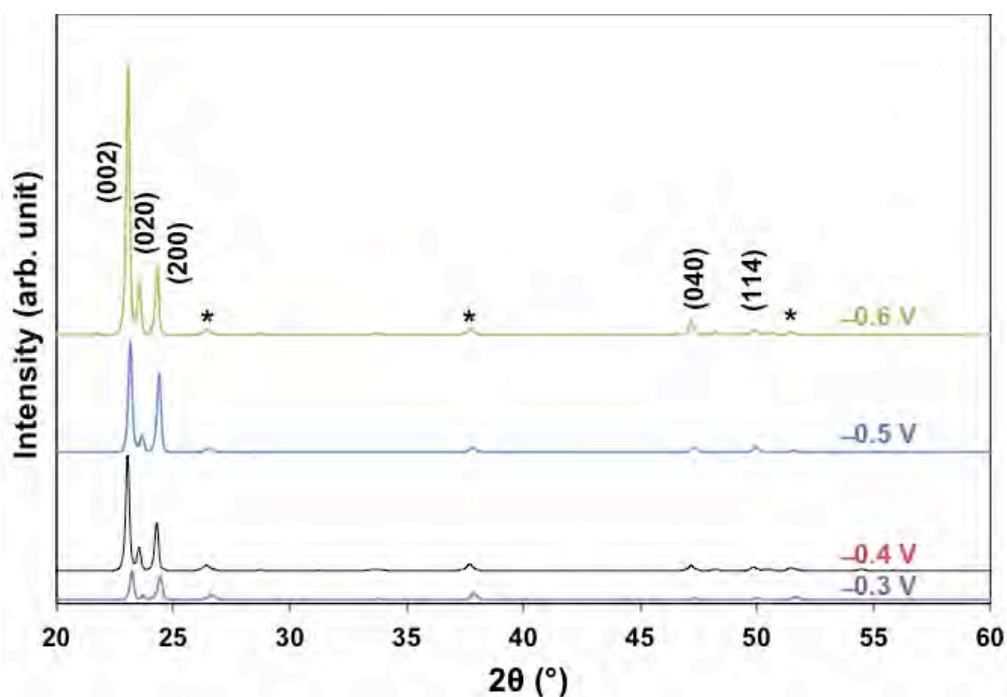


**Figure 4.4:** XRD spectra of WO<sub>3</sub> thin films deposited at various deposition potentials from PTA of 0.05 mol L<sup>-1</sup> tungsten concentration (\* indicates peaks of FTO substrate) and annealed at 450°C for 2 h.

#### 4.2.2.3 Optical Properties

Figure 4.5 shows the optical transmittance spectra of the annealed WO<sub>3</sub> thin films deposited at various potentials. It can be seen that the transmittance of the films deposited at -0.3 V to -0.5 V were fairly constant (~70%) in the wavelength range of >400 nm. The relatively low transmittance in the same wavelength range of the film deposited at -0.6 V probably resulted from this potential being a transition point for both stable growth and film thickness, although examination of the microstructures revealed insignificant difference compared to that of the films deposited at lower potentials.

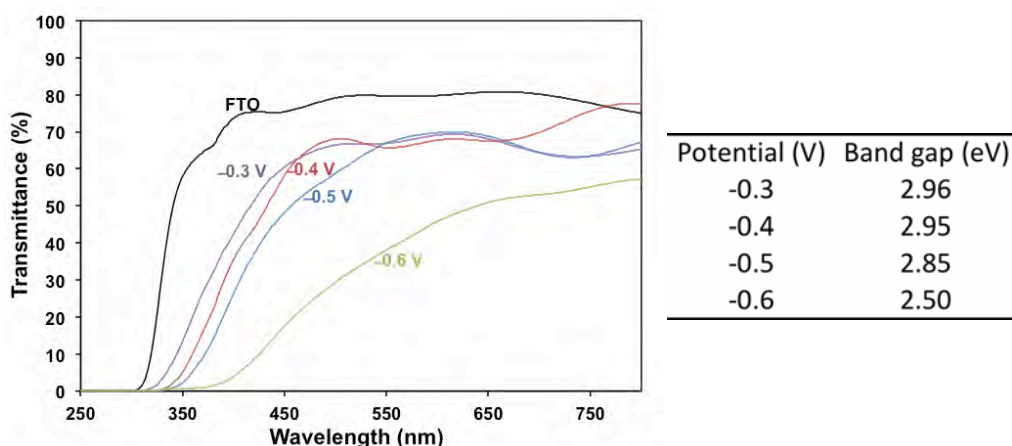


**Figure 4.5:** Optical transmittance spectra as a function of wavelength of  $\text{WO}_3$  thin films deposited at various deposition potentials from PTA of  $0.05 \text{ mol L}^{-1}$  tungsten concentration and annealed at  $450^\circ\text{C}$  for 2 h.

In addition, the absorption edges of the films shifted to longer wavelengths (red-shift) with increasing deposition potential owing to the decreasing optical band gaps. Also, the gradient of the absorption edge of the film deposited at  $-0.6 \text{ V}$  was significantly lower than those of the three thinner films. It is well known that such transmittance curve was associated with high concentration of grain boundary defects, which is responsible for light scattering [151]. These grain boundaries serve as exciton recombination sites. It was noted that the optical transmittance spectra ( $\sim 70\%$  in the wavelength range of  $>400 \text{ nm}$  and sharp absorption edges at  $\sim 420\text{--}435 \text{ nm}$ ) of the films deposited at  $-0.3 \text{ V}$  to  $-0.5 \text{ V}$  were comparable with that of the  $\text{WO}_3$  films deposited using other synthesis methods including wet-chemical self-assembly technique, sol-gel, and magnetron sputtering [138, 139, 152, 153].

The optical indirect band gaps of the films were estimated using Tauc's method [154]:

$$(\alpha h\nu)^{1/2} = C(h\nu - E_g) \quad (\text{Eq. 4.1})$$

where:  $\alpha$  =  $-(1/d)\ln(T/100)$   
 $d$  = Film thickness  
 $T$  = Optical transmittance  
 $h$  = Planck's constant

$\nu$	=	Frequency of light
$C$	=	Constant
$E_g$	=	Optical indirect band gap

The values of the optical indirect band gap ( $E_g$ ) were estimated by extrapolating the absorption edge to the abscissa of the plot of  $(\alpha h\nu)^{1/2}$  versus  $h\nu$ . The  $E_g$  values of the films were in the range of 2.50-2.96 eV, which decreased with increasing deposition potential. The reason for this is that the band gap consists of contributions from both the surface and volume band gaps, where the volume component usually is larger with thicker films [115, 155]. As the film thickness increased, the volume band gap dominated over surface band gap. The effects of impurities (compositional variation), particle sizes, and roughnesses were irrelevant or minimal for these nanostructures because the films were deposited from the electrolyte solutions of the same composition and consisted of similar matrix particle sizes. However, the low band gap of the film deposited at  $-0.6$  V also was possibly due to inhomogeneity of the film as evidenced in the indistinct (low gradient) absorption edge [156].

#### 4.2.2.4 Photoelectrochemical Properties

Figure 4.6 shows the photocurrent densities of the films measured under chopped illumination (50 W tungsten-halogen lamp; light source-to-sample distances of  $\sim 45$  cm; intensity of  $\sim 30$  mW m<sup>-2</sup>) and at a fixed applied potential of 0.70 V. The photocurrent densities dropped to nearly zero when the illumination was chopped off and rose instantly when the films were illuminated. It can be seen that the photocurrent density increased with increasing deposition potentials from  $-0.30$  V to  $-0.50$  V. This was attributed to the improved light absorption at longer wavelengths owing to decreasing optical indirect band gaps, which enhanced the photogeneration of excitons for water photolysis. Since the average WO<sub>3</sub> particle sizes showed minimal changes (80-90 nm) (see Figure 4.2) and no trend with increasing deposition potential, it was believed that the surface area did not play significant role in the photoelectrochemical activity of the films.

However, a lower photocurrent density was obtained for the film deposited at the higher potential of  $-0.60$  V, despite its relatively low optical band gap. This was attributed to the competing mechanisms of photogeneration and recombination of excitons. Since the potential of  $-0.60$  V represented the transition from stable to unstable film growth and associated drying shrinkage stresses, this nanostructure was likely to have been more defective than those deposited at lower deposition potentials. These defects equated to increase in recombination sites, which caused the loss of photogenerated excitons and thereby lowered the photocurrent density. The work in this chapter showed that the optimal deposition potential was in the range of  $-0.3$  V to  $-0.5$  V. The following Chapters 5-7 adopted the midpoint of the preceding range, *viz.*,  $-0.4$  V, in the electrodeposition of  $\text{WO}_3$  thin films.

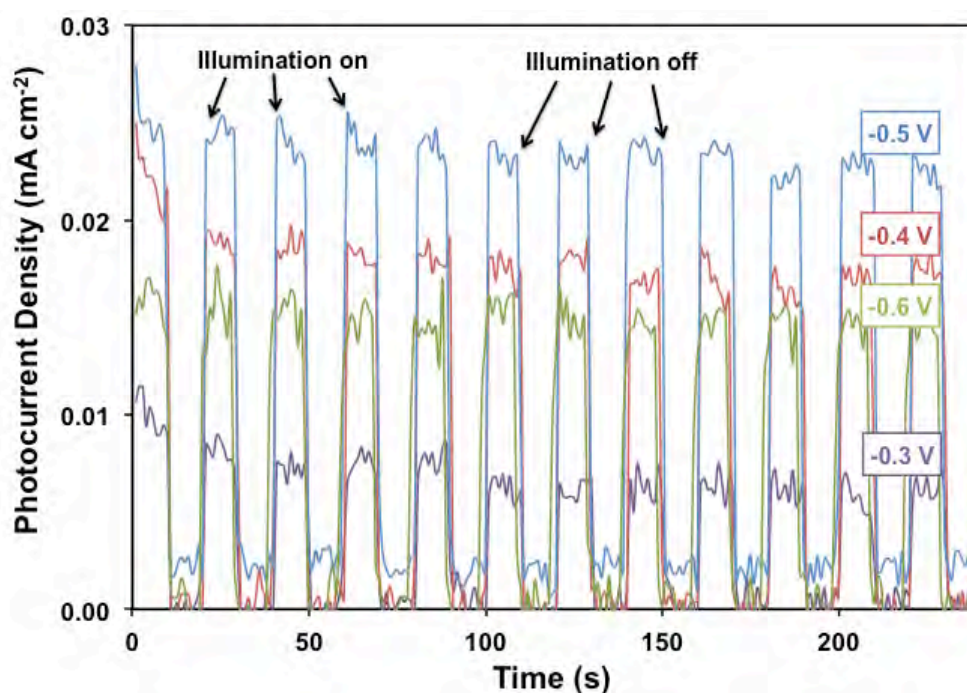


**Figure 4.6:** Potentiostatic photocurrent densities of  $\text{WO}_3$  thin films (deposited from PTA of  $0.05 \text{ mol L}^{-1}$  tungsten concentration and annealed at  $450^\circ\text{C}$  for 2 h) measured under chopped illumination (50 W tungsten-halogen lamp; light source-to-sample distances of  $\sim 45$  cm; intensity of  $\sim 30 \text{ mW m}^{-2}$ ) at  $0.7$  V versus Ag/AgCl in  $0.5 \text{ mol L}^{-1}$  NaCl aqueous electrolyte.

### 4.3 Key Results

- The electrodeposited films were composed of monoclinic  $\text{WO}_3$ , where the degree of crystallinity and preferred orientation of the orthogonal planes increased with increasing deposition potential and associated increasing film thickness.
- The grain sizes were in the range of ~80-90 nm, which were minimally influenced by the deposition potential.
- While films deposited at the potential range of  $-0.30$  to  $-0.60$  V showed controlled nanostructures with thicknesses in the range 168-431 nm, increasing the deposition potential from  $-0.70$  to  $-0.90$  V resulted in a rapid increase in the film thickness, which led to cracking from drying stress.
- Linear voltammetry data suggested that the optimal potential for the deposition of stable films was in the range  $-0.38$  to  $-0.68$  V. However, the data for the film deposited at a potential of  $-0.30$  V indicated a film of high quality. In contrast, the data for the film deposited at a potential of  $-0.60$  V indicated a film of a low quality and so this voltage represented a transition point for stable-unstable film growth and unstressed-stressed nanostructure from drying.
- The trends in the optical transmission properties showed that the photocatalytic activity of the films could be expected to decrease with increasing potential, thickness, and crystallinity. That is, the band gap and projected absorption edge exhibited a red shift. This was attributed to the relative effects of the surface and volume band gaps, in which the latter would increase relative to the former with increasing thickness.
- The photocurrent densities reflected the effects of increasing solid volume and decreasing band gap with increasing film thickness. The exception was the reduced performance of the film deposited at the potential of  $-0.60$  V. This outcome was attributed to the competition between the photogeneration and recombination of excitons, where the potential of  $-0.60$  V represented the transition point described above.

## CHAPTER 5

### Synthesis of Tungsten Oxide Thin Films by Electrodeposition: Effects of Tungsten Concentration of Peroxotungstic Acid and Deposition Time

#### 5.1 Introduction

The work reported in Chapter 4 identified the optimal range of deposition potentials for the electrodeposition of  $WO_3$  thin films. This chapter details the investigation of the effects of (i) tungsten concentrations of the peroxotungstic acid (PTA) solutions and (ii) deposition times, on the resultant physical, optical, and photoelectrochemical properties of the films. The tungsten concentration of PTA solution, which represents the availability of PTA ions in the solution; and the deposition time, which controls the reaction time of these PTA ions to form tungsten oxides on the working electrode; are two important parameters that affect the growth mechanism and consequently the physical and optical properties of the films. The correlations between these preceding properties and the photoelectrochemical response of the films were investigated. Part of the work presented in this chapter has been published in *Electrochimica Acta*, year 2012, volume 75, and pages 371-380. A copy of the publication is provided in Appendix 7.

#### 5.2 Results and Discussion

##### 5.2.1 Potentiostatic Current Transient as a Function of Tungsten Concentration of Peroxotungstic Acid – Growth Mechanism of Tungsten Oxide Thin Films

The deposition current density versus time curves as a function of tungsten concentration (at deposition potential of  $-0.4$  V) were measured as shown in Figure 5.1 in order to study the effect of tungsten concentration on the electrochemical reduction of PTA ions to form tungsten oxide thin films. The deposition current density was dependent on both the sheet resistance of the working electrode and the electrical conductivity of the PTA electrolyte solution. Since identical substrates were used as the working electrodes, the higher initial deposition current density observed in the PTA electrolyte solution of higher tungsten concentration resulted from the higher conductivity of the electrolyte. Once electrical power was applied to the electrochemical cell, the deposition current density initially decreased rapidly to approximately half its value, then more gradually, and finally approaching a steady value.

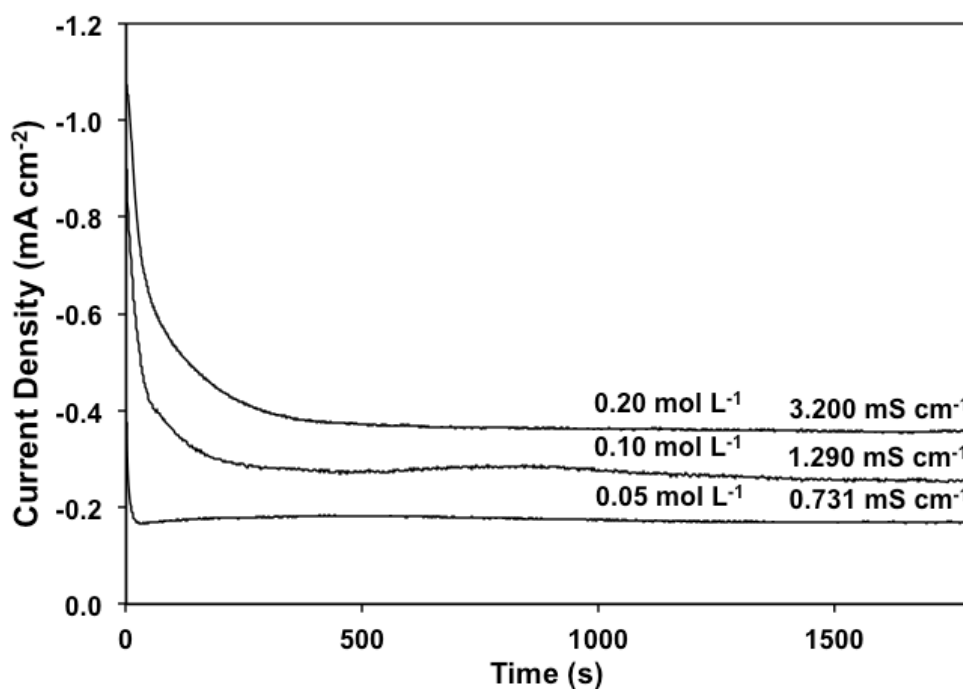


**Figure 5.1:** Deposition current densities as a function of time and tungsten concentration of  $\text{WO}_3$  thin films deposited at  $-0.4$  V vs Ag/AgCl for 30 min (PTA electrolyte solution conductivities before electrodeposition also given).

The FTO substrate is conducting while  $\text{WO}_3$  grains are semiconducting and the contributions of the two components determine the effective sheet resistance of the working electrode. The growth of semiconducting  $\text{WO}_3$  grains reduced the exposed surface area of the conducting FTO electrode, which reduced the deposition current density. It was observed that the extent of decrease in the deposition current density prior to its stabilisation was proportional to the tungsten concentration of PTA solution.

On the other hand, the amount of time required for the stabilisation of the deposition current density was largely a function of the grain size of the film or, to be more precise, the time to impingement/percolation of  $\text{WO}_3$  grains. Once grain impingement occurs, the substrate is completely covered by a crystalline layer of  $\text{WO}_3$ , thereby stabilising the deposition current density (subsequent grain growth has very little effect on the sheet resistivity). However, the amount of time required for grain impingement depends not only on the diameter but also on the thickness of the grain. Since the volume of a grain increases with increasing diameter and thickness, the amount of time required to form a volume of coherent layer increases with increasing tungsten concentration, where the greater amount of tungsten available facilitates the growth of thicker grains. In other words, larger grain sizes were formed in films deposited from higher tungsten concentrations, which was confirmed by the SEM observations shown in Figure 5.2.

**Table 5.1:** Summary of analytical data (photoconversion efficiencies measured using tungsten-halogen lamp).

#	[W] (mol L <sup>-1</sup> )	t (min)	d (nm)	Average grain size (nm)	Standard deviation of grain size (nm)	True porosity (%)	$E_g$ (eV)	$\eta$ (%)
t	0.05	30	258	78	6	4.5	3.05	0.02
u	0.05	60	263	86	11	2.8	3.05	0.04
v	0.05	90	325	77	10	4.3	2.95	0.06
w	0.05	120	588	84	7	2.8	2.70	0.10
x	0.10	30	307	109	13	1.0	2.95	0.03
y	0.10	60	1394	105	17	1.1	2.60	0.14
z	0.20	30	466	122	9	0.8	2.70	0.08

# = sample name; [W] = tungsten concentration; t = deposition time; d = film thickness;  $E_g$  = optical indirect band gap;  $\eta$  = photoconversion efficiency. The average grain size and true porosity were measured using SEM and *ImageJ*, respectively.

Once impingement/percolation of the grains (and their volumes) has occurred, the sheet resistance of  $\text{WO}_3$  thin film becomes constant. The final (constant) deposition current density is dominated by the tungsten concentration since the deposition current density and tungsten concentration are proportional. These data suggested the following film growth mechanism:

- (i) The nucleation and growth of monolayer-like grains of semiconducting  $\text{WO}_3$  upon the supply of power across the electrochemical cell – this corresponded to the section showing the most rapid drop in the current density (~30-60 sec).
- (ii) Lateral and outward growth of individual  $\text{WO}_3$  nuclei into larger particles – this corresponded to the transition region in the curve.
- (iii) Impingement/percolation of individual grains and establishment of a coherent nanoscale crystalline film – this corresponded to the end of the transition region.
- (iv) Nucleation on pre-existing grains, which does not affect the sheet resistance of the electrode – this corresponded to the initial region of constant current density.
- (v) Outward grain growth to increase the film thickness – this corresponded to the later region of constant current density.

### 5.2.2 Effects of Tungsten Concentration of Peroxotungstic Acid and Deposition Time on The Properties of Tungsten Oxide Thin Films

The following sections present the results of the characterisation of the films deposited at -0.4 V for 30-120 min from PTA of 0.05-0.20 mol L<sup>-1</sup> tungsten concentrations. The as-deposited films were annealed at 450°C for 2 h.

#### 5.2.2.1 Morphological and Mineralogical Properties

The SEM images of the annealed films deposited from PTA of 0.05-0.20 mol L<sup>-1</sup> tungsten concentrations for various deposition times are shown in Figure 5.2. Relatively dense  $\text{WO}_3$  thin films of equiaxed nanoparticles were obtained. The porosities of the films were <5% (see Table 5.1). These nanoparticles were of average diameter of ~78 nm for samples

deposited from  $0.05 \text{ mol L}^{-1}$ , which increased to 109 nm and 122 nm for the depositions from  $0.10 \text{ mol L}^{-1}$  and  $0.20 \text{ mol L}^{-1}$ , respectively, as shown in Figure 5.2 (a) and Table 5.1. There were no discernible changes in the surface morphologies of  $\text{WO}_3$  thin films deposited for different deposition times at fixed tungsten concentrations (see Figures 5.2 (b) and (c)). The grain size was affected by the tungsten concentration because grain growth occurred rapidly at high tungsten concentrations owing to a greater number of PTA ions and a shorter diffusion distance from the solution to the solid/liquid interface.

The cross-sectional images, as seen in the insets of Figure 5.2, show that the film thickness increased with both tungsten concentration and deposition time. The reason for this was the increased availability of PTA ions in the electrolyte solution and the time required for the delivery of ions to the growing film. In addition, it can be seen that the increase in the average size of the  $\text{WO}_3$  grains with increasing tungsten concentration caused a decrease in the porosity of the film, which was consistent with the conventional mechanism of grain growth during densification [157]. However, the deposition times  $>120$  min and the tungsten concentrations  $>0.20 \text{ mol L}^{-1}$  resulted in cracked and peeled films owing to drying stresses arising from surface dehydration [158].

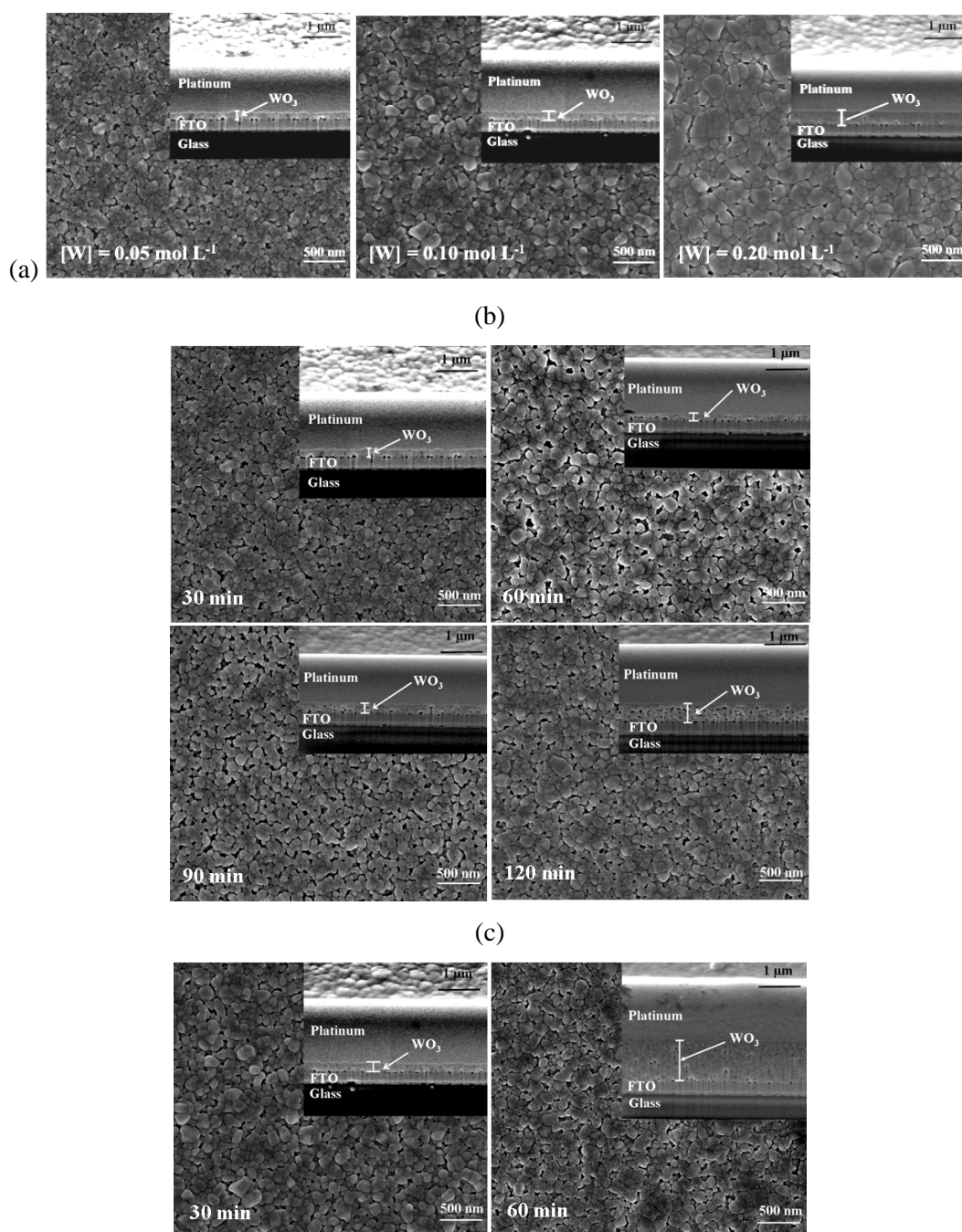


**Figure 5.2:** SEM images of WO<sub>3</sub> thin films deposited from PTA of tungsten concentrations of: (a) 0.05-0.20 mol L<sup>-1</sup> for 30 min, (b) 0.05 mol L<sup>-1</sup> for 30-120 min, (c) 0.10 mol L<sup>-1</sup> for 30-60 min and annealed at 450°C for 2 h (insets: cross-sectional views).

Figure 5.3 shows the XRD data for the annealed films deposited from PTA of 0.05-0.20 mol L<sup>-1</sup> tungsten concentrations for various deposition times. Three major peaks at ~23.1°, 23.6°, and 24.3° 2θ were obtained, which were indexed to the (002), (020), and (200) planes of monoclinic phase [97], respectively. In contrast to the equivalent XRD peak intensities of the three major planes for randomly distributed monoclinic WO<sub>3</sub>[97], the XRD data in the present work suggested that some preferred orientation occurred, where the (002) plane was favoured as a function of both tungsten concentration and deposition time. However, while this was the case for all time points, it can be seen that increasing tungsten concentration favoured the (200) orientation at the highest level. Detailed investigation on the preferred crystallographic orientations of monoclinic WO<sub>3</sub> thin films is presented in Chapter 6.

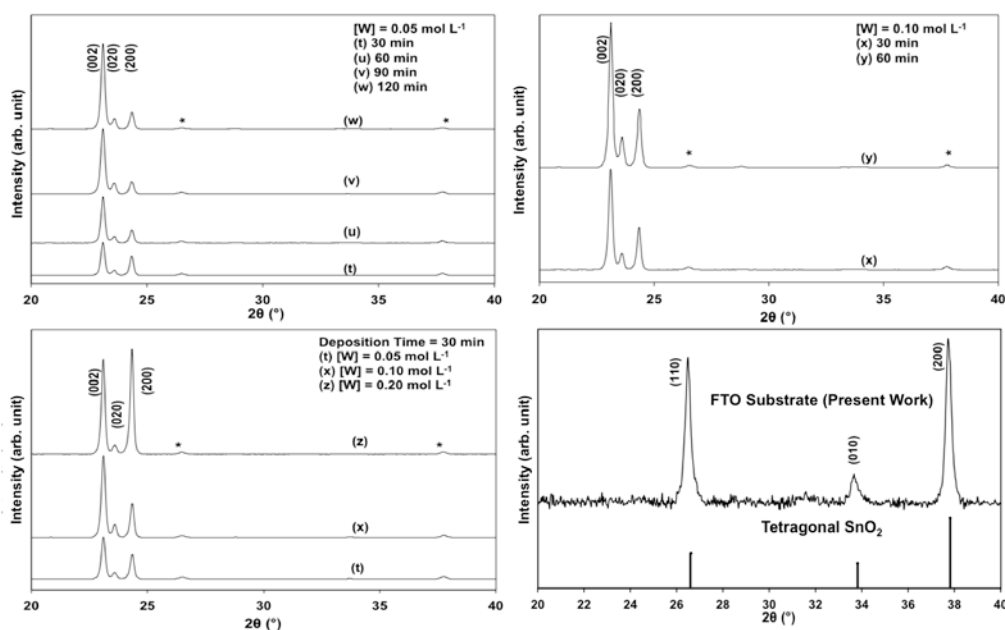


**Figure 5.3:** XRD spectra of WO<sub>3</sub> thin films deposited from PTA of tungsten concentrations of 0.05 mol L<sup>-1</sup> for 30-120 min (a-d), 0.10 mol L<sup>-1</sup> for 30-60 min (e-f), and 0.20 mol L<sup>-1</sup> for 30 min (g) and annealed at 450°C for 2 h. XRD spectra of FTO substrate of the present work and the reference data for tetragonal SnO<sub>2</sub> [159] also given (\* indicates peak from FTO substrate).

## 5.2.2.2 Optical Properties

UV-VIS spectrophotometry was done in order to investigate the optical properties of the films. Figure 5.4 shows the transmittance spectra of the films deposited from PTA of different tungsten concentrations for various times. In general, the optical transmittance of the films decreased with increasing film thickness. This was likely a result of (i) the increasing absorption owing to greater cross-sectional volume, and (ii) the reflection (scattering) owing to a higher density of grain boundaries. In addition, the absorption edge shifted to longer wavelength (red-shift) as the thickness of the film increased, showing the maximal extension of the optical absorption limit to 370 nm in film (y) (deposited from PTA of  $0.10 \text{ mol L}^{-1}$  tungsten concentration for 60 min).

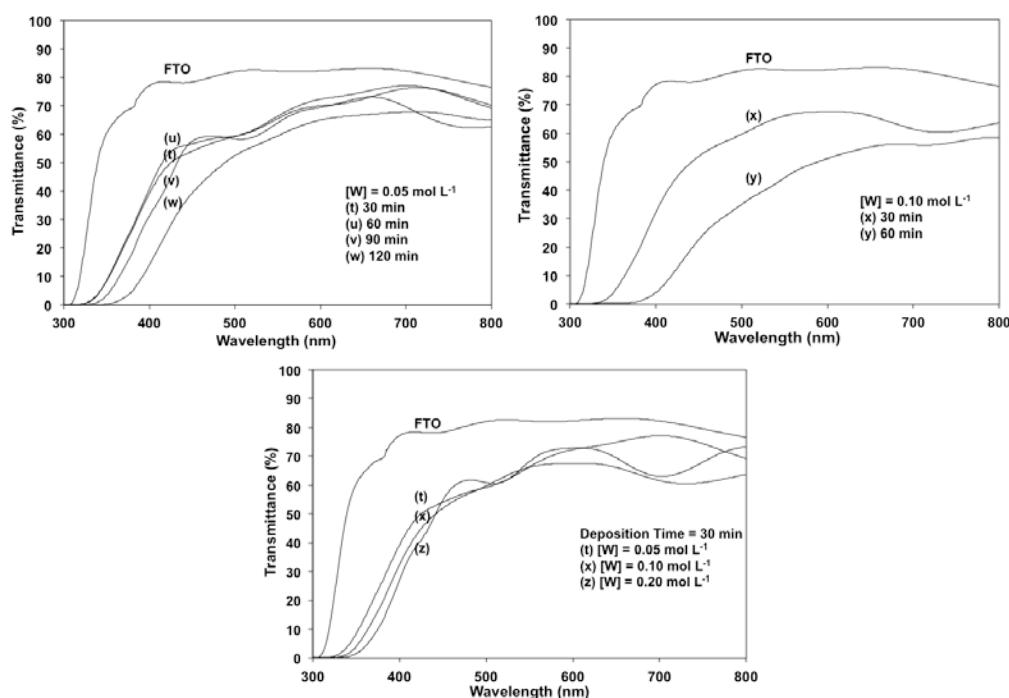


**Figure 5.4:** Transmittance spectra of  $\text{WO}_3$  thin films deposited from PTA of tungsten concentrations of:  $0.05 \text{ mol L}^{-1}$  for 30-120 min (a-d),  $0.10 \text{ mol L}^{-1}$  for 30-60 min (e-f), and  $0.20 \text{ mol L}^{-1}$  for 30 min (g) and annealed at  $450^\circ\text{C}$  for 2 h. Transmittance spectrum of FTO substrate also is shown for reference.

These transmittance spectra were used to obtain the optical indirect band gap of WO<sub>3</sub> thin films by drawing Tauc plots [160] according to Equation 4.1. The optical indirect band gaps of WO<sub>3</sub> thin films were obtained by the extrapolation to the abscissa of the plot of  $(\alpha h\nu)^{1/2}$  against  $h\nu$ . Representative examples of three such plots are shown in Figure 5.5. Figure 5.6 shows the plot of optical indirect band gap of WO<sub>3</sub> as a function of film thickness; these values are listed in Table 5.1. The optical indirect band gap of WO<sub>3</sub> decreased from 3.05 eV to 2.60 eV for film thicknesses (cross-sections) from 258 nm to 1394 nm.

There was an inflection in the data for the thickness at ~500 nm, which corresponded to the optical indirect band gap of ~2.6 eV. The inflection was an indication of the relative effects of the volume and surface band gaps, where the surface is that of the film itself and not the grain boundary area. This was supported by the work on sputtered WO<sub>3</sub> films by Weinhardt *et al.* [115], who measured a surface band gap of 3.28 eV and a bulk band gap in the range 2.5-2.6 eV. This variation arose owing to the differences in surface band gap and band edge position relative to those of the bulk as a result of alterations in both structure and composition. Since thicker films are associated with higher volumes, then the bulk band gap should dominate. This was confirmed by the reported bands gaps (*viz.*, bulk band gap range) in the range of ~2.5-2.7 eV [105, 108, 115].

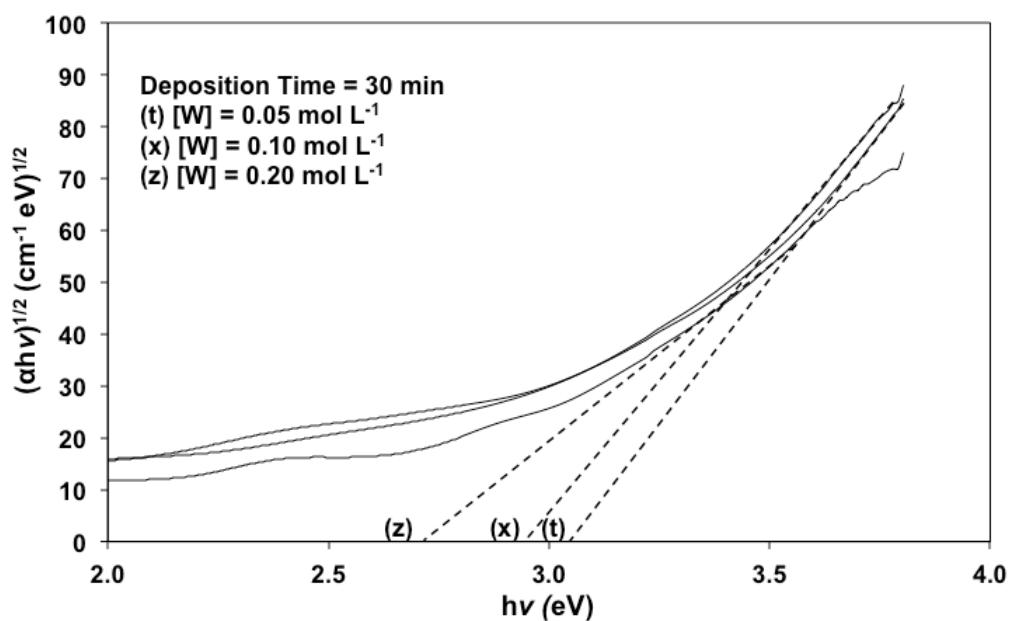


**Figure 5.5:** Tauc plots of WO<sub>3</sub> thin films deposited from PTA of 0.05-0.20 mol L<sup>-1</sup> tungsten concentration for 30 min and annealed at 450°C for 2 h.

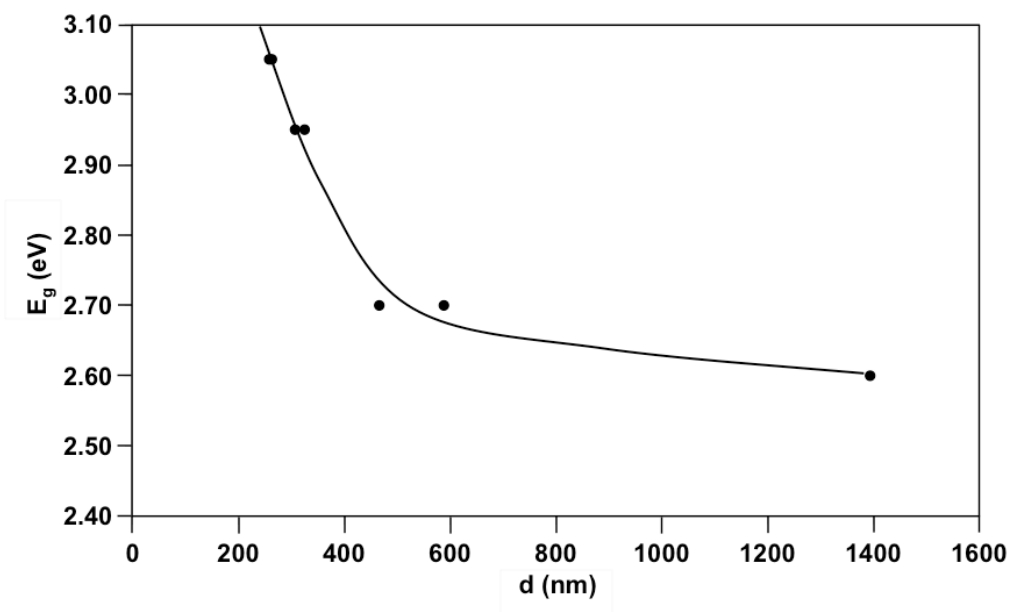


**Figure 5.6:** Optical indirect band gaps  $E_g$  of WO<sub>3</sub> thin films as a function of film thickness  $d$ . These films were deposited from PTA of 0.05-0.20 mol L<sup>-1</sup> tungsten concentration for 30-120 min and annealed at 450°C for 2 h.

These data were important because they showed that there was a threshold minimal film thickness suitable for optimal photosensitivity. Further, these data showed that the overall band gap can be tailored by balancing the relative contributions of the surface and bulk band gap components by the control of the film thickness.

Further, the decrease in the optical indirect band gap at the higher thicknesses was likely due to compressive stress owing to lateral grain growth established by impingement on neighbouring grains, after which outward growth normal to the substrate was facilitated. The rounded and relatively dense particles showed that grain impingement stopped lateral grain growth within 30 min, thereby resulting in consistent grain size (for identical tungsten concentration). At the point at which the grains impinged, only outward grain growth occurred, which resulted in increased film thickness with deposition time. Grain impingement and the associated compressive stress would increase the repulsive electron potential and hence increase the minimal photon energy required to excite an electron from the valence band to the conduction band [161]. These stresses were possible to exist even after annealing because the cooling process from 450°C to room temperature involved phase transformation from orthogonal to monoclinic, which involved a ~2% volume contraction of the unit cell [95, 97, 162]. However, with increasing film thickness, the distance from the constrained substrate/film interface increased, so these stresses were reduced and the grains were induced towards an equilibrium stress condition. Similar experimental observations have been reported by Mohanty *et al.* [163] for magnetron-sputtered Al-doped ZnO thin films in which compressive stresses in the film relaxed with increasing thickness, resulting in a reduction in the optical band gap.

### 5.2.2.3 Photoelectrochemical Properties

Figure 5.7 shows the dependence of the photocurrent density on the applied potential measured in 0.5 mol L<sup>-1</sup> NaCl aqueous solution under chopped illumination (50 W tungsten-halogen lamp; light source-to-sample distances of ~45 cm; intensity of ~30 mW m<sup>-2</sup>) for all samples. The measurements were taken at a scan rate of 5 mV s<sup>-1</sup> and a step size of 1 mV. The photocurrent density of the films followed a general trend of increase

with increasing applied potential owing to the (i) higher band-bending at the photoanode/electrolyte interface, which led to higher mobilities of the photogenerated excitons, and (ii) expansion of the depletion width with increasing applied potential [4]. These phenomena facilitated the photogeneration and separation of excitons.

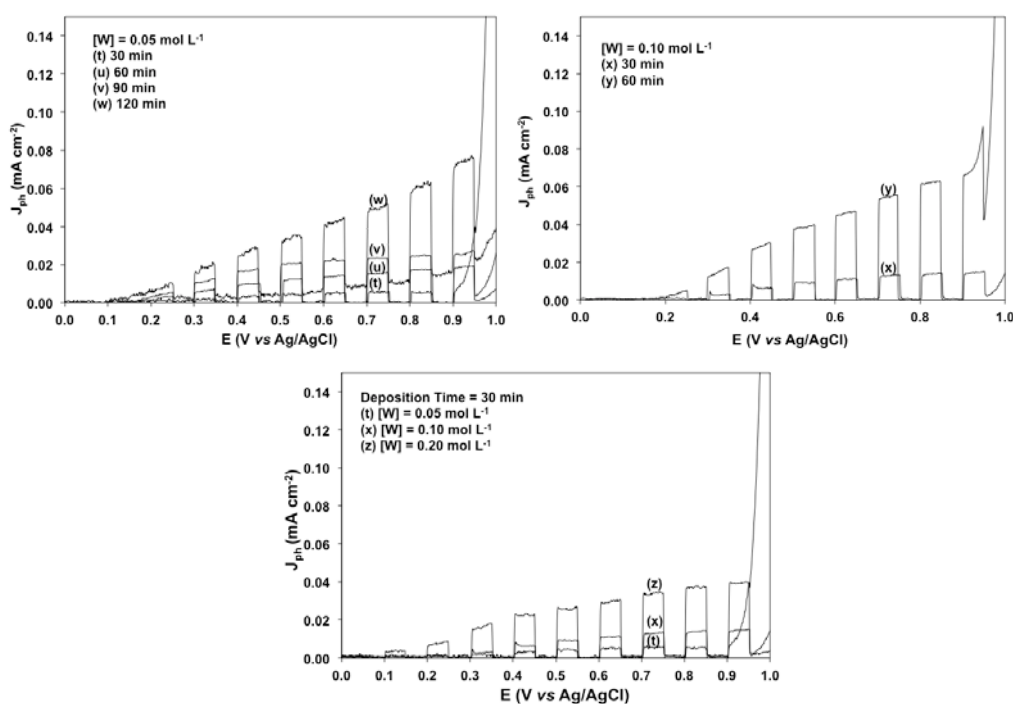


**Figure 5.7:** Linear potentiodynamic voltammograms (photocurrent density  $J_{ph}$  vs applied potential  $E$ ), under chopped illumination (50 W tungsten-halogen lamp; light source-to-sample distances of  $\sim 45$  cm; intensity of  $\sim 30$   $\text{mW m}^{-2}$ ), in aqueous  $0.5$   $\text{mol L}^{-1}$  NaCl (pH 6.27), of  $\text{WO}_3$  thin films deposited from  $0.05$ - $0.20$   $\text{mol L}^{-1}$  tungsten concentration for 30-120 min and annealed at  $450^\circ\text{C}$  for 2 h. The scan rate and step size were  $5$   $\text{mV s}^{-1}$  and  $1$  mV, respectively.

The formation of a depletion layer on the grain surface is controlled not only by the applied potential but also by the grain size relative to the width of the depletion layer [5]. If the grain radius of a porous photoanode is smaller than the depletion layer width, then the depletion layer will not form. In this case, the mechanisms of charge transport and separation are dominated by diffusion, and these facilitate enhanced photoelectrochemical

performance in contrast with that of a photoanode with large grains that suppress the recombination of photogenerated excitons [65]. On the other hand, with larger grains, such as those in the present work, a depletion layer of width smaller than the grain radius is formed. The establishment of a depletion layer can be confirmed using Butler's equation [31]:

$$J_{\text{ph}} = \varphi \alpha \sqrt{\frac{2q\epsilon}{N_d}} (E - V_{\text{fb}}) \quad (\text{Eq. 5.1})$$

where  $J_{\text{ph}}$  is the photocurrent density at applied potential  $E$ ,  $\varphi$  is the incident photon flux,  $\alpha$  is the optical absorption coefficient,  $q$  is the electron charge,  $\epsilon$  is the dielectric constant,  $N_d$  is the donor concentration, and  $V_{\text{fb}}$  is the flat-band potential. The equation can be applied according to the Schottky-Gartner model [164] by plotting  $J_{\text{ph}}^2$  against the applied potential and noting whether or not a linear plot is generated. If it is linear, it can be concluded that a Schottky depletion layer has been established at the grain surface. The electric field associated with the layer contributes to the separation and migration of the photogenerated excitons. Figure 5.8 shows representative plots that confirmed a Schottky depletion layer. A flat-band potential of +0.2 V to +0.3 V was obtained by extrapolating plots to the abscissa. The positive sign indicated that a biasing potential was required for water photolysis [165].

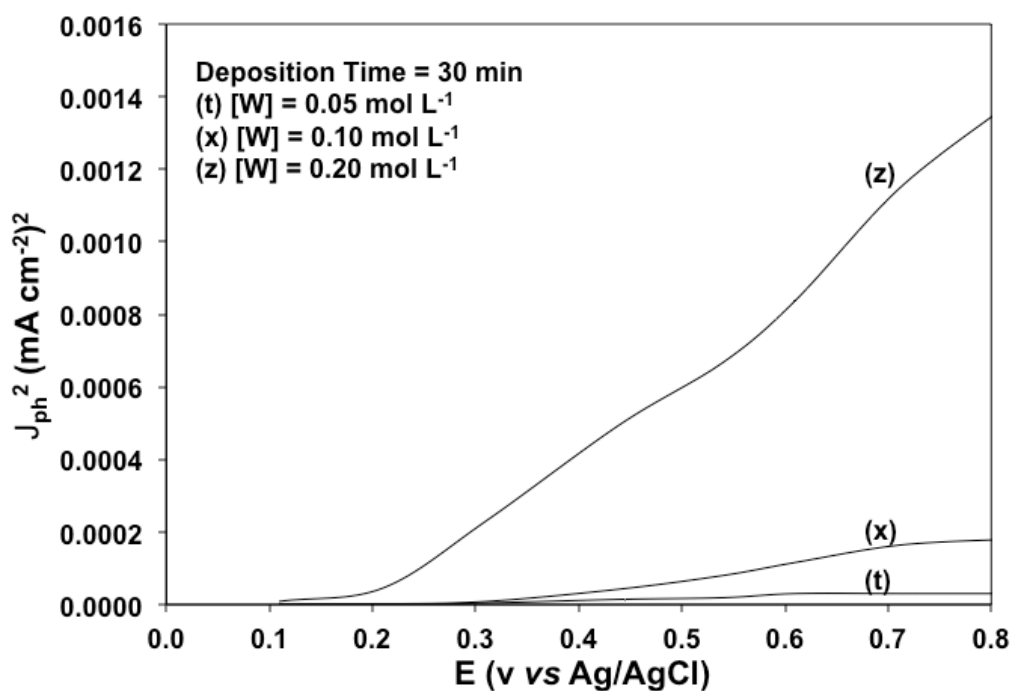


**Figure 5.8:** Plots of  $J_{ph}^2$  as a function of applied potential  $E$  of  $WO_3$  thin films deposited from PTA of 0.05-0.20 mol L<sup>-1</sup> tungsten concentration for 30 min and annealed at 450°C for 2 h.

The photoconversion efficiencies were quantified using Equation 3.5 [4]:

$$\text{Photoconversion efficiency} = \left[ \frac{J_{ph}(1.23 - E)}{J_{light}} \right] \times 100\% \quad (\text{Eq. 3.5})$$

where  $J_{ph}$  is the photocurrent density generated at the applied potential of  $E$  under incident light of intensity  $J_{light}$ . Figure 5.9 shows the photoconversion efficiencies of the films as a function of applied potential. The optimal range of applied potential fell in the range ~0.65-0.75 V, where the maximal photoconversion efficiencies were obtained. It is interesting that film (z) (deposited from PTA of 0.20 mol L<sup>-1</sup> tungsten concentration for 30 min) appeared to exhibit photolysis at applied potentials lower than the flat-band potential. It may be noted that this sample had the largest grain size of 122 nm (see Table 5.1). It is well known that the flat band potential depends on the pH [166]. It is less well known that the pH is influenced significantly by the particle size [167, 168]. Consequently, these data

suggested the importance of grain size and its effect on the net pH at the photoanode/electrolyte interface in altering the flat-band potential in order to reduce or eliminate the need for an external applied potential to achieve photolysis.

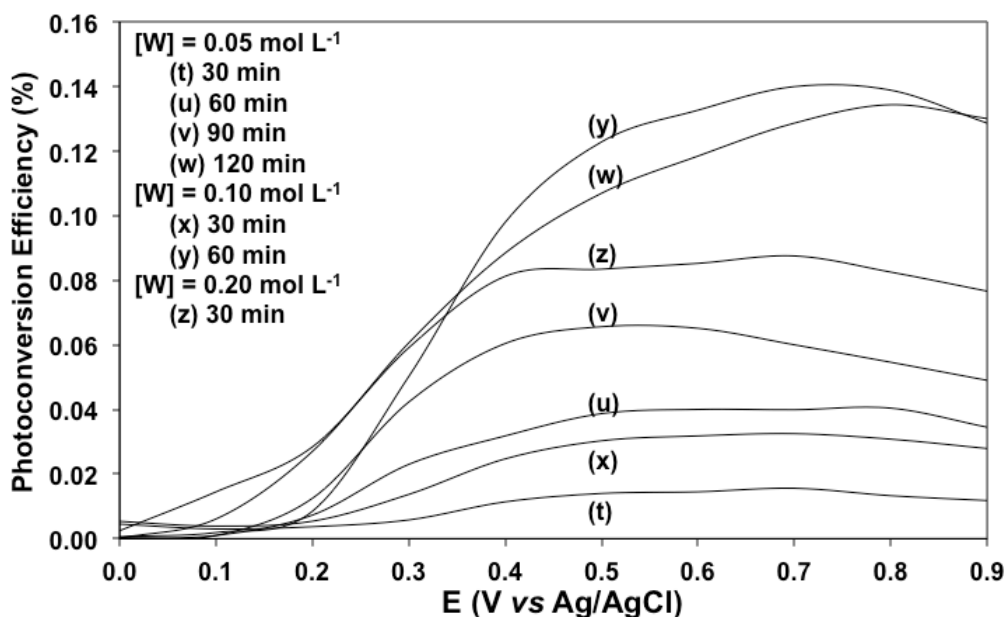


**Figure 5.9:** Photoconversion efficiencies of  $\text{WO}_3$  thin films as a function of applied potential  $E$ . These films were deposited from PTA of 0.05-0.20  $\text{mol L}^{-1}$  tungsten concentration for 30-120 min and annealed at  $450^\circ\text{C}$  for 2 h.

A benchmark of an applied potential of 0.70 V, which is the midpoint of the preceding range, is used commonly to compare efficiencies [30, 68, 165]. The photoconversion efficiencies of the films at this applied potential were plotted as a function of film thickness, as shown in Figure 5.10; these values, which ranged from 0.02% to 0.14%, also were listed in Table 5.1. It can be seen that there was a clear relation between the film thickness and the photoconversion efficiency, which appeared to be three regimes:

- (i) ~280-300 nm: This range was close to both the cut-off wavelength (~300 nm; from the light source supplier) of the halogen light source and what was

likely to be the mean free path of the visible light (~280 nm; from the data), although these cannot be differentiated.

- (ii) ~300-500 nm: This range of moderate increase in photoconversion efficiency with increasing film thickness was dominated by the surface band gap of  $\text{WO}_3$  and its rapid decrease in the overall band gap with increasing film thickness.
- (iii) ~500-1400 nm: This range of gradual increase in photoconversion efficiency with increasing film thickness was dominated by the bulk band gap of  $\text{WO}_3$  and its very slow decrease in the overall band gap with increasing film thickness.

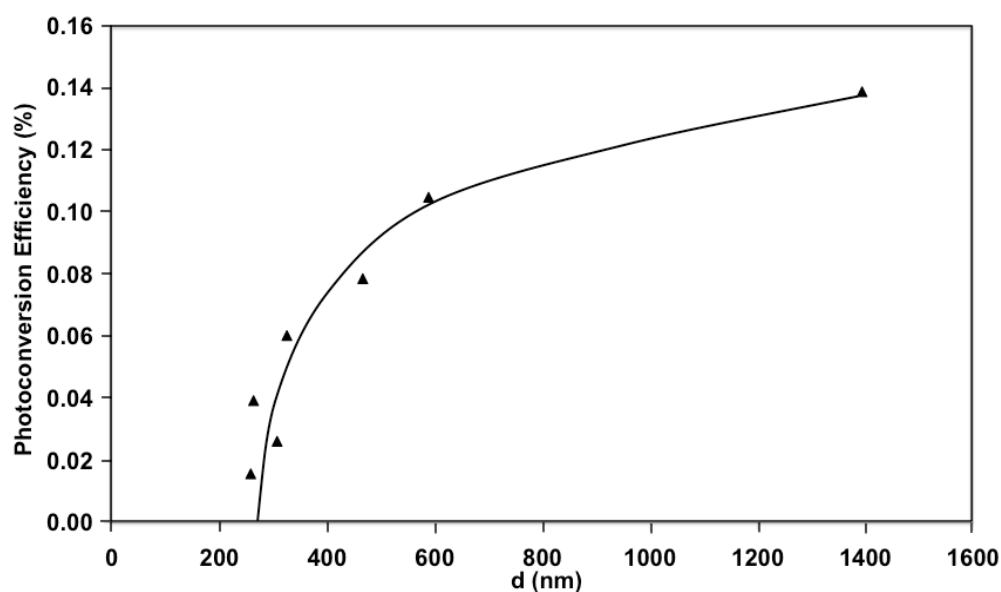


**Figure 5.10:** Photoconversion efficiencies of  $\text{WO}_3$  thin films as a function of film thickness  $d$ . These films were deposited from PTA of 0.05-0.20 mol  $\text{L}^{-1}$  tungsten concentration for 30-120 min and annealed at 450°C for 2 h.

The increase in photoconversion efficiency with increasing film thickness was attributed to the decrease in the optical indirect band gap and the improved light absorption of the films. A similar inflection at ~500-530 nm in the photocurrent as a function of film thickness for

WO<sub>3</sub> films was obtained by Miller *et al.*[33] for films of thicknesses 530-2830 nm. More generally, other studies [33, 70, 105, 169] have shown more or less similar behaviour for WO<sub>3</sub>, where the authors have commented that increasing film thickness can result in excessive charge carrier (electron) diffusion distance [70, 105], increased film resistivity [105], increased charge carrier equilibration time [105], and/or increased volume of grain boundaries as exciton recombination sites [169]. In the present work, increasing the film thicknesses beyond 1394 nm was anticipated to increase the optical absorption of the films. However, the optical band gap would change minimally, as evidenced by the gradual change in the optical band gap at thickness >500 nm in Figure 5.6, due to the intrinsic limitation of the electronic properties of WO<sub>3</sub>. While the improved optical absorption would be beneficial for photogeneration of excitons, thick films were associated with risk of cracking due to drying stress and limited photoelectrochemical efficiency due to high exciton recombination rate.

As tabulated in Table 5.1, the photoconversion efficiency of film (x) (0.10 mol L<sup>-1</sup> tungsten concentration for 30 min) was less than that of film (u) (0.05 mol L<sup>-1</sup> tungsten concentration for 60 min), even though it had a larger film thickness, suggesting that the porosity of the film deposited from 0.05 mol L<sup>-1</sup> tungsten played an important role in increasing the total surface area and allowing the permeation of electrolyte into the film.

As mentioned in Section 5.2, the photoelectrochemical performances of the films in the present work were not directly comparable with those of other researchers. There were several reasons for this, including the use of (i) light sources with different spectral outputs (tungsten-halogen *versus* xenon lamp) [170], (ii) light sources with different radiant intensities (30 mW cm<sup>-2</sup> in the present work *versus* typically 100 mW cm<sup>-2</sup> for xenon [30, 32, 33, 67, 87, 93, 114, 171], and (iii) differing sample-light distances (~45 cm in the present work *versus* typically unstated distances). The highest photocurrent density under tungsten-halogen light at the benchmark of an applied potential of 0.70 V was measured to be ~0.05 mA cm<sup>-2</sup> for film (y), as shown in Figure 5.7. However, an approximation of this maximal photocurrent density, comparable to that under xenon light, can be obtained. That is, the ratio of the integrated light intensities of tungsten-halogen to xenon light sources

[170] up to the cut-off region of the band gap (2.6 eV or 477 nm), as shown in Appendix 3, was calculated to be 1:50. Assuming a linear photoelectrochemical response of the films to the light intensities [114], the photocurrent density can be multiplied by 50 in order to approximate an equivalent value under xenon light of  $\sim 2.5 \text{ mA cm}^{-2}$ , which was mid-range for values of  $\sim 1\text{-}5 \text{ mA cm}^{-2}$  for state-of-the-art  $\text{WO}_3$  films produced by both traditional wet-chemical methods (*e.g.*, anodisation, solvothermal, sol-gel) and advanced physical vapour deposition methods (*e.g.*, reactive sputtering) [30, 32, 33, 44, 67, 77, 87, 93, 114, 171-173].

### 5.3 Key Results

- The films consisted of monoclinic  $\text{WO}_3$  of grain sizes in the range 77-122 nm and thicknesses in the range 258-1394 nm; the true porosities were  $<5\%$ . These microstructural and morphological parameters were dependent largely upon the tungsten concentration and deposition time.
- The optical transmission data revealed significant decrease in the optical indirect band gap, from 3.05 eV to 2.60 eV, as a function of increasing film thickness. This was considered to result from different contributions from the surface and bulk band gap components as well as compressive stress at the film/substrate interface.
- The voltammetry data and associated Butler plot revealed the establishment of a Schottky depletion layer and a flat-band potential of +0.2 V to +0.3 V.
- Although the calculated photoconversion efficiencies were in the range 0.02% to 0.14%, which was commensurate with the use of a tungsten-halogen light rather than xenon, there was a trend of increasing efficiency as a function of increasing film thickness. This was attributed to decreasing band gap and increasing light absorption. The shape of the curve of the preceding data supported the conclusion of different contributions from the surface and bulk band gap components.
- Evidence of photolysis in the absence of an external applied potential suggested the importance of the effect of grain size on the pH and its alteration of the flat-band potential.

## CHAPTER 6

### Critical Role of {002} Preferred Orientations on Electronic Band Structures of Monoclinic Tungsten Oxide Thin Films

#### 6.1 Introduction

Preferred crystallographic orientation and associated differences in properties result from anisotropic crystal growth in specific directions. The photocatalytic performances of materials, which are determined by their physical and electronic properties, are strongly dependent on the crystallographic orientations of the exposed surfaces [63, 99, 174-176]. Therefore, it is important to understand and control the crystallography of a material for optimisation of its properties. The present work demonstrated the use of a novel approach to control the crystallographic {002} orientations of electrodeposited monoclinic  $\text{WO}_3$  thin films uncontaminated by growth directing agents through the manipulation of the deposition and annealing parameters. That is, the crystallographic growth of the films was controlled by varying the tungsten concentrations of the peroxotungstic acid (PTA) precursors and the post-deposition annealing temperatures and times. This chapter shows for the first time that decoupling the concurrent effects of the dominant crystallographic orientation and the trend of the oxygen vacancy concentration on the optical indirect band gap of  $\text{WO}_3$  thin films offered a means of engineering the electronic band structure of the films.

#### 6.2 Results and Discussion

For the investigation of crystallographic preferred orientation, the films were prepared such that they were of the same thicknesses  $\sim 650$  nm. These films were deposited from PTA of 0.05-0.20 mol  $\text{L}^{-1}$  tungsten concentrations owing to the observation of preferred crystallographic orientations in the films as described in Chapters 4 and 5.

### 6.2.1 Films Deposited From PTA Solution of High Tungsten Concentration (0.20 mol L<sup>-1</sup>)

Films deposited from PTA containing 0.20 mol L<sup>-1</sup> tungsten were heat-treated at various conditions in order to study the effect of the annealing process on the crystallographic development of the films. Figure 6.1 shows the XRD spectra of the films annealed at 25°-500°C for 0.5 h. The as-deposited film and the film annealed at 250°C were amorphous, as indicated by the absence of WO<sub>3</sub> peaks. The films began to recrystallise at ~275°C. The crystalline films were monoclinic, with dominant (002), (020), and (200) planes at 23.1°, 23.6°, and 24.3° 2θ, respectively [97]. In addition to the increasing peak intensities with increasing annealing temperature, preferred crystallographic growth parallel to the substrate also was observed, where the (200) peak intensity increased more than that of (002) but the (020) peak intensity remained fairly constant. The mirror plane perpendicular to the *k* axis is known to facilitate ion deposition in the [002] and [200] directions[97]. Similar changes in the preferred crystallographic orientations with annealing temperature have been observed in electrochromic studies of electrodeposited WO<sub>3</sub> films [35, 37].

The differences in the X-ray attenuation coefficients [177] between these planes were considered irrelevant to the differences in the X-ray peak intensities observed in the present work because randomly oriented WO<sub>3</sub> powders display almost equivalent intensities for the three dominant peaks of (002), (020), and (200) planes [97] although the ionic population density of the (020) plane is greater than those of the (002) and (200) planes [178, 179].

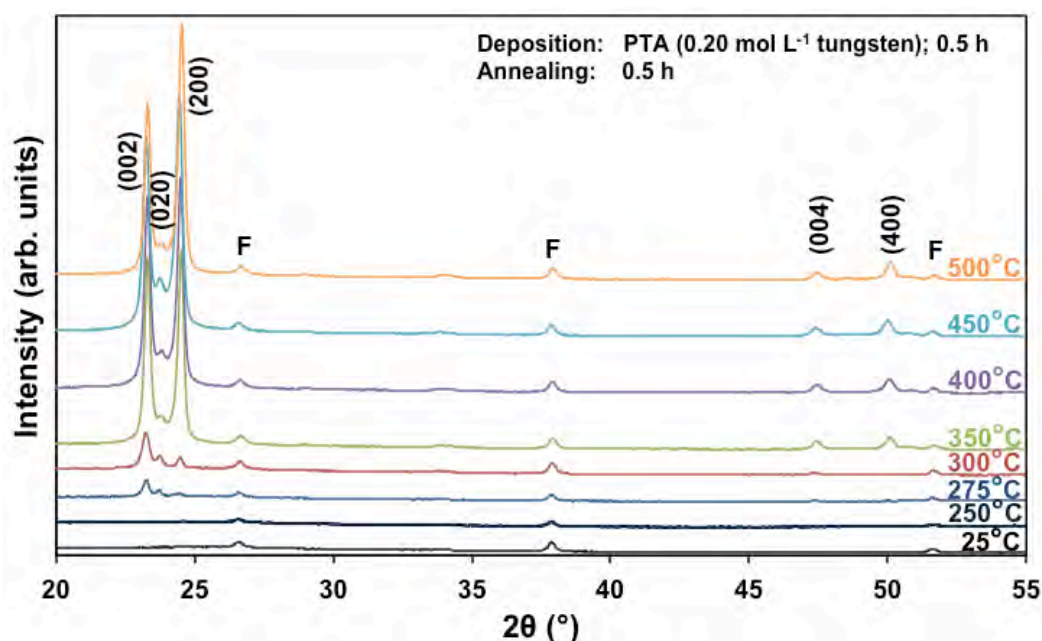


**Figure 6.1:** XRD spectra of the films deposited from PTA of 0.20 mol L<sup>-1</sup> tungsten and annealed for 0.5 h at temperatures 25°-500°C; F denotes peaks for FTO.

In order to study the relationship between the predominance of the crystallographic planes parallel to the substrate and the annealing parameters (*i.e.*, temperature and time), the relative intensity ratios (based on peak heights in the absence of a standard)  $R_x = I_x / (I_{002} + I_{020} + I_{200})$  (where  $x=002, 020, \text{ or } 200$ ) were determined from the XRD spectra as shown in Figure 6.2. The intensities of the peaks other than {002} in the present work were negligibly small and so have no significant influence on the values of  $R_x$ . Consideration of the standard X-ray diffraction pattern [97] over the  $2\theta$  range of 20°-25° indicates that the  $R_x$  for each of the {002} planes in randomly distributed powders should be  $\sim 0.33$  (see Figure 6.8 subsequently). The change in this ratio is a reflection of the competing growth rates of the crystal planes. It has been noted that the relative ratios calculated from the XRD peak intensities and peak areas are close (<10% difference) [180].

At low annealing temperature of 275°C, increasing the annealing time significantly increased the proportion of (200) plane largely at the expense of the (002) plane during the first 8 h of annealing, although the latter remained the principal plane parallel to the substrate of the films throughout the annealing period. At 300°C, the  $R_{002}$  and  $R_{200}$  followed the same significant change in amount as at 275°C during initial annealing but they equalised after 8 h. For these two low annealing temperatures, there was a slight decrease in the  $R_{020}$ . In contrast, at high annealing temperatures ( $\geq 350^\circ\text{C}$ ), the  $R_x$  of all three planes changed insignificantly as a function of time but the variations in the  $R_{002}$  and  $R_{200}$  as a function of temperature showed a clear trend of increase in the latter at the expense of the former, while the  $R_{020}$  remained approximately constant. These results indicated that, in general, the annealing temperature played the dominant role in the development of preferred orientation through recrystallisation and grain growth while the annealing time had minimal impact.

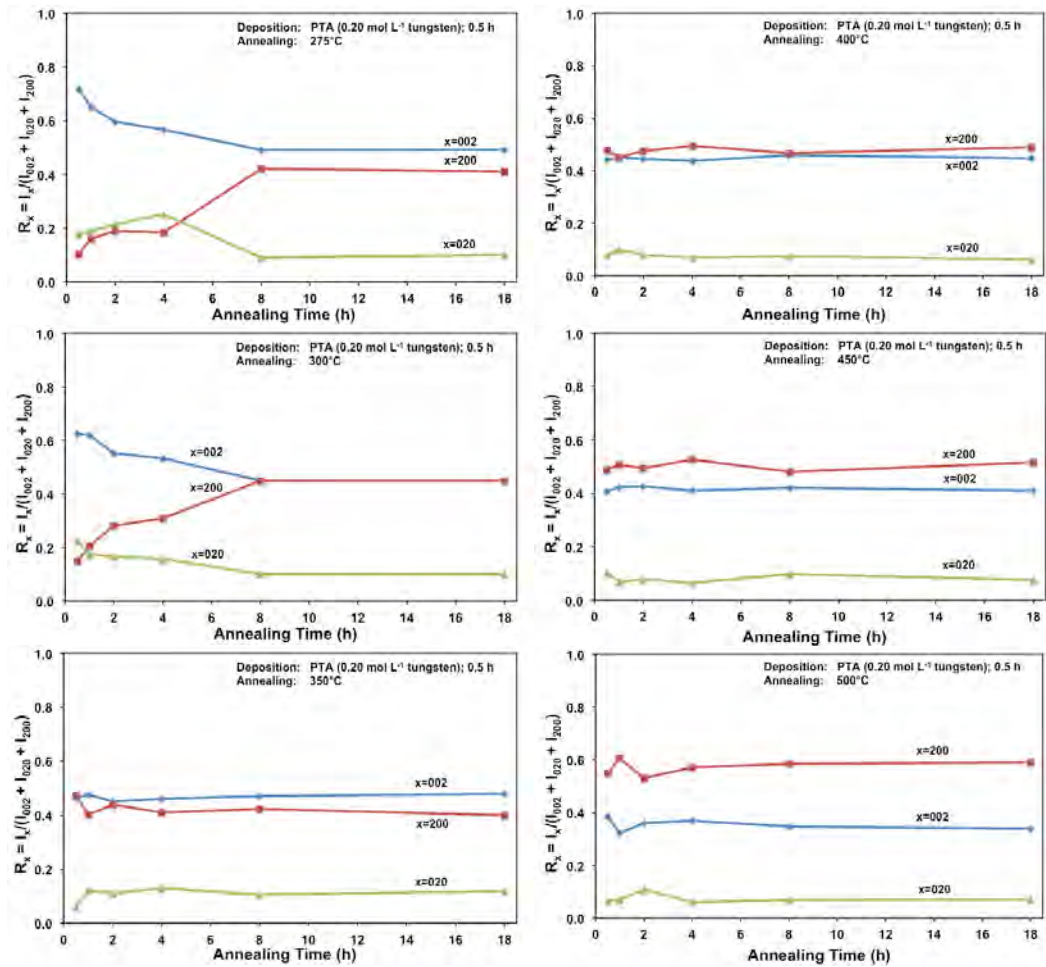


**Figure 6.2:** Relative XRD intensities  $R_x = (I_x / (I_{002} + I_{020} + I_{200}))$  (where  $x = 002, 020,$  or  $200$ ) as a function of annealing time for the films deposited from PTA of  $0.20 \text{ mol L}^{-1}$  tungsten and annealed at fixed temperatures in the range  $275^\circ\text{-}500^\circ\text{C}$ .

The preceding data were quantified further in the bar charts in Figure 6.3. Figure 6.3 (a) shows that, for the point of early recrystallisation at 0.5 h annealing, there were two temperature regions for the evolution of preferred orientation parallel to the substrate:

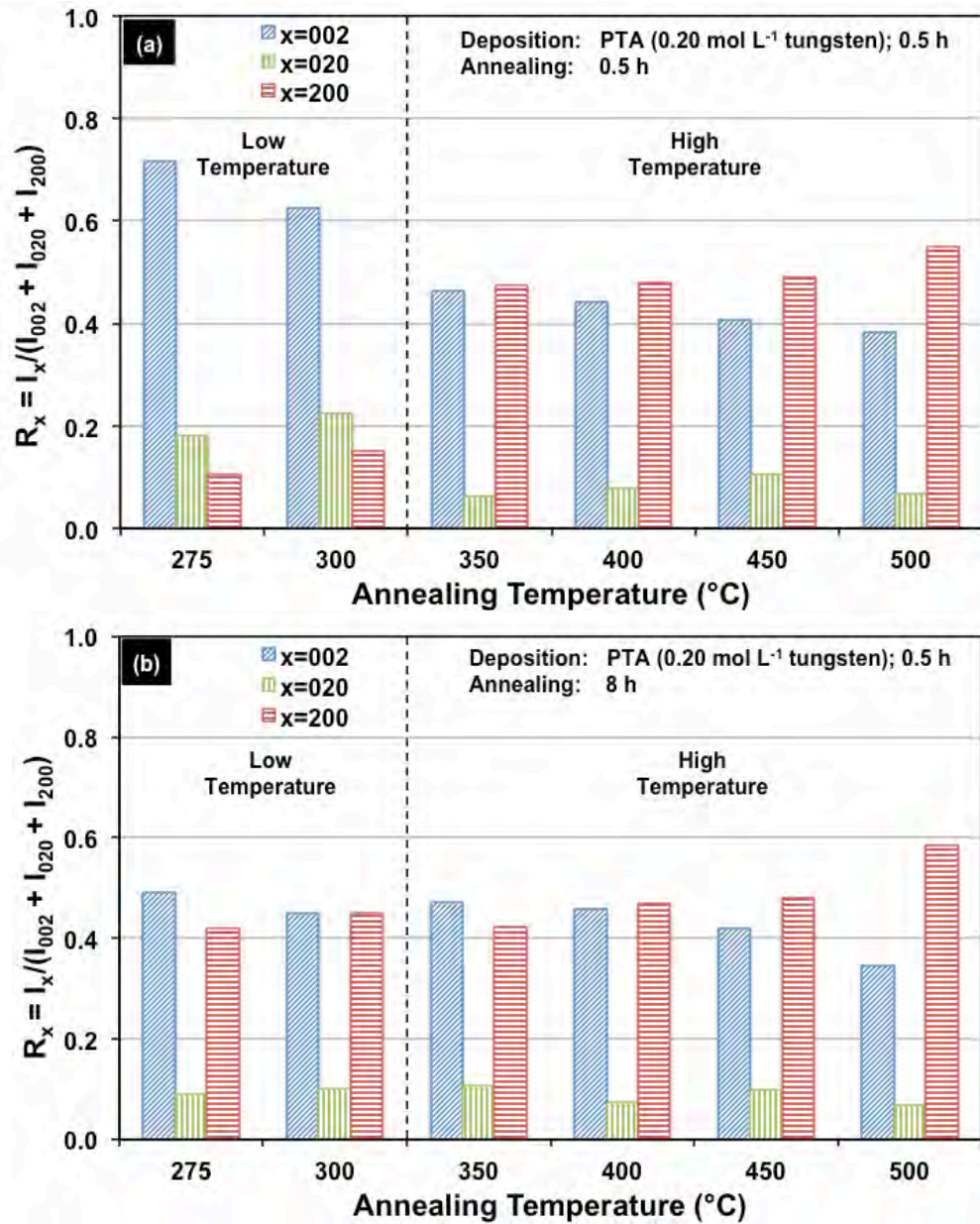


**Figure 6.3:** Relative XRD intensities  $R_x = (I_x / (I_{002} + I_{020} + I_{200}))$  (where  $x = 002, 020,$  or  $200$ ) as a function of annealing temperature for the films deposited from PTA of  $0.20 \text{ mol L}^{-1}$  tungsten and annealed for (a) 0.5 h and (b) 8 h.

(i) *Low temperatures (<350 °C):*

The ratio  $R_{002} > 0.33$  indicated the predominance of the (002) plane. However, increasing the temperature within the low temperature region enhanced the relative growth rates of the (020) and (200) planes, thereby decreasing the  $R_{002}$ .

(ii) *High temperature ( $\geq 350$  °C):*

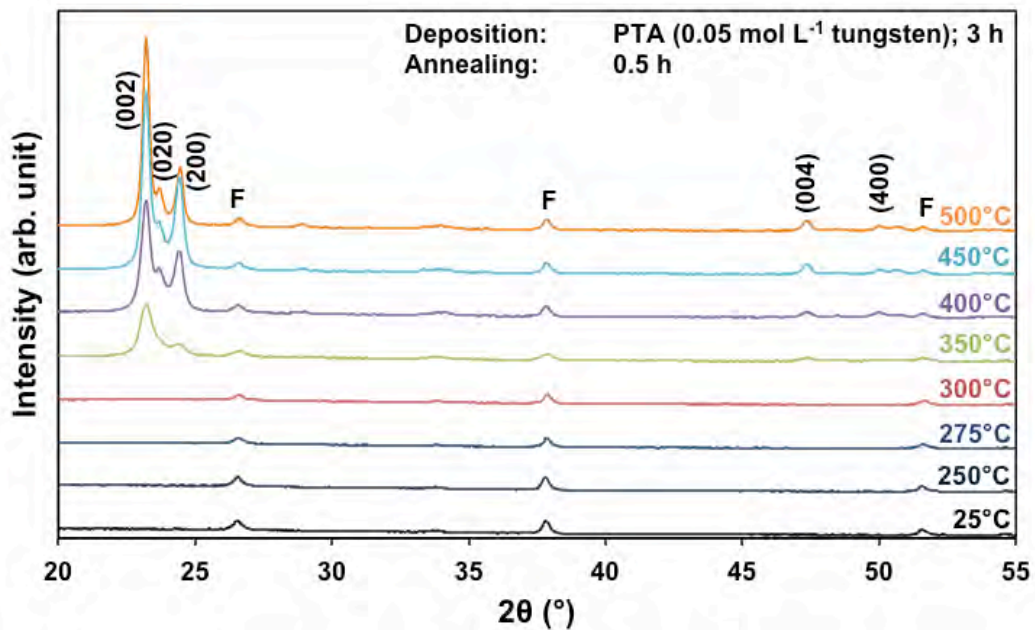
The  $R_{002}$  and  $R_{200}$  were  $>0.33$ , indicating the continued predominance of the (002) and (200) orientations. However, the latter gradually increased with increasing annealing temperature while the former decreased (and the (020) orientation remains low). The predominance of the (200) plane indicated that it was thermodynamically the most stable. This was emphasised by the change in data at 500 °C in Figures 6.3(a) and (b), in which the  $R_{200}/R_{002}$  ratio after 8 h annealing showed the greatest differential in the high temperature region, compared to that after 0.5 h annealing. This conclusion was applicable provided there was no epitaxial growth or growth directing agent, neither of which was the case in the present work.

Figure 6.3(b) shows that, for the point at which the rate of recrystallisation stabilised at 8 h annealing, the trends were approximately the same as was the case of annealing for 0.5 h. That is, the similar two regions of low temperatures and high temperatures can be observed. In this case, both the  $R_{002}$  and  $R_{200}$  were  $>0.33$ , which indicated predominance in these two orientations, and the differential between the  $R_{002}$  and  $R_{200}$  at low temperatures was less significant than that of the early point (0.5 h annealing) of recrystallisation in Figure 6.3(a). This was a reflection of the kinetics of recrystallisation, where the relatively greater  $R_{200}$  levels in the low temperature region at the longer annealing time of 8 h were a reflection of the greater thermodynamic stability of the (200) plane compared to that of the (002) plane.

### 6.2.2 Films Deposited From PTA Solution of Low Tungsten Concentration (0.05 mol L<sup>-1</sup>)

The effects of annealing temperature and time on the preferred orientation parallel to the substrate of the films also were investigated for the films deposited from PTA of low

tungsten concentration of  $0.05 \text{ mol L}^{-1}$ . Figure 6.4 shows the XRD spectra of the films annealed at different temperatures for 0.5 h. It can be seen that, in contrast to the data for high tungsten concentration in Figure 6.1, the (002) plane was predominant at all annealing temperatures  $\geq 350^\circ\text{C}$ . The  $R_x$  trends, shown in Figures 6.5 and 6.6, confirmed that the (002) plane remained predominant for the investigated ranges of annealing temperature and time. This was in contrast to the trends shown in Figures 6.2 and 6.3 for the films deposited from PTA of higher tungsten concentration of  $0.20 \text{ mol L}^{-1}$ , which changed from (002) to (200) preferred orientation with increasing annealing temperature.



**Figure 6.4:** XRD spectra of the films deposited from PTA of  $0.05 \text{ mol L}^{-1}$  tungsten and annealed for 0.5 h at  $25^\circ\text{C}$ - $500^\circ\text{C}$ ; F denotes peaks for FTO.

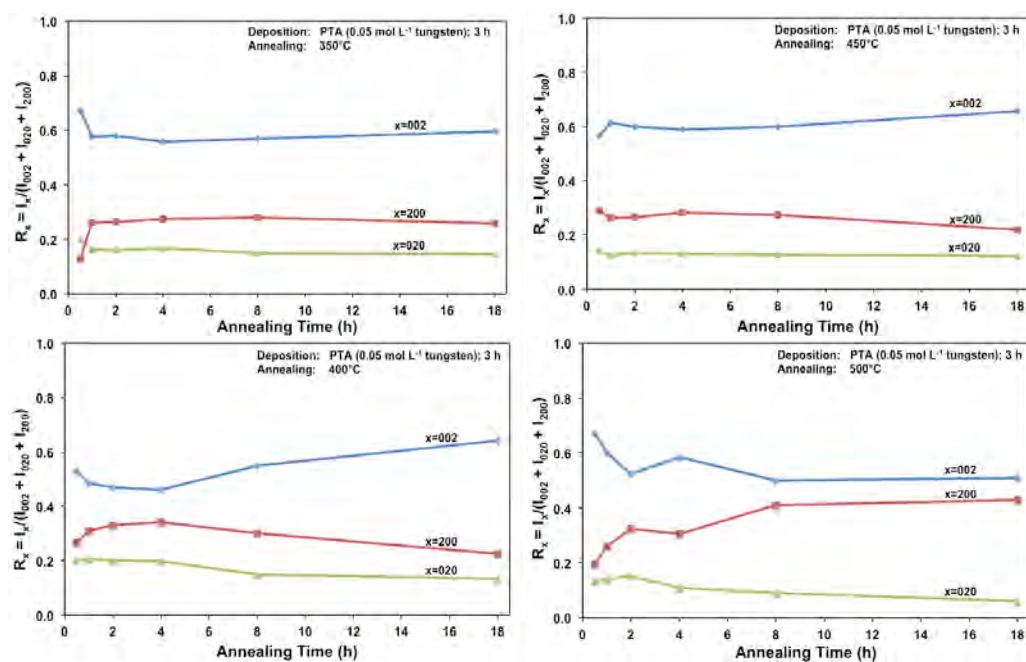


**Figure 6.5:** Relative XRD intensities  $R_x = (I_x / (I_{002} + I_{020} + I_{200}))$  (where  $x = 002, 020, \text{ or } 200$ ) as a function of annealing time for the films deposited from PTA of  $0.05 \text{ mol L}^{-1}$  tungsten and annealed at fixed temperatures in the range  $350^\circ\text{-}500^\circ\text{C}$ .

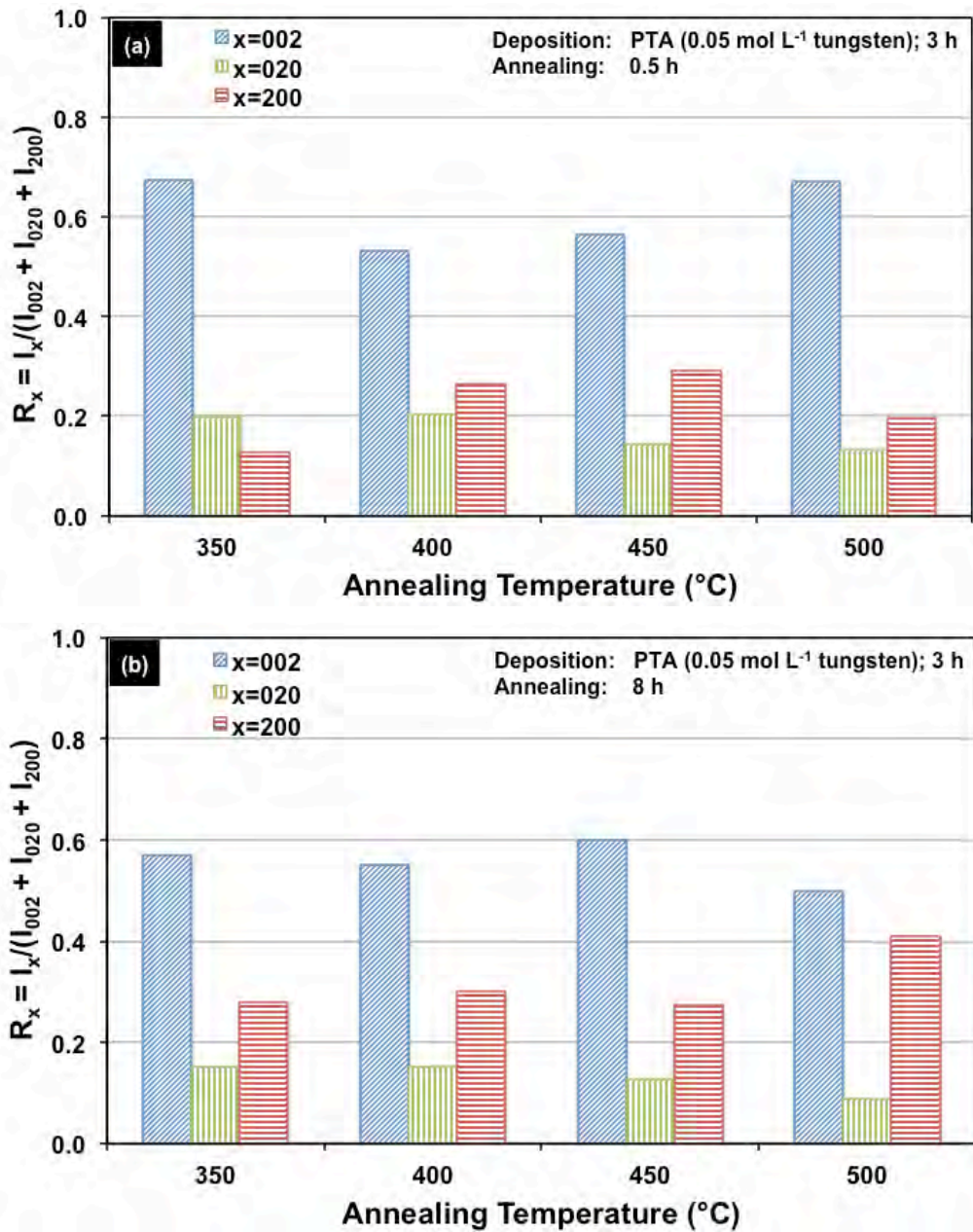


**Figure 6.6:** Relative XRD intensities  $R_x = (I_x / (I_{002} + I_{020} + I_{200}))$  (where  $x = 002, 020,$  or  $200$ ) as a function of annealing temperature for the films deposited from PTA of  $0.05 \text{ mol L}^{-1}$  tungsten and annealed for (a) 0.5 h and (b) 8 h.

These data suggested that the tungsten concentration of the PTA solution determined the homogeneity of the films and the latter strongly affected the grain growth and associated

development of preferred orientation during annealing. That is, depositions from PTA consisting of low ( $0.05 \text{ mol L}^{-1}$ ) and high ( $0.20 \text{ mol L}^{-1}$ ) tungsten concentrations yielded inhomogeneously and homogeneously nanostructured films, respectively. The XRD data for the films deposited from PTA solutions consisting of low tungsten concentration, which had inhomogeneous nanostructures, indicated the following:

- (i) A higher apparent onset recrystallisation temperature of  $>300^\circ\text{C}$  was required owing to the sparse nucleation distribution and small particle sizes; hence a higher annealing temperature was required to activate recrystallisation and allow the X-ray diffractometer to detect the grains.
- (ii) The consistent predominance of the  $R_{002}$  at all annealing temperatures and times indicated that the (002) plane was favoured for grain growth where the large grains grew at the expense of adjacent smaller ones.
- (iii) The absence of trend in the  $R_{200}/R_{002}$  ratio as a function of annealing temperatures and times for annealing temperatures  $<500^\circ\text{C}$  indicated a greater hindrance of the growth of the thermodynamically stable (200) plane.
- (iv) The requirement of higher annealing temperature ( $500^\circ\text{C}$ ) and longer annealing time ( $\sim 8 \text{ h}$ ) to increase the  $R_{200}/R_{002}$  ratio further confirmed the high thermodynamic stability of the (200) plane.
- (v) The higher  $R_{020}$  at all annealing temperatures and times confirmed the lower levels of (200) preferred orientation.

### 6.2.3 Mechanism of Preferred Crystallography in Electrodeposited Tungsten Oxide Thin Films

The surface energy of a thin-film system originates from the (i) film/atmosphere interface (ii) film/substrate interface, and (iii) intergranular interfaces. When an amorphous film recrystallises during annealing, the crystals that form reconfigure their surfaces by developing the crystal planes with low surface energy in order to minimise the total surface energy of the system. In order to understand the mechanism of preferred growth of specific crystallographic planes produced from various tungsten concentrations of the PTA

solutions and annealing conditions, the surface properties of the three major crystal planes of the monoclinic  $\text{WO}_3$  unit cell were examined, where the projections of the planes were derived from the atomic positions of the crystal structure as shown in Figure 6.7 (computational details for the construction of the crystal structure are described in Section 3.2.1). For this, it was assumed that the W-O bond was of uniform energy, although the out-of-plane W-O bond lengths, determined from structural simulation, are in the ranges 0.190-1.191 nm for the (200) plane, 0.177-0.214nm for the (020) plane, and 0.175-0.223nm for the (002) plane.

As shown in Table 6.1, the surface energies per unit area, which were based on the number of dangling bonds formed by dividing the crystal across a specific plane in Figure 6.7 [181], followed the order (002) > (020) > (200). This order also has been obtained from density functional theory calculations [63]. A high surface energy is a reflection of the high reactivity and associated high growth rate of a crystal plane [182, 183], which is associated with low thermodynamic stability (although grain growth is a parameter of transient-state kinetics, thermodynamics reflect a steady-state condition) .

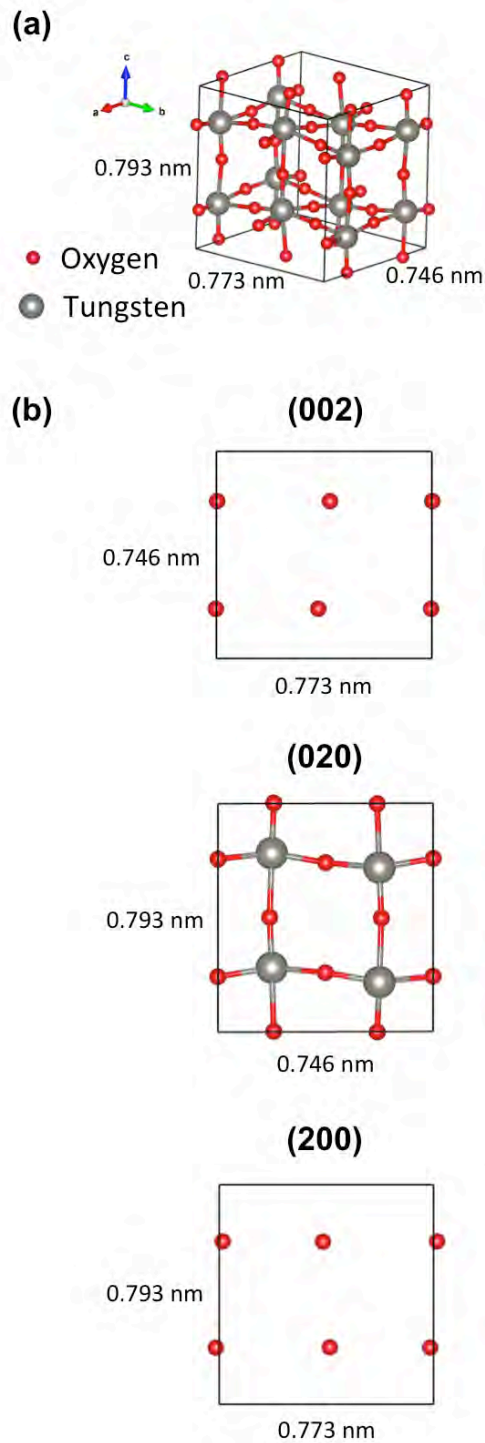


**Figure 6.7:** Schematic diagram of the (a) unit cell and (b) three major crystal planes(002), (020), and (200) of monoclinic  $\text{WO}_3$ .

**Table 6.1:** Surface properties of crystal planes of monoclinic WO<sub>3</sub>; E is the energy of the W-O bond.

	Crystal Plane		
	(002)	(020)	(200)
Number of dangling bonds per atom	1	1	1
Number of atoms with dangling bonds	4	4	4
Total dangling bond energy (J)	4E	4E	4E
Surface area of crystal plane (nm <sup>2</sup> )	0.5767	0.5916	0.6130
Surface energy per unit area (J nm <sup>-2</sup> )	6.94E	6.76E	6.53E

The differential in the surface energies per unit area of the crystal planes suggested the explanation for the preferred crystallographic orientation observed in the present work. More specifically:

(i) *(002) Plane:*

The (002) plane, which has the highest surface energy per unit area compared to those of the (020) and (200) planes, is the most reactive and grows at the highest rate. This explained the predominance of this plane under the adverse conditions of (i) low annealing temperature and time for the activation of grain growth, as in the case of the films deposited from PTA containing the high tungsten concentration of 0.20 mol L<sup>-1</sup>, and (ii) low nucleation distribution density, in which the activation energy for grain growth is large due to the relatively long diffusion distance between the nuclei, as in the case of the films deposited from PTA containing the low tungsten concentration of 0.05 mol L<sup>-1</sup>. Under these adverse conditions, the growth of thermodynamically stable (200) and (020) planes were not facilitated.

(ii) *(020) Plane:*

A (020) mirror plane commonly is present in monoclinic structures but, in the case of the monoclinic WO<sub>3</sub> (space group P2<sub>1</sub>/n), it is absent [97]. It was possible that the reduced symmetry associated with its absence was responsible for the hindrance of the growth of this plane. Furthermore, the surface energy per unit area of the (020) plane is intermediate

between those of the (200) and (002) planes. These two factors suggested that the activation energy for grain growth of the (020) plane could be relatively high.

(iii) *(200) Plane:*

The highest thermodynamic stability of the (200) plane was attributed to the lowest surface energy per unit area, which made it the least reactive plane. Hence, the predominance of the (200) plane was favoured under the conditions of high nucleation distribution density resulted from the deposition from the PTA containing high tungsten concentration, high annealing temperatures, and/or long annealing times.

During recrystallisation, the lack of material for grain growth from above and below a thin-film nanostructure establishes effectively a two-dimensional spatial constraint in a thin film. Therefore, a preferred growth direction is limited to being within the film and thus facilitates the development of grains of preferred orientation. In contrast, the growth of individual grains in powders is effectively three-dimensional because it is constrained only by the misalignment of impinging grains and the presence of pores at localised interfaces. Therefore, the effect of preferred growth directions, as reflected in the surface energies shown in Table 6.1, is greater in thin films than it is in powders. Consequently, the X-ray diffraction peak intensities differ between these two sample morphologies accordingly.

#### 6.2.4 Effect of Preferred Orientation

##### 6.2.4.1 Degree of Crystallinity

In order to study the effect of preferred orientation on the photoelectrochemical performance of  $\text{WO}_3$  thin films, the films with different predominant crystal planes parallel to the substrate were prepared. As shown in Table 6.2, these films,  $T_{002}$ ,  $T_{002+200}$ , and  $T_{200}$ , were deposited from PTA consisting of different tungsten concentrations and were subjected to different annealing conditions in order to attain similar degrees of crystallinity. The degrees of crystallinity were determined from the data in Figure 6.8 using the standard method of measuring the integrated areas for the three major peaks (within  $23\text{-}25^\circ 2\theta$ ) and

the underlying amorphous hump [184-187]. Dividing the former by the total area resulted in a percentage crystallinity of  $92.8 \pm 0.5\%$ .

**Table 6.2:** Analytical data for films  $T_{002}$ ,  $T_{002+200}$ , and  $T_{200}$ .

Film	Tungsten concentration in PTA ( $\text{mol L}^{-1}$ )	Annealing conditions	Predominant crystal orientation	$R_{002}$	$R_{020}$	$R_{200}$	Optical indirect band gap (eV)	Oxygen (relative at%)	
								O(1s)A	O(1s)B
$T_{002}$	0.05	500°C; 2.0 h	[002]	0.74	0.14	0.12	2.55	88.1	11.9
$T_{002+200}$	0.20	350°C; 8.0 h	[002] and [200]	0.50	0.10	0.40	2.65	87.4	12.6
$T_{200}$	0.20	500°C; 0.5 h	[200]	0.32	0.10	0.58	2.70	87.1	12.9

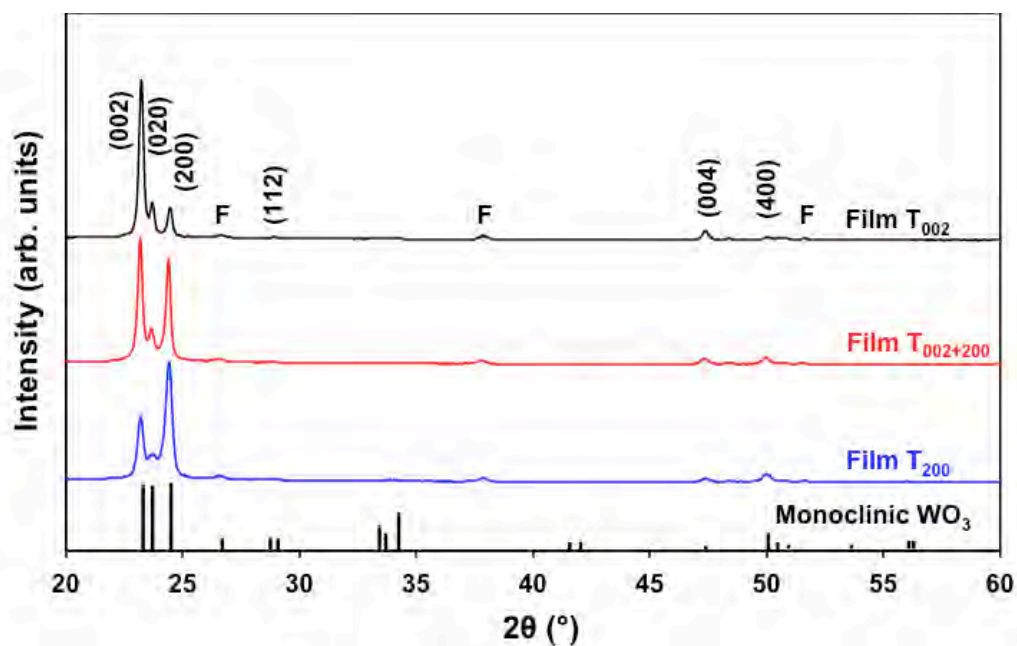


**Figure 6.8:** XRD spectra of films  $T_{002}$ ,  $T_{002+200}$ , and  $T_{200}$ ; reference data for monoclinic  $\text{WO}_3$  [97] also are shown; F denotes peaks for FTO substrate.

#### 6.2.4.2 Microstructure

Figure 6.9 (a-c) shows the surface morphologies of films  $T_{002}$ ,  $T_{002+200}$ , and  $T_{200}$  examined by SEM. These films exhibited different microstructures as follows:

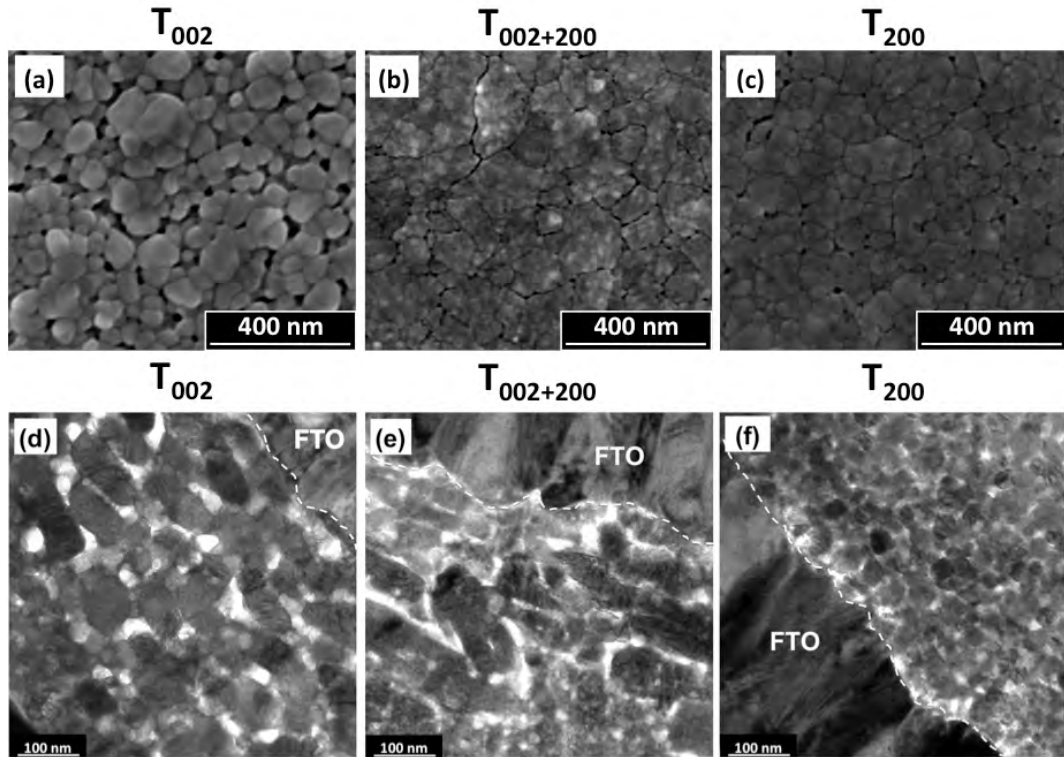


**Figure 6.9:** SEM secondary electron images of the surface morphologies (a-c) and corresponding TEM cross-sectional images (d-f) of films  $T_{002}$ ,  $T_{002+200}$ , and  $T_{200}$ .

(i) *Film  $T_{002}$ :*

The low nucleation distribution density of the film deposited from PTA consisting of the lower tungsten concentration ( $0.05 \text{ mol L}^{-1}$ ) and annealed at  $500^\circ\text{C}$  for 2 h caused the formation of a porous nanostructure of discrete bounded grains upon annealing. These features were a reflection of the low nuclei distribution density, which encouraged the growth of isolated grains, where those nuclei in mutual contact coalesced into isolated agglomerates. These agglomerates grew into well formed grains with smooth surfaces and little indication of subgrain boundaries owing to the high annealing temperature of  $500^\circ\text{C}$ .

(ii) *Film  $T_{002+200}$ :*

The deposition from PTA containing high tungsten concentration ( $0.20 \text{ mol L}^{-1}$ ) and annealing at  $350^\circ\text{C}$  for 8 h resulted in the formation of a denser nanostructure consisting of

large agglomerates of small subgrains. These features were a reflection of the high nucleation density, which facilitated retention of small grains prior to impingement with others and consequent densification within the agglomerates, which was highlighted by the delamination from the shrinkage of the agglomerates. That is, the mixture of predominantly (002) and (200) orientations restricted coalescence and the preferred growth of one plane over the other. The agglomerate surfaces were rough because the low annealing temperature of 350°C was insufficient to facilitate mass transfer and subgrain growth such that smooth and faceted grains would form.

(iii) *Film T<sub>200</sub>*:

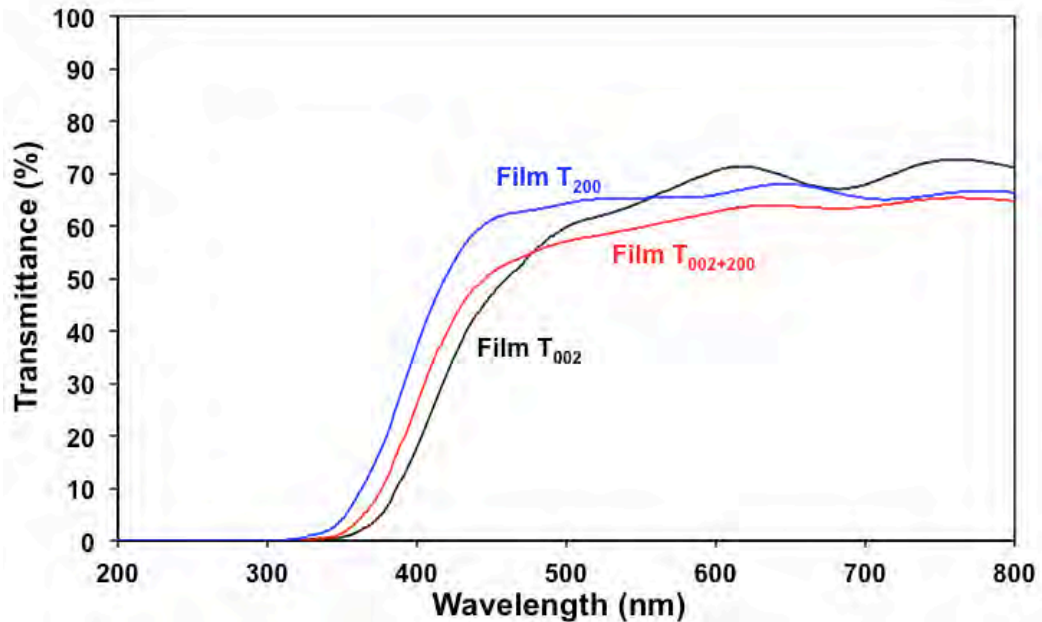
The deposition from PTA containing high tungsten concentration (0.20 mol L<sup>-1</sup>) and annealing at 500°C for 0.5 h resulted in features that reflected a compromise between annealing temperature (high) and annealing time (short): smaller agglomerates, larger subgrains (as indicated by the reduced charging from particles of greater diameter and hence less roughness), and less agglomerate shrinkage and delamination compared to film T<sub>002+200</sub>. That is, the dominant influence on the morphology was insufficient time for grain growth, *viz.*, the kinetics, contrary to the potential for the thermodynamically stable (200) plane to moderate the growth of large and well formed grains, which did not form.

Figure 6.9 (d-f) shows TEM cross-sectional images of films T<sub>002</sub>, T<sub>002+200</sub>, and T<sub>200</sub>. Film T<sub>002</sub> demonstrated that the annealing conditions of high temperature (500°C) and relatively short time (2 h) generated a nanostructure with a high proportion of discrete tabular WO<sub>3</sub> grains oriented parallel to the substrate, although unaligned grains also were present. This tabular morphology has been observed before [188, 189]. In contrast, film T<sub>200</sub> exhibited a nanostructure that was essentially equiaxed. In this case, the dominance of time was emphasised since these grains had insufficient time (0.5 h) to grow even though the highest temperature (500°C) was used and generated the thermodynamically stable orientation. In the case of the T<sub>002+200</sub> film, a high proportion of tabular forms can be seen but their outlines were not distinct and the mottled appearance confirmed the agglomerated nature of these grains observed in Figure 6.9(b). The X-ray data in Figure 6.8, which showed mixed (002) and (200) orientations, supported the conclusion of the presence of biaxially oriented

subgrains within these tabular forms. The apparent contradiction that biaxially oriented subgrains within the agglomerates comprised uniaxially oriented tabular forms was resolved by the fact that the tabular shape derived from the agglomerates that formed parallel to the substrate.

#### 6.2.4.3 Optical Properties

The optical transmittance spectra of the films are illustrated in Figure 6.10. All films showed transmittances of ~60-70% in the wavelength range >500 nm. The optical absorption edges followed the wavelength order of film  $T_{002}$  > film  $T_{002+200}$  > film  $T_{200}$ , giving indirect optical band gaps of ~2.55, 2.65, and 2.70 eV (obtained by the Tauc plot method [160]). It has been observed that the optical band gap depends on the crystallographic orientation of metal oxide films (*viz.*,  $WO_3$  [63],  $TiO_2$  [190],  $ZnO$  [174]) and  $(1-x)Pb(Mg_{1/3}Nb_{2/3})O_3-xPbTiO_3$  single crystals [191]; this has been attributed to differences in the surface electronic properties associated with the crystallographic orientations.



**Figure 6.10:** Optical transmittance spectra of films  $T_{002}$ ,  $T_{002+200}$ , and  $T_{200}$ .

## 6.2.4.4 Chemical Properties

The surface elemental compositions of the films were investigated by XPS and these data are shown in Figure 6.11 and Table 6.2. The deconvoluted doublet peaks of W(4f<sub>7/2</sub>) and W(4f<sub>5/2</sub>) in Figure 6.11 (a) were located at binding energies of 35.53-35.73 eV and 37.68-37.88 eV, respectively. The binding energies of W(4f<sub>7/2</sub>) and W(4f<sub>5/2</sub>) peaks of film T<sub>002</sub> at 35.73 eV and 37.88 eV agreed well with that for the presence of W<sup>6+</sup> [192], indicating that film T<sub>002</sub> consisted mainly of stoichiometric WO<sub>3</sub>. In contrast, the W(4f) doublet peaks of films T<sub>002+200</sub> and T<sub>200</sub> shifted to lower binding energies owing to the presence of W of valence <6+ and consequent hypostoichiometric WO<sub>3-x</sub>. The O(1s) peaks of the films in Figure 6.11 (b) can be deconvoluted into three peaks. The O(1s)A peak at the highest binding energy derived from the oxygen in the strong W-O bonds in stoichiometric WO<sub>3</sub> [14, 192, 193]. The O(1s)B peak may be assigned to the oxygen in hypostoichiometric WO<sub>3-x</sub> [194, 195] and/or the oxygen present in the chemisorbed hydroxyl species [14, 193]. The O(1s)C peaks corresponded to the oxygen present in the water molecules physisorbed on the surface [14].

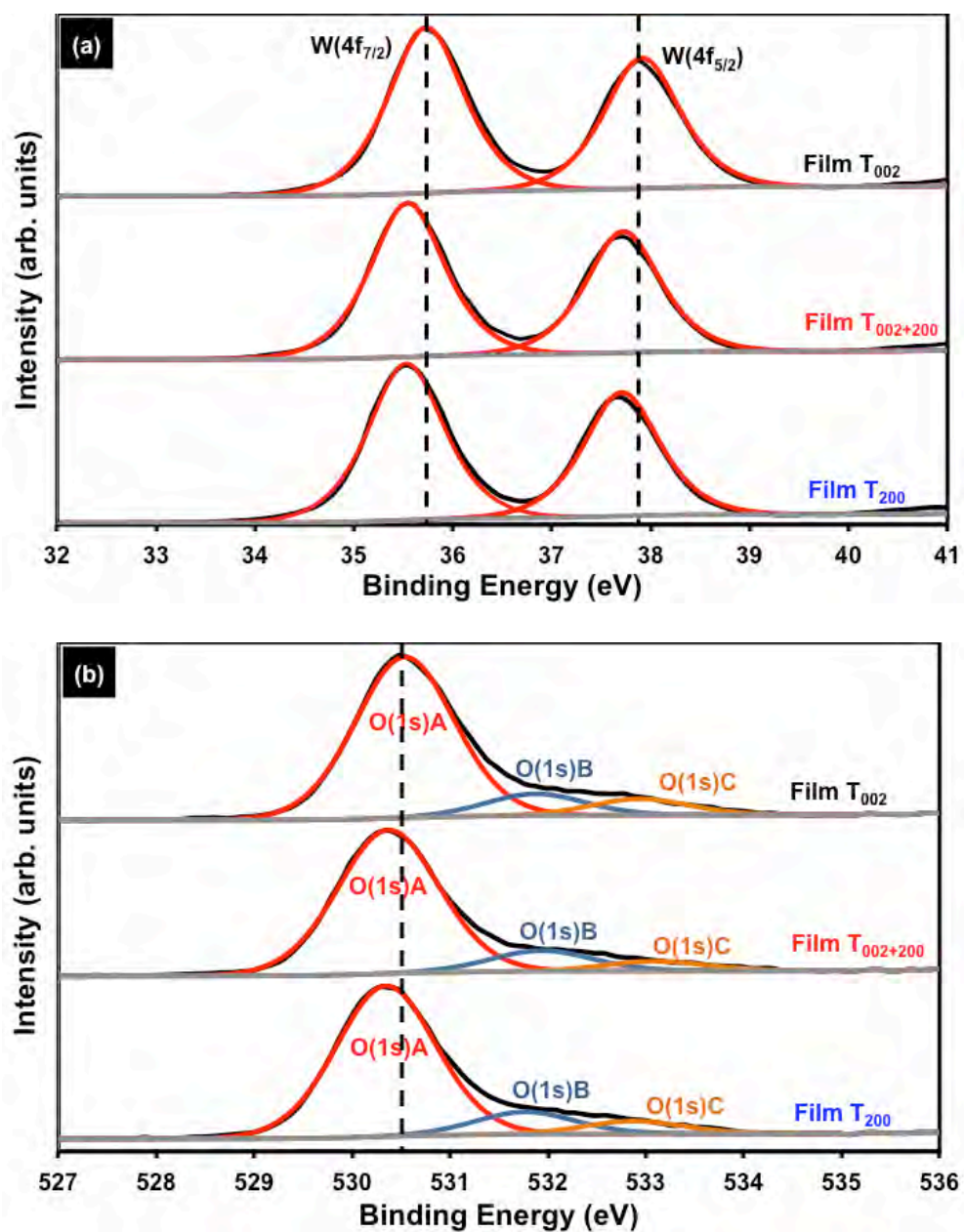


**Figure 6.11:** XPS spectra of (a) W(4f) and (b) O(1s) for films  $T_{002}$ ,  $T_{002+200}$ , and  $T_{200}$ .

The O(1s)A peak for film  $T_{002}$  at 530.54 eV corroborated that the tungsten oxide composition was principally stoichiometric [192]. This showed that the O(1s)B peak in film  $T_{002}$  must be due mainly to the presence of oxygen in the chemisorbed hydroxyl species. Similar to the W(4f) peaks, all three O(1s) peaks in films  $T_{002+200}$  and  $T_{200}$  also

shifted to lower binding energies and this is due to their hypostoichiometry. Table 6.2 shows the relative atomic percentages of the O(1s)A and O(1s)B calculated from the areas under the deconvoluted peaks. The relative atomic percentage of O(1s)A, which represented the proportion of stoichiometric  $\text{WO}_3$ , followed in the order film  $T_{002}$  > film  $T_{002+200}$  > film  $T_{200}$ . This order suggested that oxygen vacancies were formed more readily on the (200) plane than the (002) plane, which was consistent with the data in Table 6.1, in which the (002) plane had the highest surface energy and hence was most likely to equilibrate and so reduced the potential to form oxygen vacancies.

In addition to the crystallographic effect on the formation of oxygen vacancies, there also may be a microstructural effect. That is, oxygen vacancies may form preferentially on the subgrain and grain boundary areas of the agglomerates of films  $T_{002+200}$  and  $T_{200}$  since these are well known as regions of highly defective structure that readily adsorb  $\text{OH}^-$  groups to oxide surfaces [196]. This microstructural effect cannot be differentiated between these two films owing to the difficulty in distinguishing precisely the subgrain boundaries within the agglomerates, although film  $T_{002+200}$  appeared to exhibit higher subgrain boundary area (smaller subgrains) and lower grain boundary area (larger agglomerates) while film  $T_{200}$  appeared to exhibit lower subgrain boundary area (larger subgrains) and higher grain boundary area (smaller agglomerates).

The density functional theory calculation has shown that the oxygen vacancies associated with hypostoichiometric monoclinic  $\text{WO}_{3-x}$  (space group  $P2_1/n$ ) decreased the band gap owing to the decreased W-O bonding-antibonding interaction [197]. This also has been shown in the work on  $\text{WO}_3$  films deposited on (100) single-crystal Si substrates by Diaz-Reyes *et al.* [198], who observed a direct correlation between the oxygen vacancy concentration and the optical indirect band gap. However, neither of these studies considered the potential effect of preferred orientation. Inspection of the X-ray diffraction data of Diaz-Reyes *et al.* [198] shows that their films exhibited {002} preferred orientations and so this parameter may have had an unrecognised influence on the data.

It is well known that oxygen vacancies in randomly oriented transition metal oxide are responsible for the reduced band gaps compared to those of stoichiometric oxides [199-201]. In contrast, the density functional theory calculation of the oxygen vacancy formation in W-O chains of monoclinic  $\text{WO}_3$  along different crystallographic directions indicated that the crystallographic locations of the oxygen vacancies altered the electronic band structure [202]. Similar to the theoretical-experimental validation described in the preceding paragraph, the present work also provided experimental validation for theoretical calculation, both of which indicated that the twofold correlation between the oxygen vacancy concentration and the band gap was more correctly a threefold correlation that also included the crystallographic locations of the oxygen vacancies.

#### 6.2.4.5 Correlation between Crystallographic Orientation, Oxygen Vacancy Concentration, and Band Gap

The threefold correlation between the crystallographic orientation, oxygen vacancy concentration, and optical indirect band gap is illustrated in Figure 6.12, which showed quantitatively the effect of the preferred orientation and qualitatively the effect of oxygen vacancy concentration on the band gap. These data illustrated the following points:

- (i) The (002) preferred orientation was critical to obtaining a minimal band gap.
- (ii) Enhancement of the (002) preferred orientation was achieved by suppressing the (200) preferred orientation.
- (iii) The (020) preferred orientation played little role in alteration of the band gap.
- (iv) Extrapolation of the  $R_{002}$  plot to  $R_{002} = 1.0$  and hence a fully (002)-oriented film indicated that the minimal band gap that can be achieved is  $\sim 2.47$  eV.
- (v) Since the  $R_{200}$  and  $R_{020}$  plots did not extrapolate to zero, the extrapolation of the  $R_{002}$  plot can be considered only indicative.

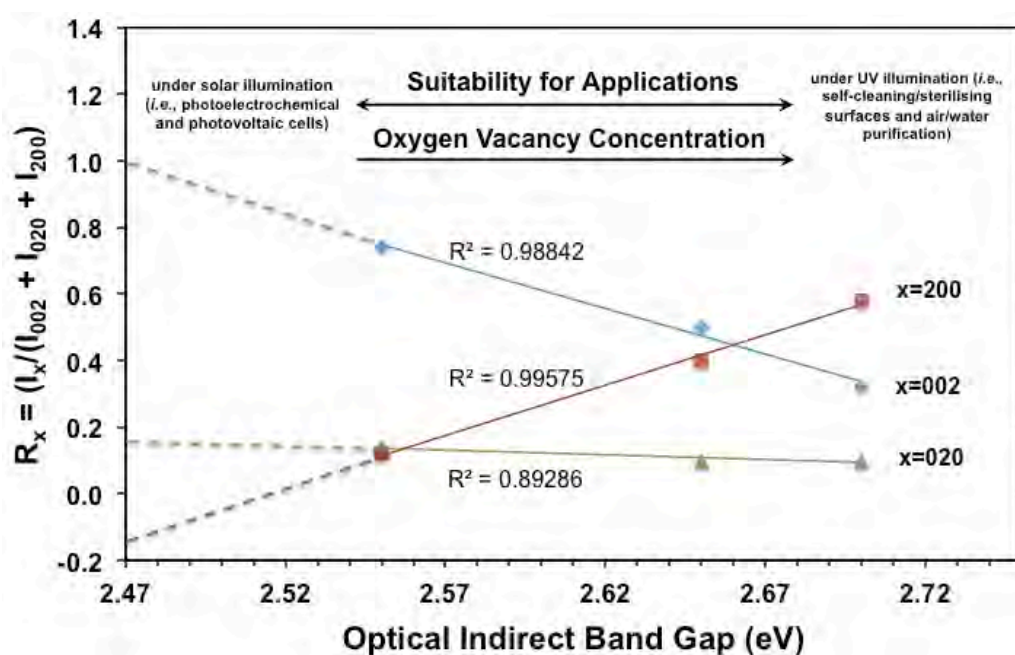


**Figure 6.12:** Threefold correlation between crystallographic orientation, oxygen vacancy concentration, and optical indirect band gap.

It can be seen that the data in Figure 6.12 can be used potentially as a diagnostic tool to engineer the electronic band structure of monoclinic  $\text{WO}_3$  thin films by control of their crystallographic orientation. These data also allowed the effect of crystallographic orientation on the band gap and, by extension, the oxygen vacancy concentration of  $\text{WO}_3$  thin films to be isolated.

It should be noted that, in addition to the two concurrent factors that affected the band gap, as examined above, there also were other controllable and uncontrollable factors that must be considered. These factors included the microstructures (film thickness, grain size, roughness, porosity [155, 203]), mineralogies (polymorphs, degree of crystallinity [49, 156]), chemical compositions (stoichiometry, dopants, impurities [113, 126]), and structural defects (type and concentration [87, 195]). The films were prepared such that they possessed the same thickness, degree of crystallinity, and elemental composition and so the effects from these factors have been minimised. That is, the present work has

attempted to normalise all of the controllable variables, while the uncontrollable variables were those that were generated intrinsically in the films.

#### 6.2.4.6 Electronic Properties

The band gap values obtained from the UV-visible spectra in Figure 6.10 and the XPS valence band data in Figure 6.13 (a) were used to produce the schematic diagram of the band structures of the films shown in Figure 6.13 (b). It can be seen that the valence band maxima of the films ranged from low for film T<sub>002</sub> (~2.87 eV) to intermediate for film T<sub>002+200</sub> (~2.68 eV) and to high for film T<sub>200</sub> (~2.61 eV).

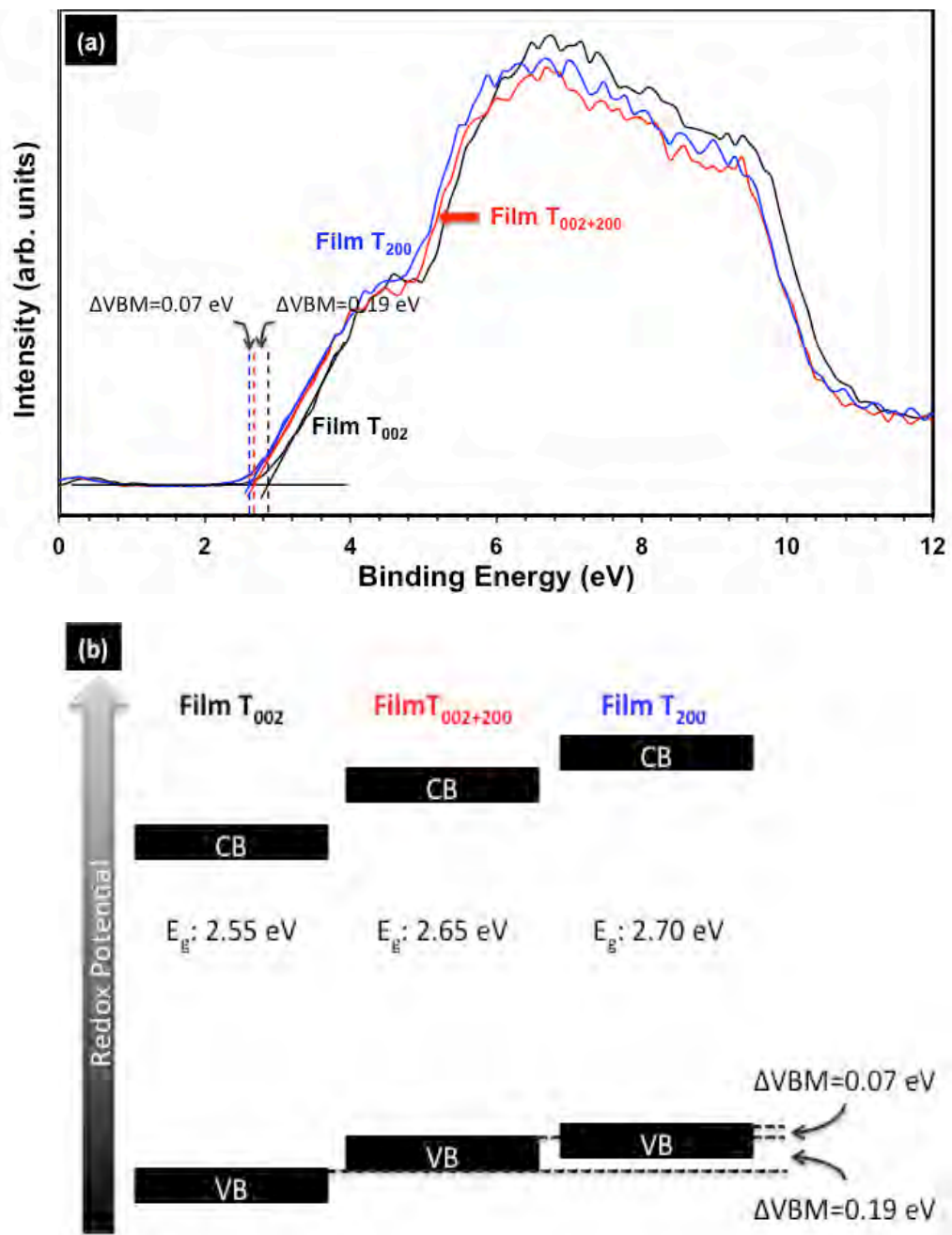


**Figure 6.13:** (a) XPS valence band and (b) electronic band structure of films  $T_{002}$ ,  $T_{002+200}$ , and  $T_{200}$ ;  $E_g$ , CB, VB, and  $\Delta\text{VBM}$  are optical indirect band gap, conduction band, valence band, and energy difference in valence band maxima, respectively.

## 6.2.4.7 Photoelectrochemical Properties

The photoelectrochemical performances of films  $T_{002}$ ,  $T_{002+200}$ , and  $T_{200}$  were investigated by measuring the linear potentiodynamic photocurrent densities in  $0.5 \text{ mol L}^{-1}$  NaCl aqueous solution under the chopped illumination from a 300 W Xe lamp ( $\sim 280 \text{ mW cm}^{-2}$ ) coupled with air mass 1.5 global and UV ( $< 305 \text{ nm}$ ) blocking filters. These data are shown in Figure 6.14. The highest effective photocurrent density (difference between photocurrent density and dark current density) of  $\sim 2.9 \text{ mA cm}^{-2}$  at 0.9 V was measured in film  $T_{002}$ , followed by films  $T_{002+200}$  and  $T_{200}$ . These data were attributed to the combined factors of the electronic band structure (as shown in Figure 6.13 (b)) and the role of oxygen vacancies as follows:

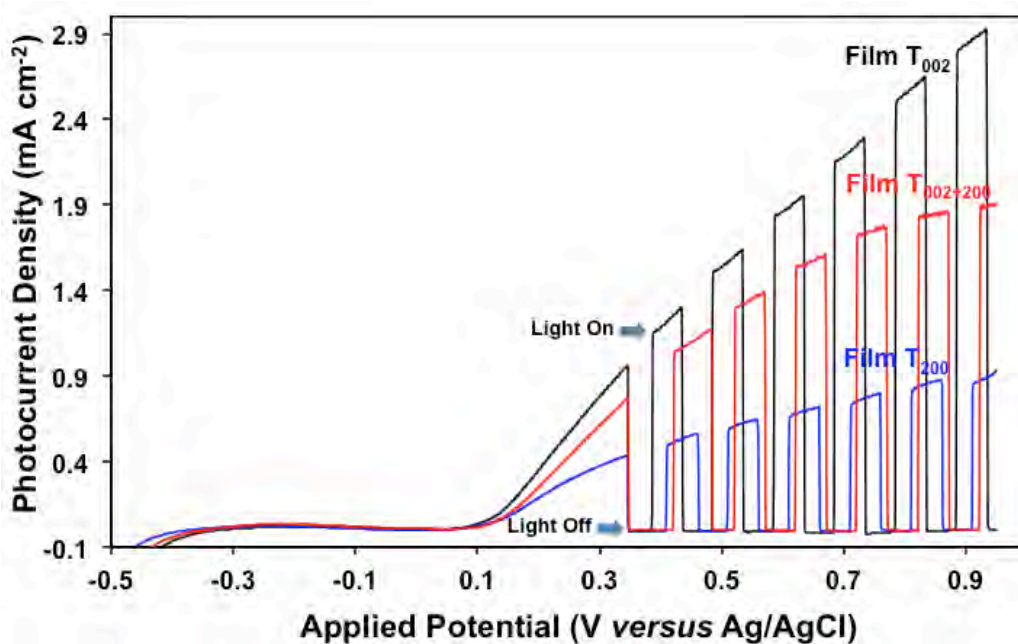


**Figure 6.14:** Linear potentiodynamic photocurrent densities of films  $T_{002}$ ,  $T_{002+200}$ , and  $T_{200}$  measured in  $0.5 \text{ mol L}^{-1}$  NaCl aqueous solution under the chopped illumination from a 300 W Xe lamp ( $\sim 280 \text{ mW cm}^{-2}$ ) coupled with air mass 1.5 global and UV ( $< 305 \text{ nm}$ ) blocking filters.

(i) *Optical band gap*

The low band gap of film T<sub>002</sub> was beneficial to optical absorption, which enhanced the photogeneration of excitons.

(ii) *Valence band maximum*

The low valence band maximum of film T<sub>002</sub> resulted in the strong oxidising power of the photogenerated holes, which facilitated the oxidation of water molecules.

(iii) *Oxygen vacancy*

It has been reported that there are two types of roles that oxygen vacancies play in the photoelectrochemical performance of a photoelectrode. If present on the surface of the photoelectrode, oxygen vacancies may act as reaction sites to facilitate the adsorption of reactants (*viz.*, water molecules)[74, 195, 204]; if present in the bulk of the photoelectrode, oxygen vacancies may act as recombination sites to trap photogenerated excitons [74, 195].

The photocurrent measurements showed that the oxygen vacancies associated with the crystallographic orientations and microstructures had a negative effect on the photoelectrochemical properties of the films. Assuming that the oxygen vacancy concentrations of the surface and bulk of the films were the same, as supported by the XPS depth profile of ~5-10 nm, the oxygen vacancies present in the bulk of films T<sub>020+200</sub> and T<sub>200</sub> may have trapped and thereby enhanced the recombination of charge carriers during their transport to the back-contact of the films. The influence of preferred orientation in thin-film photoelectrodes on the photoelectrochemical performance has been reported in  $\alpha$ -Fe<sub>2</sub>O<sub>3</sub> films, where (001) orientation normal to the substrate improved the charge transport properties of the films [205]. There did not appear to be any data on this effect on WO<sub>3</sub> thin-film photoelectrodes.

#### 6.2.4.8 Electrochemical Properties

Parenthetically, it can be noted that the peak current densities of the cyclic voltammograms of the films at approximately -0.2 V, shown in Figure 6.15, which corresponded to the amount of H<sup>+</sup> intercalated in the films due to electrochromism [206], were in the order film

$T_{200}$  > film  $T_{002+200}$  > film  $T_{002}$ . These data were consistent with those reported by others, where lower current densities from the cyclic voltammograms were obtained in electrochromic  $\text{WO}_3$  samples with lower oxygen vacancy concentrations [207, 208]. Vuong *et al.* [208] related these observations to a decrease in the number of  $\text{H}^+$ -capture sites.

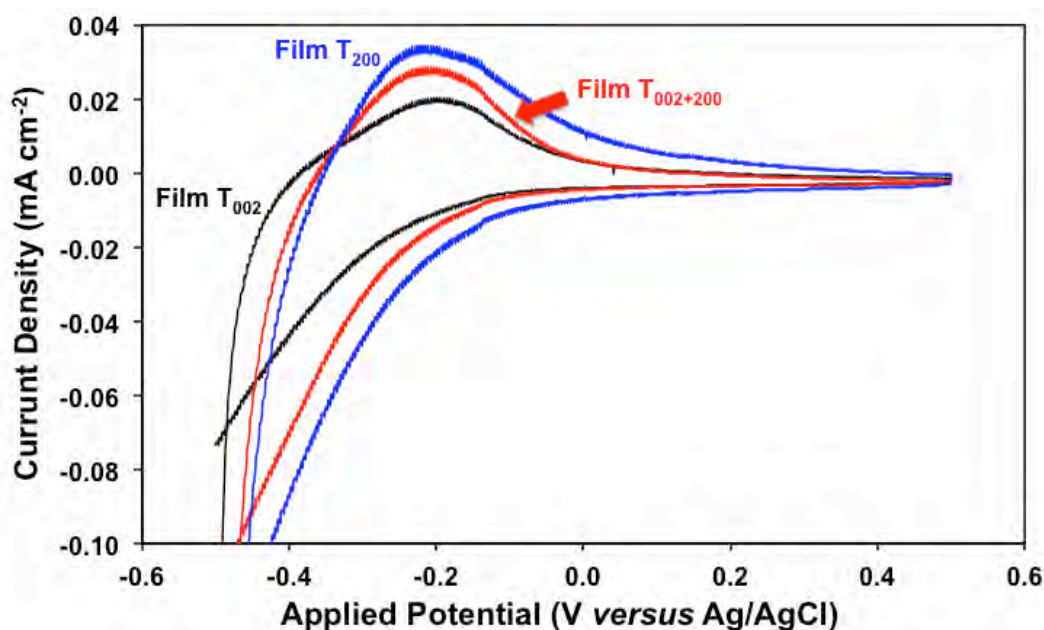


**Figure 6.15:** Cyclic voltammograms of films  $T_{002}$ ,  $T_{002+200}$ , and  $T_{200}$  measured in 0.5 mol  $\text{L}^{-1}$  NaCl aqueous solution in dark environment.

#### 6.2.4.9 Photocatalytic Properties

The role of oxygen vacancies was verified further by measurement of the photodegradation of methylene blue, as shown in Figure 6.16. These measurements were obtained using a UV lamp of major spectral output of  $\sim 254$  nm, which was much lower than the minimal band gap wavelength (absorption edge of  $\sim 460$  nm or 2.7 eV) of the films (see Table 6.2). This was done in order to isolate the effect of the oxygen vacancies by excluding the effect of the band gap. It can be seen that the photodegradation of methylene blue was most efficient in film  $T_{200}$ , followed by  $T_{002+200}$  and  $T_{002}$ . This was attributed to the surface oxygen vacancy in the films, which was in the order of concentration of  $T_{200} > T_{002+200} > T_{002}$ ,

that enhanced the surface adsorption of methylene blue [74, 199, 201]. In this case, the sample surface oxygen vacancies acted as reaction sites while the bulk oxygen vacancies had minimal effect on the overall photocatalytic activity since photocatalysis does not involve the transport of charge carriers within films [209]. These observations demonstrated that the role of oxygen vacancies was dependent on their locations on or in photocatalytic films, where they acted as reaction and recombination sites, respectively.

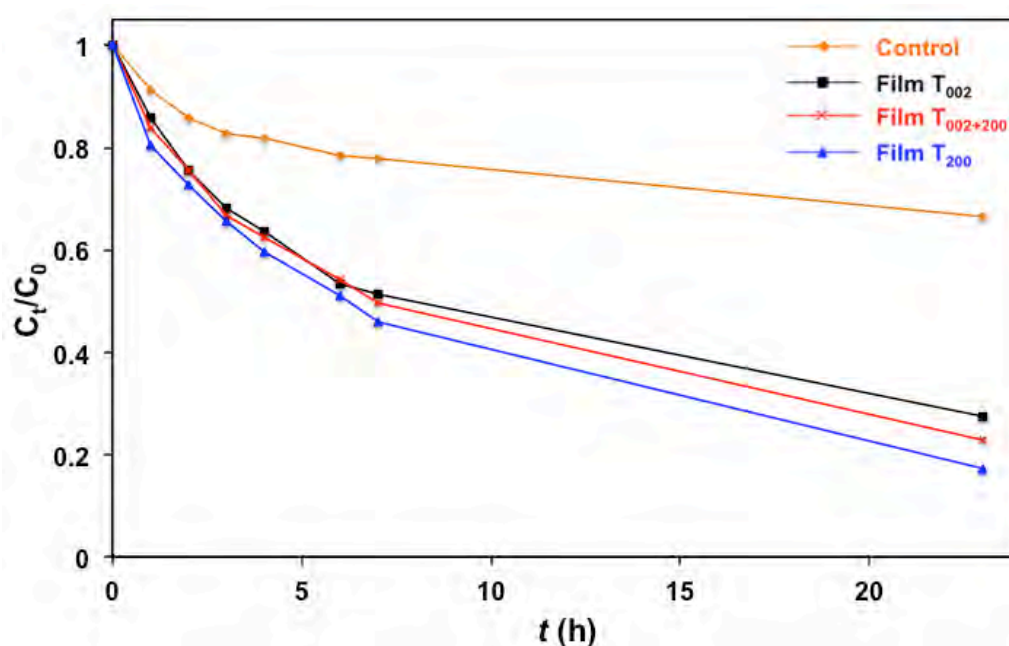


**Figure 6.16:** Photocatalytic degradation of methylene blue as a function of irradiation time  $t$ .  $C_t$  and  $C_0$  are the concentrations of methylene blue at irradiation time  $t$  and  $t = 0$ , respectively.

The difference in the photodegradation performances of films T<sub>200</sub> and T<sub>002</sub> at 24 h irradiation, where film T<sub>200</sub> was ~1.67 times more efficient than film T<sub>002</sub>, was considered statistically significant as justified by the small amounts of WO<sub>3</sub> samples (films of 1.5 cm × 1.5 cm area and 650 nm thickness) used in the photodegradation measurements. The weight of the samples was estimated using the density of WO<sub>3</sub> (7.28 g cm<sup>-3</sup> [97]) to be ~11 μg. This was significantly lesser than those reported in the literature, which commonly used WO<sub>3</sub> samples in powder form (>10 mg [52, 210]) for photocatalytic measurements. It was

anticipated that the irradiation time would be shortened and  $C_p/C_0$  would be lower if greater amounts of samples were used. There had been two replicates performed for the photocatalytic measurements and the results were consistent.

The data in Figures 6.14 and 6.16 suggested the different applications to which the data in Figure 6.12 can be used. That is, for applications typically requiring UV irradiation, such as self-cleaning and self-sterilising surfaces and air and water purification, a high oxygen vacancy concentration is advantageous, so (200) preferred orientation is beneficial. Alternatively, for applications requiring photosensitivity in the visible light region, such as solar energy applications, the (002) preferred orientation is desirable.

### 6.3 Key Results

- Monoclinic  $\text{WO}_3$  thin films with tunable (002) and (200) orientations parallel to FTO substrates were electrodeposited from PTA solutions and subjected to annealing ( $\leq 500^\circ\text{C}$ ).
- The crystallographic orientations of the films were dependent on the nucleation density and the thermally induced recrystallisation kinetics, which can be controlled respectively by the tungsten concentration of the PTA solutions and the annealing conditions. This approach allowed the fabrication of films with preferred (002), equally mixed (002) and (200), and (200) orientations.
- The concurrent effects of crystallographic orientation and trend in oxygen vacancy concentration on the optical indirect band gap of  $\text{WO}_3$  thin films were decoupled, where the linear correlation between these three variables can be used as a diagnostic tool to engineer the electronic band structure of the films for applications requiring photosensitivities in different regions of the solar spectrum.
- In effect, a low valence band maximum, low oxygen vacancy concentration, and resultant low band gap associated with (002) preferred orientation resulted in the highest photoelectrochemical performance, which was relevant to applications under solar illumination.

- In contrast, a high concentration of oxygen vacancies, which acted as surface reaction sites associated with (200) preferred orientation, resulted in the highest efficiency in the photodegradation of methylene blue, which was relevant to applications under UV illumination.

## CHAPTER 7

### Carboxylic Acid-Assisted Electrodeposition of Tungsten Oxide Thin Films

#### 7.1 Introduction

Metal oxide nanomaterials have attracted considerable research interest as photoelectrodes because of their advantageous properties [29] compared to those of their bulk counterparts [30, 65]. These include large specific surface areas, ease of material synthesis, enhanced photoelectrochemical properties due to suppressed photogenerated exciton recombination, and enhanced light absorption [5]. However, reducing the sizes of nanomaterials also may have adverse effects on their crystallinity and electrical transport properties as a result of the increased grain boundary area and the associated increase in the number of surface defects [60, 73]. Thus, it is important to optimise the grain size of  $\text{WO}_3$  nanocrystalline thin-film photoelectrodes by controlling the synthesis parameters in order to achieve a compromise between the microstructural parameters and the resultant optical and photoelectrochemical properties, thereby yielding an optimal photoelectrochemical performance.

The present chapter reports the electrodeposition of  $\text{WO}_3$  thin films using peroxotungstic acid (PTA) containing different carboxylic acids of various concentrations in order to investigate the effectiveness of tailoring the grain sizes. The effects of these acids on the electrodeposition kinetics of  $\text{WO}_3$  thin films and the resultant morphological, mineralogical, and optical properties were investigated. The correlation and optimisation of these properties of the films for photoelectrochemical applications were discussed. Parts of the work presented in this chapter have been published in (i) *Journal of Physical Chemistry C*, year 2013, volume 117, and pages 17766-17776, and (ii) *Thin Solid Films*, year 2013,

volume 544, pages 191-196. Copies of these publications are provided in Appendices 8 and 9, respectively.

## 7.2      Results and Discussion

### 7.2.1      Effect of The Type of Carboxylic Acid

#### 7.2.1.1      Film Thickness

Figure 7.1 shows the film thickness variation as a function of deposition times for depositions done in pure PTA of  $0.20 \text{ mol L}^{-1}$  tungsten concentration and PTA containing  $0.03 \text{ mol L}^{-1}$  carboxylic acids and annealed at  $450^\circ\text{C}$  for 2 h. The film thicknesses were measured from the cross-sections of the films, which were milled by FIB. All films adhered well to the substrates (as shown by the resistance to robust handling) except for those deposited for times longer than 30 min in pure PTA, which cracked owing to drying stresses. Compared to pure PTA, the deposition thicknesses increased, remained constant, and decreased when the depositions were done from PTA containing oxalic, formic, and citric acids, respectively. Table 7.1 shows that the same order and the reverse order were seen in the trends of the electrolyte conductivities and pH values, respectively. These observations suggested that the deposition thickness was a function of these two variables, which were determined by the hydronium ions and conjugate bases produced upon the dissociation of the acids in aqueous solutions [211].

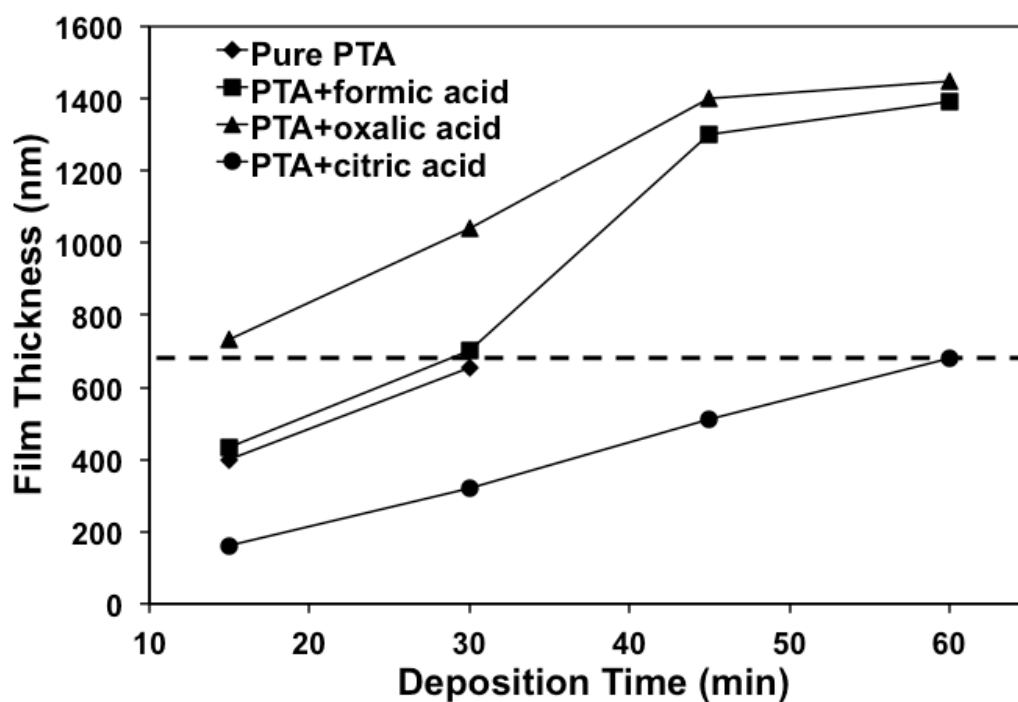


**Figure 7.1:** Thicknesses of  $\text{WO}_3$  thin films as a function of deposition times. Dashed line indicates film thickness  $\sim 700$  nm. These films were deposited from pure PTA of  $0.20 \text{ mol L}^{-1}$  tungsten concentration and PTA containing  $0.03 \text{ mol L}^{-1}$  carboxylic acids and annealed at  $450^\circ\text{C}$  for 2 h.

**Table 7.1:** Analytical data obtained for all the samples from the different tests.

Electrolyte composition	Electrolyte pH	$\kappa$ (mS cm <sup>-1</sup> )	$t$ (min)	Microstructure	Grain size* (nm)	Crystallite size^ (nm)	Film strain^ (x10 <sup>-4</sup> )	(002) peak area	(200) peak area	True porosity (%)	$E_g$ (eV)
0.2 M PTA	1.71	2.900	30	Large agglomerates	131±16	107	7	9383.89	10066.76	0.87	2.55
0.2 M PTA+0.03 M formic acid	1.70	3.120	30	Small agglomerates	94±12	82	4	7149.8	4251.69	1.21	2.70
0.2 M PTA+0.03 M oxalic acid	1.41	6.570	15	Small agglomerates	83±10	92	6	3640.11	1759.7	1.91	2.65
0.2 M PTA+0.03 M citric acid	1.84	0.009	60	Individual particles	45±4	43	4	6478.43	9588.08	2.12	2.63

$\kappa$ , electrolyte conductivity;  $t$ , deposition time;  $E_g$ , optical indirect band gap; \* measured from SEM images; ^ measured from Williamson-Hall plots

According to the logarithm of the first proton acid dissociation constant ( $pK_{a1}$ ), the dissociation of the acids follows in the order oxalic > citric > formic. The small change in the pH of the PTA containing formic acid was caused by the limited dissociation of the acid, which produced a minimal amount of hydronium ions. In contrast, the increase in pH of PTA containing citric acid suggested that the pH was controlled by hydrogen bonding between the relatively large number of highly electronegative oxygen atoms in the citrate ion and the hydronium ions, thereby reducing the availability of hydronium ions. In further contrast, the decrease in pH in PTA containing oxalic acid confirmed the release of a large amount of hydronium ions upon the dissociation of the acid, thereby resulting in high availability of the hydronium ions in the PTA electrolyte despite their formations of hydrogen bonds with the electronegative oxygen atoms in the small oxalate ion. As a consequence of the formation of hydrogen bonds between the hydronium and PTA ions (PTA-hydronium complex ions), a net positive charge developed around the PTA ions, as shown in Figure 7.2. This aided the deposition process by driving the PTA-hydronium complex ions to the cathodically biased working electrode, thereby resulting in thicker films deposited from PTA containing oxalic acid. On the other hand, the electrolyte conductivity can be affected by the  $pK_{a1}$  values of the acids, which determined the amounts of ions formed in the electrolytes and the molecular weights and associated sizes of the conjugate bases of the acids (in this case, the order is citrate > oxalate > formate), which determined the molecular drag in the electrolyte.

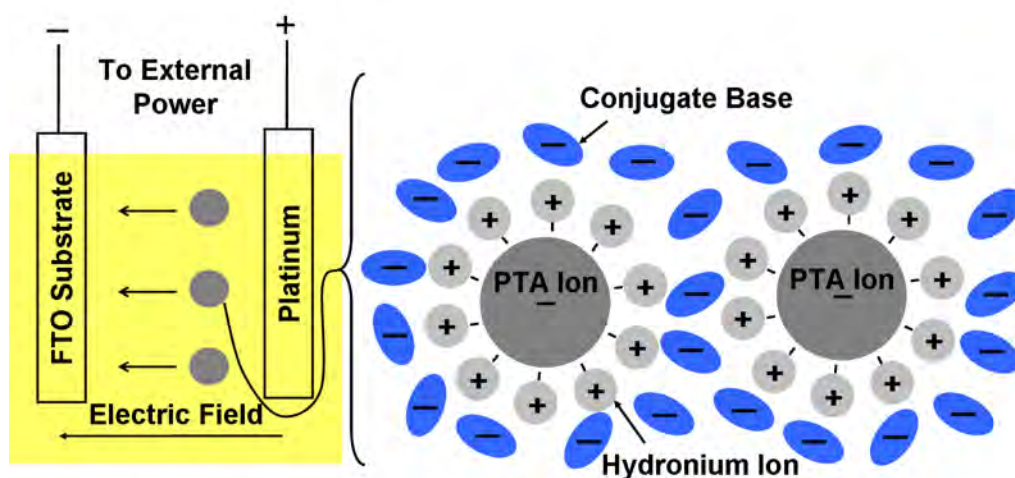


**Figure 7.2:** Schematic diagram of the effects of hydronium ions and conjugate bases on deflocculation and dispersion of PTA ions.

The preceding observations showed that the relationships between the controlling variables such as  $pK_{a1}$ , molecular weight of the conjugate bases, electrolyte pH, and electrolyte conductivity were complex and their influences on the film thickness cannot be correlated independently. Figure 7.1 also shows that there was an apparent decrease in the deposition rates at longer times. The main reasons for this were assumed to be the decreasing PTA concentrations during deposition [212, 213] and the decreasing electrical conductivities of the films with increasing thicknesses [148]. Since the film thickness is known to influence photoelectrochemical performance [77, 155],  $WO_3$  films of similar thicknesses ( $\sim 700$  nm), deposited for various times from different electrolyte compositions, were characterised further using SEM, XRD, UV-VIS spectrophotometry, and photoelectrochemical measurements.

#### 7.2.1.2 Surface Morphology

Figure 7.3 shows the surface morphologies of the films. It is clear that there are three types of microstructures, *viz.*, individual particles, small agglomerates, and large agglomerates, as summarised in Table 7.1. The individual particles consisted of discrete grains with possible subgrains whereas the agglomerates were polycrystalline, containing multiple particles.

The average sizes of the  $\text{WO}_3$  grains (individual particles or agglomerates), measured by the line-intercept method ( $300,000\times$  photographs, 10 lines, 5-10 grains per line), were smaller for the films deposited from PTA containing carboxylic acids compared to that of the film deposited from pure PTA. This was considered to result from the deflocculation and dispersion mechanism of electrosteric stabilisation [214] shown in Figure 7.2. The effectiveness of the separation of PTA ions was controlled by the relative availability of hydronium ions for hydrogen bonding with the electronegative oxygen atoms of the PTA ions and the molecular weight and associated sizes of the conjugate bases that occupied the volume of the electrolyte.

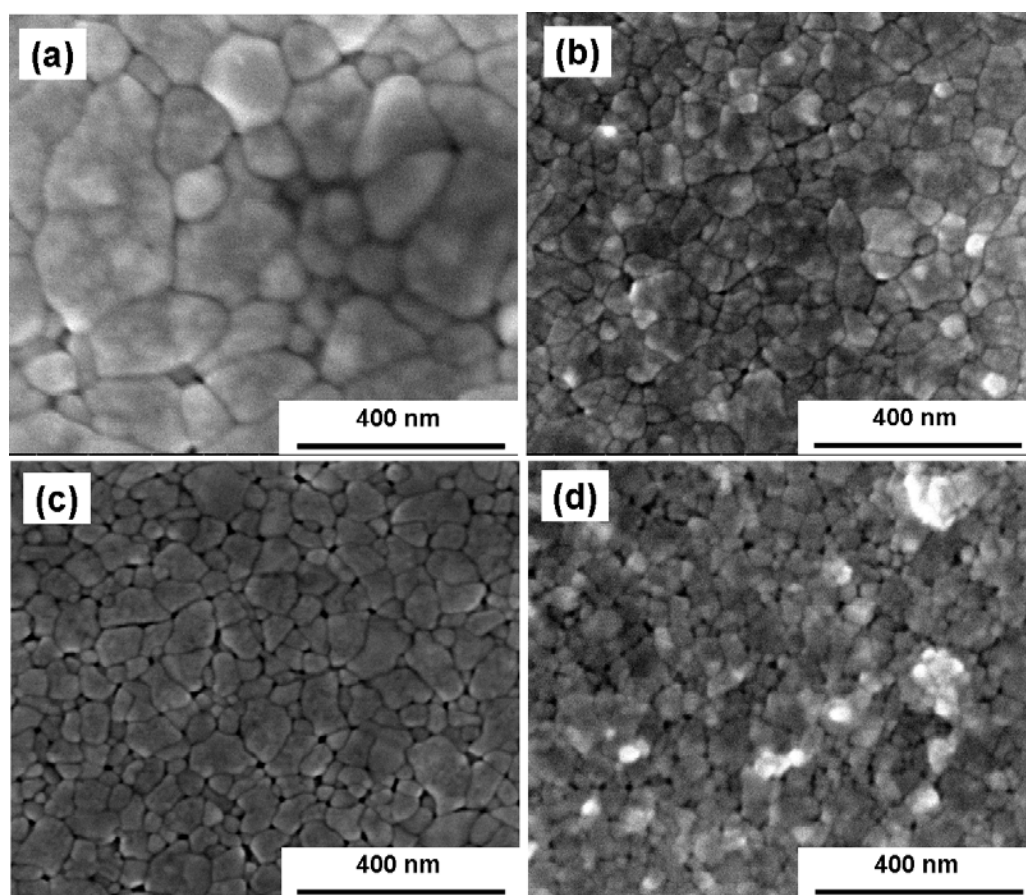


**Figure 7.3:** SEM images of  $\text{WO}_3$  thin films of similar thicknesses  $\sim 700$  nm deposited from (a) pure PTA of  $0.20 \text{ mol L}^{-1}$  tungsten concentration and PTA containing  $0.03 \text{ mol L}^{-1}$  (b) formic acid, (c) oxalic acid, and (d) citric acid and annealed at  $450^\circ\text{C}$  for 2 h.

*Pure PTA – Large agglomerates of size ~131 nm (~500 nm maximum):* In pure PTA, the absence of particle separation by any deflocculation mechanism caused solute agglomeration, rapid grain growth, and consequent agglomeration during annealing since the proximity of the ion complexes minimised the diffusion distance.

*PTA containing formic acid – Small agglomerates of size ~94 nm and PTA containing oxalic acid – Small agglomerates of size ~83 nm:* In PTA containing carboxylic acids, with conjugate bases of molecular weights  $45 \text{ g mol}^{-1}$  (formate) and  $125 \text{ g mol}^{-1}$  (oxalate), the hydronium ions provided a basic deflocculation mechanism of electrosteric stabilisation [214] and the volumes occupied by the conjugate bases in solutions contributed to an increase in the degree of separation of the PTA ions and the resultant diffusion distance.

*PTA containing citric acid – Individual particles of size ~45 nm:* In PTA containing citric acid, with conjugate base of molecular weight  $209 \text{ g mol}^{-1}$ , deflocculation by electrosteric stabilisation occurred but the larger volume occupied by the citrate ions in the solution separated the PTA ions and increased the diffusion distance such that little grain growth took place during annealing.

In summary, it can be seen that the use of carboxylic acids was effective in facilitating deflocculation and suppressing solute clustering before electrodeposition. Therefore, the microstructures of the annealed films can be manipulated by using carboxylic acids of different molecular weights and associated sizes of conjugate bases since the sizes of the conjugate bases controlled the distribution density of the  $\text{WO}_3$  nuclei, their proximity, the corresponding diffusion distances, the resultant tendency to undergo grain growth during annealing, and hence their susceptibility to form solid agglomerates. It may be noted that the conjugate bases and hydronium ions were oxidised and effectively removed from the films upon annealing.

$\text{WO}_3$  exhibits an orthorhombic  $\rightarrow$  monoclinic phase transformation upon cooling from  $\sim 330^\circ\text{C}$  and this is associated with an extremely high thermal contraction of  $\sim 13 \times 10^{-6} \text{ }^\circ\text{C}^{-1}$  from this temperature to room temperature, measured both directly and calculated from the

lattice parameters[95, 215]. Although the high thermal contraction and the phase transformation experienced during cooling from 450°C could be expected to facilitate delamination between agglomerates, this was not supported by the observation that the film deposited from pure PTA (with the largest agglomerates) did not exhibit delamination. It is well known that agglomerates shrink independently during heating and so this also represents a possible mechanism of delamination [157]. Again, the SEM images in Figure 7.3 showed that the largest agglomerates in the film deposited from pure PTA, which would be expected to show the largest annealing shrinkage, did not undergo delamination.

These two observations supported the conclusion of the importance of the separation effect by the conjugate bases. That is, for the film deposited from pure PTA, the absence of the conjugate bases allowed close proximity of all particles, thereby facilitating effective intergranular bonding *within* and *between* agglomerates. For the films deposited from PTA containing formic or oxalic acid, the separation effect was such that effective bonding occurred *within* the agglomerates but thermal contraction and annealing shrinkage were sufficient to overcome the bonding *between* the agglomerates. For the film deposited from PTA containing citric acid, the separation effect prevented agglomeration in the first place.

The true porosity data, which were determined by image analysis, in Table 7.1 supported the preceding conclusions. The film deposited from pure PTA had the lowest true porosity (closed pores only). Even though the agglomerate size was large, delaminations between agglomerates was avoided owing to the strong bonding between the tightly packed agglomerates. In contrast, the films deposited from PTA containing carboxylic acids exhibited porosities that had been enhanced by delaminations between agglomerates, which resulted from the separation effect of the conjugate bases. Therefore, the true porosity reflected the effect of separation. That is, with PTA containing citric acid (the largest conjugate base), the separation between individual particles was the greatest and so the true porosity also was the greatest. However, delaminations were not visible because the thermal contraction stresses were distributed more evenly across the homogeneous particle array rather than concentrating along inhomogeneously distributed agglomerate boundaries.

## 7.2.1.3 Mineralogy

Figure 7.4 shows the XRD results of the films. The major peaks for monoclinic  $\text{WO}_3$  were present at  $23.3^\circ$ ,  $23.7^\circ$ , and  $24.4^\circ$   $2\theta$ , which corresponded to the (002), (020), and (200) planes [97], respectively. The XRD peaks of the films deposited from PTA containing carboxylic acids were weaker (lower intensities and smaller areas) and broader compared to the film deposited from pure PTA, despite having similar thicknesses (the small FTO peaks served as *in situ* normalising standard). The explanations were as follows:

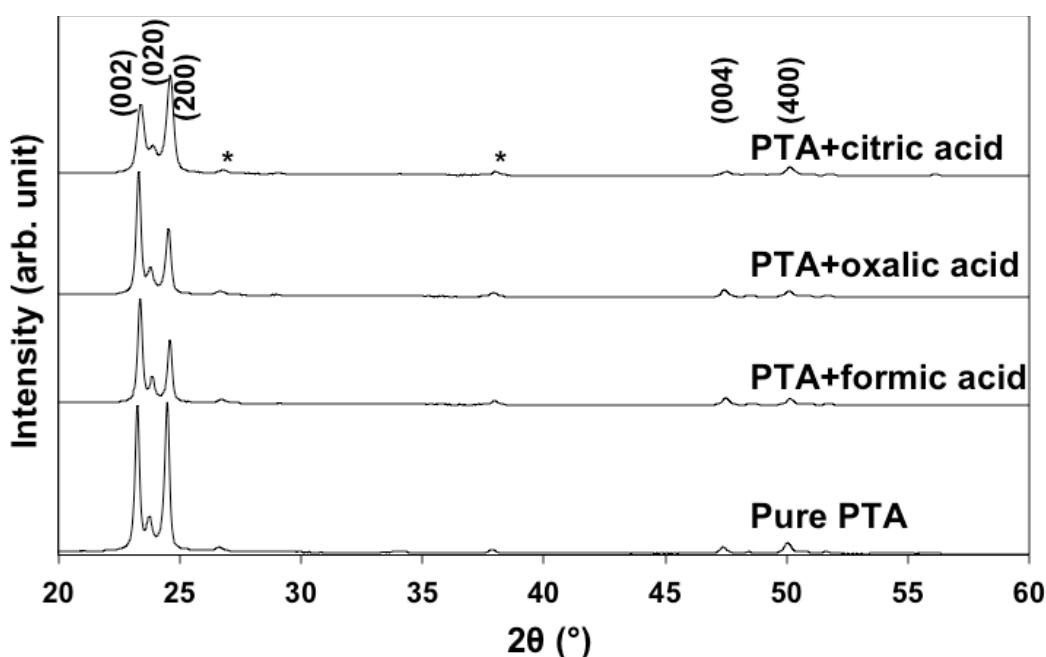


**Figure 7.4:** XRD patterns of  $\text{WO}_3$  thin films of similar thicknesses  $\sim 700$  nm deposited from pure PTA of  $0.20 \text{ mol L}^{-1}$  tungsten concentration and PTA containing  $0.03 \text{ mol L}^{-1}$  carboxylic acids and annealed at  $450^\circ\text{C}$  for 2 h. \* marks the FTO peaks.

*XRD peak areas:* As shown in Table 7.1, the XRD peak areas of the films deposited from pure PTA and from PTA containing formic and oxalic acids showed inverse trend with the true porosities and parallel trend with the grain sizes of the films. This was consistent with the beam intensity reduction effect of true porosity (which reduced the area of scanned solid) and the scattering from the agglomerates (which reduced the planarity of the surface profile). Consequently, the XRD peaks of the film deposited from PTA containing citric

acid showed anomalously high intensities because, as shown in Table 7.1 and the preceding text, the true porosity was the highest and agglomerates were absent.

*XRD peak breadths:* The XRD peak breadths of the films depended on the perfection of crystallinity of the individual grains and the randomness of the grain orientations. The Williamson-Hall approach [216] usually is used to determine the crystallite (subgrain) size and this involves measurement of the breadth of the peak at half-height. Table 7.1 shows that the crystallite sizes and grain sizes were similar, which indicated that the individual grains were single crystals (*i.e.*, no subgrains) and that the image analysis was relatively accurate. The strain values of the films, which were estimated from the Williamson-Hall plot (representative plot shown in Figure 7.5), were negligibly small and thus the broadening of the XRD peaks was unlikely to be caused by the strain in the film [216].

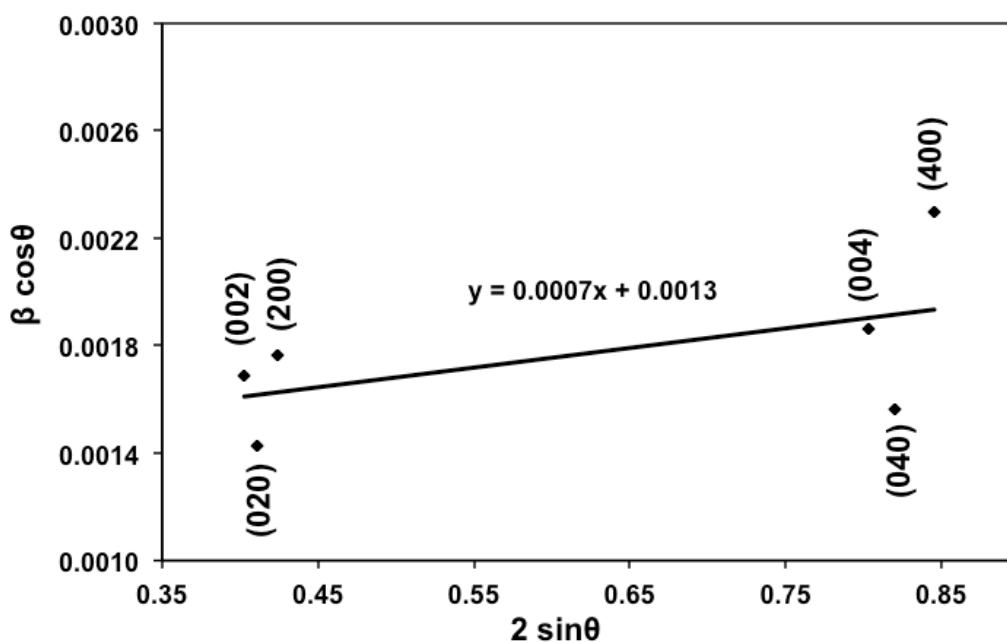


**Figure 7.5:** Representative Williamson-Hall plot ( $\beta \cos\theta = 2\varepsilon \sin\theta + 0.9\lambda/r$ ) [216] of  $\text{WO}_3$  thin films deposited from pure PTA of  $0.20 \text{ mol L}^{-1}$  tungsten concentration and annealed at  $450^\circ\text{C}$  for 2 h.  $\beta$  is the full-width-half-maximum of the XRD peak while  $\varepsilon$ ,  $r$ , and  $\lambda$  are the sample strain and crystallite size and the X-ray wavelength, respectively.  $\varepsilon$  and  $r$  can be obtained respectively from the gradient and the extrapolation of the plot to the abscissa.

## 7.2.1.4 Optical Properties

Figure 7.6 shows the optical transmittance spectra of the films. The transmittance of the films differed marginally in the near-UV (<400 nm) and visible (400-800 nm) regions. The main differences were a small blue-shift (<15 nm) in the optical absorption edge of the films deposited from PTA containing carboxylic acids (differentiation between these films was ambiguous) and the slightly lower optical transmittance in the visible region of the film deposited from PTA containing citric acid. The blue shift was attributed to microstructural defects, as described subsequently. The lower transmittance was attributed to scattering losses resulting from the high true porosity of the film deposited from PTA containing citric acid, as shown in Table 7.1.

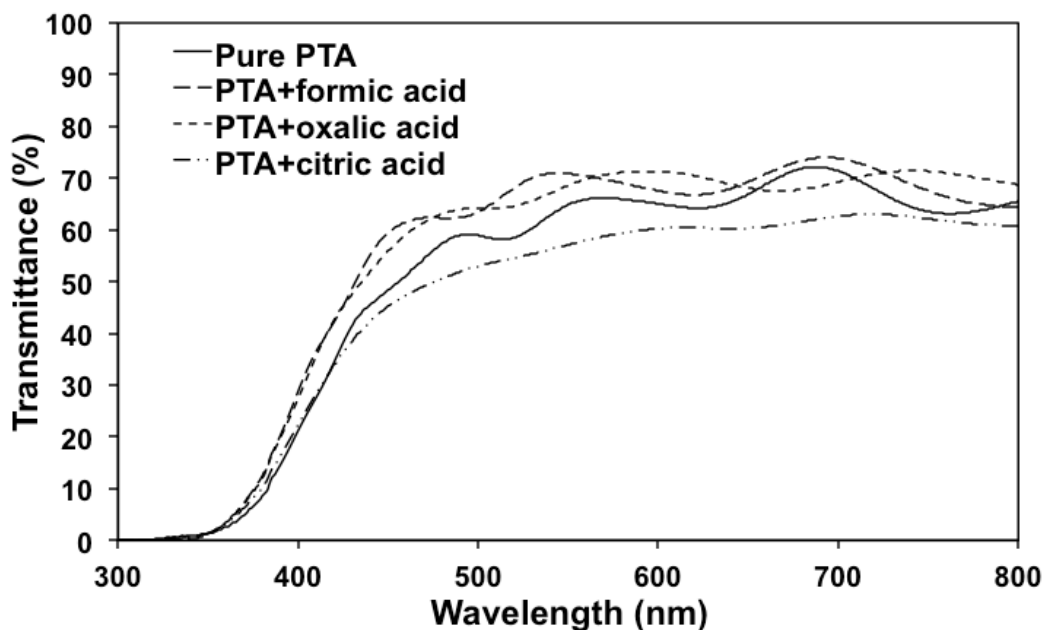


**Figure 7.6:** Optical transmittance spectra of  $\text{WO}_3$  thin films of similar thicknesses  $\sim 700$  nm deposited from pure PTA of  $0.20 \text{ mol L}^{-1}$  tungsten concentration and PTA containing  $0.03 \text{ mol L}^{-1}$  carboxylic acids and annealed at  $450^\circ\text{C}$  for 2 h.

Tauc plots were used to obtain the optical indirect band gaps of the films and the results are shown in Table 7.1. The optical indirect band gaps of the films varied in the range 2.55–

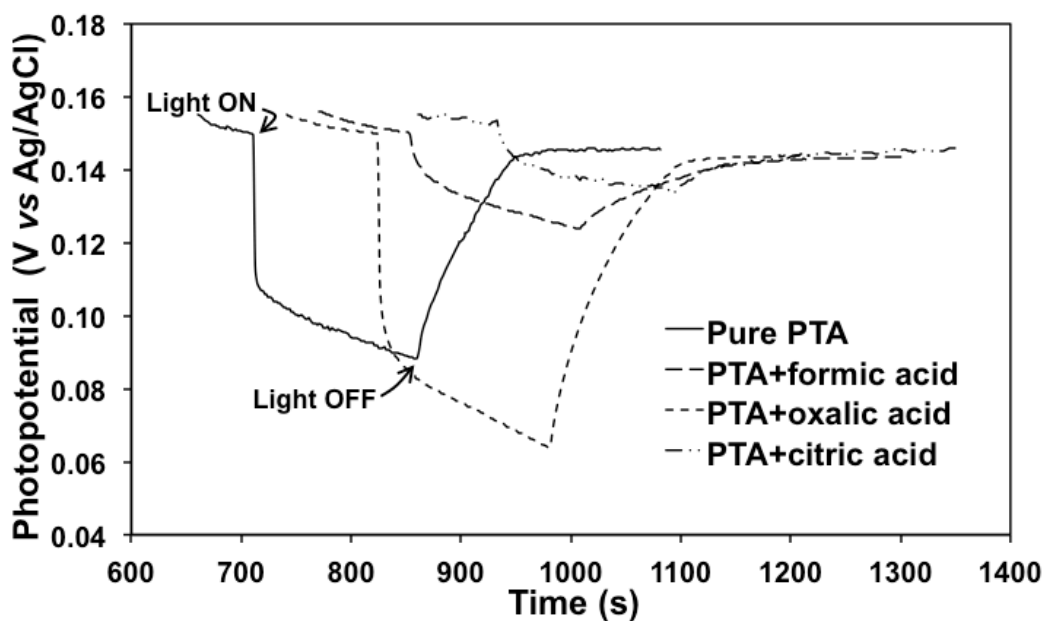
2.70 eV, which was in good agreement with previous work [105, 108, 115]. Since the films showed variations in true porosity (small variation) and grain size (large variation), the associated variation in surface areas would be expected to affect the proportion of surface defects, an increase in which is known to increase the optical band gaps of materials [43, 79]. However, the variation between the band gaps, which were determined by a graphical technique involving extrapolation, was too small to differentiate between films.

#### 7.2.1.5 Photoelectrochemical Properties

When a photoanode is in contact with an electrolyte in a dark environment, energy band bending occurs at the photoanode/electrolyte interface in order to achieve thermal equilibrium [4]. On illumination, excitons are generated at the photoanode, with the electrons' being excited to the conduction band and the holes' reaching the photoanode/electrolyte interface. This in turn decreases the band bending, where the extent of decrease corresponds to the photopotential [1]. When the illumination is switched off, the photopotential diminishes as the energy band bending is re-established. The relaxation time of the photopotential determines the recombination rate of the photogenerated excitons [77].

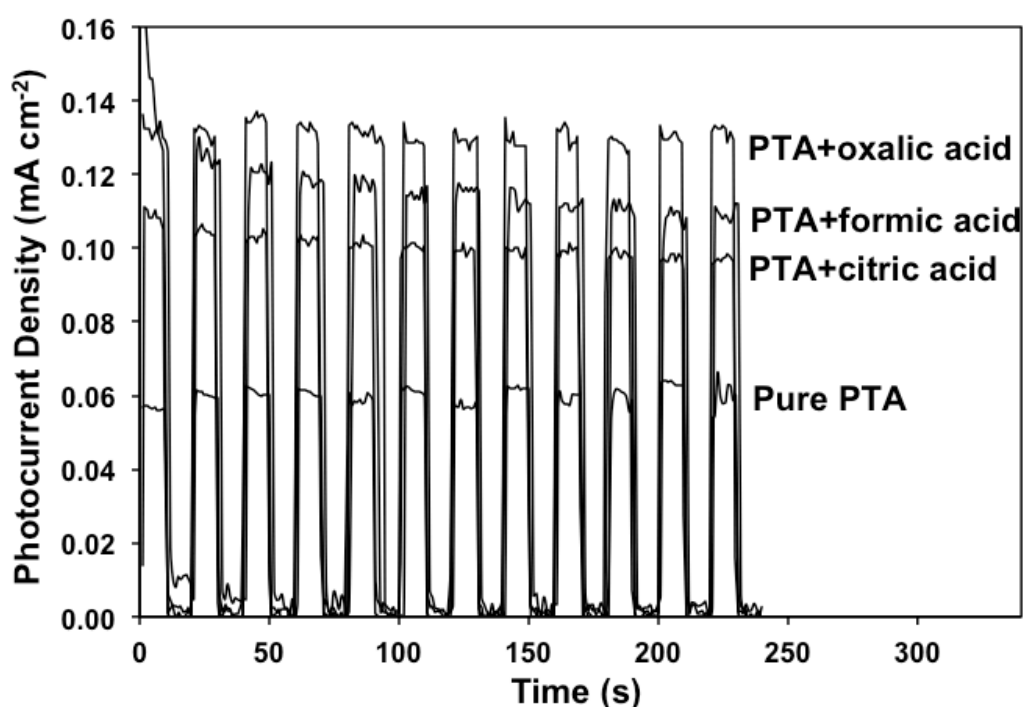
The transient open-circuit photopotential measurements of the films are shown in Figure 7.7. The stable potentials attained in the dark were ~0.15 V. Once illumination (50 W tungsten-halogen lamp; light source-to-sample distances of ~25 cm; intensity of ~100 mW m<sup>-2</sup>) was switched on, the photopotentials developed immediately and then commenced the approach to steady values. The times taken for the photopotentials to decay to their initial value of ~0.15 V after the illumination was turned off were ~110 s, 160 s, 150 s, and 120 s for the films deposited from pure PTA and PTA containing formic acid, oxalic acid, and citric acid, respectively. The relatively long photopotential relaxation times (~150-160 s) of the films consisting of small agglomerates (~83-94 nm), which were deposited from PTA containing formic or oxalic acid, suggested that the recombination rates of the photogenerated excitons were slow. This was attributed to the relatively short hole diffusion distance to the photoanode/electrolyte interface owing to the small agglomerate

sizes. Therefore the photogenerated holes had a higher probability of oxidising water before they could recombine with the photogenerated electrons. The relatively high specific surface area associated with the small agglomerate sizes also may have contributed to the long photopotential relaxation time since this provided a large number of reaction sites for water oxidation. For the film consisting of individual particles, which was deposited from PTA containing citric acid, the large grain boundary area associated with the small particle sizes resulted in a high fraction of surface defects (*viz.*, dangling bonds), which acted as exciton recombination sites [217]. In addition, the grain boundaries also acted as weak links that hindered electron transport to the back contact (substrate) [218], thereby increasing the recombination rate.



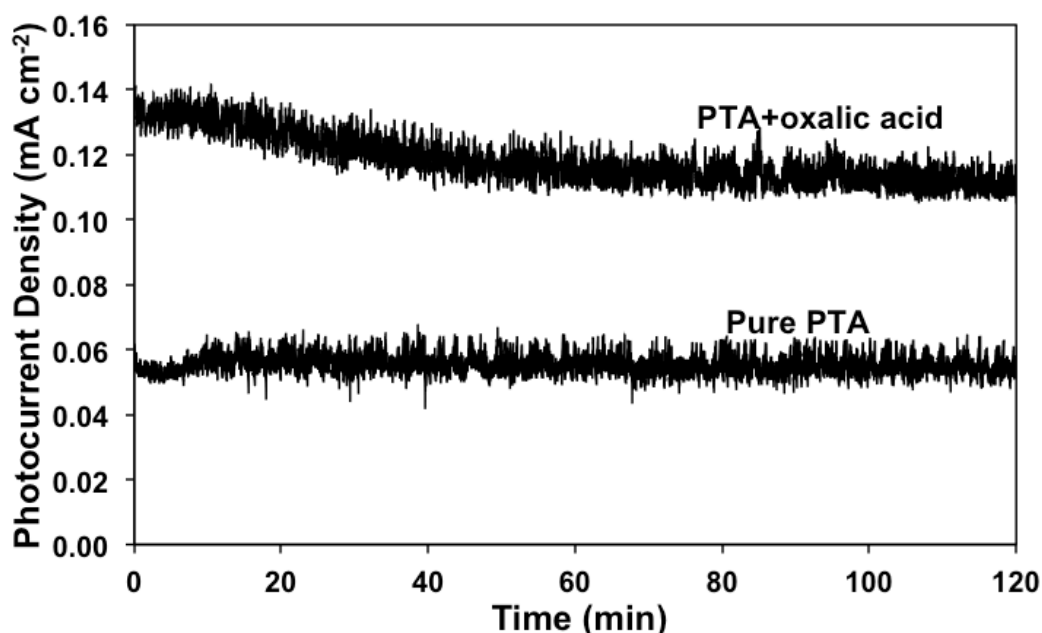
**Figure 7.7:** Transient open-circuit photopotential measurements of  $\text{WO}_3$  thin films of similar thicknesses  $\sim 700$  nm deposited from pure PTA of  $0.20 \text{ mol L}^{-1}$  tungsten concentration and PTA containing  $0.03 \text{ mol L}^{-1}$  carboxylic acids and annealed at  $450^\circ\text{C}$  for 2 h. The light source used was a 50 W tungsten-halogen lamp with intensity of  $\sim 100 \text{ mW m}^{-2}$  (light source-to-sample distance of  $\sim 25$  cm).

Figure 7.8 shows the transient photocurrent densities of the films measured under a chopped illumination (50 W tungsten-halogen lamp; light source-to-sample distances of  $\sim 25$  cm; intensity of  $\sim 100 \text{ mW m}^{-2}$ ) at an applied potential of 0.7 V. The trend of the photocurrent densities was in the same order as the photopotential relaxation times. This suggested that, as expected, the photocurrent density measurements were dominated by the photogenerated exciton separation rate, which was dependent on the electron transport, the hole transport, the number of reaction sites for water oxidation, and the number of exciton recombination sites. The maximal photocurrent density, which was measured in the film consisting of small agglomerates (deposited from PTA containing oxalic acid), was an outcome of a positive balance of these preceding factors.



**Figure 7.8:** Transient photocurrent measurements of  $\text{WO}_3$  thin films of similar thicknesses  $\sim 700$  nm deposited from pure PTA of  $0.20 \text{ mol L}^{-1}$  tungsten concentration and PTA containing  $0.03 \text{ mol L}^{-1}$  carboxylic acids and annealed at  $450^\circ\text{C}$  for 2 h. Measurements were taken under a chopped illumination (50 W tungsten-halogen lamp; light source-to-sample distances of  $\sim 25$  cm; intensity of  $\sim 100 \text{ mW m}^{-2}$ ) at an applied potential of 0.7 V.

The measurements for 2 h of the transient photocurrent densities of the films deposited from pure PTA (lowest photocurrent density) and PTA containing oxalic acid (highest photocurrent density) are shown in Figure 7.9. The photocurrent density of the film deposited from pure PTA remained stable at  $\sim 0.06 \text{ mA cm}^{-2}$  throughout the measurement. The film deposited from PTA containing oxalic acid showed a decrease in the photocurrent density from  $\sim 0.135 \text{ mA cm}^{-2}$  to  $\sim 0.110 \text{ mA cm}^{-2}$  ( $\sim 19\%$ ) after an hour of measurement and remained stable for the rest of the measurement. Overall the films demonstrated stability as photoanodes for photoelectrochemical cells.



**Figure 7.9:** Transient photocurrent measurements of  $\text{WO}_3$  thin films of similar thicknesses  $\sim 700 \text{ nm}$  deposited from pure PTA of  $0.20 \text{ mol L}^{-1}$  tungsten concentration and PTA containing  $0.03 \text{ mol L}^{-1}$  carboxylic acids and annealed at  $450^\circ\text{C}$  for 2 h. Measurements were taken under the illumination from a 50 W tungsten-halogen lamp (light source-to-sample distances of  $\sim 25 \text{ cm}$ ; intensity of  $\sim 100 \text{ mW m}^{-2}$ ) at an applied potential of 0.7 V.

It may be noted that, as observed before [139, 219], the photocurrent densities increased linearly with increasing light intensity, which was varied in the range  $30\text{-}100 \text{ mW cm}^{-2}$ . It is well known that photon absorption; which depends on the light intensity, absorption edge,

transmission, and reflection; results in the generation of excitons, which dominates the photoelectrochemical performance [139, 219].

## 7.2.2 Effect of The Oxalic Acid Concentrations

### 7.2.2.1 Film Thickness

Further studies on the effect of varied oxalic acid concentrations were carried out considering the advantages of yielding enhanced deposition thickness from PTA containing oxalic acid. Higher concentrations of oxalic acid in PTA also resulted in increasing deposition thicknesses, which were attributed to the increasing availability of hydronium ions to form hydrogen bonds with the PTA ions. However, the initial trials revealed that longer deposition times resulted in cracked and poorly adhered thick films. To avoid this, films of similar thicknesses ( $400 \pm 20$  nm) were prepared where shorter deposition times ( $\leq 20$  min) were applied to PTA containing higher oxalic acid concentrations. The films were named as films A, B, C, D, and E according to their depositions from pure PTA of  $0.20 \text{ mol L}^{-1}$  tungsten concentration and PTA containing  $0.01 \text{ mol L}^{-1}$ ,  $0.03 \text{ mol L}^{-1}$ ,  $0.05 \text{ mol L}^{-1}$ , and  $0.10 \text{ mol L}^{-1}$  oxalic acid, respectively

### 7.2.2.2 Surface Morphology

Figures 7.10 and 7.11 present the surface morphologies of the films deposited from pure PTA and PTA containing  $0.01\text{-}0.10 \text{ mol L}^{-1}$  oxalic acid, as examined by SEM and AFM, respectively. The scan areas of the AFM images were  $3 \mu\text{m} \times 3 \mu\text{m}$ . The films consisted of agglomerates/particles with sizes in the range  $42\text{-}132$  nm, where the size decreased with the increasing oxalic acid concentration (see Table 7.2). Varying the oxalic acid concentration revealed that the separation effect of the conjugate bases was not only size-dependent but it also depended on the amount present in the PTA electrolytes. Figures 7.10 (a) and (e) show insets at lower magnifications, which illustrated the two characteristic types of larger-scale microstructures that were observed. The microstructure in Figure 7.10 (a) was relatively homogeneous in terms of grain size distribution and true porosity. While this image was

for the film A, it was similar to the images for films B-D. In contrast, Figure 7.10 (e) shows a completely different microstructure of film E, that was consisting of isolated islands of unagglomerated particles, which were generated by excessive shrinkage of the high-surface-area/energy particles (~39 nm) during the annealing. The shrinkage appeared to have been so extreme that the microstructures of the islands were highly disrupted, with uneven steps and concavities. This was in contrast to other agglomerated films, which consisted of coarser particles of lower surface area/energy[157].

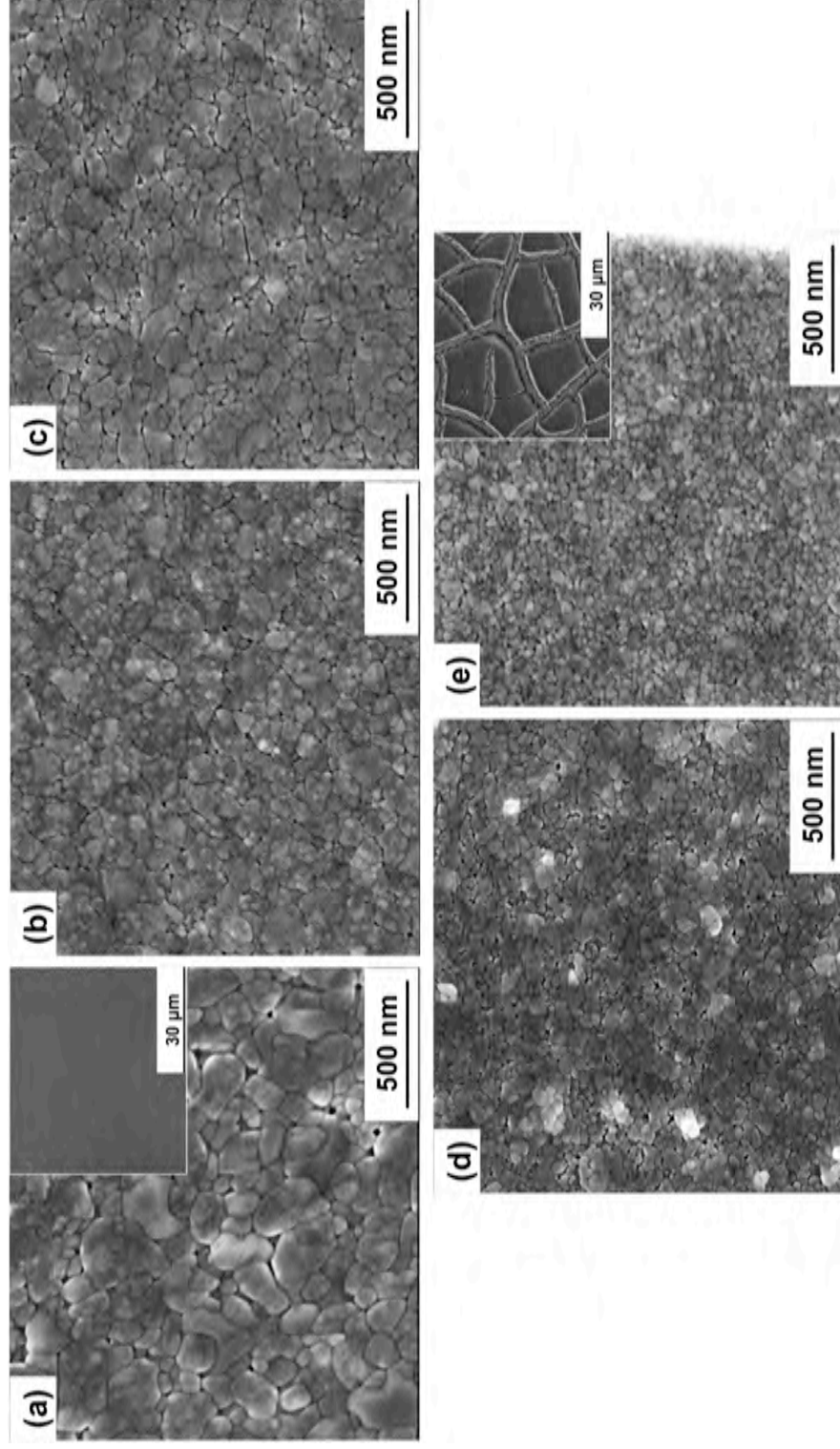


**Figure 7.10:** SEM images of  $\text{WO}_3$  thin films of similar thicknesses  $\sim 400$  nm deposited from (a) pure PTA of  $0.20 \text{ mol L}^{-1}$  tungsten concentration and PTA containing oxalic acid of concentrations (b)  $0.01 \text{ mol L}^{-1}$ , (c)  $0.03 \text{ mol L}^{-1}$ , (d)  $0.05 \text{ mol L}^{-1}$ , and (e)  $0.10 \text{ mol L}^{-1}$  and annealed at  $450^\circ\text{C}$  for 2 h. Insets in (a) and (e) are at lower magnification.

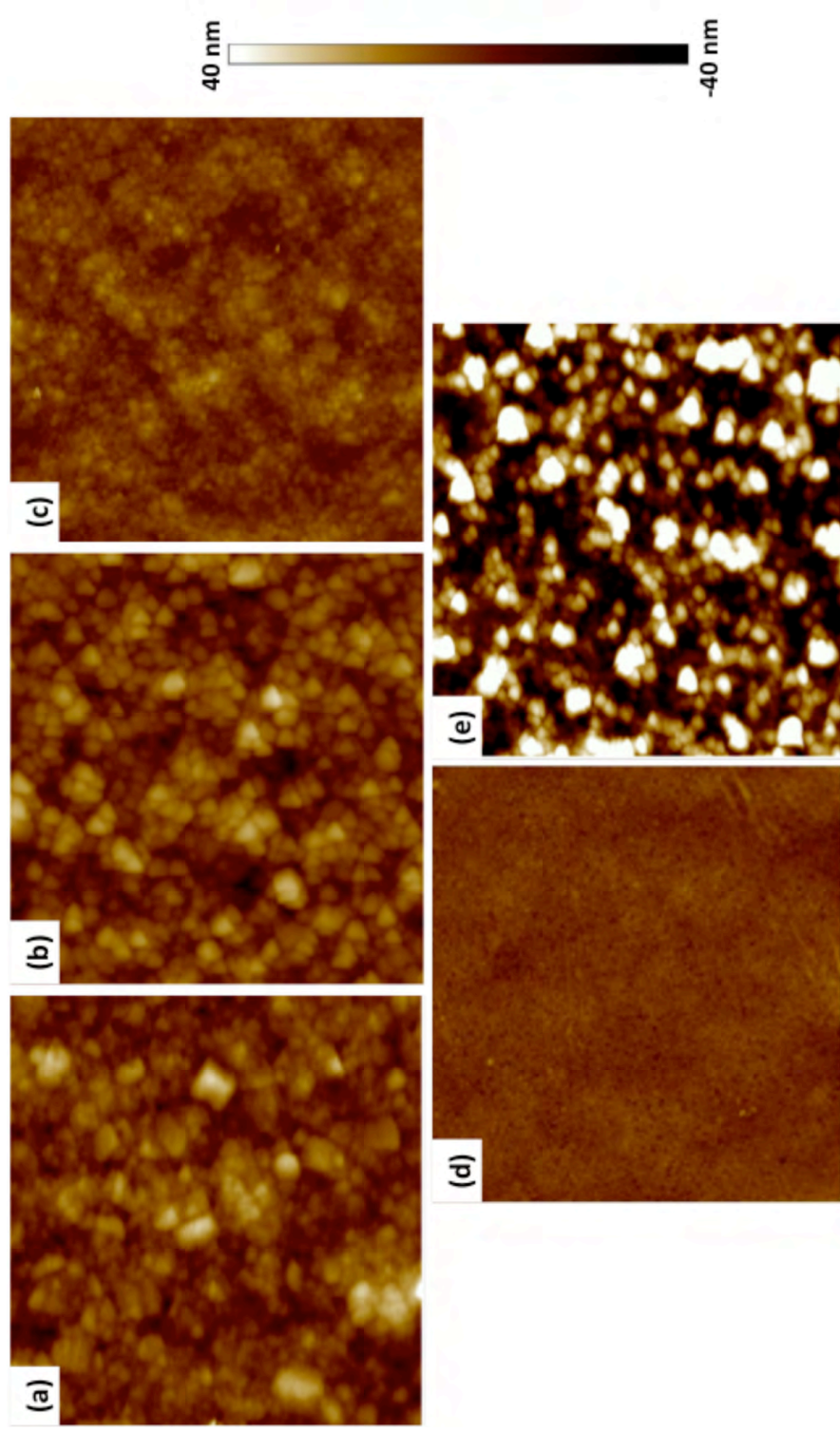


**Figure 7.11:** AFM images of  $\text{WO}_3$  thin films of similar thicknesses  $\sim 400$  nm deposited from (a) pure PTA of  $0.20 \text{ mol L}^{-1}$  tungsten concentration and PTA containing oxalic acid of concentrations (b)  $0.01 \text{ mol L}^{-1}$ , (c)  $0.03 \text{ mol L}^{-1}$ , (d)  $0.05 \text{ mol L}^{-1}$ , and (e)  $0.10 \text{ mol L}^{-1}$  and annealed at  $450^\circ\text{C}$  for 2 h.



Bruker NanoScope Analysis v1.4 software was used to analyse the AFM images of films A-E for information on the root-mean-square (RMS) surface roughness and the surface area ratio (3D surface area/2D projected surface area)[139, 220]. The results were plotted as a function of the grain size, as illustrated in Figure 7.12. Interestingly, the data for both the surface area ratios and the RMS surface roughness were bimodal. An abrupt increase in the specific surface area with decreasing grain size was observed at the transition from small agglomerates to particles, owing to the island-like microstructure in Film E, as explained subsequently. A small grain is an advantage in terms of the specific surface area for photoelectrochemical applications, which depend on, *inter alia*, the number of reaction sites for water photolysis [5].

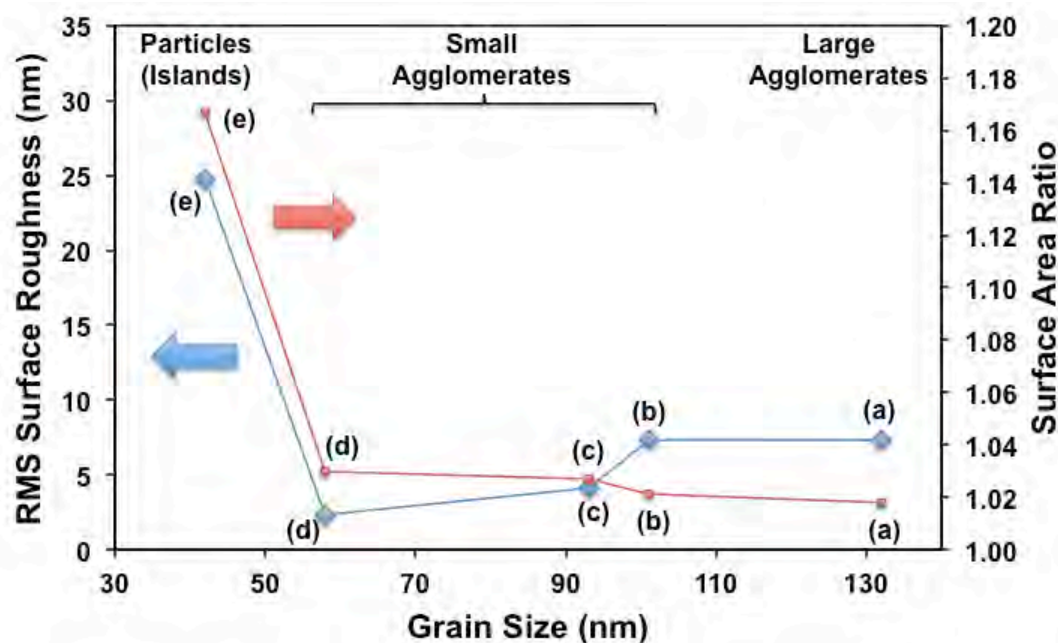


**Figure 7.12:** RMS surface roughnesses ( $\blacklozenge$ ) and surface area ratios ( $\blacksquare$ ) as a function of grain size of  $\text{WO}_3$  thin films of similar thicknesses  $\sim 400$  nm deposited from (a) pure PTA of  $0.20 \text{ mol L}^{-1}$  tungsten concentration and PTA containing oxalic acid of concentrations (b)  $0.01 \text{ mol L}^{-1}$ , (c)  $0.03 \text{ mol L}^{-1}$ , (d)  $0.05 \text{ mol L}^{-1}$ , and (e)  $0.10 \text{ mol L}^{-1}$  and annealed at  $450^\circ\text{C}$  for 2 h.

At lower oxalic acid concentrations ( $\leq 0.05 \text{ mol L}^{-1}$ ), the RMS surface roughness decreased from  $\sim 7$  nm to  $\sim 2$  nm with decreasing agglomerate size, as expected. In contrast, film E, which was deposited from PTA containing the highest oxalic acid

concentration ( $0.10 \text{ mol L}^{-1}$ ) and consisted of small particles rather than fine agglomerates, gave an unexpectedly high roughness of  $\sim 24.8 \text{ nm}$ . This resulted from the island-like microstructure shown in Figure 7.10 (e), which caused the AFM tip to register the uneven steps and concavities created by the annealing shrinkage. For the agglomerated films A-D, which were deposited from PTA containing  $\leq 0.05 \text{ mol L}^{-1}$  oxalic acid, the trend of the RMS surface roughnesses was consistent with the results from others in which  $\text{WO}_3$  thin films were synthesised by various methods, and coarsened and agglomerated by annealing at  $400^\circ\text{-}950^\circ\text{C}$ [60, 77, 96, 134, 139].

### 7.2.2.3 Mineralogy

Figure 7.13 shows the raw XRD results of the films deposited from pure PTA and PTA containing  $0.01\text{-}0.10 \text{ mol L}^{-1}$  oxalic acid, with major peaks at  $23.3^\circ$ ,  $23.7^\circ$ , and  $24.4^\circ 2\theta$ , which corresponded to the (002), (020), and (200) planes of monoclinic  $\text{WO}_3$ [97], respectively. The contributions of the FTO (positions, intensities, and full-width-half-maxima) were approximately equivalent for all films, so direct comparison of  $\text{WO}_3$  films of variable thicknesses was facilitated. Compared to film A, films B-E showed weaker and broader peaks with increasing oxalic acid concentration. These data were consistent with the SEM images in Figure 7.10 and the data in Table 7.2. That is, true porosity controlled the peak intensities since it decreased the solid material area scanned by the X-ray beam (the grain size of  $<0.5 \mu\text{m}$  is much smaller than the beam diameter of  $6.4\text{-}24 \text{ mm}$ ). The areas under the three main peaks scaled in inverse proportion to the true porosities, as shown in Table 7.2.

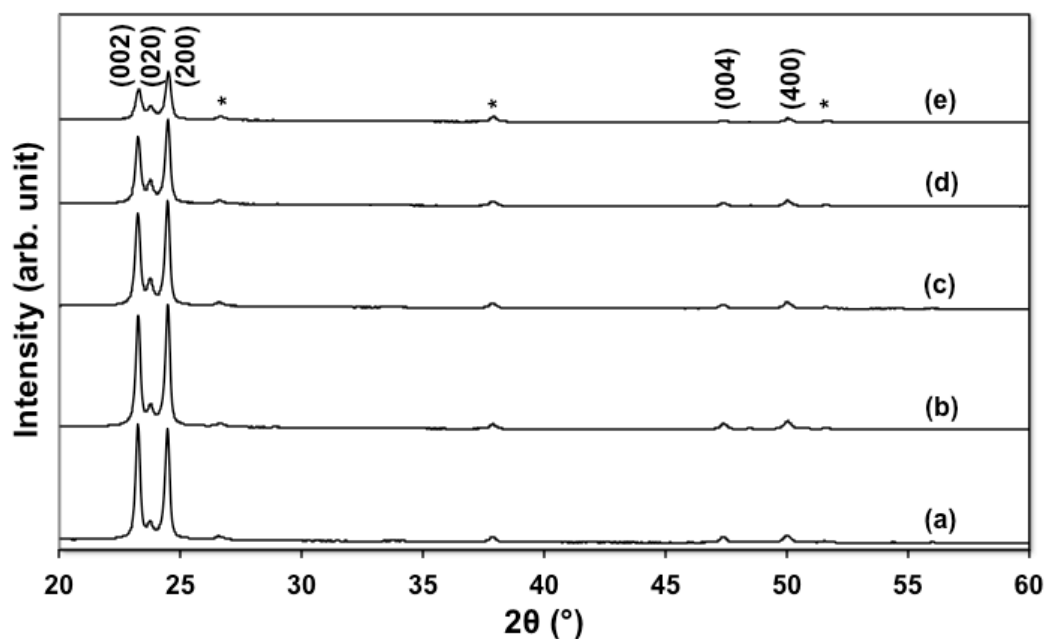


**Figure 7.13:** XRD spectra of monoclinic  $\text{WO}_3$  thin films of similar thicknesses  $\sim 400$  nm deposited from (a) pure PTA of  $0.20 \text{ mol L}^{-1}$  tungsten concentration and PTA containing oxalic acid of concentrations (b)  $0.01 \text{ mol L}^{-1}$ , (c)  $0.03 \text{ mol L}^{-1}$ , (d)  $0.05 \text{ mol L}^{-1}$ , and (e)  $0.10 \text{ mol L}^{-1}$  (\* FTO peaks) and annealed at  $450^\circ\text{C}$  for 2 h.

In contrast, for colloidal  $\text{WO}_3$  particles, Sun *et al.* observed that the particle size, degree of aggregation, and crystallinity decreased with increasing concentration of oxalic acid in the colloid suspension[78]. The first two observations were consistent with the role of the separation effect of the conjugate bases. The effect on crystallinity probably was not comparable since Sun *et al.* did not mention annealing of their samples[78].

The crystallite (subgrains comprising discrete grains) sizes of  $\text{WO}_3$ , as shown in Table 7.2, were estimated using the Debye-Scherrer equation by averaging those of the three major XRD reflections (002), (020), and (200) [150]. The crystallite sizes were found to decrease from 35 nm to 29 nm with increasing oxalic acid concentration. The grain sizes, suggested in Figure 7.9, showed the same trend where they decreased from 132 nm to 42 nm for the same oxalic acid concentrations. These data showed that the grains consisted of multiple crystallites per grain ( $\sim 3.8$  crystallites/grain) in the absence of oxalic acid and approach unity ( $\sim 1.4$  crystallites/grain) at the highest oxalic acid concentration.

## 7.2.2.4 Optical Properties

Figure 7.14 shows the optical transmittance spectra of the films deposited from pure PTA and PTA containing 0.01-0.10 mol L<sup>-1</sup> oxalic acid. In general, films A-D, which were deposited from PTA containing  $\leq 0.05$  mol L<sup>-1</sup> oxalic acid, absorbed light in the near-UV region ( $< 350$  nm). Their optical absorption edges fell in the wavelength range of 350-450 nm. Relatively high transmittances ( $\sim 60$ -80%) in the wavelength range  $> 450$  nm were observed, and these were consistent for all of the films except for film E, which showed an indistinct optical absorption edge and very low transmittance owing to the scattering losses from its having the highest RMS surface roughness and porosity resulting from the channels between the islands, uneven steps, and concavities.

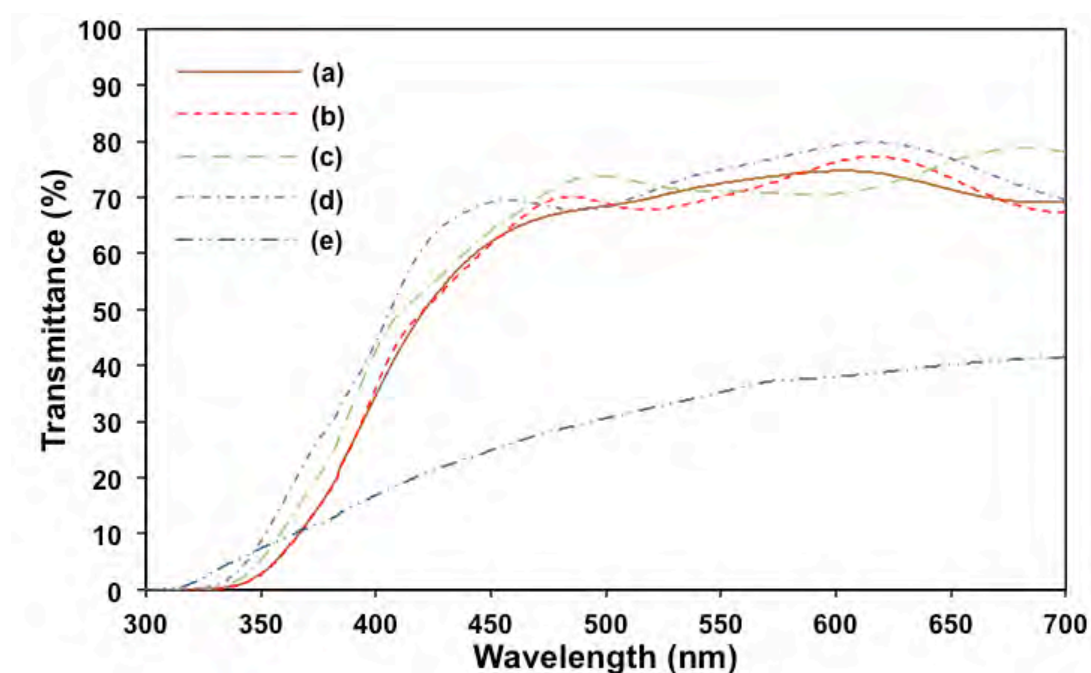


**Figure 7.14:** Transmittance spectra of WO<sub>3</sub> thin films of similar thicknesses  $\sim 400$  nm deposited from (a) pure PTA of 0.20 mol L<sup>-1</sup> tungsten concentration and PTA containing oxalic acid of concentrations (b) 0.01 mol L<sup>-1</sup>, (c) 0.03 mol L<sup>-1</sup>, (d) 0.05 mol L<sup>-1</sup>, and (e) 0.10 mol L<sup>-1</sup> and annealed at 450°C for 2 h.

Blue-shifts of  $< 20$  nm in the optical absorption edge, relative to film A, were observed in films B-D. The shifts followed the alphabetical order of the films, where film D showed the largest shift. This suggested that the optical band gaps of the films were

dependent on the agglomerate/particle sizes. Tauc plots were used to obtain the optical indirect band gaps of the films and the results are shown in Table 7.2 [160]. The band gaps of the films varied in the range 2.90-3.30 eV (wavelength range 376-428 nm). These values were significantly higher than the expected (theoretical) value of 2.60 eV for pure  $\text{WO}_3$  [221]. The principal reason for this was that the band gaps of thin films are dependent on their mineralogical and morphological characteristics, which in turn depend on the synthesis techniques employed. For electrodeposited  $\text{WO}_3$  films of thicknesses in the range ~250-1400 nm, the reported band gap values were 2.60-3.30 eV, with lower band gaps being measured for thicker films [26, 155, 222]. Similar trends between the band gap and film thickness also have been reported for  $\text{WO}_3$  films synthesised using other techniques [223-225]. Films with band gaps close to the theoretical value have been reported to have typical thicknesses of several microns [25, 66, 67]. The main reason for these variations lies in the effect of residual stress on the thin films owing to thermal expansion mismatch between film and substrate as well as grain impingement in the film. While these residual stresses give rise to structural imperfections and defects, which are known to affect the band gap [115, 155, 163, 226-228], these stresses decrease as the distance from the substrate to film surface increases in thicker film and thus lowering the band gap. More generally, the relevant effects, including macrostructural and microstructural, on the band gap were as follows:

*Bulk Chemistry:* All of the films had the same bulk composition, so this effect should not be relevant.

*Defect Chemistry:* It is known that dopants affect the optical band gaps of materials [87, 108, 229]. Although no dopants were added, it was possible that contamination from Sn, F, Na, Ca, and/or Si might have occurred owing to diffusion from the FTO substrates during annealing. However, since all of the films were subjected to the same annealing conditions, this effect should be minimal or absent.

*Mineralogy:* There are five known atmospheric-pressure polymorphs of  $\text{WO}_3$  [95], of which two are stable at room temperature (15°-25°C) and one of which could be quenched from the annealing temperature (450°C). However, the X-ray diffraction data

showed that only the monoclinic polymorph was present, so this effect should not be relevant.

*Macrostructure:* The variations in structure, composition, and grain-impingement-induced compressive stress as a function of film thickness are known to affect the band gaps of materials [115, 155, 163, 226-228]. However, since the film thicknesses were similar ( $400 \pm 20$  nm), this effect should not be significant.

*Microstructure:* The films consisted of interconnected networks of grains in which the grain boundary areas (within the bulk and at the exposed surface) increased with the decreasing grain size and the increasing porosity. The increase in these grain boundary areas, which represent terminating structural and bonding regions and discontinuities in the lattice order, is known to increase the band gaps of materials [43, 73, 79, 138]. Table 7.2 shows that the true porosity and the grain size varied with the amount of oxalic acid present in PTA. The associated variation in grain boundary areas would be expected to be relevant since these affected the proportion of defects.

In light of the preceding brief survey, it was probable that the principal factor affecting the band gap was the density of the defects associated with grain boundary areas.

#### 7.2.2.5 Photoelectrochemical Properties

The linear potentiodynamic photocurrent density measurements of the films deposited from pure PTA and PTA containing 0.01-0.10 mol L<sup>-1</sup> oxalic acid are shown in Figure 7.15. The measurements were taken under the illumination from a 50 W tungsten-halogen lamp (light source-to-sample distances of ~25 cm; intensity of ~100 mW m<sup>-2</sup>). Effective photocurrents were measured as the difference between photocurrents (with illumination) and dark currents (without illumination). Gaussian-shaped peaks, which correspond to electrochromic reactions of WO<sub>3</sub> films, were barely visible in the potentiodynamic scans in the present work owing to (i) the starting potential of -0.2 V *versus* Ag/AgCl, which was close to the peak potentials that occurred in the typical range of ~-0.2 V to -0.1 V *versus* Ag/AgCl [220, 230-232] and (ii) the relatively low

scan rate of  $5 \text{ mV s}^{-1}$ , which was much lower than the typical rate of  $>50 \text{ mV s}^{-1}$  reported in the literature [233-236].

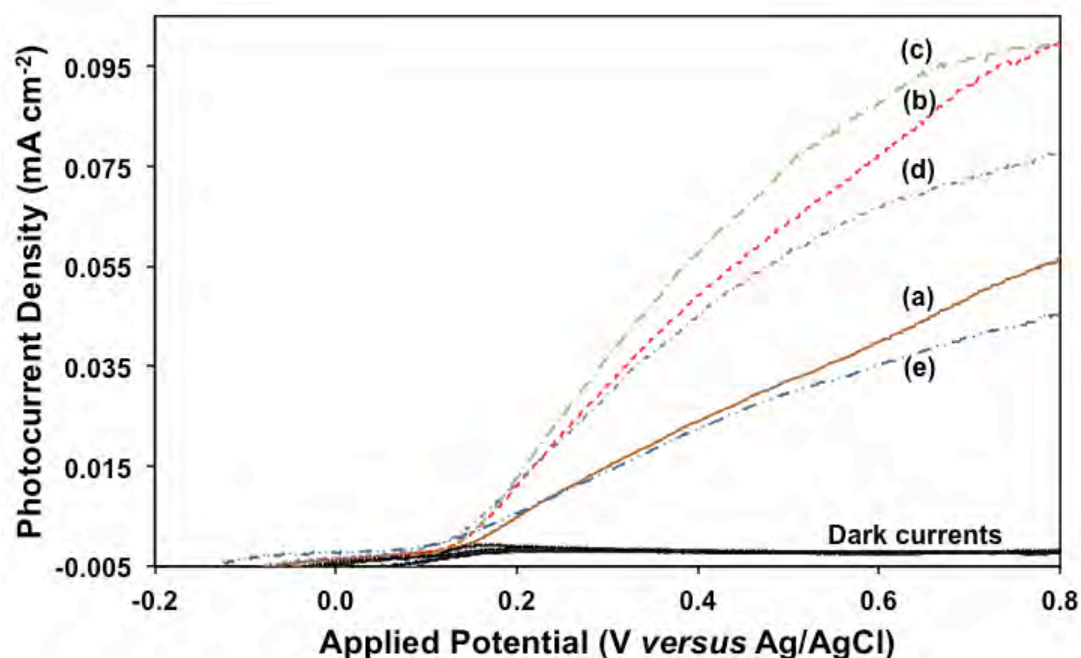


**Figure 7.15:** Linear potentiodynamic photocurrent densities of  $\text{WO}_3$  thin films deposited from (a) pure PTA of  $0.20 \text{ mol L}^{-1}$  tungsten concentration and PTA containing oxalic acid of concentrations (b)  $0.01 \text{ mol L}^{-1}$ , (c)  $0.03 \text{ mol L}^{-1}$ , (d)  $0.05 \text{ mol L}^{-1}$ , and (e)  $0.10 \text{ mol L}^{-1}$  and annealed at  $450^\circ\text{C}$  for 2 h. Illumination was from a 50 W tungsten-halogen lamp (light source-to-sample distances of  $\sim 25 \text{ cm}$ ; intensity of  $\sim 100 \text{ mW m}^{-2}$ ). Dark currents (measured without illumination) also are shown.

There were various microstructural (and structural) variables that influenced the photoelectrochemical results of the films, as summarised in Table 7.3. Decreasing grain sizes are beneficial in (i) providing large specific surface areas and associated number of reaction sites (oxygen vacancies) [237] for water photolysis and (ii) improving hole transport since the holes photogenerated in the outermost grains travel a shorter distance to the photoanode/electrolyte interface and oxidise water before they can recombine with the photogenerated electrons [5]. Vacancy filling by oxidation may degrade the photoelectrochemical activity owing to the reduced number of reaction sites [238]. The hole transport is moderated by the hopping distance, where long distances require more energy than short ones [239]. However, the large specific surface area also is associated

with a high fraction of dangling bonds owing to the terminations of the crystal continuity[240]. These dangling bonds introduce deep localised levels in the energy band gap, which can trap photogenerated excitons, thereby increasing their probabilities of surface recombination [217, 241]. These undesirable dangling bonds may be removed by surface passivation [217]. For photogenerated electrons, the grain boundaries also act as weak links that hinder electron transport to the substrate [242]. It is well known that high-angle grain boundaries are associated with greater lattice mismatch and higher interfacial energies than low-angle grain boundaries [157]. Consequently, the greater the grain boundary angle, the weaker the link for electron transport [218]. The present work showed that these variables, which acted concurrently, and their consequent influences on the photoelectrochemical performance of the films can be manipulated through grain size variation. The explanation of these data was as follows:

*Pure PTA:* Film A had the largest agglomerates (~132 nm average; ~500 nm maximum) and hence a relatively long hole diffusion distance and a limited specific surface area for both reaction and recombination sites. Across the film thickness of ~400 nm, the number of agglomerates was ~3, so requiring the electrons to cross this relatively low number of transport barriers. This facilitated the electron transport.

*PTA containing 0.01-0.05 mol L<sup>-1</sup> oxalic acid:* Films B-D had small agglomerates (~58-101 nm), therefore the hole diffusion distances were decreased. These small agglomerates also were associated with large specific surface areas for reaction sites. Nonetheless these specific surface areas also were associated with a relatively high fraction of dangling bonds as recombination sites. The number of agglomerates in the cross-section was ~4-7, so the electrons must cross a greater number of transport barriers, which hindered the electron transport.

*PTA containing 0.10 mol L<sup>-1</sup> oxalic acid:* Film E had individual particles of ~42 nm. The large specific surface area was associated with a high fraction of dangling bonds. This disadvantage was dominant over the advantages of a large number of reaction sites and short hole diffusion distance. The intersection density of ~10 grains required the

electrons to cross a great number of transport barriers, thereby minimising the electron transport.

**Table 7.3:** Effect of decreasing grain size on photoelectrochemical (PEC) performance factors and associated photocurrent densities of WO<sub>3</sub> thin films.

Microstructural variable	PEC performance factor	Effect of decreasing grain size on	
		PEC performance factor	Photocurrent density
Specific surface area	Number of reaction sites	Increase	Increase
	Number of recombination sites	Increase	Decrease
Grain radius	Hole transport	Increase	Increase
Grain boundary distribution density	Number of electron transport barriers	Increase	Decrease

The concept, which condenses the main principles in terms of the size effect and the corresponding microstructural features that result in a maximum in the photocurrents, is summarised schematically in Figure 7.16. Since the nuclei that precede recrystallisation are amorphous, they show negligible photocurrents [43] and, since single crystals have minimal specific surface area, they show minimal photocurrents[65]. It has been reported that WO<sub>3</sub> in quantum dot form (<1.8 nm diameter) showed enlarged band gap of >2.9 eV, which blue-shifted its optical absorption edge to <428 nm [243]. This suggested that WO<sub>3</sub> in quantum dot form was unlikely to improve photoelectrochemical performance under solar illumination because it was photosensitive only in the UV light region. Therefore, it was clear that, in microstructures that ranged from individual particles to small agglomerates to large agglomerates, there must be a maximum in the photocurrent density. Hence, the observed maximum at a small agglomerate size of ~90 nm corresponded to a balance between (i) the surface reaction and recombination sites and (ii) the hole and electron transports.

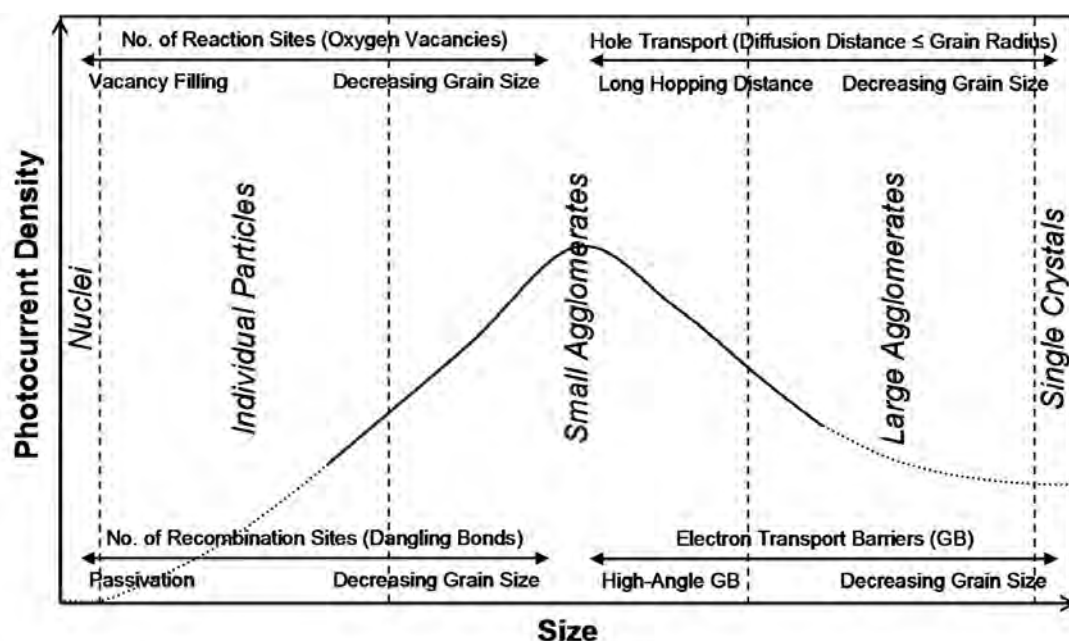


**Figure 7.16:** Schematic of trend of size effect on photocurrent density, where arrows indicate effect of fundamental microstructural feature (below arrows) on the photoelectrochemical performance factor (above arrows) ( $\rightarrow$  indicates increase in performance factor;  $\leftarrow$  indicates decrease in performance factor). Solid line (—) indicates experimental data; dotted line ( $\cdots$ ) indicates extrapolation; GB = grain boundaries.

Similar bell-shaped relationships also have been observed by Li *et al.* and Hong *et al.* [60, 73]. Both observed optimal photoelectrochemical performance in  $\text{WO}_3$  films consisted of what appeared to be small agglomerates of sizes  $\sim 60$  nm. The difference in the optimal size value could be the result of the different processing techniques employed in the synthesis of  $\text{WO}_3$  films. These studies illustrated that the microstructures of these materials must be tuned so that the combination of the preceding four main photoelectrochemical performance factors can be optimised for maximal photoelectrochemical performance.

### 7.3 Key Results

- $\text{WO}_3$  thin films with controlled grain sizes were electrodeposited from PTA containing different carboxylic acids (formic, oxalic, and citric). The

electrodeposition of the films from PTA containing oxalic acid of different concentrations also was investigated.

- The deposited  $\text{WO}_3$  film thickness was dependent on the availability of hydronium ions (for hydrogen bonding with PTA ions) and molecular drag in the electrolytes, both of which were controlled through the use of carboxylic acids of different concentrations, degrees of dissociation, molecular weights, and associated sizes of the conjugate bases.
- The films consisted of agglomerates/particles (42–132 nm), the sizes of which decreased and true porosities (<6%) of which increased with the amounts and sizes of the conjugate bases of carboxylic acid. These observations were considered to result from the separation of the PTA ions according to the amounts and sizes of the conjugate bases, the effects of which consequently changed the mechanisms of nucleation and grain growth.
- A nonlinear relationship between the grain sizes and the photoelectrochemical performances of the films was obtained where a maximum in the photocurrent density was observed for the film consisting of small agglomerates of ~93 nm (deposited from PTA containing  $0.03 \text{ mol L}^{-1}$  oxalic acid). This was considered to result from the positive balance of (i) surface reaction and recombination sites and (ii) the hole and electron transports in the film.

# CHAPTER 8

## Conclusions

### 8.1 Conclusions

WO<sub>3</sub> thin-film photoanodes were electrodeposited from PTA solutions onto FTO substrates and annealed at  $\leq 500^\circ\text{C}$  for times up to 18 h. The effects of processing parameters, including deposition potentials and times, compositions of the PTA solutions, and post-deposition annealing conditions on the physical, mineralogical, optical, and photoelectrochemical properties of the films were investigated as follows:

- **Deposition rate**

The deposition rates of the films were dependent on the deposition potentials, the tungsten concentrations of PTA solutions, and the amounts and types of the carboxylic acids added to the PTA solutions. Low deposition rates required long deposition times to produce films of thickness suitable for photoelectrochemical application. While high deposition rates involved short deposition times, the former were associated with the risk of producing thick films that cracked as a result of drying stresses. Modification of the deposition rate and time ( $\leq 3$  h) resulted in films of various thicknesses ranging from 168-1400 nm.

*Deposition potential*

Higher deposition rates were obtained by increasing the deposition potential ( $-0.3$  to  $-0.6$  V), which determined the flux of PTA ions toward the FTO substrate. The linear sweep voltammetry data suggested that deposition potentials in the range of approximately  $-0.30$  V to  $-0.60$  V were optimal for film growth. The film deposited at a potential of  $-0.30$  V appeared to be of good quality. In contrast, the deposition potential of  $-0.60$  V appeared to represent a transition between stable and unstable film growth as well as a transition between films undamaged and damaged by drying stresses.

*Tungsten concentration of PTA solution*

Higher deposition rates were obtained by increasing the tungsten concentration of PTA solution ( $0.05\text{-}0.20\text{ mol L}^{-1}$ ), which determined the flux of PTA ions toward the FTO substrate. The growth kinetics of the films depended largely on grain impingement/percolation and film thickness during grain growth, which themselves were dependent largely on the tungsten concentration.

#### *Amount and type of carboxylic acid*

The deposition rates were dependent on the types (oxalic, formic, and citric acids) and amounts ( $0.01\text{-}0.10\text{ mol L}^{-1}$ ) of carboxylic acid added to the PTA solution as dispersing agent. The hydronium ions and conjugate bases formed upon dissolution of carboxylic acids participated in solute dispersion and separation, which altered the mechanisms of nucleation and grain growth. The highest deposition rate was obtained in the PTA solution containing oxalic acid owing to (i) its highest degree of dissociation, which generated the highest amount of hydronium ions, which provided the driving force for the PTA ions, by creating net positively charged PTA ions through hydrogen bonding, to migrate under cathodically biased condition for deposition, and (ii) the intermediate sizes of the conjugate bases, which did not cause molecular drag in the PTA solutions.

- **Grain (agglomerate/particle) size**

The grain sizes of the films differed slightly ( $77\text{-}122\text{ nm}$ ) with the tungsten concentrations of PTA solutions and significantly ( $42\text{-}132\text{ nm}$ ) with the sizes of the conjugate bases of carboxylic acids added to the PTA solutions. The films consisting of small grains showed large surface-area-to-volume ratios, high true porosities, and smooth surfaces.

#### *Tungsten concentration of PTA solution*

Large grain sizes resulted from high tungsten concentrations because the grain growth occurred rapidly owing to the great number of PTA ions, which had to travel only a short distance from the solution to the solid/liquid interface for deposition.

*Amount and type of carboxylic acid*

The grain sizes of the films decreased with increasing concentrations and sizes of the conjugate bases of carboxylic acids. The use of carboxylic acids with different concentrations and sizes of conjugate bases contributed to the separation of the PTA ions, distribution density of the  $\text{WO}_3$  nuclei, their proximity, the corresponding diffusion distances, the tendency to undergo grain growth during annealing, and hence their susceptibility to form agglomerates.

- **Crystallinity**

The as-deposited films were amorphous, which transformed to the polycrystalline monoclinic phase upon annealing  $\geq 275^\circ\text{C}$ . The crystallinities of the films, measured using X-ray diffraction, increased with (i) increasing film thickness owing to reduction in film/substrate physical mismatch stress and (ii) increasing grain size owing to the decreasing surface defect density (terminating structural and bonding regions and discontinuities in the lattice order) associated with the grain boundary areas within the bulk and at the exposed surfaces of the films.

- **Crystallographic preferred orientation**

The preferred {002} orientations parallel to the substrate of the films were controlled by the nucleation density and the thermally induced recrystallisation kinetics, where the former and the latter were manipulated respectively by the tungsten concentrations of PTA solutions and the annealing conditions. The importance of the nanostructures of the films was emphasised in that both the annealing temperature and time that generated specific crystallographic predominance depended significantly on the tungsten concentration of the PTA solution, which in turn determined the distribution density of the tungsten oxide nuclei and the proximity of the resultant grains. These grains underwent growth of the thermodynamically stable (200) plane such that, under the conditions of maximal annealing temperature and/or time, a preferred (200) orientation resulted. Hence, the tungsten concentration of the PTA solution and the annealing temperature and time can be controlled to yield nanostructures of specific proportions of preferred crystallographic orientations in electrodeposited  $\text{WO}_3$  thin films.

- **Optical absorption and indirect band gap**

Transmittance of the films (~40-80%) decreased with (i) increasing film thickness owing to the increasing solid volume for optical absorption, and (ii) decreasing grain size owing to the larger density of delaminations between the agglomerates and the greater amount of true porosities, which scattered light maximally.

Reduced band gaps (2.5-3.3 eV) were obtained by increasing the thicknesses and grain sizes of the films, both of which were associated with improved film crystallinity. The band gap-film thickness relationship was nonlinear owing to the differential contributions from the surface and bulk band gap components. The band gaps of the films also were dependent on the concurrent factors of preferred {002} orientation and oxygen vacancy concentration, where the linear correlation between these three variables can be used as a diagnostic tool to engineer the electronic band structure of the films for applications requiring photosensitivities in different regions of the solar spectrum.

- **Photoelectrochemical performance**

Enhanced photocurrent densities were measured for the films that exhibited the following properties:

*Optical indirect band gap and light absorption*

The low band gap and improved light absorption of the films enhanced the photogeneration of excitons. The nonlinear band gap-photoelectrochemical efficiency relationship was due to the relative contributions of the surface and bulk band gap components, where the surface component was dominant at low film thickness ( $\leq 500$  nm) and the bulk component was dominant at higher film thickness.

*Grain size*

Small grains were beneficial for their (i) large specific surface areas and the associated number of reaction sites (oxygen vacancies) for water photolysis, and (ii) short distances for the holes photogenerated in the outermost grains to diffuse to the

photoanode/electrolyte interface for water oxidation before recombining with the photogenerated electrons. However, small grains were associated with disadvantages of (i) high fraction of dangling bonds owing to the terminations of crystal continuity, which acted as traps for photogenerated charge carriers, and (ii) large grain boundary areas, which acted as weak links that hindered the transport of the photogenerated electrons to the back contact (substrate). The nonlinear grain size-photoelectrochemical performance relationship of the films suggested that the optimal photoelectrochemical performance was a result of the tuning of (i) surface reaction and recombination sites, and (ii) the hole and electron transports. The positive balance of the preceding four factors resulted in a maximal photocurrent density at an agglomerate size ~93 nm. Although it usually is assumed that nanomaterials with large specific surface areas are beneficial owing to the associated number of reaction sites, the present work shows that optimisation of the concurrent factors that affect the photoelectrochemical properties requires a more nuanced approach to processing. That is, small agglomerates appear to offer a means of controlling the effective grain boundary area, which needs to be tuned between extremes.

#### *Crystallographic preferred orientation*

Among the films with three types of preferred orientations parallel to the substrate, *viz.*, (002), both (002) and (200), and (200), the highest photocurrent density measured under the illumination of simulated solar light was obtained in the film with (002) preferred orientation, which exhibited a relatively small optical band gap, low valence band maximum, and low oxygen vacancy concentration. These conditions favoured the photogeneration of charge carriers with photogenerated holes of strong oxidising power and the suppression of charge carrier recombination owing to the minimal bulk oxygen vacancy concentration, which trapped charge carriers. In contrast, the highest efficiency in the photodegradation of methylene blue under UV illumination (254 nm) was obtained in the film with (200) preferred orientation, which showed the highest concentration of oxygen vacancies, which acted as surface reaction sites. The capacity to control the crystallographic orientations of WO<sub>3</sub> thin films without the use of expensive substrates for epitaxial growth or growth-directing agents (which are more applicable to powder synthesis, not films) provides a feasible technique for tuning the nanostructures for specific performance parameters. Further, the data for the correlation

between the crystallographic orientation, oxygen vacancy concentration, and optical indirect band gap can be used as a diagnostic tool that is applicable to the fabrication of films suitable for uses requiring photosensitivities in different regions of the solar spectrum.

## 8.2 Recommendations For Future Work

The WO<sub>3</sub> thin films prepared by electrodeposition in the present work had demonstrated considerable potential as cost-effective photoanodes applicable in photoelectrochemical water splitting. There are various approaches, which can be taken as future work, to improve the photoelectrochemical efficiencies of the films. These approaches include:

### *Crystallographic effect*

The present work had shown that the tungsten concentration of peroxotungstic acid solutions and the annealing conditions influenced the preferred {002} planes of the films. The substrate used for the film deposition was fluorine-doped tin oxide. However, this study can be further expanded by depositing the films on different electrically conducting substrates including metal plates and transparent-conducting oxides. This would yield useful information on the influence of substrates of different electrical and crystallographic properties on the resultant preferred crystallographic orientation of the films. Furthermore, it is worthwhile to run density-functional-theory calculations on {002} slabs of monoclinic WO<sub>3</sub> in order to establish understanding of the mechanism of crystal growth in preferred <002> orientations, the formation of oxygen vacancy on these slabs, and the roles of orientations in photoelectrochemical application at the atomic-scale.

### *Heterojunction metal oxide photoelectrodes*

The photoelectrochemical performance of a photoelectrode is dependent on its excellence in solar absorptivity, photogenerated charge separation, and charge transport properties. The preceding properties of a photoelectrode consisting of single material are limited by the intrinsic properties of that material. However, these properties can be enhanced by fabricating heterojunction metal oxide photoelectrodes. The heterojunction films, which consist of two or more metal oxides, exhibit combined

properties of the multiple oxides that are not available in a single oxide material [244]. The oxides (*e.g.*  $\text{WO}_3$ ,  $\text{Fe}_2\text{O}_3$ ,  $\text{ZnO}$  *etc.*) should be chosen such that they are stable against corrosion and photocorrosion, photosensitive to different parts of the solar spectrum, and possess the appropriate conduction and valence band edge positions that aid in the separation of photogenerated excitons.

---

## REFERENCES

- [1] C.A. Grimes, O.K. Varghese, and S. Ranjan, *Light, Water, Hydrogen. The Solar Generation of Hydrogen by Water Photoelectrolysis*. Springer Science+Business Media, New York, 2008.
- [2] T. Wallner, "Correlation between Speciated Hydrocarbon Emissions and Flame Ionization Detector Response for Gasoline/Alcohol Blends", *J. Eng. Gas Turbines Power*, **133**, 082801 (2011).
- [3] T. Bak, J. Nowotny, M. Rekas, and C.C. Sorrell, "Photo-Electrochemical Hydrogen Generation from Water Using Solar Energy. Materials-Related Aspects", *Int. J. Hydrogen Energy*, **27**, 991–1022 (2002).
- [4] E.L. Miller, "Solar Hydrogen Production by Photoelectrochemical Water Splitting: The Promise and Challenge", pp. 3—36 in *On Solar Hydrogen and Nanotechnology*. Edited by L. Vayssieres. John Wiley and Sons, Singapore, 2009.
- [5] J.J. Kelly, and D. Vanmaekelbergh, "Porous-Etched Semiconductors: Formation and Characterization", pp. 103–139 in *Electrochemistry of Nanomaterials*. Edited by G. Hodes. Wiley-VCH, Weinheim, 2001.
- [6] A. Heller, and R.G. Vadimsky, "Efficient Solar to Chemical Conversion: 12% Efficient Photoassisted Electrolysis in the [*P*-Type Inp(Ru)]/HCl-KCl/Pt(Rh) Cell", *Phys. Rev. Lett.*, **46**, 1153—1156 (1981).
- [7] J.W. Sun, C. Liu, and P.D. Yang, "Surfactant-Free, Large-Scale, Solution-Liquid-Solid Growth of Gallium Phosphide Nanowires and Their Use for Visible-Light-Driven Hydrogen Production from Water Reduction", *J. Am. Chem. Soc.*, **133**, 19306—19309 (2011).
- [8] P.A. Chate, S.S. Patil, J.S. Patil, D.J. Sathe, and P.P. Hankare, "Nanocrystalline Cdse: Structural and Photoelectrochemical Characterization", *Electron. Mater. Lett.*, **8**, 553–558 (2012).
- [9] Y.P. Guo, and X.N. Deng, "Electrodeposition of Cdte Thin-Films and Their Photoelectrochemical Behavior", *Sol. Energy Mater. Sol. Cells*, **29**, 115—122 (1993).
- [10] H. Gerischer, "On the Stability of Semiconductor Electrodes against Photodecomposition", *J. Electroanal. Chem.*, **82**, 133–143 (1977).
- [11] A. Fujishima, and K. Honda, "Electrochemical Photolysis of Water at a Semiconductor Electrode", *Nature*, **238**, 37–38 (1972).

- [12] G. Liu, L.Z. Wang, H.G. Yang, H.M. Cheng, and G.Q. Lu, "Titania-Based Photocatalysts-Crystal Growth, Doping and Heterostructuring", *J. Mater. Chem.*, **20**, 831—843 (2010).
- [13] R.M. Liang, Y.M. Chang, P.W. Wu, and P. Lin, "Effect of Annealing on the Electrodeposited Cu<sub>2</sub>O Films for Photoelectrochemical Hydrogen Generation", *Thin Solid Films*, **518**, 7191—7195 (2010).
- [14] S. Ostachaviciute, J. Baltrusaitis, and E. Valatka, "Photoactive WO<sub>3</sub> and Se-WO<sub>3</sub> Thin Films for Photoelectrochemical Oxidation of Organic Compounds", *J. Appl. Electrochem.*, **40**, 1337—1347 (2010).
- [15] Y.F. Wei, L. Ke, E.S.P. Leong, H. Liu, L.L. Liew, J.H. Teng, H.J. Du, and X.W. Sun, "Enhanced Photoelectrochemical Performance of Bridged ZnO Nanorod Arrays Grown on V-Grooved Structure", *Nanotechnology*, **23**, 365704 (2012).
- [16] C.M. McShane, and K.S. Choi, "Photocurrent Enhancement of N-Type Cu<sub>2</sub>O Electrodes Achieved by Controlling Dendritic Branching Growth", *J. Am. Chem. Soc.*, **131**, 2561—2569 (2009).
- [17] F. Wang, Y. Liu, Z. Ma, H.T. Li, Z.H. Kang, and M.R. Shen, "Enhanced Photoelectrochemical Response in SrTiO<sub>3</sub> Films Decorated with Carbon Quantum Dots", *New J. Chem.*, **37**, 290—294 (2013).
- [18] S. Upadhyay, J. Shrivastava, A. Solanki, S. Choudhary, V. Sharma, P. Kumar, N. Singh, V.R. Satsangi, R. Shrivastav, U.V. Waghmare, and S. Dass, "Enhanced Photoelectrochemical Response of BaTiO<sub>3</sub> with Fe Doping: Experiments and First-Principles Analysis", *J. Phys. Chem. C*, **115**, 24373—24380 (2011).
- [19] D.A.H. Hanaor, G. Triani, and C.C. Sorrell, "Morphology and Photocatalytic Activity of Highly Oriented Mixed Phase Titanium Dioxide Thin Films", *Surf. Coat. Technol.*, **205**, 3658—3664 (2011).
- [20] K. Sivula, F. Le Formal, and M. Gratzel, "Solar Water Splitting: Progress Using Hematite (Alpha-Fe<sub>2</sub>O<sub>3</sub>) Photoelectrodes", *ChemSusChem*, **4**, 432—449 (2011).
- [21] J.H. Kennedy, and K.W. Frese, "Photooxidation of Water at Alpha-Fe<sub>2</sub>O<sub>3</sub> Electrodes", *J. Electrochem. Soc.*, **124**, C130-C130 (1977).
- [22] S. Somasundaram, C.R.N. Chenthamarakshan, N.R. de Tacconi, and K. Rajeshwar, "Photocatalytic Production of Hydrogen from Electrodeposited P-Cu<sub>2</sub>O Film and Sacrificial Electron Donors", *Int. J. Hydrogen Energy*, **32**, 4661—4669 (2007).

- [23] H.R. Schoppel, and Gerische.H, "Cathodic Reduction of Cu-I Oxide Electrodes as Example for Reduuction Mechanism of Semiconductor Crystal", *Ber. Bunsen Ges. Phys. Chem.*, **75**, 1237—1239 (1971).
- [24] P.P. Gonzalez-Borrero, F. Sato, A.N. Medina, M.L. Baesso, A.C. Bento, G. Baldissera, C. Persson, G.A. Niklasson, C.G. Granqvist, and A.F. da Silva, "Optical Band-Gap Determination of Nanostructured  $\text{WO}_3$  Film", *Appl. Phys. Lett.*, **96**, 061909 (2010).
- [25] C. Ng, C.H. Ye, Y.H. Ng, and R. Amal, "Flower-Shaped Tungsten Oxide with Inorganic Fullerene-Like Structure: Synthesis and Characterization", *Cryst. Growth Des.*, **10**, 3794—3801 (2010).
- [26] D. Monllor-Satoca, L. Borja, A. Rodes, R. Gomez, and P. Salvador, "Photoelectrochemical Behavior of Nanostructured  $\text{WO}_3$  Thin-Film Electrodes: The Oxidation of Formic Acid", *ChemPhysChem*, **7**, 2540—2551 (2006).
- [27] B. Yang, Y.J. Zhang, E. Drabarek, P.R.F. Barnes, and V. Luca, "Enhanced Photoelectrochemical Activity of Sol-Gel Tungsten Trioxide Films through Textural Control", *Chem. Mater.*, **19**, 5664—5672 (2007).
- [28] X.T. Su, F. Xiao, J.L. Lin, J.K. Jian, Y.N. Li, Q.J. Sun, and J.D. Wang, "Hydrothermal Synthesis of Uniform  $\text{WO}_3$  Submicrospheres Using Thiourea as an Assistant Agent", *Mater. Character.*, **61**, 831—834 (2010).
- [29] X. Liu, F. Wang, and Q. Wang, "Nanostructure-Based  $\text{WO}_3$  Photoanodes for Photoelectrochemical Water Splitting", *Phys. Chem. Chem. Phys.*, **14**, 7894—7911 (2012).
- [30] Y. Li, and J.Z. Zhang, "Hydrogen Generation from Photoelectrochemical Water Splitting Based on Nanomaterials", *Laser Photonics Rev.*, **4**, 517—528 (2010).
- [31] M.A. Butler, "Photoelectrolysis and Physical Properties of the Semiconducting Electrode  $\text{WO}_3$ ", *J. Appl. Phys.*, **48**, 1914—1920 (1977).
- [32] R. Solarzka, B.D. Alexander, A. Braun, R. Jurczakowski, G. Fortunato, M. Stiefel, T. Graule, and J. Augustynski, "Tailoring the Morphology of  $\text{WO}_3$  Films with Substitutional Cation Doping: Effect on the Photoelectrochemical Properties", *Electrochim. Acta*, **55**, 7780—7787 (2010).
- [33] E.L. Miller, B. Marsen, B. Cole, and M. Lum, "Low-Temperature Reactively Sputtered Tungsten Oxide Films for Solar-Powered Water Splitting Applications", *Electrochem. Solid-State Lett.*, **9**, G248—G250 (2006).

- [34] G. Leftheriotis, and P. Yianoulis, "Development of Electrodeposited  $W\text{O}_3$  Films with Modified Surface Morphology and Improved Electrochromic Properties", *Solid State Ionics*, **179**, 2192—2197 (2008).
- [35] M. Deepa, A.K. Srivastava, T.K. Saxena, and S.A. Agnihotry, "Annealing Induced Microstructural Evolution of Electrodeposited Electrochromic Tungsten Oxide Films", *Appl. Surf. Sci.*, **252**, 1568—1580 (2005).
- [36] H.M.A. Soliman, A.B. Kashyout, M.S. El Nouby, and A.M. Abosehly, "Preparation and Characterizations of Tungsten Oxide Electrochromic Nanomaterials", *J. Mater. Sci.: Mater. Electron.*, **21**, 1313—1321 (2010).
- [37] M. Deepa, M. Kar, and S.A. Agnihotry, "Electrodeposited Tungsten Oxide Films: Annealing Effects on Structure and Electrochromic Performance", *Thin Solid Films*, **468**, 32—42 (2004).
- [38] M. Deepa, A.K. Srivastava, and S.A. Agnihotry, "Influence of Annealing on Electrochromic Performance of Template Assisted, Electrochemically Grown, Nanostructured Assembly of Tungsten Oxide", *Acta Mater.*, **54**, 4583—4595 (2006).
- [39] B. Yang, H.J. Li, M. Blackford, and V. Luca, "Novel Low Density Mesoporous  $W\text{O}_3$  Films Prepared by Electrodeposition", *Curr. Appl. Phys.*, **6**, 436—439 (2006).
- [40] S.H. Baeck, T. Jaramillo, G.D. Stucky, and E.W. McFarland, "Controlled Electrodeposition of Nanoparticulate Tungsten Oxide", *Nano Lett.*, **2**, 831—834 (2002).
- [41] G. Hodes, D. Cahen, and J. Manassen, "Tungsten Trioxide as a Photoanode for a Photoelectrochemical Cell (Pec)", *Nature*, **260**, 312—313 (1976).
- [42] A.B. Murphy, P.R.F. Barnes, L.K. Randeniya, I.C. Plumb, I.E. Grey, M.D. Horne, and J.A. Glasscock, "Efficiency of Solar Water Splitting Using Semiconductor Electrodes", *Int. J. Hydrogen Energy*, **31**, 1999—2017 (2006).
- [43] F. Di Quarto, A. Dipaola, S. Piazza, and C. Sunseri, "Influence of Thermal-Treatment on the Photoelectrochemical Behavior of  $W\text{O}_3$  Photoanodes Electrochemically Grown", *Sol. Energy Mater.*, **11**, 419—433 (1985).
- [44] A. Watcharenwong, W. Chanmanee, N.R. de Tacconi, C.R. Chenthamarakshan, P. Kajitvichyanukul, and K. Rajeshwar, "Anodic Growth of Nanoporous  $W\text{O}_3$  Films: Morphology, Photoelectrochemical Response and Photocatalytic Activity for Methylene Blue and Hexavalent Chrome Conversion", *J. Electroanal. Chem.*, **612**, 112—120 (2008).

- [45] X.P. Shen, G.X. Wang, and D. Wexler, "Large-Scale Synthesis and Gas Sensing Application of Vertically Aligned and Double-Sided Tungsten Oxide Nanorod Arrays", *Sens. Actuators, B*, **143**, 325—332 (2009).
- [46] Z.F. Deng, Y.C. Gong, Y.P. Luo, and Y. Tian, "WO<sub>3</sub> Nanostructures Facilitate Electron Transfer of Enzyme: Application to Detection of H<sub>2</sub>O<sub>2</sub> with High Selectivity", *Biosens. Bioelectron.*, **24**, 2465—2469 (2009).
- [47] M. Ulmann, C. Santato, J. Augustynski, and V. Shklover, 4th Electrode Materials and Processes for Energy Conversion and Storage Symposium Electrochemical Society Proceedings, 1997, pp. 328—339.
- [48] W. Gissler, and R. Memming, "Photoelectrochemical Processes at Semiconducting WO<sub>3</sub> Layers", *J. Electrochem. Soc.*, **124**, 1710—1714 (1977).
- [49] F. Di Quarto, G. Russo, C. Sunseri, and A. Di Paola, "Photoelectrochemical Study of the Amorphous-WO<sub>3</sub>-Semiconductor-Electrolyte Junction", *J. Chem. Soc., Faraday Trans. 1*, **78**, 13 (1982).
- [50] E. Kikuchi, K. Iida, A. Fujishima, and K. Itoh, "Photochromism and Photoelectrochemistry of Amorphous and Polycrystalline WO<sub>3</sub> Films", *J. Electroanal. Chem.*, **351**, 105—114 (1993).
- [51] J.M. Ortega, A.I. Martínez, D.R. Acosta, and C.R. Magaña, "Structural and Electrochemical Studies of WO<sub>3</sub> Films Deposited by Pulsed Spray Pyrolysis", *Sol. Energy Mater. Sol. Cells*, **90**, 2471—2479 (2006).
- [52] H. Kim, K. Senthil, and K. Yong, "Photoelectrochemical and Photocatalytic Properties of Tungsten Oxide Nanorods Grown by Thermal Evaporation", *Mater. Chem. Phys.*, **120**, 452—455 (2010).
- [53] D. Lu, A. Ogino, B. Liang, J.B. Liu, and M. Nagatsu, "Field-Emission Properties of Nanostructured WO<sub>3</sub> Arrays Fabricated Using Tungsten Hot-Filament Chemical Vapor Deposition", *Jpn. J. Appl. Phys.*, **48**, 090206 (2009).
- [54] L.F. Chi, S.Z. Deng, N.S. Xu, J. Chen, J.C. She, and X.H. Liang, "The Study of Optimizing Growth Conditions for Improving Field Emission Property of W<sub>18</sub>O<sub>49</sub> Nanorod Arrays", *J. Phys.: Conf. Ser.*, **188**, (2009).
- [55] J. Zhou, L. Gong, S.Z. Deng, J. Chen, J.C. She, N.S. Xu, R.S. Yang, and Z.L. Wang, "Growth and Field-Emission Property of Tungsten Oxide Nanotip Arrays", *Appl. Phys. Lett.*, **87**, 223108 (2005).

- [56] L.F. Chi, N.S. Xu, S.Z. Deng, J. Chen, and J.C. She, "An Approach for Synthesizing Various Types of Tungsten Oxide Nanostructure", *Nanotechnology*, **17**, 5590–5595 (2006).
- [57] K. Huang, Q. Pan, F. Yang, S. Ni, and D. He, "The Catalyst-Free Synthesis of Large-Area Tungsten Oxide Nanowires Arrays on Ito Substrate and Field Emission Properties", *Mater. Res. Bull.*, **43**, 7 (2008).
- [58] A.Z. Sadek, H.D. Zheng, M. Breedon, V. Bansal, S.K. Bhargava, K. Latham, J.M. Zhu, L.S. Yu, Z. Hu, P.G. Spizzirri, W. Wlodarski, and K. Kalantar-zadeh, "High-Temperature Anodized  $\text{WO}_3$  Nanoplatelet Films for Photosensitive Devices", *Langmuir*, **25**, 9545–9551 (2009).
- [59] K. Kalantar-Zadeh, A.Z. Sadek, H.D. Zheng, V. Bansal, S.K. Bhargava, W. Wlodarski, J.M. Zhu, L.S. Yu, and Z. Hu, "Nanostructured  $\text{WO}_3$  Films Using High Temperature Anodization", *Sens. Actuators, B*, **142**, 230–235 (2009).
- [60] S.J. Hong, H. Jun, P.H. Borse, and J.S. Lee, "Size Effects of  $\text{WO}_3$  Nanocrystals for Photooxidation of Water in Particulate Suspension and Photoelectrochemical Film Systems", *Int. J. Hydrogen Energy*, **34**, 3234–3242 (2009).
- [61] X.M. Zhang, K.F. Huo, L.S. Hu, and P.K. Chu, 3rd International Nanoelectronics Conference (INEC), IEEE, Hong Kong, 2010, pp. 1090–1091.
- [62] M. Yang, N.K. Shrestha, and P. Schmuki, "Thick Porous Tungsten Trioxide Films by Anodization of Tungsten in Fluoride Containing Phosphoric Acid Electrolyte", *Electrochem. Commun.*, **11**, 1908–1911 (2009).
- [63] Y.P. Xie, G. Liu, L. Yin, and H.-M. Cheng, "Crystal Facet-Dependent Photocatalytic Oxidation and Reduction Reactivity of Monoclinic  $\text{WO}_3$  for Solar Energy Conversion", *J. Mater. Chem.*, **22**, 6746–6751 (2012).
- [64] J.A. Glasscock, P.R.F. Barnes, I.C. Plumb, and N. Savvides, "Enhancement of Photoelectrochemical Hydrogen Production from Hematite Thin Films by the Introduction of Ti and Si", *J. Phys. Chem. C*, **111**, 16477–16488 (2007).
- [65] C. Santato, M. Ulmann, and J. Augustynski, "Enhanced Visible Light Conversion Efficiency Using Nanocrystalline  $\text{WO}_3$  Films", *Adv. Mater.*, **13**, 511–514 (2001).
- [66] D.D. Qin, C.L. Tao, S.A. Friesen, T.H. Wang, O.K. Varghese, N.Z. Bao, Z.Y. Yang, T.E. Mallouk, and C.A. Grimes, "Dense Layers of Vertically Oriented  $\text{WO}_3$  Crystals as Anodes for Photoelectrochemical Water Oxidation", *Chem. Commun.*, **48**, 729–731 (2012).

- [67] J. Su, X. Feng, J.D. Sloppy, L. Guo, and C.A. Grimes, "Vertically Aligned  $\text{WO}_3$  Nanowire Arrays Grown Directly on Transparent Conducting Oxide Coated Glass: Synthesis and Photoelectrochemical Properties", *Nano Lett.*, **11**, 203–208 (2011).
- [68] Y.F. Guo, X. Quan, N. Lu, H.M. Zhao, and S. Chen, "High Photocatalytic Capability of Self-Assembled Nanoporous  $\text{WO}_3$  with Preferential Orientation of (002) Planes", *Environ. Sci. Technol.*, **41**, 4422–4427 (2007).
- [69] B. Yang, P.R.F. Barnes, Y. Zhang, and V. Luca, "Tungsten Trioxide Films with Controlled Morphology and Strong Photocatalytic Activity Via a Simple Sol–Gel Route", *Catal. Lett.*, **118**, 280–284 (2007).
- [70] V.S. Vidyarthi, M. Hofmann, A. Sayan, K. Sliozberg, D. Konig, R. Beranek, W. Schuhmann, and A. Ludwig, "Enhanced Photoelectrochemical Properties of  $\text{WO}_3$  Thin Films Fabricated by Reactive Magnetron Sputtering", *Int. J. Hydrogen Energy*, **36**, 4724–4731 (2011).
- [71] C.A. Grimes, and G.K. Mor, *TiO<sub>2</sub> Nanotube Arrays: Synthesis, Properties, and Applications*. Springer, New York, USA, 2009.
- [72] K. Zhu, N.R. Neale, A. Miedaner, and A.J. Frank, "Enhanced Charge-Collection Efficiencies and Light Scattering in Dye-Sensitized Solar Cells Using Oriented  $\text{TiO}_2$  Nanotubes Arrays", *Nano Lett.*, **7**, 69–74 (2007).
- [73] W. Li, J. Li, X. Wang, J. Ma, and Q. Chen, "Photoelectrochemical and Physical Properties of  $\text{WO}_3$  Films Obtained by the Polymeric Precursor Method", *Int. J. Hydrogen Energy*, **35**, 13137–13145 (2010).
- [74] X. Pan, M.Q. Yang, X. Fu, N. Zhang, and Y.J. Xu, "Defective  $\text{TiO}_2$  with Oxygen Vacancies: Synthesis, Properties and Photocatalytic Applications", *Nanoscale*, **5**, 3601–3614 (2013).
- [75] R.M. Navarro Yerga, M. Consuelo Álvarez Galván, F. del Valle, J.A. Villoria de la Mano, and J.L.G. Fierro, "Water Splitting on Semiconductor Catalysts under Visible-Light Irradiation", *ChemSusChem*, **2**, 471–485 (2009).
- [76] X. Chen, Y. Zhou, Q. Liu, Z. Li, J. Liu, and Z. Zou, "Ultrathin, Single-Crystal  $\text{WO}_3$  Nanosheets by Two-Dimensional Oriented Attachment toward Enhanced Photocatalytic Reduction of  $\text{CO}_2$  into Hydrocarbon Fuels under Visible Light", *ACS Appl. Mater. Interfaces*, **4**, 3372–3377 (2012).
- [77] L. Meda, G. Tozzola, A. Tacca, G. Marra, S. Caramori, V. Cristino, and C.A. Bignozzi, "Photo-Electrochemical Properties of Nanostructured  $\text{WO}_3$  Prepared with

- Different Organic Dispersing Agents", *Sol. Energy Mater. Sol. Cells*, **94**, 788—796 (2010).
- [78] M. Sun, N. Xu, Y.W. Cao, J.N. Yao, and E.G. Wang, "Preparation, Microstructure and Photochromism of a New Nanocrystalline  $\text{WO}_3$  Film", *J. Mater. Sci. Lett.*, **19**, 1407—1409 (2000).
- [79] M. Sun, N. Xu, Y.W. Cao, J.N. Yao, and E.G. Wang, "Nanocrystalline Tungsten Oxide Thin Film: Preparation, Microstructure, and Photochromic Behavior", *J. Mater. Res.*, **15**, 927—933 (2000).
- [80] N. Beermann, L. Vayssieres, S.E. Lindquist, and A. Haqfeldt, "Photoelectrochemical Studies of Oriented Nanorod Thin Films of Hematite", *J. Electrochem. Soc.*, **147**, 2456—2461 (2000).
- [81] J. Sun, D.K. Zhong, and D.R. Gamelin, "Composite Photoanodes for Photoelectrochemical Solar Water Splitting", *Energy Environ. Sci.*, **3**, 1252—1261 (2010).
- [82] W.J. Youngblood, S.-H.A. Lee, Y. Kobayashi, E.A. Hernandez-Pagan, P.G. Hoertz, T.A. Moore, A.L. Moore, D. Gust, and T.E. Mallouk, "Photoassisted Overall Water Splitting in a Visible Light-Absorbing Dye-Sensitized Photoelectrochemical Cell", *J. Am. Chem. Soc.*, **131**, 926—927 (2009).
- [83] Z. Li, W. Luo, M. Zhang, J. Feng, and Z. Zou, "Photoelectrochemical Cells for Solar Hydrogen Production: Current State of Promising Photoelectrodes, Methods to Improve Their Properties, and Outlook", *Energy Environ. Sci.*, **6**, 347—370 (2013).
- [84] J. Lim, P. Murugan, N. Lakshminarasimhan, J.Y. Kim, J.S. Lee, S.H. Lee, and W. Choi, "Synergic Photocatalytic Effects of Nitrogen and Niobium Co-Doping in  $\text{TiO}_2$  for the Redox Conversion of Aquatic Pollutants under Visible Light", *J. Catal.*, in press.
- [85] D.W. Hwang, J. Kim, T.J. Park, and J.S. Lee, "Mg-Doped  $\text{WO}_3$  as a Novel Photocatalyst for Visible Light-Induced Water Splitting", *Catal. Lett.*, **80**, 53—57 (2002).
- [86] M. Grundmann, *The Physics of Semiconductors: An Introduction Including Devices and Nanophysics*. Springer-Verlag Berlin Heidelberg, Germany, 2006.
- [87] B. Cole, B. Marsen, E. Miller, Y.F. Yan, B. To, K. Jones, and M. Al-Jassim, "Evaluation of Nitrogen Doping of Tungsten Oxide for Photoelectrochemical Water Splitting", *J. Phys. Chem. C*, **112**, 5213—5220 (2008).

- [88] Y.H. Ng, A. Iwase, A. Kudo, and R. Amal, "Reducing Graphene Oxide on a Visible-Light  $\text{BiVO}_4$  Photocatalyst for an Enhanced Photoelectrochemical Water Splitting", *J. Phys. Chem. Lett.*, **1**, 2607–2612 (2010).
- [89] C. Janáky, K. Rajeshwar, N.R. de Tacconi, W. Chanmanee, and M.N. Huda, "Tungsten-Based Oxide Semiconductors for Solar Hydrogen Generation", *Catal. Today*, **199**, 53–64 (2013).
- [90] H. Shi, X. Huang, H. Tian, J. Lv, Z. Li, J. Ye, and Z. Zou, "Correlation of Crystal Structures, Electronic Structures and Photocatalytic Properties in W-Based Oxides", *J. Phys. D: Appl. Phys.*, **42**, 125402 (2009).
- [91] D.W. Kim, I.S. Cho, S.S. Shin, S. Lee, T.H. Noh, D.H. Kim, H.S. Jung, and K.S. Hong, "Electronic Band Structures and Photovoltaic Properties of  $\text{MWO}_4$  ( $\text{M} = \text{Zn, Mg, Ca, Sr}$ ) Compounds", *J. Solid State Chem.*, **184**, 2103–2107 (2011).
- [92] S. Choudhary, S. Upadhyay, P. Kumar, N. Singh, V.R. Satsangi, R. Shrivastav, and S. Dass, "Nanostructured Bilayered Thin Films in Photoelectrochemical Water Splitting: A Review", *Int. J. Hydrogen Energy*, **37**, 18713–18730 (2012).
- [93] S.J. Hong, S. Lee, J.S. Jang, and J.S. Lee, "Heterojunction  $\text{BiVO}_4/\text{WO}_3$  Electrodes for Enhanced Photoactivity of Water Oxidation", *Energy Environ. Sci.*, **4**, 1781–1787 (2011).
- [94] Y. Tachibana, L. Vayssieres, and J.R. Durrant, "Artificial Photosynthesis for Solar Water-Splitting", *Nat. Photonics*, **6**, 511–518 (2013).
- [95] E. Lassner, and W.D. Schubert, *Tungsten: Properties, Chemistry, Technology of the Element, Alloys, and Chemical Compounds* Kluwer Academic/Plenum Publishers, New York, 1999.
- [96] G. Xin, W. Guo, and T. Ma, "Effect of Annealing Temperature on the Photocatalytic Activity of  $\text{WO}_3$  for  $\text{O}_2$  Evolution", *Appl. Surf. Sci.*, **256**, 165–169 (2009).
- [97] P.M. Woodward, A.W. Sleight, and T. Vogt, "Structure Refinement of Triclinic Tungsten Trioxide", *J. Phys. Chem. Solids*, **56**, 1305–1315 (1995).
- [98] X. Han, X. Han, L. Lia, and C. Wang, "Controlling the Morphologies of  $\text{WO}_3$  Particles and Tuning the Gas Sensing Properties", *New J. Chem.*, **36**, 2205–2208 (2012).
- [99] D. Zhang, S. Wang, J. Zhu, H. Li, and Y. Lu, " $\text{WO}_3$  Nanocrystals with Tunable Percentage of (0 0 1)-Facet Exposure", *Appl. Catal., B*, **123–124**, 398–404 (2012).

- [100] W.Z. Li, J. Li, X. Wang, S. Luo, J.A. Xiao, and Q.Y. Chen, "Visible Light Photoelectrochemical Responsiveness of Self-Organized Nanoporous  $\text{WO}_3$  Films", *Electrochim. Acta*, **56**, 620—625 (2010).
- [101] A. Phuruangrat, D.J. Ham, S.J. Hong, S. Thongtem, and J.S. Lee, "Synthesis of Hexagonal  $\text{WO}_3$  Nanowires by Microwave-Assisted Hydrothermal Method and Their Electrocatalytic Activities for Hydrogen Evolution Reaction", *J. Mater. Chem.*, **20**, 1683—1690 (2010).
- [102] J.L. Zhang, G.M. Zhang, D.Z. Guo, Y. Wu, and Z.G. Xi, "A Simple Method for the Synthesis of Tungsten Trioxide Nanorods Array without Catalyst", *Surf. Rev. Lett.*, **14**, 607—610 (2007).
- [103] M. Epifani, J. Arbiol, R. Díaz, T. Andreu, P. Siciliano, and J.R. Morante, "Morphological and Structural Characterization of  $\text{WO}_3$  and Cr- $\text{WO}_3$  Thin Films Synthesized by Sol-Gel Process", *Thin Solid Films*, **3** (2010).
- [104] S. Fardindoost, A. Irají zad, F. Rahimi, and R. Ghasempour, "Pd Doped  $\text{WO}_3$  Films Prepared by Sol-Gel Process for Hydrogen Sensing", *Int. J. Hydrogen Energy*, **35**, 7 (2010).
- [105] B. Yang, P.R.F. Barnes, W. Bertram, and V. Luca, "Strong Photoresponse of Nanostructured Tungsten Trioxide Films Prepared Via a Sol-Gel Route", *J. Mater. Chem.*, **17**, 2722—2729 (2007).
- [106] L.M. Bertus, C. Faure, A. Danine, C. Labrugere, G. Campet, A. Rougier, and A. Duta, "Synthesis and Characterization of  $\text{WO}_3$  Thin Films by Surfactant Assisted Spray Pyrolysis for Electrochromic Applications", *Mater. Chem. Phys.*, **140**, 49—59 (2013).
- [107] A. Enesca, and A. Duta, "Tailoring  $\text{WO}_3$  Thin Layers Using Spray Pyrolysis Technique", *Phys. Status Solidi C*, **5**, 3499—3502 (2008).
- [108] Y. Sun, C.J. Murphy, K.R. Reyes-Gil, E.A. Reyes-Garcia, J.M. Thornton, N.A. Morris, and D. Raftery, "Photoelectrochemical and Structural Characterization of Carbon-Doped  $\text{WO}_3$  Films Prepared Via Spray Pyrolysis", *Int. J. Hydrogen Energy*, **34**, 8476—8484 (2009).
- [109] S. Pokhrel, J. Birkenstock, M. Schowalter, A. Rosenauer, and L. Madler, "Growth of Ultrafine Single Crystalline  $\text{WO}_3$  Nanoparticles Using Flame Spray Pyrolysis", *Cryst. Growth Des.*, **10**, 632—639 (2010).
- [110] J.H. Bang, Y.T. Didenko, R.J. Helmich, and K.S. Suslick, "Nanostructured Materials through Ultrasonic Spray Pyrolysis", *Mater. Matters*, **7**, 15—20 (2012).

- [111] B.G. Jeyaprakash, R. Ashok Kumar, K. Kesavan, and A. Amalarani, "Structural and Optical Characterization of Spray Deposited SnS Thin Film", *J. Am. Sci.*, **6**, 22—26 (2010).
- [112] E.L. Miller, D. Paluselli, B. Marsen, and R.E. Rocheleau, "Development of Reactively Sputtered Metal Oxide Films for Hydrogen-Producing Hybrid Multijunction Photoelectrodes", *Sol. Energy Mater. Sol. Cells*, **88**, 131—144 (2005).
- [113] D. Paluselli, B. Marsen, E.L. Miller, and R.E. Rocheleau, "Nitrogen Doping of Reactively Sputtered Tungsten Oxide Films", *Electrochem. Solid-State Lett.*, **8**, G301—G303 (2005).
- [114] B. Marsen, B. Cole, and E.L. Miller, "Influence of Sputter Oxygen Partial Pressure on Photoelectrochemical Performance of Tungsten Oxide Films", *Sol. Energy Mater. Sol. Cells*, **91**, 1954—1958 (2007).
- [115] L. Weinhardt, M. Blum, M. Bar, C. Heske, B. Cole, B. Marsen, and E.L. Miller, "Electronic Surface Level Positions of  $\text{WO}_3$  Thin Films for Photoelectrochemical Hydrogen Production", *J. Phys. Chem. C*, **112**, 3078—3082 (2008).
- [116] N. Gaillard, J. Kaneshiro, E.L. Miller, L. Weinhardt, M. Bar, C. Heske, K.S. Ahn, Y. Yan, and M.M. Al-Jassim, "Surface Modification of Tungsten Oxide-Based Photoanodes for Solar-Powered Hydrogen Production", pp. 42–47 in *MRS Proceedings. MRS Spring Meeting* (2009).
- [117] M. Bar, L. Weinhardt, B. Marsen, B. Cole, N. Gaillard, E. Miller, and C. Heske, "Mo Incorporation in  $\text{WO}_3$  Thin Film Photoanodes: Tailoring the Electronic Structure for Photoelectrochemical Hydrogen Production", *Appl. Phys. Lett.*, **96**, 032107 (2010).
- [118] S.J. Yoo, S.U. Yun, Y.E. Sung, and K.S. Ahn, "Tungsten Oxide Bilayer Electrodes for Photoelectrochemical Cells", *J. Power Sources*, **195**, 5422—5425 (2010).
- [119] H. Wang, X. Quan, Y. Zhang, and S. Chen, "Direct Growth and Photoelectrochemical Properties of Tungsten Oxide Nanobelt Arrays", *Nanotechnology*, **19**, 065704 (2008).
- [120] J.M. Wang, E. Khoo, P.S. Lee, and J. Ma, "Synthesis, Assembly, and Electrochromic Properties of Uniform Crystalline  $\text{WO}_3$  Nanorods", *J. Phys. Chem. C*, **112**, 14306—14312 (2008).
- [121] F. Amano, D. Li, and B. Ohtani, "Fabrication and Photoelectrochemical Property of Tungsten (VI) Oxide Films with a Flake-Wall Structure", *Chem. Commun.*, **46**, 2769–2771 (2010).

- [122] K. Huang, Q. Pan, F. Yang, S. Ni, X. Wei, and D. He, "Controllable Synthesis of Hexagonal  $\text{WO}_3$  Nanostructures and Their Application in Lithium Batteries", *J. Phys. D: Appl. Phys.*, **41**, 155417 (2008).
- [123] F. Zheng, M. Guo, and M. Zhang, "Hydrothermal Preparation and Optical Properties of Orientation-Controlled  $\text{WO}_3$  Nanorod Arrays on Ito Substrates", *CrystEngComm*, **15**, 277–284 (2013).
- [124] H. Tsuchiya, J.M. Macak, I. Sieber, L. Taveira, A. Ghicov, K. Sirotna, and P. Schmuki, "Self-Organized Porous  $\text{WO}_3$  Formed in Naf Electrolytes", *Electrochem. Commun.*, **7**, 295—298 (2005).
- [125] N. Mukherjee, M. Paulose, O.K. Varghese, G.K. Mor, and C.A. Grimes, "Fabrication of Nanoporous Tungsten Oxide by Galvanostatic Anodization", *J. Mater. Res.*, **18**, 2296—2299 (2003).
- [126] Y.C. Nah, I. Paramasivam, R. Hahn, N.K. Shrestha, and P. Schmuki, "Nitrogen Doping of Nanoporous  $\text{WO}_3$  Layers by  $\text{NH}_3$  Treatment for Increased Visible Light Photoresponse", *Nanotechnology*, **21**, 105704 (2010).
- [127] Y.C. Nah, A. Ghicov, D. Kim, and P. Schmuki, "Enhanced Electrochromic Properties of Self-Organized Nanoporous  $\text{WO}_3$ ", *Electrochem. Commun.*, **10**, 1777—1780 (2008).
- [128] E.A. Meulenkaamp, "Mechanism of  $\text{WO}_3$  Electrodeposition from Peroxy-Tungstate Solution", *J. Electrochem. Soc.*, **144**, 1664—1671 (1997).
- [129] K. Yamanaka, H. Oakamoto, H. Kidou, and T. Kudo, "Peroxytungstic Acid Coated Films for Electrochromic Display Devices", *Jpn. J. Appl. Phys., Part 1*, **25**, 1420—1426 (1986).
- [130] K. Yamanaka, "Electrodeposited Films from Aqueous Tungstic Acid-Hydrogen Peroxide Solutions for Electrochromic Display Devices", *Jpn. J. Appl. Phys.*, **26**, 1884—1890 (1987).
- [131] T. Pauporte, "A Simplified Method for  $\text{WO}_3$  Electrodeposition", *J. Electrochem. Soc.*, **149**, C539—C545 (2002).
- [132] T. Kudo, H. Okamoto, K. Matsumoto, and Y. Sasaki, "Peroxytungstic Acids Synthesized by Direct Reaction of Tungsten or Tungsten Carbide with Hydrogen-Peroxide", *Inorg. Chim. Acta*, **111**, L27—L28 (1986).

- [133] X.L. Sun, H.T. Cao, Z.M. Liu, and J.Z. Li, "Influence of Annealing Temperature on Microstructure and Optical Properties of Sol-Gel Derived Tungsten Oxide Films", *Appl. Surf. Sci.*, **255**, 8629—8633 (2009).
- [134] P.G. Su, and T.T. Pan, "Fabrication of a Room-Temperature NO<sub>2</sub> Gas Sensor Based on WO<sub>3</sub> Films and WO<sub>3</sub>/Mwcnt Nanocomposite Films by Combining Polyol Process with Metal Organic Decomposition Method", *Mater. Chem. Phys.*, **125**, 351—357 (2011).
- [135] C.M. White, J.S. Jang, S.H. Lee, J. Pankow, and A.C. Dillon, "Photocatalytic Activity and Photoelectrochemical Property of Nano-WO<sub>3</sub> Powders Made by Hot-Wire Chemical Vapor Deposition", *Electrochem. Solid-State Lett.*, **13**, B120—B122 (2010).
- [136] F. Fang, J. Kennedy, J. Futter, T. Hopf, A. Markwitz, E. Manikandan, and G. Henshaw, "Size-Controlled Synthesis and Gas Sensing Application of Tungsten Oxide Nanostructures Produced by Arc Discharge", *Nanotechnology*, **22**, 335702 (2011).
- [137] R.S. Vemuri, K.K. Bharathi, S.K. Gullapalli, and C.V. Ramana, "Effect of Structure and Size on the Electrical Properties of Nanocrystalline WO<sub>3</sub> Films", *ACS Appl. Mater. Interfaces*, **2**, 2623—2628 (2010).
- [138] S.K. Gullapalli, R.S. Vemuri, and C.V. Ramana, "Structural Transformation Induced Changes in the Optical Properties of Nanocrystalline Tungsten Oxide Thin Films", *Appl. Phys. Lett.*, **96**, 171903 (2010).
- [139] N. Naseri, S. Yousefzadeh, E. Daryaei, and A.Z. Moshfegh, "Photoresponse and H<sub>2</sub> Production of Topographically Controlled Peg Assisted Sol-Gel WO<sub>3</sub> Nanocrystalline Thin Films", *Int. J. Hydrogen Energy*, **36**, 13461—13472 (2011).
- [140] P.K. Shen, and A.C.C. Tseung, "Study of Electrodeposited Tungsten Trioxide Thin-Films", *J. Mater. Chem.*, **2**, 1141—1147 (1992).
- [141] P.M.S. Monk, R.D. Partridge, R. Janes, and M.J. Parker, "Electrochromic Tungsten Oxide: Doping with Two or Three Other Metal Oxides", *J. Mater. Chem.*, **4**, 1071—1074 (1994).
- [142] J. Augustynski, R. Solarska, H. Hagemann, and C. Santato, "Nanostructured Thin-Film Tungsten Trioxide Photoanodes for Solar Water and Sea-Water Splitting", pp. 63400J in *Proceedings of SPIE Solar Hydrogen and Nanotechnology* (2006).
- [143] B.D. Alexander, and J. Augustynski, "Nanostructured Thin-Film WO<sub>3</sub> Photoanodes for Solar Water and Sea-Water Splitting", pp. 333—348 in *On Solar*

---

*Hydrogen and Nanotechnology*. Edited by L. Vayssieres. John Wiley and Sons, Singapore, 2009.

[144] M. Ulmann, N.R. Detacconi, and J. Augustynski, "Behavior of Surface Peroxo Species in the Photoreactions at  $\text{TiO}_2$ ", *J. Phys. Chem.*, **90**, 6523—6530 (1986).

[145] P. Bermejo, and J.A. Cocho de Juan, "Analytical Procedures for the Lead Determination in Biological and Environmental Samples", pp. 229—338 in *Lead: Chemistry, Analytical Aspects, Environmental Impact and Health Effects*. Edited by J.S. Casas, and J. Sordo. Elsevier Amsterdam, 2006.

[146] D. Sarkar, and A. Haldar, *Physical and Chemical Methods in Soil Analysis: Fundamental Concepts of Analytical Chemistry and Instrumental Techniques*. New Age International, New Delhi, 2005.

[147] M. Paunovic, and M. Schlesinger, *Fundamentals of Electrochemical Deposition, Second ed.* John Wiley and Sons, New Jersey, 2006

[148] S. Bijani, L. Martinez, M. Gabas, E.A. Dalchiele, and J.-R. Ramos-Barrado, "Low-Temperature Electrodeposition of  $\text{Cu}_2\text{O}$  Thin Films: Modulation of Micro-Nanostructure by Modifying the Applied Potential and Electrolytic Bath Ph", *J. Phys. Chem. C*, **113**, 19482—19487 (2009).

[149] L. Wu, L.-K. Tsui, N. Swami, and G. Zangari, "Photoelectrochemical Stability of Electrodeposited  $\text{Cu}_2\text{O}$  Films", *J. Phys. Chem. C*, **114**, 11551—11556 (2010).

[150] Y. Waseda, E. Matsubara, and K. Shinoda, *X-Ray Diffraction Crystallography: Introduction, Examples and Solved Problems*. Springer, New York, 2011.

[151] J.D. Zook, "Effects of Grain Boundaries in Polycrystalline Solar Cells.", *Appl. Phys. Lett.*, **37**, 223—226 (1980).

[152] H. Zhang, G. Duan, G. Liu, Y. Li, X. Xu, Z. Dai, J. Wang, and W. Cai, "Layer-Controlled Synthesis of  $\text{WO}_3$  Ordered Nanoporous Films for Optimum Electrochromic Application", *Nanoscale*, **5**, 2460—2468 (2013).

[153] H.M.A. Soliman, A.B. Kashyout, M.S. El Nouby, and A.M. Abosehly, "Effect of Hydrogen Peroxide and Oxalic Acid on Electrochromic Nanostructured Tungsten Oxide Thin Films", *Int. J. Electrochem. Sci.*, **7**, 258—271 (2012).

[154] J. Tauc, and A. Menth, "States in the Gap", *J. Non-Cryst. Solids*, **8-10**, 569—585 (1972).

- 
- [155] W.L. Kwong, N. Savvides, and C.C. Sorrell, "Electrodeposited Nanostructured  $\text{WO}_3$  Thin Films for Photoelectrochemical Applications", *Electrochim. Acta*, **75** 371—380 (2012).
- [156] A. Nakaruk, D. Ragazzon, and C.C. Sorrell, "Anatase–Rutile Transformation through High-Temperature Annealing of Titania Films Produced by Ultrasonic Spray Pyrolysis", *Thin Solid Films*, **518**, 3735–3742 (2010).
- [157] W.D. Kingery, H.K. Bowen, and D.R. Uhlmann, *Introduction to Ceramics, Second ed.* John Wiley and Sons, New York, 1976.
- [158] X. Pang, I. Zhitomirsky, and M. Niewczas, "Cathodic Electrolytic Deposition of Zirconia Films", *Surf. Coat. Technol.*, **195**, 138—146 (2005).
- [159] S.R. Vishwakarma, J.P. Upadhyay, and H.C. Prasad, "Physical Properties of Arsenic-Doped Tin Oxide Thin Films", *Thin Solid Films*, **176**, 99–110 (1989).
- [160] J. Tauc, "Optical Properties and Electronic Structure of Amorphous Ge and Si", *Mater. Res. Bull.*, **3**, 37—46 (1968).
- [161] Y. Sun, S.E. Thompson, and T. Nishida, *Strain Effect in Semiconductors: Theory and Device Applications*. Springer Science+Business Media, New York, 2010.
- [162] E. Salje, "The Orthorhombic Phase of  $\text{WO}_3$ ", *Acta Crystallogr. B*, **33**, 574–577 (1977).
- [163] B.C. Mohanty, Y.H. Jo, D.H. Yeon, I.J. Choi, and Y.S. Cho, "Stress-Induced Anomalous Shift of Optical Band Gap in  $\text{ZnO:Al}$  Thin Films", *Appl. Phys. Lett.*, **95**, 062103 (2009).
- [164] W.W. Gartner, "Depletion-Layer Photoeffects in Semiconductors", *Phys. Rev.*, **116**, 84–87 (1959).
- [165] M. Radecka, P. Sobas, M. Wimbicka, and M. Rekas, "Photoelectrochemical Properties of Undoped and Ti-Doped  $\text{WO}_3$ ", *Physica B*, **364**, 85—92 (2005).
- [166] N. Sato, *Electrochemistry at Metal and Semiconductor Electrodes*. Elsevier Science, Amsterdam, 1998.
- [167] R.E. Stevens, and M.K. Carron, "Simple Field Test for Distinguishing Minerals by Abrasion Ph", *Am. Mineral.*, **33**, 31—49 (1948).
- [168] W.H. Grant, "Abrasion Ph, an Index of Chemical Weathering", *Clay Clay Miner.*, **17**, 151—155 (1969).

- [169] S.J. Hong, H. Jun, and J.S. Lee, "Nanocrystalline  $\text{WO}_3$  Film with High Photo-Electrochemical Activity Prepared by Polymer-Assisted Direct Deposition", *Scripta Mater.*, **63**, 757—760 (2010).
- [170] W.S. Yoo, and K. Kang, "Electrical Activation of Ultra-Shallow B and  $\text{Bf}_2$  Implanted Silicon by Flash Anneal", *Nucl. Instrum. Methods Phys. Res., Sect. B*, **237**, 12—17 (2005).
- [171] V. Chakrapani, J. Thangala, and M.K. Sunkara, " $\text{WO}_3$  and  $\text{W}_2\text{n}$  Nanowire Arrays for Photoelectrochemical Hydrogen Production", *Int. J. Hydrogen Energy*, **34**, 9050–9059 (2009).
- [172] W. Lee, D. Kim, K. Lee, P. Roy, and P. Schmuki, "Direct Anodic Growth of Thick  $\text{WO}_3$  Mesosponge Layers and Characterization of Their Photoelectrochemical Response", *Electrochim. Acta*, **56**, 828—833 (2010).
- [173] N.R. de Tacconi, C.R. Chenthamarakshan, G. Yogeewaran, A. Watcharenwong, R.S. de Zoysa, N.A. Basit, and K. Rajeshwar, "Nanoporous  $\text{TiO}_2$  and  $\text{WO}_3$  Films by Anodization of Titanium and Tungsten Substrates: Influence of Process Variables on Morphology and Photoelectrochemical Response", *J. Phys. Chem. B*, **110**, 25347–25355 (2006).
- [174] M. Wang, Y. Zhang, Y. Zhou, F. Yang, E.J. Kim, S.H. Hahn, and S.G. Seong, "Rapid Room-Temperature Synthesis of Nanosheet-Assembled  $\text{ZnO}$  Mesocrystals with Excellent Photocatalytic Activity", *CrystEngComm*, **15**, 754—763 (2013).
- [175] Z. Lai, F. Peng, Y. Wang, H. Wang, H. Yu, P. Liu, and H. Zhao, "Low Temperature Solvothermal Synthesis of Anatase  $\text{TiO}_2$  Single Crystals with Wholly {100} and {001} Faceted Surfaces", *J. Mater. Chem.*, **22**, 23906–23912 (2012).
- [176] H.G. Yang, G. Liu, S.Z. Qiao, C.H. Sun, Y.G. Jin, S.C. Smith, J. Zou, H.M. Cheng, and G.Q. Lu, "Solvothermal Synthesis and Photoreactivity of Anatase  $\text{TiO}_2$  Nanosheets with Dominant {001} Facets", *J. Am. Chem. Soc.*, **131**, 4078–4083 (2009).
- [177] G.W. Grodstein, "X-Ray Attenuation Coefficients from 10 Kev to 100 Mev", pp. 1–54 in *N.B.o.S.C. 583*. United States Department of Commerce (1957).
- [178] S. Tanisaki, "Crystal Structure of Monoclinic Tungsten Trioxide at Room Temperature", *J. Phys. Soc. Jpn.*, **15**, 573—581 (1960).
- [179] M.N. Huda, Y. Yan, C.Y. Moon, S.H. Wei, and M.M. Al-Jassim, "Density-Functional Theory Study of the Effects of Atomic Impurity on the Band Edges of Monoclinic  $\text{WO}_3$ ", *Phys. Rev. B*, **77**, 195102 (2008).

- [180] A. Nakaruk, G. Kavei, and C.C. Sorrell, "Synthesis of Mixed-Phase Titania Films by Low-Temperature Ultrasonic Spray Pyrolysis", **64**, 1365–1368 (2010).
- [181] Z. Guo, and L. Tan, *Fundamentals and Applications of Nanomaterials*. Artech House, Norwood, MA, 2009.
- [182] K. Tomioka, and T. Fukui, "Iii–V Semiconductor Nanowires on Si by Selective-Area Metal-Organic Vapor Phase Epitaxy", pp. 67–102 in *Semiconductor Nanostructures for Optoelectronic Devices: Processing, Characterization, and Applications*. Edited by G.C. Yi. Springer-Verlag, Berlin Heidelberg, 2012.
- [183] H. Fredriksson, and U. Akerlind, *Solidification and Crystallization Processing in Metals and Alloys*. John Wiley & Sons, United Kingdom, 2012.
- [184] S.A. Manafi, M.R. Rahimipour, and A. Soltanmoradi, "Low Temperature Hydrothermal Synthesis of Batio<sub>3</sub> with Ultra-High Crystallinity", *Int. J. Phys. Sci.*, **7**, 5772—5778 (2012).
- [185] S. Park, J.O. Baker, M.E. Himmel, P.A. Parilla, and D.K. Johnson, "Cellulose Crystallinity Index: Measurement Techniques and Their Impact on Interpreting Cellulase Performance", *Biotechnol. Biofuels*, **3**, 10 (2010).
- [186] K.S. Kim, C.M. Ryu, C.S. Park, G.S. Sur, and C.E. Park, "Investigation of Crystallinity Effects on the Surface of Oxygen Plasma Treated Low Density Polyethylene Using X-Ray Photoelectron Spectroscopy", *Polymer*, **44**, 6287—6295 (2003).
- [187] A. Kumar, and D. Saikia, "Ion Conducting Polymers", pp. 441–474 in *Specialty Polymers: Materials and Applications*. Edited by F. Mohammad. I. K. International Publishing House, New Delhi, 2007.
- [188] D.L. Chen, X.X. Hou, T. Li, L. Yin, B.B. Fan, H.L. Wang, X.J. Li, H.L. Xu, H.X. Lu, R. Zhang, and J. Sun, "Effects of Morphologies on Acetone-Sensing Properties of Tungsten Trioxide Nanocrystals", *Sens. Actuators. B*, **153**, 373–381 (2011).
- [189] L.N. Geng, "Gas Sensitivity Study of Polypyrrole/Wo<sub>3</sub> Hybrid Materials to H<sub>2</sub>S", *Synt. Met.*, **160**, 1708–1711 (2010).
- [190] G. Liu, C. Sun, H.G. Yang, S.C. Smith, L. Wang, G.Q. Lu, and H.M. Cheng, "Nanosized Anatase Tio<sub>2</sub> Single Crystals for Enhanced Photocatalytic Activity", *Chem. Commun.*, **46**, 755—757 (2010).

- [191] X. Wan, X. Zhao, H.L.W. Chan, C.L. Choy, and H. Luo, "Crystal Orientation Dependence of the Optical Bandgap of  $(1-X)\text{Pb}(\text{Mg}_{1/3}\text{Nb}_{2/3})\text{O}_{3-x}\text{PbTiO}_3$  Single Crystals", *Mater. Chem. Phys.*, **92**, 123–127 (2005).
- [192] J.F. Moulder, W.F. Stickle, P.E. Sobol, and K.D. Bomben, *Handbook of X-Ray Photoelectron Spectroscopy*. Perkin-Elmer Corporation, Minnesota, USA, 1992.
- [193] M. Deepa, A.K. Srivastava, S.N. Sharma, Govind, and S.M. Shivaprasad, "Microstructural and Electrochromic Properties of Tungsten Oxide Thin Films Produced by Surfactant Mediated Electrodeposition", *Appl. Surf. Sci.*, **254**, 2342–2352 (2008).
- [194] J. Wang, Z. Wang, B. Huang, Y. Ma, Y. Liu, X. Qin, X. Zhang, and Y. Dai, "Oxygen Vacancy Induced Band-Gap Narrowing and Enhanced Visible Light Photocatalytic Activity of ZnO", *ACS Appl. Mater. Interfaces*, **4**, 4024–4030 (2012).
- [195] J. Gan, X. Lu, J. Wu, S. Xie, T. Zhai, M.Y. Zhang, Z. , Y. Mao, S.C.I. Wang, Y. Shen, and Y. Tong, "Oxygen Vacancies Promoting Photoelectrochemical Performance of  $\text{In}_2\text{O}_3$  Nanocubes", *Sci. Rep.*, **3**, 1021 (2013).
- [196] J.Q. Yan, G.J. Wu, N.J. Guan, L.D. Li, Z.X. Li, and X.Z. Cao, "Understanding the Effect of Surface/Bulk Defects on the Photocatalytic Activity of  $\text{TiO}_2$ : Anatase Versus Rutile", *Phys. Chem. Chem. Phys.*, **15**, 10978–10988 (2013).
- [197] R. Chatten, A.V. Chadwick, A. Rougier, and P.J.D. Lindan, "The Oxygen Vacancy in Crystal Phases of  $\text{WO}_3$ ", *J. Phys. Chem. B*, **109**, 3146–3156 (2005).
- [198] J. Diaz-Reyes, R. Castillo-Ojeda, M. Galvan-Arellano, and O. Zaca-Moran, "Characterization of  $\text{WO}_3$  Thin Films Grown on Silicon by Hfmod", *Adv. Condens. Matter Phys.*, **2013**, 591787 (2013).
- [199] Q. Kang, J. Cao, Y. Zhang, L. Liu, H. Xu, and J. Ye, "Reduced  $\text{TiO}_2$  Nanotube Arrays for Photoelectrochemical Water Splitting", *J. Mater. Chem. A*, **1**, 5766–5774 (2013).
- [200] S.A. Ansari, M.M. Khan, S. Kalathil, A. Nisar, J. Lee, and M.H. Cho, "Oxygen Vacancy Induced Band Gap Narrowing of ZnO Nanostructures by an Electrochemically Active Biofilm", *Nanoscale*, **5**, 9238–9246 (2013).
- [201] Y. Lv, Y. Liu, Y. Zhu, and Y. Zhu, "Surface Oxygen Vacancy Induced Photocatalytic Performance Enhancement of a  $\text{BiPO}_4$  Nanorod", *J. Mater. Chem. A*, **2**, 1174–1182 (2014).

- [202] F. Wang, C. Di Valentin, and G. Pacchioni, "Semiconductor-to-Metal Transition in  $\text{WO}_{3-x}$ : Nature of the Oxygen Vacancy", *Phys. Rev. B*, **84**, 073103 (2011).
- [203] W.L. Kwong, A. Nakaruk, P. Koshy, and C.C. Sorrell, "Tunable Photoelectrochemical Properties by Nanostructural Control in  $\text{WO}_3$  Thin Films Prepared by Carboxylic Acid-Assisted Electrodeposition", *J. Phys. Chem. C*, **117**, 17766–17776 (2013).
- [204] M. Ahsan, M.Z. Ahmad, T. Tesfamichael, J. Bell, W. Wlodarski, and N. Motta, "Low Temperature Response of Nanostructured Tungsten Oxide Thin Films toward Hydrogen and Ethanol", *Sens. Actuators, B*, **173**, 789–796 (2012).
- [205] I. Cesar, A. Kay, J.A.G. Martinez, and M. Gratzel, "Translucent Thin Film  $\text{Fe}_2\text{O}_3$  Photoanodes for Efficient Water Splitting by Sunlight: Nanostructure-Directing Effect of Si-Doping", *J. Am. Chem. Soc.*, **128**, 4582–4583 (2006).
- [206] L.L. Yang, D.T. Ge, J.P. Zhao, Y.B. Ding, X.P. Kong, and Y. Li, "Improved Electrochromic Performance of Ordered Macroporous Tungsten Oxide Films for Ir Electrochromic Device", *Sol. Energy Mater. Sol. Cells*, **100**, 251–257 (2012).
- [207] C.C. Liao, F.R. Chen, and J.J. Kai, "Annealing Effect on Electrochromic Properties of Tungsten Oxide Nanowires", *Sol. Energy Mater. Sol. Cells*, **91**, 1258–1266 (2007).
- [208] N.M. Vuong, D. Kim, and H. Kim, "Electrochromic Properties of Porous  $\text{WO}_3$ - $\text{TiO}_2$  Core-Shell Nanowires", *J. Mater. Chem. C*, **1**, 3399–3407 (2013).
- [209] W.Y. Wang, and B.R. Chen, "Characterization and Photocatalytic Activity of  $\text{TiO}_2$  Nanotube Films Prepared by Anodization", *Int. J. Photoenergy*, **2013**, 348171 (2013).
- [210] M. Amini, B. Pourbadiiei, T.P.A. Ruberu, and L.K. Woo, "Catalytic Activity of  $\text{MnO}_x/\text{WO}_3$  Nanoparticles: Synthesis, Structure Characterization and Oxidative Degradation of Methylene Blue", *New J. Chem.*, **38**, 1250–1255 (2014).
- [211] J.C. Kotz, P.M. Treichel, and J.R. Townsend, *Chemistry and Chemical Reactivity, Seventh ed.* Brooks/Cole, Belmont, 2010.
- [212] I. Zhitomirsky, L. Galor, A. Kohn, and H.W. Henniske, "Electrochemical Preparation of Pbo Films", *J. Mater. Sci. Lett.*, **14**, 807–810 (1995).
- [213] I. Zhitomirsky, and L. Galor, "Ruthenium Oxide Deposits Prepared by Cathodic Electrosynthesis", *Mater. Lett.*, **31**, 155–159 (1997).
- [214] *Biological and Biomedical Coatings Handbook: Processing and Characterization* Edited by S. Zhang. CRC Press, Portland, 2011.

- [215] S. Sawada, R. Ando, and S. Nomura, "Thermal Expansion and Specific Heat of Tungsten Oxide at High Temperatures", *Phys. Rev.*, **84**, 1054—1055 (1951).
- [216] S.T. Tan, B.J. Chen, X.W. Sun, W.J. Fan, H.S. Kwok, X.H. Zhang, and S.J. Chua, "Blueshift of Optical Band Gap in ZnO Thin Films Grown by Metal-Organic Chemical-Vapor Deposition", *J. Appl. Phys.*, **98**, 013505 (2005).
- [217] B.G. Yacobi, *Semiconductor Materials: An Introduction to Basic Principles*. Kluwer Academic/Plenum Publishers, New York, 2003.
- [218] J.K.F. Yau, and C.C. Sorrell, "High- $J_c$  (Bi,Pb) $_2$ Sr $_2$ Ca $_2$ Cu $_3$ O $_{10+x}$  Tapes Fabricated by Electrophoretic Deposition", *Physica C*, **282–287**, 2563—2564 (1997).
- [219] H. Wang, T. Lindgren, J. He, A. Hagfeldt, and S.E. Lindquist, "Photoelectrochemistry of Nanostructured  $W_3O_3$  Thin Film Electrodes for Water Oxidation: Mechanism of Electron Transport", *J. Phys. Chem. B*, **104**, 5686—5696 (2000).
- [220] D. Vernardou, H. Drosos, E. Spanakis, E. Koudoumas, C. Savvakisab, and N. Katsarakis, "Electrochemical and Photocatalytic Properties of  $W_3O_3$  Coatings Grown at Low Temperatures", *J. Mater. Chem.*, **21**, 513—517 (2011).
- [221] F.P. Koffyberg, K. Dwight, and A. Wold, "Interband Transitions of Semiconducting Oxides Determined from Photoelectrolysis Spectra", *Solid State Commun.*, **30**, 433–437 (1979).
- [222] L. Hechavarria, H. Hu, M. Miranda, and M.E. Nicho, "Electrochromic Responses of Low-Temperature-Annealed Tungsten Oxide Thin Films in Contact with a Liquid and a Polymeric Gel Electrolyte", *J. Solid State Electrochem.*, **13**, 687—695 (2009).
- [223] R. Azimirad, O. Akhavan, and A.Z. Moshfegh, "Influence of Coloring Voltage and Thickness on Electrochromical Properties of E-Beam Evaporated  $W_3O_3$  Thin Films", *J. Electrochem. Soc.*, **153**, E11–E16 (2006).
- [224] M.B. Johansson, G. Baldissera, I. Valyukh, C. Persson, H. Arwin, G.A. Niklasson, and L. Osterlund, "Electronic and Optical Properties of Nanocrystalline  $W_3O_3$  Thin Films Studied by Optical Spectroscopy and Density Functional Calculations", *J. Phys. Condens. Matter*, **25**, 205502 (2013).
- [225] S.S. Kalagi, S.S. Mali, D.S. Dalavi, A.I. Inamdar, H. Im, and P.S. Patil, "Transmission Attenuation and Chromic Contrast Characterization of R.F. Sputtered  $W_3O_3$  Thin Films for Electrochromic Device Applications", *Electrochim. Acta*, **85**, 501–508 (2012).

- [226] R.E. Marotti, D.N. Guerra, C. Bello, G. Machado, and E.A. Dalchiele, "Bandgap Energy Tuning of Electrochemically Grown ZnO Thin Films by Thickness and Electrodeposition Potential", *Sol. Energy Mater. Sol. Cells*, **82**, 85—103 (2004).
- [227] M. Pandiaraman, N. Soundararajan, and C. Vijayan, "Effect of Thickness on the Optical Band Gap of Silver Telluride Thin Films ", *J. Ovonic Res.*, **7**, 21—27 (2011).
- [228] E.S.M. Goh, T.P. Chen, C.Q. Sun, and Y.C. Liu, "Thickness Effect on the Band Gap and Optical Properties of Germanium Thin Films", *J. Appl. Phys.*, **107**, 024305 (2010).
- [229] J. Tang, D. Wang, Z. Zou, and J. Ye, "Modification of Photophysical Properties of  $\text{WO}_3$  by Doping Different Metals", *Mater. Sci. Forum*, **423—425**, 163—166 (2003).
- [230] M. Deepa, M. Kar, D.P. Singh, A.K. Srivastava, and S. Ahmad, "Influence of Polyethylene Glycol Template on Microstructure and Electrochromic Properties of Tungsten Oxide", *Sol. Energy Mater. Sol. Cells*, **92**, 170—178 (2008).
- [231] K.S. Ahn, S.H. Lee, A.C. Dillon, C.E. Tracy, and R. Pitts, "The Effect of Thermal Annealing on Photoelectrochemical Responses of  $\text{WO}_3$  Thin Films", *J. Appl. Phys.*, **101**, 093524 (2007).
- [232] C.C. Liao, F.R. Chen, and J.J. Kai, "Electrochromic Properties of Nanocomposite  $\text{WO}_3$  Films", *Sol. Energy Mater. Sol. Cells*, **91**, 1282—1288 (2007).
- [233] J. García-Cañadas, I. Mora-Seró, F. Fabregat-Santiago, J. Bisquert, and G. Garcia-Belmonte, "Analysis of Cyclic Voltammograms of Electrochromic  $\alpha\text{-WO}_3$  Films from Voltage-Dependent Equilibrium Capacitance Measurements", *J. Electroanal. Chem.*, **565**, 329—334 (2004).
- [234] I. Shiyankovskaya, M. Hepel, and E. Tewksbury, "Electrochromism in Electrodeposited Nanocrystalline  $\text{WO}_3$  Films I. Electrochemical and Optical Properties", *J. New Mater. Electrochem. Syst.*, **3**, 241—247 (2000).
- [235] D.H. Kim, "Effects of Phase and Morphology on the Electrochromic Performance of Tungsten Oxide Nano-Urchins", *Sol. Energy Mater. Sol. Cells*, **107**, 81—86 (2012).
- [236] J. Zhang, X.L. Wang, X.H. Xia, C.D. Gu, and J.P. Tu, "Electrochromic Behavior of  $\text{WO}_3$  Nanotree Films Prepared by Hydrothermal Oxidation", *Sol. Energy Mater. Sol. Cells*, **95**, 2107—2112 (2011).
- [237] S. Wendt, R.T. Vang, and F. Besenbacher, "Fundamental Reactions on Rutile  $\text{TiO}_2$  (110) Model Photocatalysts Studied by High-Resolution Scanning Tunneling

---

Microscopy", pp. 91–124 in *On Solar Hydrogen and Nanotechnology*. Edited by L. Vayssieres. John Wiley and Sons, Singapore, 2009

[238] S. Wang, A. Verma, Y.L. Yang, A.J. Jacobson, and B. Abeles, "The Effect of the Magnitude of the Oxygen Partial Pressure Change in Electrical Conductivity Relaxation Measurements: Oxygen Transport Kinetics in  $\text{La}_{0.5}\text{Sr}_{0.5}\text{COO}_{3-\text{D}}$ ", *Solid State Ionics*, **140**, 125–133 (2001).

[239] D. Feng, and G. Jin, *Introduction to Condensed Matter Physics*. World Scientific Publishing, Singapore, 2005.

[240] M.R. Pai, A.M. Banerjee, A.K. Tripathi, and S.R. Bharadwaj, "Fundamentals and Applications of the Photocatalytic Water Splitting Reaction", pp. 579–606 in *Functional Materials: Preparation, Processing and Applications*. Edited by S. Banerjee, and A.K. Tyagi. Elsevier, Waltham, 2012.

[241] B.G. Mendis, L. Bowen, and Q.Z. Jiang, "A Contactless Method for Measuring the Recombination Velocity of an Individual Grain Boundary in Thin-Film Photovoltaics", *Appl. Phys. Lett.*, **97**, 092112 (2010).

[242] G. Deutscher, "Origin of Weak-Link Behavior of Grain Boundaries in Superconducting Cuprates and Pnictides", *Appl. Phys. Lett.*, **96**, 122502 (2010).

[243] D. Tanaka, Y. Oaki, and H. Imai, "Enhanced Photocatalytic Activity of Quantum-Confined Tungsten Trioxide Nanoparticles in Mesoporous Silica", *Chem. Commun.*, **46**, 5286–5288 (2010).

[244] C.X. Kronawitter, L. Vayssieres, S. Shen, L. Guo, D.A. Wheeler, J.Z. Zhang, B.R. Antoun, and S.S. Mao, "A Perspective on Solar-Driven Water Splitting with All-Oxide Hetero-Nanostructures", *Energy Environ. Sci.*, **4**, 3889–3899 (2011).

# APPENDICES

## APPENDIX 1: SPECTRAL OUTPUT OF THE 300 W OZONE FREE Xe LAMP (NEWPORT; PART NUMBER 6258).

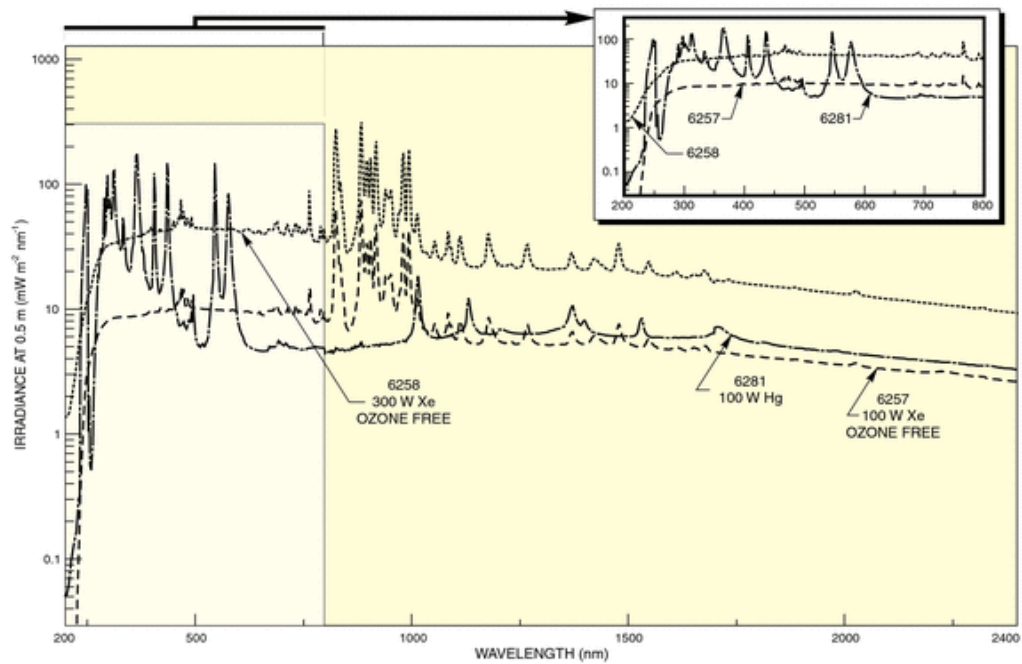


Figure A-1: Spectral output of the 300 W ozone free Xe lamp (Newport; part number 6258).

Source from manufacturer: [http://search.newport.com/?q=\\*&x2=sku&q2=6258](http://search.newport.com/?q=*&x2=sku&q2=6258)

**APPENDIX 2: SPECTRAL OUTPUT OF THE 8 W Hg LAMP (UVP; MAJOR SPECTRAL OUTPUT AT 254 NM).**

**UV Spectral Chart**  
**254nm UV without Filter**

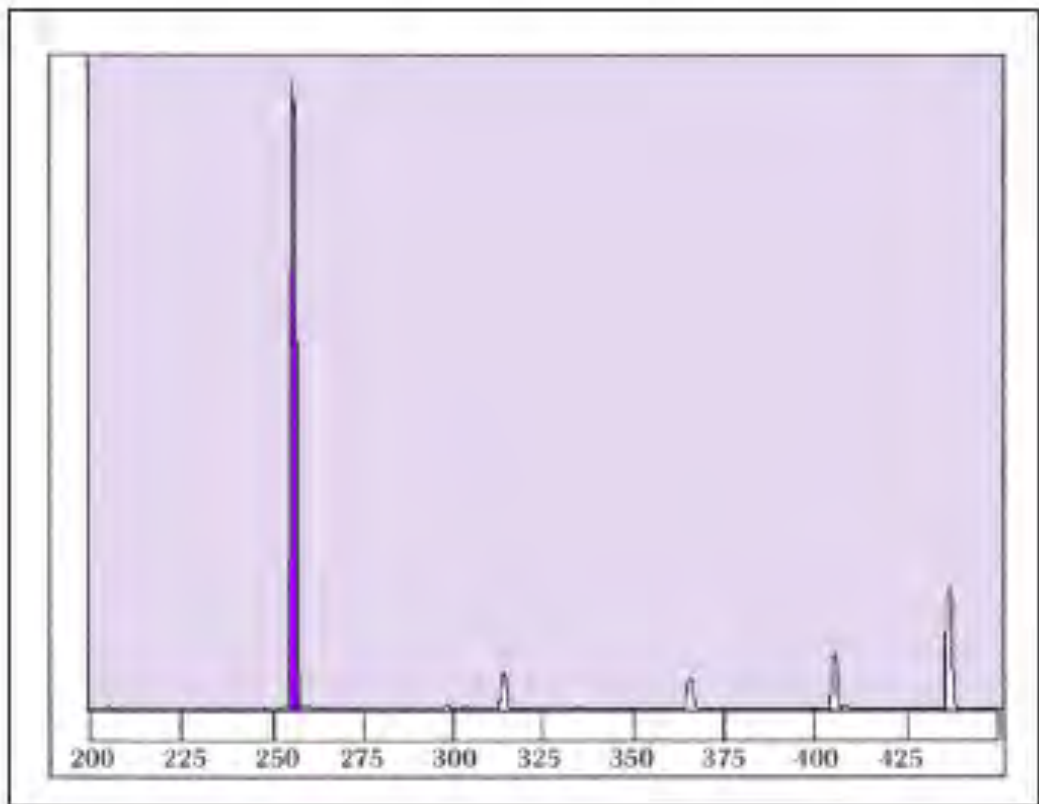


Figure A-2: Spectral output of the 8 W Hg lamp (UVP; major spectral output at 254 nm).

Source from manufacturer: <http://uvp.com/spectralcharts.html>

**APPENDIX 3: RATIO OF THE INTEGRATED LIGHT INTENSITIES OF TUNGSTEN-HALOGEN TO Xe LAMPS.**

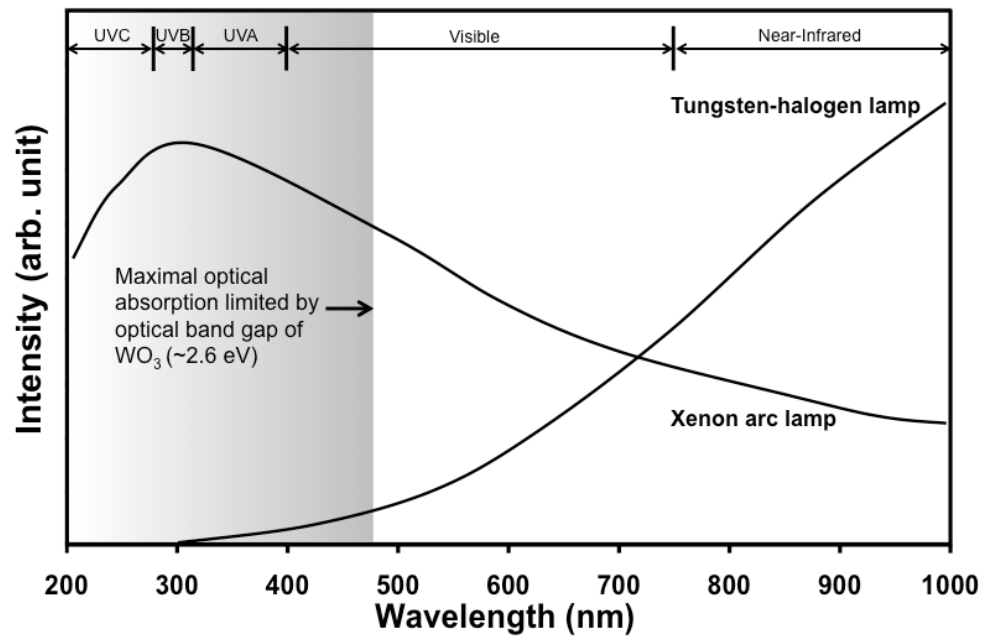


Figure A-3: Spectral output of the tungsten-halogen and Xe arc lamps [A1].

The ratio of the integrated light intensities of tungsten-halogen to Xe lamps [A1] up to the cut-off region of the band gap of 2.6 eV or 477 nm (grey area of Figure A-3), was calculated to be 1:50.

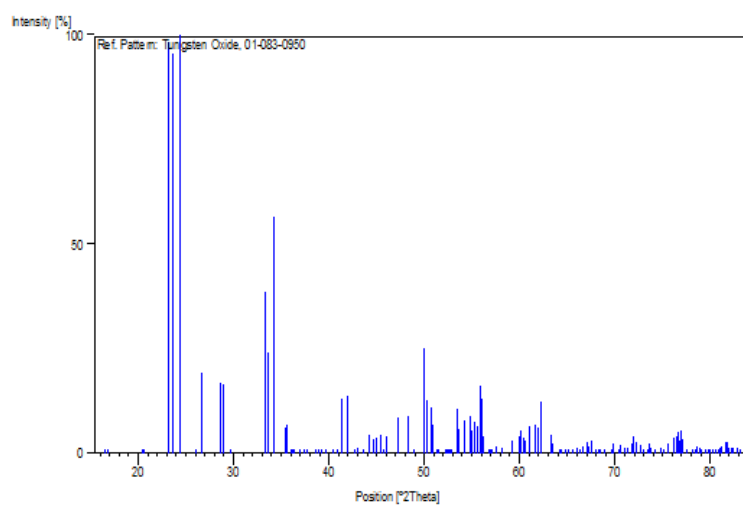
[A1] W.S. Yoo, and K. Kang, "Electrical Activation of Ultra-Shallow B and  $\text{BF}_2$  Implanted Silicon by Flash Anneal", *Nucl. Instrum. Methods Phys. Res., Sect. B*, **237**, 12—17 (2005).

**APPENDIX 4: XRD STICKPATTERN OF MONOCLINIC  $\gamma$ -WO<sub>3</sub> (SPACE GROUP: P2<sub>1</sub>/N).**

Reference code: 01-083-0950

CRYSTALLOGRAPHIC PARAMETERS

Chemical name:	Tungsten Oxide
Empirical formula:	O <sub>3</sub> W
Chemical formula:	WO <sub>3</sub>
Crystal system:	Monoclinic
Space group:	P2 <sub>1</sub> /n
Space group number:	14
a (Å):	7.3008
b (Å):	7.5389
c (Å):	7.6896
Alpha (°):	90.0000
Beta (°):	90.8920
Gamma (°):	90.0000
Volume of cell (10 <sup>6</sup> pm <sup>3</sup> ):	423.19

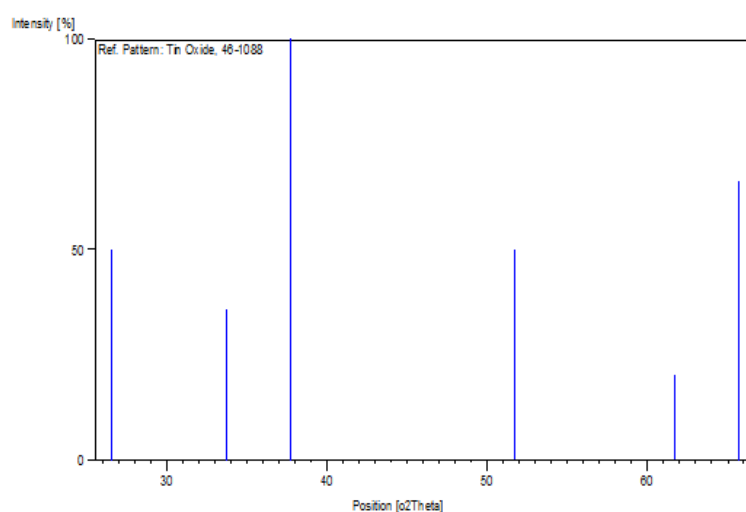
Figure A-4: XRD stick pattern of monoclinic  $\gamma$ -WO<sub>3</sub> (space group: P2<sub>1</sub>/n).

**APPENDIX 5: XRD STICKPATTERN OF TETRAGONAL SnO<sub>2</sub> (SPACE GROUP: P4<sub>2</sub>/MNM).**

Reference code: 00-046-1088

CRYSTALLOGRAPHIC PARAMETERS

Chemical name:	Tin Oxide
Empirical formula:	O <sub>2</sub> Sn
Chemical formula:	SnO <sub>2</sub>
Crystal system:	Tetragonal
Space group:	P4 <sub>2</sub> /mnm
Space group number:	136
a (Å):	4.7500
b (Å):	4.7500
c (Å):	3.1980
Alpha (°):	90.0000
Beta (°):	90.0000
Gamma (°):	90.0000
Volume of cell (10 <sup>6</sup> pm <sup>3</sup> ):	72.15

Figure A-5: XRD stick pattern of tetragonal SnO<sub>2</sub>(space group: P4<sub>2</sub>/mnm).

**APPENDIX 6: PHOTOELECTROCHEMICAL PROPERTIES OF WO<sub>3</sub> THIN FILMS PREPARED BY ELECTRODEPOSITION, *ENERGY PROCEDIA* 34 (2013) 617-626.**



10th Eco-Energy and Materials Science and Engineering  
(EMSES2012)

## Photoelectrochemical Properties of WO<sub>3</sub> Thin Films Prepared by Electrodeposition

W.L. Kwong, H. Qiu, A. Nakaruk, P. Koshy, and C.C. Sorrell\*

*School of Materials Science and Engineering  
University of New South Wales, Sydney, NSW 2052, Australia*

### Abstract

Tungsten trioxide (WO<sub>3</sub>) thin films were synthesised by electrodeposition using peroxotungstic acid as the precursor electrolyte solution for use as photoanodes in a photoelectrochemical cell for solar hydrogen applications. The films were coated at deposition potentials varying from –0.30 to –0.90 V versus Ag/AgCl in order to study the effect of the potential on the mineralogical, morphological, optical, and photoelectrochemical properties of the nanoparticulate films.

The films were composed of monoclinic WO<sub>3</sub>, the degree of crystallinity and preferred orientation of the orthogonal planes of which increased with deposition potential and associated film thickness. In contrast, increasing the deposition potential had a minimal impact on the particle sizes, which were in the range ~80-90 nm. While films deposited at the potential range of –0.30 to –0.60 V showed controlled nanostructures with thicknesses in the range 168-431 nm, increasing the deposition potential from –0.70 to –0.90 V resulted in rapid increase in film, which led to cracking from drying stress. Linear voltammetry data suggested that the optimal potential for the deposition of stable films was in the range –0.37 to –0.60 V. However, the data for the film deposited at a potential of –0.30 V indicated a film of high quality. Further, the data for the film deposited at a potential of –0.60 V indicated a film of a low quality and so this voltage represents a transition point for stable-unstable film growth and unstressed-stressed nanostructure from drying. The trends in the optical transmission properties showed that the photocatalytic activity of the films could be expected to decrease with increasing potential, thickness, and crystallinity. That is, the band gap and projected absorption edge exhibited a red shift. This was attributed to the relative effects of the surface and volume band gaps, in which the latter would increase relative to the former with increasing thickness.

The photocurrent densities reflected the effects of increasing solid volume and decreasing band gap with increasing film thickness. The exception was the reduced performance of the film deposited at the potential of –0.60 V. This outcome was attributed to the competition between the photogeneration and recombination of electron-hole pairs, where the potential of –0.60 V represents the transition point described above.

© 2013 The Authors. Published by Elsevier B.V.

Selection and peer-review under responsibility of COE of Sustainable Energy System, Rajamangala University of Technology Thanyaburi (RMUTT)

*Keywords:* Tungsten Oxide, Electrodeposition, Deposition Potential, Thin Films, Photoelectrochemical Properties

\* Corresponding author. Tel.: +61 (0)2 9385 4421; fax: +61 (0)2 9385 6565.

*E-mail address:* [c.sorrell@unsw.edu.au](mailto:c.sorrell@unsw.edu.au).

## 1. Introduction

Photoelectrochemical solar-hydrogen can be produced by the conversion of solar energy to chemical energy, which is stored in the form of hydrogen fuel. This process is environmentally clean and renewable and the principle involves the photogeneration of excitons by photosensitive semiconductor materials. These photogenerated holes and electrons oxidise and reduce water molecules, respectively, to produce oxygen and hydrogen gases, respectively, at separate electrodes of a photoelectrochemical cell [1]. In a fuel cell, the oxidation of hydrogen generates almost triple the energy obtained from fossil fuels, with water being the by-product [2,3]. The route used to synthesise semiconductor photoelectrodes is important because it determines the performance of the photoelectrochemical cell. During the past few decades, tungsten oxide ( $\text{WO}_3$ ) has become an important candidate for use as a photoanode owing to its high resistance against corrosion and photocorrosion [4] as well as its ability to absorb visible light (having a relatively small optical band gap) [5,6].

The practical implementation of  $\text{WO}_3$  photoanodes often is in the form of thin films owing to better processing flexibility and lower costs. Numerous synthesis techniques have been used to produce  $\text{WO}_3$  thin films and these include sol-gel [7], electrochemical anodisation [8], hydrothermal/solvothermal [9], cathodic electrodeposition [10], spray pyrolysis [11], magnetron sputtering [12] and thermal oxidation [13]. Of these techniques, electrodeposition is advantageous due to the following [14]:

- 1) Excellent possibility of direct coating of films on large-area conductive substrates
- 2) Simple and low-cost process, which enables large-scale production
- 3) Good potential for controlling film thickness by monitoring charge consumption during deposition

The physical properties of  $\text{WO}_3$  thin films have been demonstrated to be controllable by varying the processing conditions of electrolyte solution chemistry [10,15], during deposition [16,17], and post-deposition [18,19]. In other words, careful choice of the deposition parameters is important to control the properties of  $\text{WO}_3$  thin films and to ensure that these films are crack-free and highly crystalline and that they possess the optimal photoelectrochemical properties. The present work describes the effect of the deposition potential (voltage) on the deposition mechanisms and the resultant mineralogical, morphological, and optical properties of electrodeposited tungsten oxide thin films. The influence of these characteristics on the photoelectrochemical performance of these thin films also is analysed.

## 2. Experimental Procedure

### 2.1. Preparation of thin films

Tungsten oxide thin films were electrodeposited from peroxotungstic acid (PTA) solutions, which were prepared by dissolving tungsten foil in hydrogen peroxide. The excess hydrogen peroxide ( $\text{H}_2\text{O}_2$ ), formed upon complete dissolution of the tungsten foil, was eliminated catalytically by immersing a platinum foil into the solution. The decomposition of excess  $\text{H}_2\text{O}_2$  was accelerated by heating the solution to  $70^\circ\text{C}$  until gas evolution ceased. Clear yellow solutions of PTA were obtained by this procedure. The solutions were diluted to  $0.05 \text{ mol}\cdot\text{L}^{-1}$  (metal basis) by adding propan-2-ol and these were used as the electrolyte solutions for deposition. The pH value of the solution was 2.14 at room temperature.

A standard three-electrode electrochemical cell was employed for the sample deposition. A fluorine-doped tin oxide (FTO) substrate, Pt foil, and Ag/AgCl were used as the working, counter, and reference electrodes, respectively. All reported potential values are in relation to the reference electrode. The electrochemical cell was controlled using a potentiostat connected to a computer for datalogging. Prior to film deposition, a linear potential sweep was conducted at a scan rate of  $5 \text{ mV} \cdot \text{s}^{-1}$  and a step size of 1 mV. The depositions were done at room temperature at deposition potentials varying from  $-0.3 \text{ V}$  to  $-0.6 \text{ V}$  for a fixed deposition time of 90 min. The as-deposited samples were rinsed with distilled water, dried in air, and annealed in a muffle furnace at  $450^\circ\text{C}$  for 2 h in air (heating and initial cooling rates were  $5^\circ\text{C} \cdot \text{min}^{-1}$ ).

## 2.2. Characterisation of the films

The mineralogical analyses of the films were done using *in situ* X-ray powder diffraction (Philips X'pert Materials Powder Diffractometer,  $\text{CuK}\alpha$  radiation, 45 kV, 40 mA). The surface morphologies of the films were assessed using scanning electron microscopy (FEI Nova NanoSEM, accelerating voltage 5 kV). The film thicknesses were determined by focused ion beam milling (XT Nova Nanolab 200), followed by cross-sectional viewing at an angle of  $45^\circ$  using the NanoSEM. A UV-Visible spectrophotometer (Pelkin-Elmer Lambda 35) was used to measure the optical transmittances of the films in the wavelength region of 250 nm to 800 nm.

The same electrochemical system described above was employed for the photoelectrochemical measurements of the films.  $\text{WO}_3$  films on FTO substrates and  $0.5 \text{ mol} \cdot \text{L}^{-1}$  NaCl aqueous solution (pH = 6.27) were used as the working electrode and electrolyte, respectively. The light source was a 50 W tungsten-halogen lamp of intensity  $\sim 30 \text{ mW} \cdot \text{m}^{-2}$  (measured using a Digitech QM1587 light meter, light source-sample distance  $\sim 45 \text{ cm}$ ), chopped at a frequency of 0.05 Hz.

## 3. Results and Discussion

PTA solutions without hydrogen peroxide were unstable. Precipitation was observed readily when the PTA solutions were heated beyond the point at which gas evolution ceased and/or after a day of storage at room temperature. The instability of PTA solutions has been reported elsewhere [20,22] and the precipitate was identified as tungstic acid [22]. The addition of propan-2-ol improved the lifetime of PTA solutions and enabled their storage for more than three days without any precipitate formation.

Figure 1 shows the linear sweep voltammogram for the PTA electrolyte solution of  $0.05 \text{ mol} \cdot \text{L}^{-1}$  W concentration. The dashed lines at approximately  $-0.37 \text{ V}$  and  $-0.60 \text{ V}$ , corresponding approximately to the flattest portion of the curve, delineate the optimal potential range for the reduction of the PTA ions to tungsten oxide [23,24], as indicated by consistent quality of the films ( $-0.37 \text{ V}$  represents the minimal deposition potential required to reduce the PTA ions to tungsten oxide).

Figure 2(a) shows the SEM surfaces and cross-sectional images (insets) of the annealed films deposited at different voltages. The films consisted of irregularly shaped particles that formed a porous network. The film thicknesses (and hence the deposition rates) increased from 168 nm to 431 nm with increasing potential. The average particle sizes of the matrix grains were in the range  $\sim 80\text{-}90 \text{ nm}$  and the variations were insignificant at different deposition potentials, indicating that the nucleation and growth mechanism is not influenced significantly by the variation of deposition potential. However, the sample deposited at  $-0.60 \text{ V}$ , which is the thickest of the four, exhibited some exaggerated grain growth. This potential lies at the upper limit of the range for stable film growth, as shown in Figure 1.

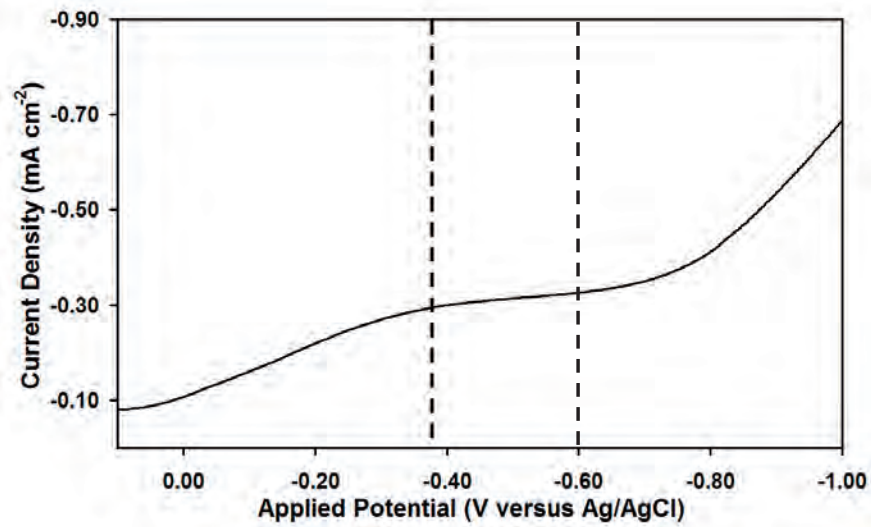


Fig. 1. Linear sweep voltammogram in peroxotungstic acid solution of  $0.05 \text{ mol} \cdot \text{L}^{-1}$  tungsten

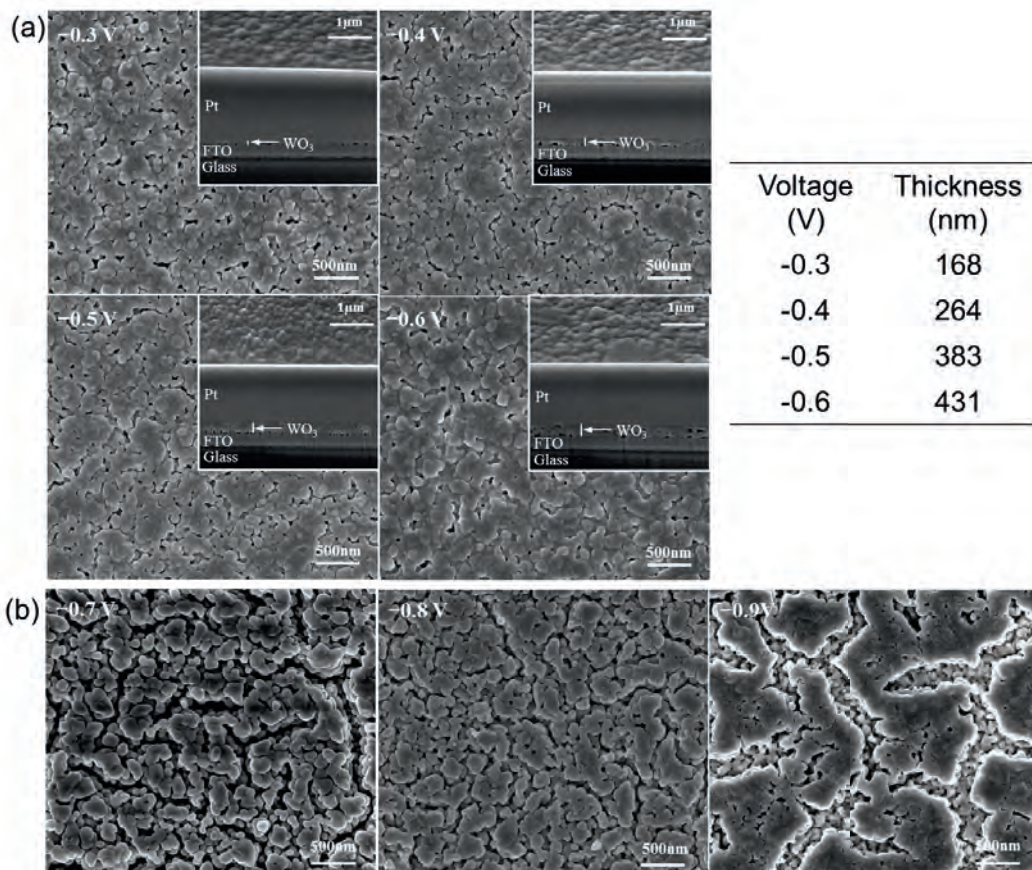


Fig. 2. SEM images of the annealed films deposited at (a)  $-0.3 \text{ V}$  to  $-0.6 \text{ V}$  and (b)  $-0.7 \text{ V}$  to  $-0.9 \text{ V}$

Increasing the deposition potential enhances the electric field strength between the working (FTO substrate) and the counter (Pt foil) electrodes and this accelerates the transport of the PTA ions for deposition at the FTO substrates, as evidenced by the overall increasing current density shown in Figure 1. The rapid increase in current density above  $-0.60$  V generated films of thickness  $>634$  nm, without significant difference in matrix particle size, and this resulted in excessive drying shrinkage and potential cracking, as shown in Figure 2(b). Hence, the potential of  $-0.60$  V also represents the upper limit to produce films of sufficient thinness to avoid drying shrinkage stresses.

The as-deposited films were amorphous, as confirmed by the characteristic broad peaks in the XRD patterns (not shown). Crystallisation of the films upon annealing was confirmed by the XRD spectra shown in Figure 3. Three major diffraction peaks at  $2\theta$  angles of  $\sim 23.1^\circ$ ,  $23.6^\circ$ , and  $24.3^\circ$  represent the (002), (020), and (200) planes, respectively, for monoclinic  $\text{WO}_3$  [25]. Some preferred crystal plane growth of the (002) and (200) planes can be seen (all three peaks are of approximately equal intensities in random orientation), as has been observed by others [10,26]. It is likely that this resulted from the easier growth of the orthogonal planes (002) and (200) relative to the non-orthogonal plane (020). The general increased peak intensities with deposition potentials are attributed to improved crystal lattice symmetry as the film grew and increased in thickness, as shown in Figure 2(a), which was associated with the relief of physical mismatch stresses at the film/substrate interface.

Figure 4 shows the optical transmittance spectra of the annealed films deposited at various potentials. It can be seen that the transmittance of the films deposited at  $-0.3$  V to  $-0.5$  V were fairly constant ( $\sim 70\%$ ) in the wavelength range of  $>400$  nm. The relatively low transmittance in the same wavelength range of the film deposited at  $-0.6$  V, which probably results from this potential representing a transition point for both stable growth and film thinness.

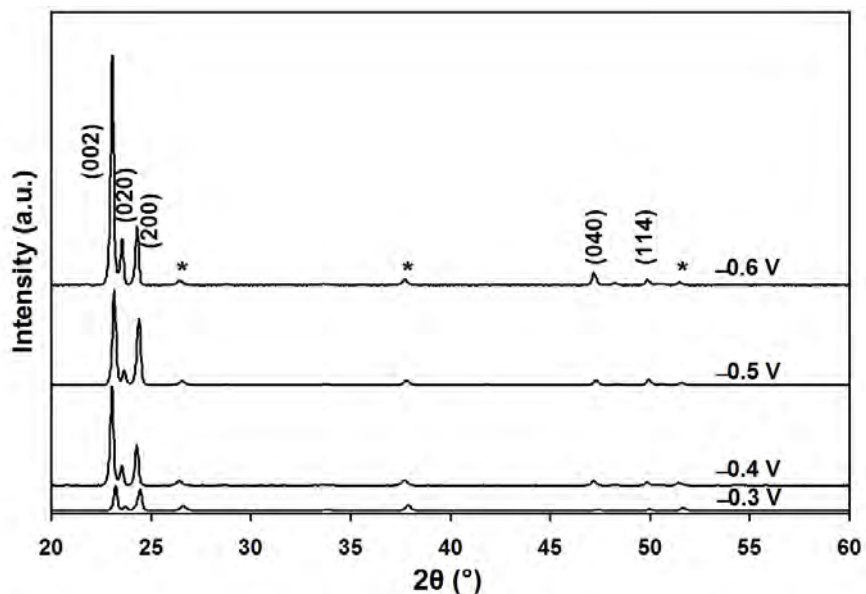


Fig. 3. XRD spectra of the annealed films deposited at various potentials (\* indicates peaks of FTO substrate)

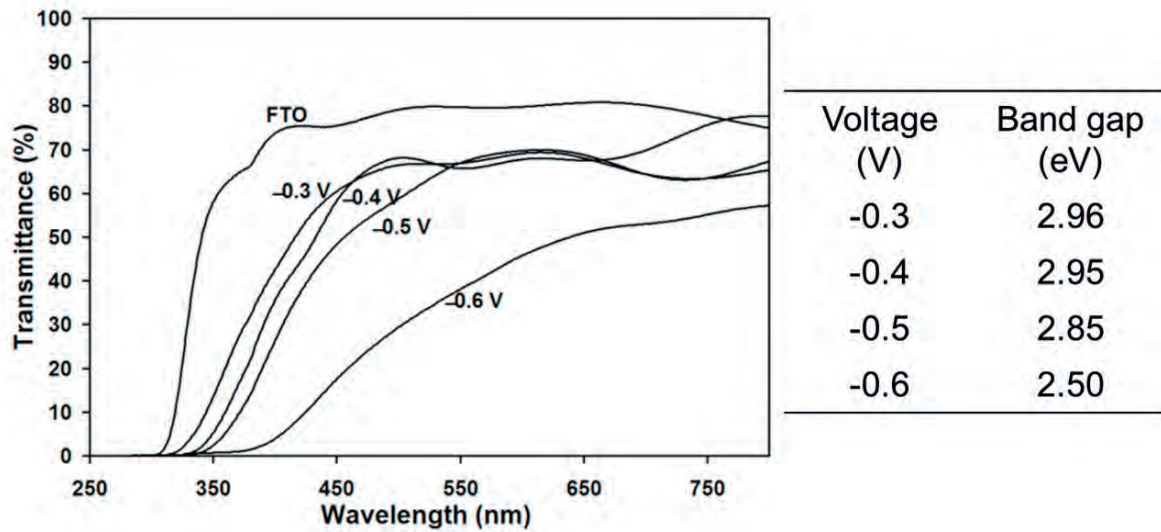


Fig. 4. Optical transmittance spectra as a function of wavelength of the annealed films deposited at various potentials

In addition, the transmission of the films shifted to longer wavelengths with increasing deposition potential. Also, the transmission of the film deposited at  $-0.6$  V was significantly lower than those of the three thinner films. The reason for the former is that the optical indirect band gap consists of contributions from both the surface and volume band gaps, where the former usually is larger with thicker films [15]. More specifically, the reason for the latter is that it is well known that such transmission curves are associated with high concentrations of grain boundary defects that serve as electron-hole recombination sites [26]. Consequently, the concentration of surface defects (relative to the total volume), which provide surface-active sites for photocatalysis, remains nearly constant while the volume, which contains recombination sites at the grain boundaries, continues to increase as the film thickness increases.

The optical indirect band gaps of the films were estimated using the method of Tauc and Menth [27]:

$$(\alpha h\nu)^{1/2} = C(h\nu - E_g) \quad (1)$$

Where:  $\alpha = -(1/d)\ln(T/100)$   
 $d$  = Film thickness  
 $T$  = Optical transmittance  
 $h$  = Planck's constant  
 $\nu$  = Frequency of light  
 $C$  = Constant  
 $E_g$  = Optical indirect band gap

The values of the optical indirect band gap ( $E_g$ ) were estimated from extrapolation from the absorption edge to the abscissa of the plot of  $(\alpha h\nu)^{1/2}$  versus  $h\nu$ . The  $E_g$  values of the films were in the range 2.50–2.96 eV, where they decreased with increasing deposition potential. Again, this variation can be attributed to the surface/volume defect considerations. Another issue related to the expected photocatalytic performance of these films is the increasing crystallinity and decreasing physical mismatch stress with increasing film thickness (where impurity, particle size, and roughness effects are irrelevant or minimal for these nanostructures). In this case, the greater crystallinity with the thicker films equates to a reduction in the defect concentration, especially at the surface, and so the photoactivity would be expected to decrease with increasing thickness.

Figure 5 shows the photocurrent densities of the films measured under chopped illumination and at a fixed applied potential of 0.70 V. The photocurrent densities dropped to nearly zero when the illumination was chopped off and rose instantly when the films were illuminated. It can be seen that the photocurrent density increased with increasing deposition potentials of  $-0.30$  V to  $-0.50$  V. This is attributed to improved light absorption at longer wavelengths owing to the decreasing optical indirect band gaps, which enhances the photogeneration of electron-hole pairs for water photolysis. However, a lower photocurrent density was obtained for the film deposited at the higher potential of  $-0.60$  V, despite its relatively low optical band gap. This is attributed to the competing mechanisms of photogeneration and recombination of electron-hole pairs. Since the potential of  $-0.60$  V represents the transition to unstable film growth and drying shrinkage stresses, this nanostructure was likely to have been more defective than those deposited at lower potentials. Hence, these defects are equated with recombination sites.

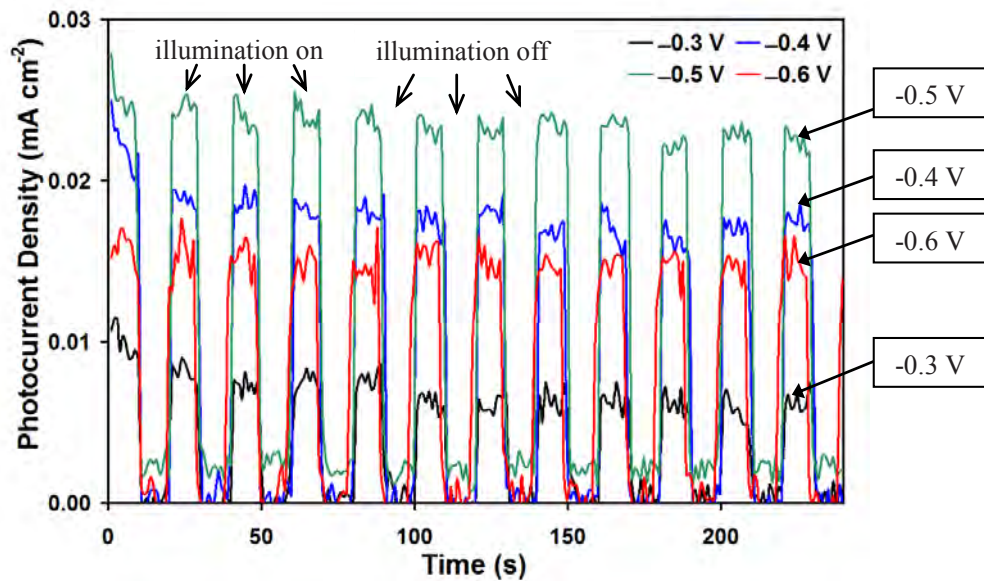


Fig. 5. Potentiostatic photocurrent densities of the annealed films measured under chopped illumination at 0.7 V vs Ag/AgCl in  $0.5 \text{ mol}\cdot\text{L}^{-1}$  NaCl aqueous electrolyte

#### 4. Conclusions

The effects of the deposition potential on the mineralogical, morphological, optical, and photoelectrochemical properties of electrodeposited  $\text{WO}_3$  thin films, electrodeposited from peroxotungstic acid (PTA) solutions, were investigated. The resultant nanostructures showed an average matrix particle size in the range ~80-90 nm and thicknesses in the range 168-431 nm. The  $\text{WO}_3$  was monoclinic and there appeared to be preferred growth of the orthogonal planes.

While increasing the deposition potential insignificantly affected the particle sizes, the deposition kinetics tended to increase, leading to rapid growth in the thickness of the films. The films were comprised of monoclinic  $\text{WO}_3$ , which increased in crystallinity with increasing thickness owing to reduction in physical mismatch stress.

A range of potentials (-0.30 V to -0.90 V) was used for film deposition. The linear sweep voltammetry data suggest that a range of -0.37 V to -0.60 V is optimal for film growth. However, the film deposited at a potential of -0.30 V appeared to be of good quality. In contrast, the deposition potential of -0.60 V appears to represent a transition between stable and unstable film growth as well as a transition between films undamaged and damaged by drying stress.

The optical transmission data revealed relatively high transmissions and low optical indirect band gaps for the films deposited at the potential range of -0.30 V to -0.50 V, with a red shift with increasing potential, associated film thickness, and crystallinity. The film deposited at the potential of -0.60 V revealed a curve consistent with a highly defective material. This trend is consistent with the relative effects from surface and volume defect conditions and associated band gaps. The significant degradation in the film deposited at the potential of -0.60 V is likely to have resulted from the fact that it represents the transition to unstable film growth and onset of drying stress.

The photocurrent densities were consistent with the effect of increasing solid volume and decreasing band gap as a function in increasing thickness, except for the film deposited at the potential of -0.60 V, which showed inferior performance. In this case, the effect was attributed to the competition between the photogeneration and recombination of electron-hole pairs, where the transition to unstable growth and residual stress suggest a significant enhancement of the defects enhancing recombination.

#### Acknowledgements

This work was supported in part by a project funded by the Australian Research Council (ARC). The authors are grateful for the characterisation facilities provided by the Australian Microscopy & Microanalysis Research Facilities (AMMRF) node at the University of New South Wales (UNSW). H. Qiu is grateful for Postgraduate Research Support Scheme funding to attend the conference at which this work was presented.

#### References

- [1] Miller EL. On Solar Hydrogen and Nanotechnology. Singapore: John Wiley and Sons; 2009.

- [2] Grimes CA, Varghese OK, Ranjan S. Light, Water, Hydrogen. The Solar Generation of Hydrogen by Water Photoelectrolysis. New York: Springer Science+Business Media; 2008.
- [3] Wallner T. Correlation between speciated hydrocarbon emissions and flame ionization detector response for gasoline/alcohol blends. *J Eng Gas Turbines Power* 2011;**133**:082801.
- [4] Hodes G, Cahen D, Manassen J. Tungsten trioxide as a photoanode for a photoelectrochemical cell (PEC). *Nature* 1976;**260(5549)**:312-13.
- [5] Hanaor DAH, Triani G, Sorrell CC. Morphology and photocatalytic activity of highly oriented mixed phase titanium dioxide thin films. *Surf Coat Technol* 2011; **205**:3658-664.
- [6] Nakaruk A, Ragazzon D, Sorrell CC. Anatase–rutile transformation through high-temperature annealing of titania films produced by ultrasonic spray pyrolysis. *Thin Solid Films* 2010;**518**:3735-742.
- [7] Solaraska R, Alexander BD, Braun A, Jurczakowski R, Fortunato G, Stiefel M et al.. Tailoring the morphology of WO<sub>3</sub> films with substitutional cation doping: effect on the photoelectrochemical properties. *Electrochim Acta* 2010, **55(26)**:7780-787.
- [8] Ng C, Ye CH, Ng YH, Amal R. Flower-shaped tungsten oxide with inorganic fullerene-like structure: synthesis and characterization. *Crys Growth Des* 2010;**10**:3794-801.
- [9] Amano F, Li D, Ohtani B. Fabrication and photoelectrochemical property of tungsten (VI) oxide films with a flake-wall structure. *Chem Comm* 2010;**46**:2769-771.
- [10] Yang B, Li HJ, Blackford M, Luca V. Novel low density mesoporous WO<sub>3</sub> films prepared by electrodeposition. *Curr Appl Phys* 2006;**6**:436-39.
- [11] Sun Y, Murphy CJ, Reyes-Gil KR, Reyes-Garcia EA, Thornton JM, Morris NA, Raftery D. Photoelectrochemical and structural characterization of carbon-doped WO<sub>3</sub> films prepared via spray pyrolysis. *Int J Hydrogen Energy* 2009;**34**: 8476-484.
- [12] Cole B, Marsen B, Miller E, Yan YF, To B, Jones K, Al-Jassim M. Evaluation of nitrogen doping of tungsten oxide for photoelectrochemical water splitting. *J Phys Chem C* 2008;**112**:5213-220.
- [13] Wang H, Quan X, Zhang Y, Chen S. Direct growth and photoelectrochemical properties of tungsten oxide nanobelt arrays. *Nanotechnol* 2008;**19**:065704.
- [14] Fulop GF, Taylor RM. Electrodeposition of semiconductors. *Annu Rev Mater Sci* 1985;**15**:197-210.
- [15] Kwong WL, Savvides N, Sorrell CC. Electrodeposited nanostructured WO<sub>3</sub> thin films for photoelectrochemical applications. *Electrochim Acta* 2012;**75**:371-80.
- [16] Baeck SH, Jaramillo T, Stucky GD, McFarland EW. Controlled electrodeposition of nanoparticulate tungsten oxide. *Nano Lett* 2002;**2(8)**:831-34.
- [17] Soliman HMA, Kashyout AB, El Nouby MS, Abosehly AM. Preparation and characterizations of tungsten oxide electrochromic nanomaterials. *J Mater Sci-Mater Electron* 2010;**21(12)**:1313-321.
- [18] Deepa M, Srivastava AK, Agnihotry SA. Influence of annealing on electrochromic performance of template assisted, electrochemically grown, nanostructured assembly of tungsten oxide. *Acta Mater* 2006;**54**:4583-595.
- [19] Deepa, M.; Srivastava, A.K.; Saxena, T.K.; and Agnihotry, S.A. Annealing induced microstructural evolution of electrodeposited electrochromic tungsten oxide films. *Appl Surface Sci* 2005;**252**:1568-580.
- [20] Shen, P.K.; and Tseung, A.C.C. Study of electrodeposited tungsten trioxide thin films. *J Mater Chem* 1992; **2(11)**:1141-147.
- [21] Shen, P.K.; Syed-bokhari, J.; and Tseung, A.C.C. The performance of electrochromic tungsten trioxide films doped with cobalt or nickel. *J Electrochem Soc* 1991;**138(9)**:2778-783.
- [22] Yamanaka K. Electrodeposited films from aqueous tungstic acid-hydrogen peroxide solutions for electrochromic display devices. *Jpn J Appl Phys* 1987;**26(11)**:1884-890.
- [23] Bijani S, Martinez L, Gabás M, Dalchiele EA, Ramos-Barrado J-R. Low-temperature electrodeposition of Cu<sub>2</sub>O thin films: modulation of micro-nanostructure by modifying the applied potential and electrolytic bath pH. *J Phys Chem C* 2009;**113**:19482-19487.
- [24] Wu L, Tsui L-K, Swami N, Zangari G. Photoelectrochemical stability of electrodeposited Cu<sub>2</sub>O films. *J Phys Chem C* 2010; **114**: 11551-1556.

- [25] Woodward PM, Sleight AW, Vogt T. Structure refinement of triclinic tungsten trioxide. *J Phys Chem Solids*; 1995, **56(10)**: 1305-315.
- [26] Zook JD. Effects of grain boundaries in polycrystalline solar cells. *Appl Phys Lett* 1980;**37(2)**: 223-26.
- [27] Tauc J, Mentha A. States in the gap. *J Non-Cryst Solids* 1972; **8-10**:569-85.

**APPENDIX 7: ELECTRODEPOSITED NANOSTRUCTURED WO<sub>3</sub> THIN FILMS FOR PHOTOELECTROCHEMICAL APPLICATIONS, *ELECTROCHIM. ACTA* 75 (2012) 371-380.**



# Electrodeposited nanostructured WO<sub>3</sub> thin films for photoelectrochemical applications

W.L. Kwong\*, N. Savvides, C.C. Sorrell

School of Materials Science and Engineering, University of New South Wales, Sydney, NSW 2052, Australia

## ARTICLE INFO

### Article history:

Received 18 October 2011  
Received in revised form 25 April 2012  
Accepted 6 May 2012  
Available online 12 May 2012

### Keywords:

Tungsten trioxide  
Electrodeposition  
Tungsten concentration  
Photocurrent  
Photoelectrochemical

## ABSTRACT

Thin films of WO<sub>3</sub> were deposited on FTO-coated glass substrates by electrodeposition using aqueous solutions of peroxotungstic acid. The effects of varying the tungsten concentration of peroxotungstic acid and deposition time on the mineralogical, microstructural, morphological, optical, and photoelectrochemical properties were determined using X-ray diffraction, scanning electron microscopy, focused ion beam milling, UV–vis spectrophotometry, and linear potentiodynamic voltammetry, respectively. The films consisted of monoclinic WO<sub>3</sub> of grain sizes in the range 77–122 nm and thicknesses in the range 258–1394 nm; the true porosities were <5%. These microstructural and morphological parameters depended largely upon the tungsten concentration and deposition time. Some preferred orientation was observed and this was considered to result from crystallographic and microstructural factors. The optical transmission data revealed significant decreases in the optical indirect band gap, from 3.05 eV to 2.60 eV, as a function of increasing film thickness. This was considered to result from differential contributions from the surface and bulk band gap components as well as compressive stress. The voltammetry data and associated Butler plot revealed the establishment of a Schottky depletion layer and a flat-band potential of +0.2 V to +0.3 V versus Ag/AgCl. Although the calculated photoconversion efficiencies were in the range 0.02–0.14%, which is commensurate with the use of a tungsten–halogen light rather than xenon, there was a trend of increasing efficiency as a function of increasing film thickness. This was attributed to decreasing band gap and increasing light absorption. The shape of the curve of the preceding data supports the conclusion of differential contributions from the surface and bulk band gap components. Finally, evidence of photolysis in the absence of an external applied potential suggests the importance of the effect of grain size on the pH and its alteration of the flat-band potential.

© 2012 Elsevier Ltd. All rights reserved.

## 1. Introduction

Methods to produce hydrogen are being pursued actively due to the potential of hydrogen to supplement or possibly replace fossil fuels in energy applications. As much as ~140 kJ g<sup>-1</sup> of energy are generated by hydrogen upon its oxidation in a fuel cell, where water is the only byproduct [1]. In contrast, conventional combustion of gasoline generates only ~43 kJ g<sup>-1</sup> [2] and CO<sub>2</sub> as byproduct. Compared to fossil fuels, the utilisation of hydrogen by combustion or in fuel cells produces no pollutants or greenhouse gases, which has allowed hydrogen to be viewed as the fuel of the future.

At present, hydrogen is produced principally by conventional electrolysis of water and steam reforming of methane, both of which are associated with greenhouse gas generation [1]. In order to develop an environmentally neutral process for hydrogen production, renewable processes, such as photoelectrochemical water

splitting, must be used. This particular approach is advantageous because it is a single-step process that utilises sunlight to decompose water, with the individual gases being produced at separate electrodes [3,4] of the cell according to the following reaction:



where h<sup>+</sup> is a photogenerated hole and e<sup>-</sup> is a photogenerated electron. For efficient cell operation, the photoelectrode must satisfy several crucial requirements, including high corrosion and photo-corrosion resistance, low electrical resistivity, sufficient radiation absorption (e.g., low optical band gap), and suitable semiconducting properties (e.g., appropriate band edge positions) [5].

Owing to shortcomings of existing materials in terms of the preceding, there is growing interest in nanostructured metal oxide thin films for photoelectrodes [6,7]. Nanostructured materials offer very high surface areas, which act as active reaction sites for the oxidation (for *n*-type semiconductors) and reduction (for *p*-type semiconductors) of water [6]. Tungsten trioxide (WO<sub>3</sub>) is an *n*-type

\* Corresponding author. Tel.: +61 2 9385 4421; fax: +61 2 9385 6565.  
E-mail address: [w.l.kwong@student.unsw.edu.au](mailto:w.l.kwong@student.unsw.edu.au) (W.L. Kwong).

semiconductor, and has been studied in the form of nanostructured thin films for a range of applications, including solar energy generation [8], photocatalysis [9], gas and biosensing [10,11], and electrochromism [12]. Also, it is being considered as an alternative to titanium dioxide (TiO<sub>2</sub>), a wide band gap (3.0–3.2 eV [13]) semiconductor. More importantly, WO<sub>3</sub> has the advantages of being stable against corrosion and photocorrosion, and it is photosensitive in the visible light region owing to its relatively small indirect optical band gap of 2.7–3.0 eV [14].

Conventional microstructures typically have the shortcoming of relatively rapid electron–hole recombination [15], which reduces or stops photolysis. Nanostructured materials offer advantages in this regard owing to the following [16]:

- (A) Upon contact of the photoanode (*n*-type semiconductor) with the electrolyte, Fermi levels of these two media align themselves to achieve thermal equilibrium, where the majority charge carriers (electrons) of the photoanode diffuse to the photoanode/electrolyte interface, thereby resulting in band-bending with a region of immobilised positively charged donor sites near the surface and a negative charge accumulation at the surface. The opposite charge accrual gives rise to an intrinsic localised electric field in this region, which is a conventional *depletion layer*.
- (B) When radiation is absorbed by the photoanode, electron–hole pairs (excitons) can be photogenerated in the depletion layer. The photogenerated excitons are separated by the bias associated with the electric field within the depletion layer, where photogenerated holes migrate to the photoanode/electrolyte interface and photogenerated electrons migrate to the photoanode. These photogenerated holes oxidise water at the photoanode/electrolyte interface, while the photogenerated electrons travel through the external circuit (hence contributing to photocurrent) to the cathode, thus reducing hydrogen ions to hydrogen gas at the cathode/electrolyte interface.
- (C) Critically, photogenerated excitons can be separated immediately outside the depletion layer within the bulk. The distance that a photogenerated hole can diffuse from this location to the edge of the depletion layer without recombining with a photogenerated electron is known as the *hole diffusion length*  $L_p$ . The sum of the hole diffusion length and the depletion layer width  $W$  is known as the *hole retrieval length*, which represents the region over which the photogenerated excitons will contribute to the photocurrent without recombining.
- (D) In contrast, in the bulk of the photoanode, there is no equivalent mechanism to enhance charge separation and so photogenerated excitons recombine readily and rapidly and hence do not contribute to the photocurrent.
- (E) The preceding comments apply to individual and multiple grains in solids, such as thin films, provided each grain is subject to irradiation and contact with the electrolyte.
- (F) It is important to note that the  $L_p$  is a key component in all photocatalytic grains because this distance must be traversed by the photogenerated hole in order to reach the intrinsic charge-separating field of the depletion layer or the surface.
- (G) In a nanostructured *n*-type photoanode, there is high probability that the grain is small relative to the hole diffusion length and thus the photogenerated holes will have sufficient lifetime to diffuse to the photoanode/electrolyte interface to oxidise water.
- (H) Moreover, in nanostructured materials, the grain size is of the same order as the wavelength of incident light. This causes the incident light to be scattered maximally at the grain boundaries, thereby increasing the optical path length and consequently the optical absorption is enhanced.

The hole diffusion length in bulk WO<sub>3</sub> is ~150 nm [15]. This means that, in principle, grains of this size or smaller can suppress electron–hole recombination since the photogenerated holes can reach the surface and oxidise the water molecule at the photoanode/electrolyte interface before they can recombine. In nanostructured form, WO<sub>3</sub> has been shown to have a *non-conventional depletion layer* (formed by a concentration gradient in the solid) in contact with the aqueous electrolyte solution, which is responsible for the mechanism of charge separation and suppression of electron–hole recombination described above. This is quite different from that of material with larger grains [17].

WO<sub>3</sub> nanostructured thin films can be fabricated by a number of techniques, including sol–gel [18], electrochemical anodisation [8,9,19,20], hydrothermal/solvothermal [10], cathodic electrodeposition [21,22], and thermal evaporation [23]. Of these, cathodic electrodeposition has the advantages of large-area deposition and low processing cost. Electrodeposited WO<sub>3</sub> nanostructured thin films have been studied previously for electrochromic applications [12,24,25] but there are few reports on their photoelectrochemical properties. Baeck et al. [21] prepared nanoparticulate WO<sub>3</sub> thin films by pulsed electrodeposition and attributed the improved photocurrents to the decrease in the particle sizes associated with enhanced surface area, which facilitated light absorption, charge transport, and surface redox activity. Yang et al. [22] modified the morphology of electrodeposited WO<sub>3</sub> through pH adjustment and found that the photoelectrochemical properties of mesoporous films were improved greatly compared to those of nonporous films due to the increased surface area of the former. These reports show that controlling the processing of WO<sub>3</sub> is important because the resultant photoelectrochemical response is influenced strongly by the associated physical, optical, and electrical properties.

The present work describes a method to synthesise WO<sub>3</sub> nanostructured thin films by electrodeposition of peroxotungstic acid. The mineralogical, physical, optical, and photoelectrochemical properties are shown to be controlled through the synthesis parameters of tungsten concentration and deposition time. The photoelectrochemical properties of WO<sub>3</sub> nanostructured thin films were investigated using 0.5 mol dm<sup>-3</sup> NaCl aqueous solution, which is similar to that of seawater [26].

## 2. Experimental

### 2.1. WO<sub>3</sub> thin film preparation

Tungsten foil (99.99%, Shanghai Leading Metal, China) was dissolved in 30% (w/w) H<sub>2</sub>O<sub>2</sub> aqueous solution (analytical reagent, UNIVAR, Australia) in a Pyrex container to form peroxotungstic acid (PTA) with composition H<sub>2</sub>[(O<sub>2</sub>)<sub>2</sub>W(O)OW(O)(O<sub>2</sub>)<sub>2</sub>] $\cdot$ *n*H<sub>2</sub>O, where (O<sub>2</sub>) denotes a peroxide ligand. Upon complete dissolution, excess H<sub>2</sub>O<sub>2</sub> was eliminated by immersing a platinum foil into the PTA solution and heating to 60 °C to catalyse the decomposition of H<sub>2</sub>O<sub>2</sub> until gas evolution ceased. The resultant PTA solution was diluted by the addition of propan-2-ol (99.5% analytical reagent, UNIVAR, Australia) to give tungsten concentrations of 0.05 mol dm<sup>-3</sup>, 0.10 mol dm<sup>-3</sup>, and 0.20 mol dm<sup>-3</sup>, which were used as the electrolytes for WO<sub>3</sub> deposition. The pH values, measured using a pH/conductivity meter (Horiba F54, Japan), were 2.14, 1.81, and 1.68, respectively. The presence of propan-2-ol is known to extend the stability of PTA solution by preventing the precipitation of an amorphous WO<sub>3</sub>-based hydrated phase [27].

The electrodeposition was performed at room temperature using a conventional three-electrode electrochemical system [21,22]. Fluorine-doped tin oxide on glass (FTO; Wuhan Ge'ao Scientific Education Instrument, China; 15 Ω sq<sup>-1</sup>; 3.0 cm × 2.5 cm), platinum foil (2.0 cm × 4.0 cm), and Ag/AgCl served as the

working, counter, and reference electrodes, respectively. The immersed areas of the FTO and Pt electrodes were  $1.5 \text{ cm} \times 1.0 \text{ cm}$  and  $2.0 \text{ cm} \times 2.0 \text{ cm}$ , respectively. All potentials reported refer to the reference electrode. A potential of  $-0.4 \text{ V}$  was applied by a computer-controlled potentiostat (EZstat Nuvant Systems, Inc.; resolution  $300 \mu\text{V}$  and  $3 \text{ nA}$  at the  $\pm 100 \mu\text{A}$  range) for time intervals up to 120 min at 30 min increments. This value of deposition potential was chosen owing to the reduction peak obtained in the linear potential sweeps prior to the deposition process. The as-deposited samples were flushed immediately with distilled water, dried for  $\sim 1 \text{ min}$  under incandescent light, placed on an aluminosilicate brick, and annealed at  $450^\circ\text{C}$  in air for 2 h (heating and initial cooling rates of  $5^\circ\text{C min}^{-1}$ ).

## 2.2. Characterisation

The phase composition was determined by *in situ* X-ray powder diffraction (Philips X'pert Materials Powder Diffractometer; Cu K $\alpha$  radiation; 45 kV; 40 mA). The microstructure was examined using scanning electron microscopy (SEM; FEI Nova NanoSEM; uncoated samples; secondary electron emission; accelerating voltage 5 kV). The grain size was measured using the line-intercept method ( $80,000\times$  photographs; 10 lines). The true porosities were determined using image analysis (*ImageJ* software, National Institutes of Health). The film thickness was determined by SEM using samples sectioned by focused ion beam milling (FIB; FEI XP200; 30 keV Ga ions). Light transmission was measured using a dual-beam UV–vis spectrophotometer (Pelkin-Elmer Lambda 35; 200–800 nm).

The photoelectrochemical properties of the samples were measured at room temperature using the same electrochemical system as described above, but using  $\text{WO}_3$  thin films on FTO substrates as the working electrodes. The PTA electrolyte solution was replaced with  $0.5 \text{ mol dm}^{-3}$  NaCl aqueous solution (pH = 6.27). Illumination from a 50 W tungsten–halogen lamp, chopped at a frequency of 0.05 Hz, was used as the light source. The intensity of the incident light was measured with a light meter (Digitech QM1587) to be  $\sim 30 \text{ mW m}^{-2}$  at a light source-to-sample distance of  $\sim 45 \text{ cm}$ . It may be noted that the light source was used for comparative test purposes only and so the measured photoelectrochemical performances are not directly comparable with those using other light sources, such as xenon. Linear potentiodynamic voltammetry was done at a scan rate of  $5 \text{ mV s}^{-1}$  with a step size of 1 mV. All of these measurements were performed with the sample housed in a light-tight box.

## 3. Results and discussion

To study the effect of tungsten concentration on the electrochemical processes that take place in the cathodic reduction of PTA electrolyte solution, the deposition current density *versus* time curves as a function of tungsten concentration (at deposition potential of  $-0.4 \text{ V}$ ) is shown in Fig. 1. The deposition current density depends on both the sheet resistance of the working electrode and the electrical conductivity of the PTA electrolyte solution. Since identical substrates were used as the working electrodes, the higher initial deposition current density in the PTA electrolyte solution of higher tungsten concentration resulted from the higher conductivity of the electrolyte. Once electrical power is applied to the electrochemical cell, the deposition current density initially decreases rapidly to approximately half its value, then more gradually, finally approaching a steady value.

The amount of decrease in deposition current density prior to its stabilisation is largely a function of the area and thickness of the film before impingement/percolation takes place. The FTO substrate is conducting while the  $\text{WO}_3$  thin film is semiconducting

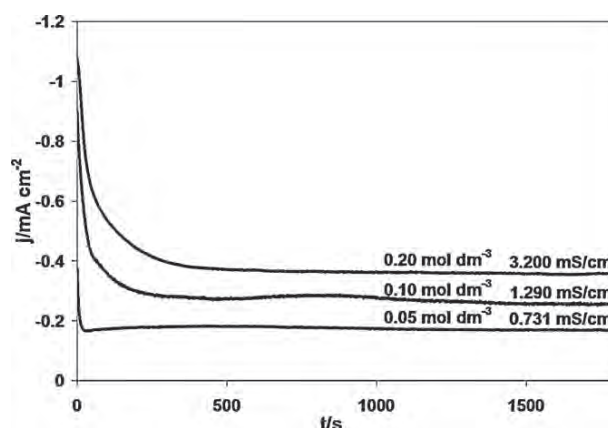


**Fig. 1.** Deposition current densities  $j$  as a function of time  $t$  and tungsten concentration of  $\text{WO}_3$  thin films deposited at  $-0.4 \text{ V}$  versus Ag/AgCl for 30 min (PTA electrolyte solution conductivities before electrodeposition also given).

and the contributions of the two components determine the relative amounts of decrease. The amount of decrease is proportional to the tungsten concentration (and hence the electrical conductivity of the solution) because semiconducting  $\text{WO}_3$  grain growth decreases the amount of exposed surface area of the conducting FTO electrode, which reduces the deposition current density.

On the other hand, the amount of time for stabilisation of the deposition current density is largely a function of the grain size of the film or, to be more precise, the time to impingement/percolation. Once impingement occurs, the substrate is completely covered by a crystalline layer of  $\text{WO}_3$ , thereby stabilising the deposition current density (subsequent grain growth has very little effect on the sheet resistivity). However, the amount of time required for impingement depends not only on the grain diameter but also on the thickness. Since the volume of a grain increases with increasing diameter and thickness, the amount of time required to form a volume of coherent layer increases with increasing tungsten concentration (the greater amount of tungsten available facilitates the growth of thicker grains). In other words, larger grain sizes are formed in films deposited from higher tungsten concentrations, which is confirmed by the SEM observations shown in Fig. 2.

Once impingement/percolation of the grains (and their volumes) has occurred, the sheet resistance of the  $\text{WO}_3$  thin film becomes constant. The final (constant) deposition current density is dominated by the tungsten concentration since the deposition current density and tungsten concentration are proportional. These data suggest the following film growth mechanism:

- (1) The nucleation and growth of monolayer-like grains of semiconducting  $\text{WO}_3$  upon the supply of power across the electrochemical cell—this corresponds to the section of the most rapid drop in the current density ( $\sim 30\text{--}60 \text{ s}$ ).
- (2) Lateral and outward growth of individual  $\text{WO}_3$  nuclei into larger particles—this corresponds to the transition region in the curve.
- (3) Impingement/percolation of individual grains and establishment of a coherent nanoscale crystalline film—this corresponds to the end of the transition region.
- (4) Nucleation on pre-existing grains, which does not affect the sheet resistance of the electrode—this corresponds to the initial region of constant current density.
- (5) Outward grain growth to increase the film thickness—this corresponds to the later region of constant current density.

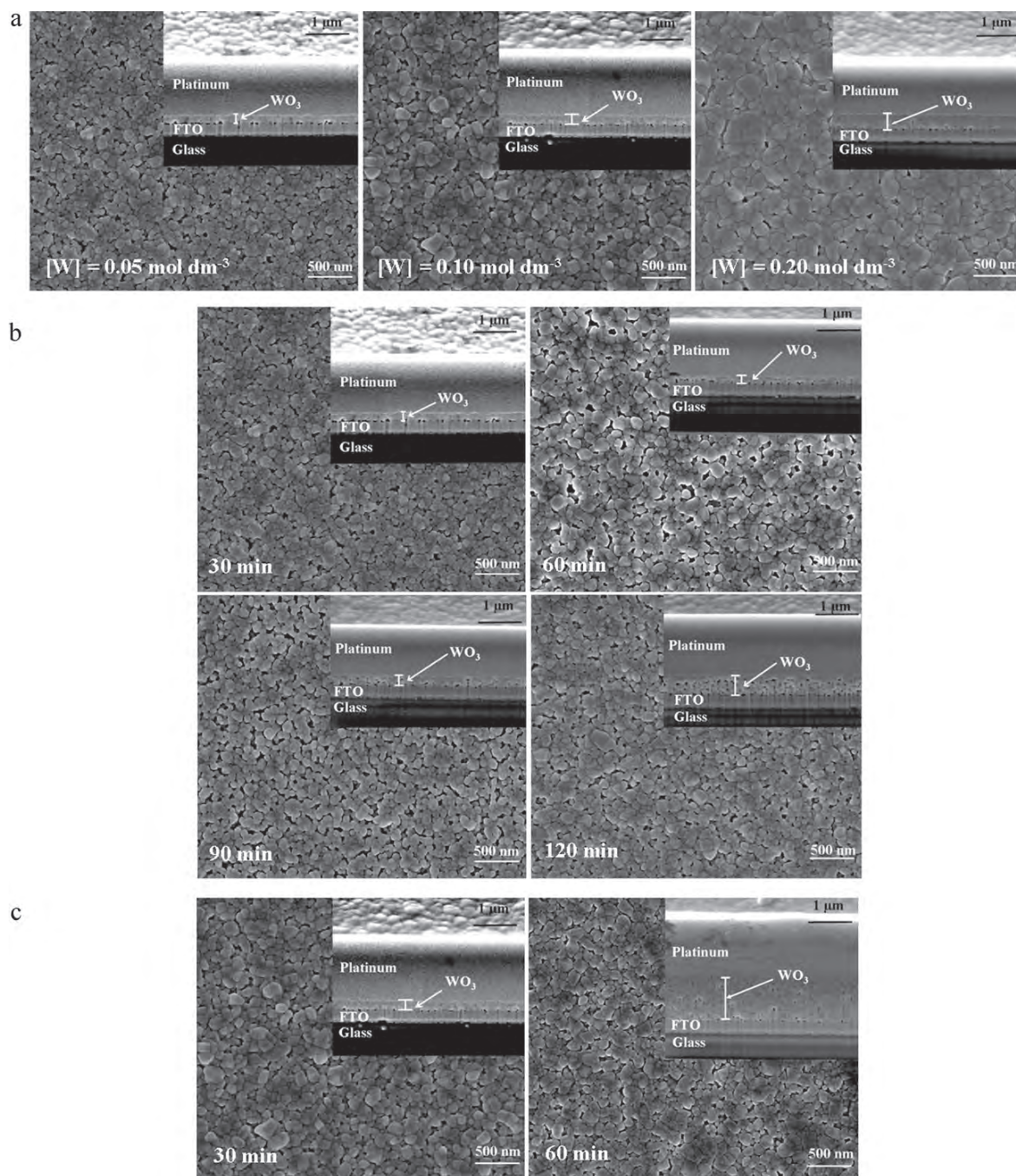


**Fig. 2.** SEM images of  $\text{WO}_3$  thin films deposited from tungsten concentrations of: (a)  $0.05\text{--}0.20\text{ mol dm}^{-3}$  for 30 min, (b)  $0.05\text{ mol dm}^{-3}$  for 30–120 min, and (c)  $0.10\text{ mol dm}^{-3}$  for 30–60 min (insets: cross-sectional views).

**Table 1**

Summary of analytical data (photoconversion efficiencies measured using tungsten–halogen lamp).

#	$[\text{W}]/\text{mol dm}^{-3}$	$t/\text{min}$	$d/\text{nm}$	Grain size/nm	Standard deviation of grain size/nm	True porosity/%	$E_g/\text{eV}$	Photoconversion efficiency/%
a	0.05	30	258	78	6	4.5	3.05	0.02
b	0.05	60	263	86	11	2.8	3.05	0.04
c	0.05	90	325	77	10	4.3	2.95	0.06
d	0.05	120	588	84	7	2.8	2.70	0.10
e	0.10	30	307	109	13	1.0	2.95	0.03
f	0.10	60	1394	105	17	1.1	2.60	0.14
	0.20	30	466	122	9	0.8	2.70	0.08

#, sample name;  $[\text{W}]$ , tungsten concentration;  $t$ , deposition time;  $d$ , film thickness;  $E_g$ , optical indirect band gap.

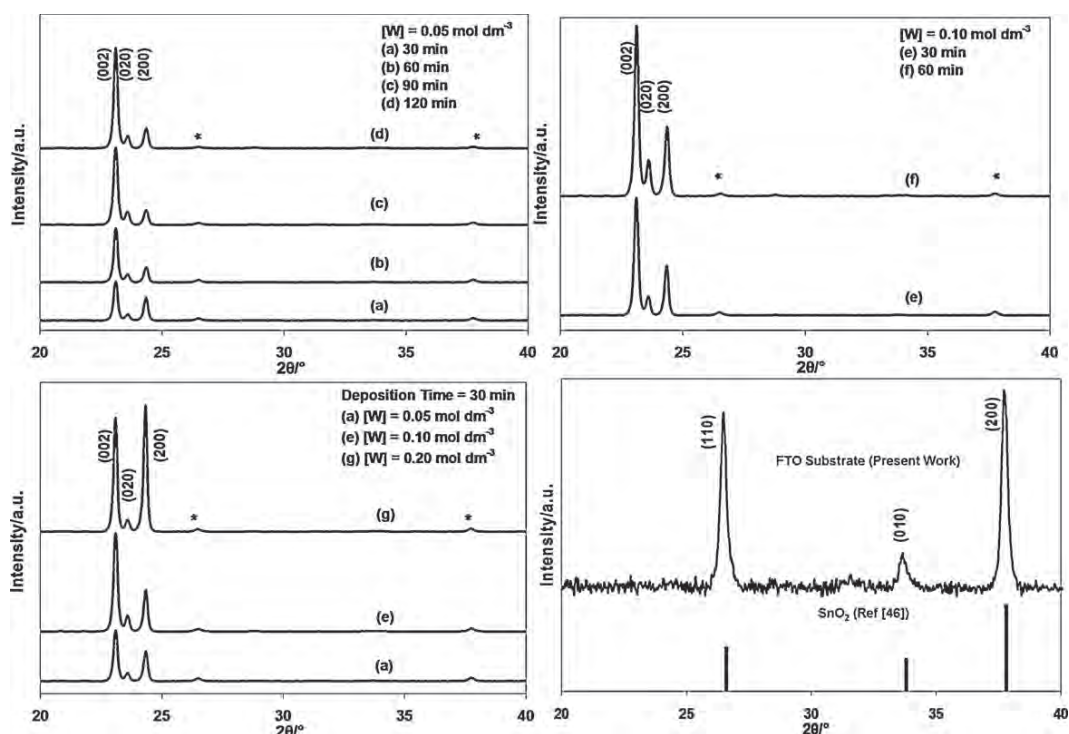


**Fig. 3.** XRD spectra of  $\text{WO}_3$  thin films deposited from tungsten concentrations of:  $0.05 \text{ mol dm}^{-3}$  for 30–120 min (a–d),  $0.10 \text{ mol dm}^{-3}$  for 30–60 min (e and f), and  $0.20 \text{ mol dm}^{-3}$  for 30 min (g). XRD spectrum of FTO substrate also given (\* indicates peak from FTO substrate). See ref. [46].

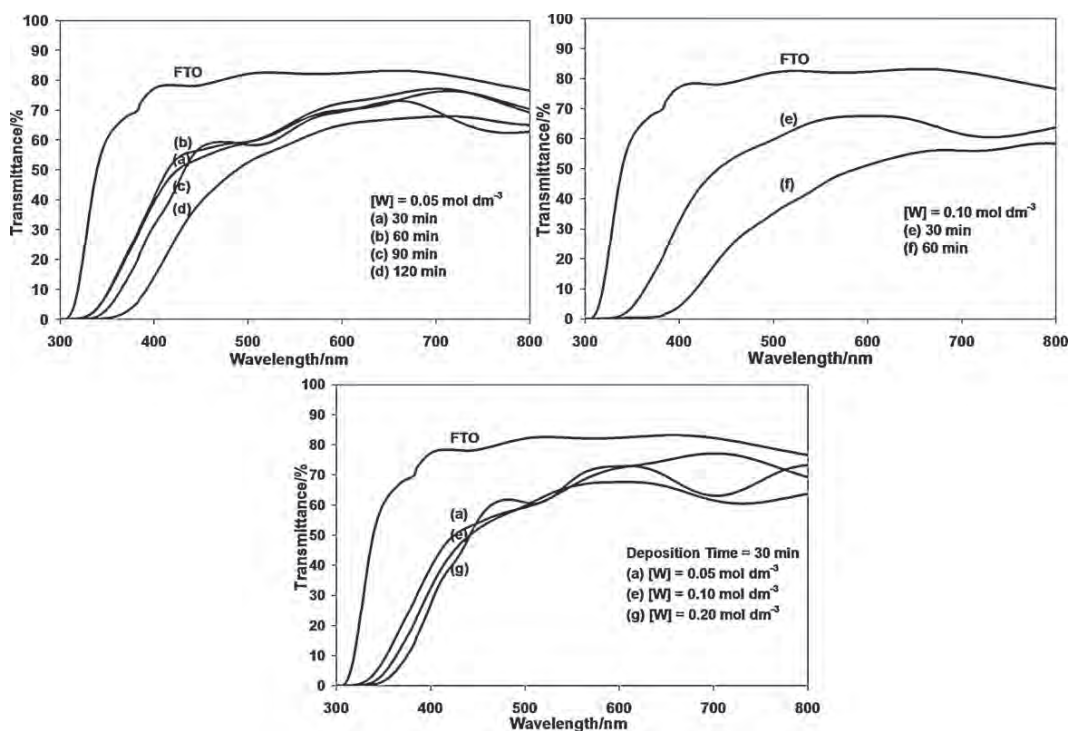


**Fig. 4.** Transmittance spectra of  $\text{WO}_3$  thin films deposited from tungsten concentrations of:  $0.05 \text{ mol dm}^{-3}$  for 30–120 min (a–d),  $0.10 \text{ mol dm}^{-3}$  for 30–60 min (e and f), and  $0.20 \text{ mol dm}^{-3}$  for 30 min (g). Transmittance spectrum of FTO substrate also shown for reference.

The SEM images of the annealed  $\text{WO}_3$  deposited from tungsten concentrations of  $0.05 \text{ mol dm}^{-3}$  to  $0.20 \text{ mol dm}^{-3}$  for various times are shown in Fig. 2. Relatively dense  $\text{WO}_3$  thin films of equiaxed nanoparticles were obtained. These nanoparticles were of average diameter of 78 nm for samples deposited from  $0.05 \text{ mol dm}^{-3}$ , increasing to 109 nm and 122 nm with  $0.10 \text{ mol dm}^{-3}$  and  $0.20 \text{ mol dm}^{-3}$ , respectively, as shown in Fig. 2(a) and Table 1. There are no discernible surface morphological changes in the  $\text{WO}_3$  thin films deposited for different times at fixed tungsten concentrations (see Fig. 2(b) and (c)). The grain size is affected by the tungsten concentration because grain growth occurs rapidly at high tungsten concentrations owing to a greater number of PTA ions and a shorter diffusion distance from the solution to the solid-liquid interface. The cross-sectional images, as seen in the insets of Fig. 2, show that the film thickness increases with both the tungsten concentration and deposition time. The reason for this is the availability of PTA ions in the electrolyte solution and the time required for the delivery of ions to the growing film. In addition, it can be seen that the increase in the average size of the  $\text{WO}_3$  grains with increasing tungsten concentration causes a decrease in the porosity of the film (see Table 1), which is consistent with the conventional mechanism of grain growth during densification [28]. However, deposition times greater than 120 min and tungsten concentrations higher than  $0.20 \text{ mol dm}^{-3}$  resulted in cracked and peeled films owing to drying stresses arising from surface dehydration [29].

According to Woodward et al. [30], from which the standard XRD pattern is derived (01-083-0951), monoclinic  $\text{WO}_3$  shows three major peaks (all ~95–100% intensity) at  $\sim 23.1^\circ$ ,  $23.6^\circ$ , and  $24.3^\circ$   $2\theta$ , which are indexed to the (002), (020), and (200) planes, respectively. The crystallographic parameters are  $a = 0.730 \text{ nm}$ ,  $b = 0.754 \text{ nm}$ ,  $c = 0.769 \text{ nm}$ ,  $\alpha = 90.0^\circ$ ,  $\beta = 90.9^\circ$ , and  $\gamma = 90.0^\circ$ . Fig. 3 shows the XRD data for the films obtained in the present work. These data suggest that some preferred orientation occurs, where the (002) plane is favoured as a function of both tungsten concentration and deposition time. However, while this is the case for all time points, it can be seen that increasing tungsten concentration favours the (200) plane at the highest level.

These data allow several conclusions about the crystal growth mechanism and morphology to be made. The growth rates in the [002] and [200] directions on the randomly oriented FTO substrates are the greatest and this is attributed to the effect of the presence of a mirror plane perpendicular to the  $k$  axis [30], which serves to assist layer-by-layer ion deposition during growth. Further, the smaller lattice parameters relevant to the (002) plane demonstrate that it is slightly more densely packed than the (200) plane. Since it is well known that close-packed planes exhibit prevailing morphologies [31,32], this explains why the (002) plane dominates over the (200) plane even though they are crystallographically equivalent. Conversely, the absence of a mirror plane relevant to the [020] direction indicates why the (020) plane has the lowest XRD peak intensity. Hence, under the influence of the mechanical stress imposed following impingement/percolation, these preferred growth directions are facilitated. These data also indicate that the effect of tungsten concentration is greater than that of the deposition time, which is not surprising since all of the XRD data are for samples that had passed the impingement/percolation onset at times less than  $\sim 7$  min, so little effect of deposition time (30–150 min) is observed. The dominant effect of the tungsten concentration in giving equivalent XRD peak intensities at the highest tungsten concentration also shows that the primary controlling effect on the crystal growth rate is the presence of the mirror plane (equivalent for both planes) and not the packing density (dominant in one plane) of the planes.

UV-vis spectrophotometry was done in order to investigate the optical properties of the  $\text{WO}_3$  thin films. Fig. 4 shows the transmittance spectra of  $\text{WO}_3$  thin films deposited from different tungsten

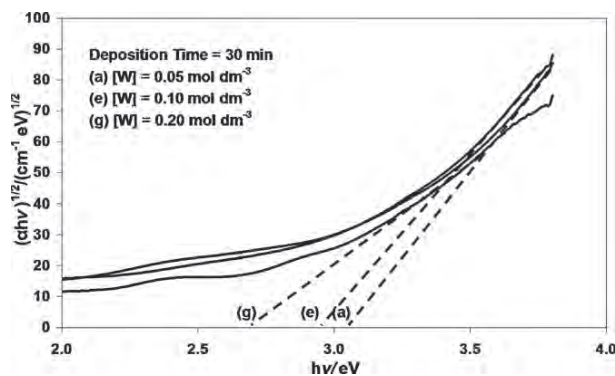


Fig. 5. Tauc plots of  $\text{WO}_3$  thin films deposited from  $0.05$  to  $0.20 \text{ mol dm}^{-3}$  tungsten for 30 min.

concentrations and times. In general, the optical transmittance of the films decreased with increasing film thickness. This is likely a result of (A) increasing absorption owing to greater cross-sectional volume and (B) reflection (scattering) owing to a higher density of grain boundaries. In addition, the absorption edge shifts to longer wavelength (red shift) as the thickness of the film increases, showing the maximal extension of the optical absorption limit to 370 nm in film (f) ( $0.10 \text{ mol dm}^{-3}$  tungsten for 60 min).

The obtained transmittance spectra were used to obtain the optical indirect band gap of  $\text{WO}_3$  thin films by drawing Tauc plots [33] according to the equation:

$$(\alpha hv)^{1/2} = C(hv - E_g) \quad (3)$$

where  $\alpha$  is the optical absorption coefficient ( $-[1/d]\ln[T/100]$ ),  $d$  is the film thickness,  $T$  is the optical transmittance,  $hv$  is the incident photon energy,  $C$  is a constant, and  $E_g$  is the optical indirect band gap energy. The optical indirect band gaps of  $\text{WO}_3$  thin films are obtained by extrapolation to the abscissa of the plot of  $(\alpha hv)^{1/2}$  against  $hv$ . Representative examples of three such plots are shown in Fig. 5. Fig. 6 shows the plot of optical indirect band gap of  $\text{WO}_3$  as a function of film thickness; these values are listed in Table 1. The optical indirect band gap of  $\text{WO}_3$  decreased from 3.05 eV to 2.60 eV for film thicknesses of 258 nm and 1394 nm, respectively. There is an inflection in the data for the thickness at  $\sim 500$  nm, which corresponds to the optical indirect band gap of  $\sim 2.6$  eV. These data suggest that the inflection is an indication of the relative effects of the volume and surface band gaps, where the surface is that of the film itself and not the grain boundary area. This is supported by the work on sputtered  $\text{WO}_3$  films by Weinhardt et al. [34], who measured a surface band gap of 3.28 eV and a bulk band gap in the range 2.5–2.6 eV. This variation arises owing to the differences in

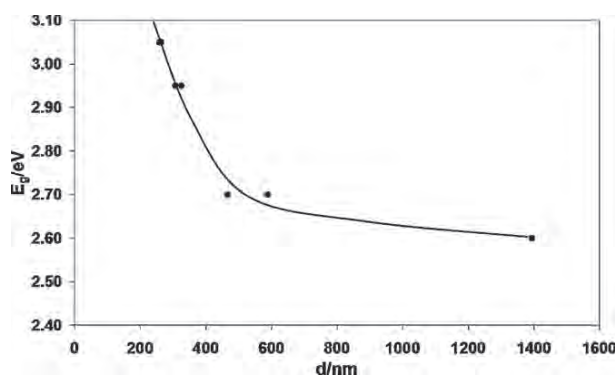
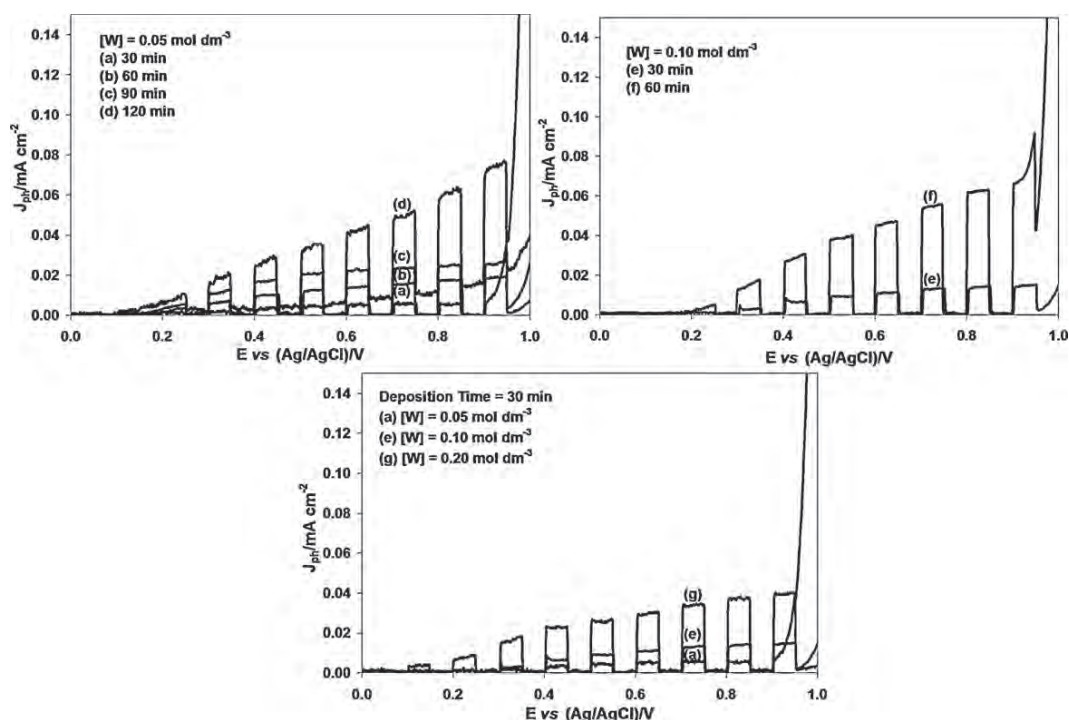


Fig. 6. Optical indirect band gaps  $E_g$  of  $\text{WO}_3$  thin films as a function of thickness  $d$ .



**Fig. 7.** Linear potentiodynamic voltammograms (photocurrent density  $J_{ph}$  versus applied potential  $E$ ), under chopped illumination, in aqueous  $0.5 \text{ mol dm}^{-3}$  NaCl (pH 6.27), of  $\text{WO}_3$  thin films deposited from  $0.05$  to  $0.20 \text{ mol dm}^{-3}$  tungsten for various times.

surface band gap and band edge position relative to those of the bulk as a result of alterations in both structure and composition. Since thicker films are associated with higher volumes, then the bulk band gap should dominate. This is confirmed by the reported bands gaps (*viz.*, bulk band gap range) of  $\sim 2.5$ – $2.7 \text{ eV}$  [34–36].

These data are important because they show that there is a threshold minimal film thickness suitable for optimal photosensitivity. Further, these data show that the overall band gap can be tailored by balancing the relative contributions of the surface and bulk band gap components by control of the film thickness.

Further, the decrease in the optical indirect band gap at the higher thicknesses is likely due to compressive stress owing to lateral grain growth established by impingement on neighbouring grains, after which outward growth normal to the substrate is facilitated. The rounded and relatively dense particles show that impingement stops grain growth within 30 min, thereby resulting in consistent grain size (for identical tungsten concentration). At the point at which the grains impinge, the only mechanisms for grain growth are lateral (which did not occur since the grains are of constant size at  $>30 \text{ min}$ ) and outward (which did occur since the film thickness increased with time). Grain impingement and the associated compressive stress would increase the repulsive electron potential and hence increase the minimal photon energy required to excite an electron from the valence band to the conduction band [37]. However, with increasing film thickness, the distance from the constrained substrate/film interface increases, so these stresses are reduced and the grains are induced towards an equilibrium stress condition. Similar experimental observations have been reported by Mohanty et al. [38] for magnetron-sputtered Al-doped ZnO thin films in which compressive stresses in the film relax with increasing thickness, resulting in a reduction in the optical band gap.

Fig. 7 shows the dependence of the photocurrent density on the applied potential measured in  $0.5 \text{ mol dm}^{-3}$  NaCl aqueous solution under chopped illumination for all samples. The

photocurrent density followed a general trend of increase with increasing applied potential owing to (A) higher band-bending at the photoanode/electrolyte interface, which leads to higher mobilities of the photogenerated excitons, and (B) expansion of the depletion width with increasing applied potential [3]. These phenomena facilitated generation and separation of excitons.

The formation of a depletion layer on the grain surface is controlled not only by the applied potential but also by the grain size relative to the width of the depletion layer. If the grain radius of a porous *n*-type photoanode is smaller than the depletion layer width, then the depletion layer will not form [16]. In this case, the mechanisms of charge transport and separation are dominated by diffusion, and these facilitate enhanced photoelectrochemical performance in contrast with that of a photoanode with large grains that suppress the recombination of photogenerated excitons [17]. On the other hand, with larger grains, such as those in the present work, a depletion layer of width smaller than the grain radius is formed. The establishment of a depletion layer can be confirmed using Butler's equation [15]:

$$J_{ph} = \phi \alpha \sqrt{\frac{2q\epsilon}{N_d}} (E - V_{fb}) \quad (4)$$

where  $J_{ph}$  is the photocurrent density at applied potential  $E$ ,  $\phi$  is the incident photon flux,  $\alpha$  is the optical absorption coefficient,  $q$  is the electron charge,  $\epsilon$  is the dielectric constant,  $N_d$  is the donor concentration, and  $V_{fb}$  is the flat-band potential. The equation can be applied according to the Schottky–Gartner model [39] by plotting  $J^2$  against the applied potential and noting whether or not a linear plot is generated. If it is linear, it can be concluded that a Schottky depletion layer has been established at the grain surface. The electric field associated with the layer contributes to the separation and migration of the photo-induced charge carriers. Fig. 8 shows representative plots that confirm a Schottky depletion layer. A flat-band potential of  $+0.2 \text{ V}$  to  $+0.3 \text{ V}$  is obtained by extrapolating plots to

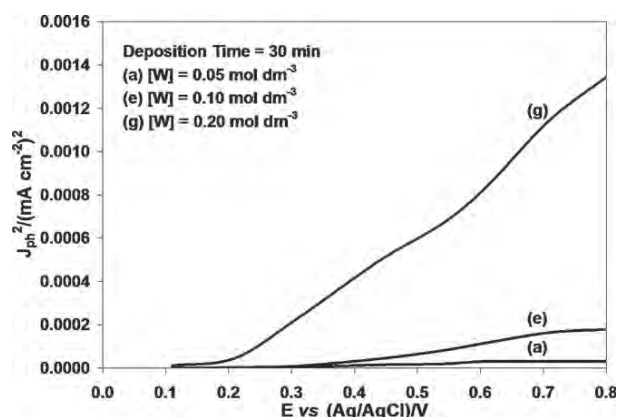


Fig. 8. Plots of  $J_{ph}^2$  as a function of applied potential  $E$  of  $WO_3$  thin films deposited from 0.05 to 0.20 mol  $dm^{-3}$  tungsten for 30 min.

the abscissa. The positive sign indicates that a biasing potential is required for water photolysis [40].

The photoconversion efficiencies were quantified using the following equation [3]:

$$\text{Photoconversion efficiency} = \left[ \frac{J_{ph}(1.23 - E)}{J_{light}} \right] \times 100\% \quad (5)$$

where  $J_{ph}$  is the photocurrent density generated at the applied potential of  $E$  under incident light of intensity  $J_{light}$ . Fig. 9 shows the photoconversion efficiencies of the  $WO_3$  thin films as a function of applied potential. The optimal range of applied potential falls in the range  $\sim 0.65$ – $0.75$  V, where the maximal photoconversion efficiencies of the films are obtained. It is interesting that film (g) appears to exhibit photolysis at applied potentials lower than the flat-band potential. If this effect is real, then it may be noted that this sample had the largest grain size of 122 nm (see Table 1). It is well known that the flat band potential depends on the pH [41]. It is less well known that the pH is influenced significantly by the particle size [42,43]. Consequently, these data suggest the importance of grain size and its effect on the net pH at the photoanode/electrolyte interface in altering the flat-band potential in order to reduce or eliminate the need for an external applied potential to achieve photolysis.

A benchmark of an applied potential of 0.70 V, which is the midpoint of the preceding range, is used commonly to compare efficiencies [20,40,44]. The photoconversion efficiencies of the films at this applied potential are plotted as a function of film thickness, as shown in Fig. 10; these values, which range from 0.02% to 0.14%,

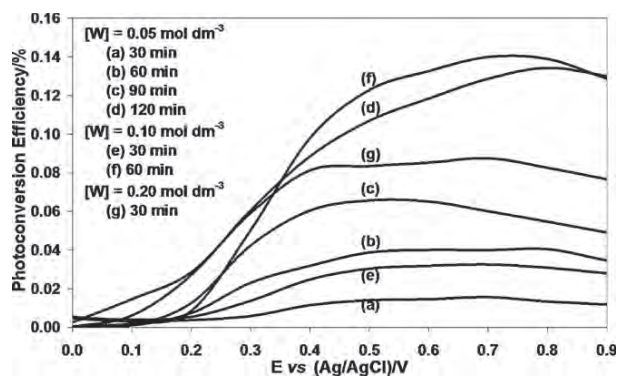


Fig. 9. Photoconversion efficiencies of  $WO_3$  thin films as a function of applied potential  $E$ .

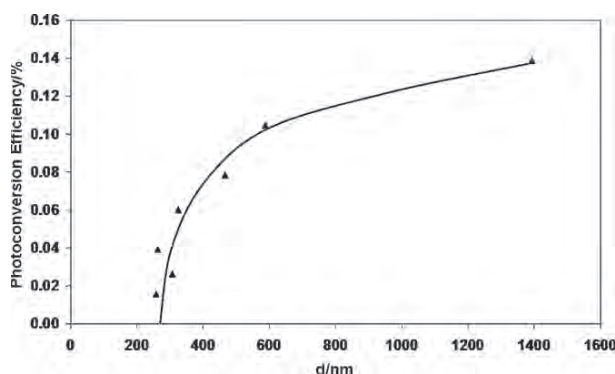


Fig. 10. Photoconversion efficiencies of  $WO_3$  thin films as a function of thickness  $d$ .

also are listed in Table 1. It can be seen that there is a clear relation between the film thickness and the photoconversion efficiency. There appear to be three regimes:

- (1)  $\sim 280$ – $300$  nm: This range is close to both the cut-off wavelength ( $\sim 300$  nm; from the light source supplier) of the halogen light source and what is likely to be the mean free path of the visible light ( $\sim 280$  nm; from the data), although these cannot be differentiated.
- (2)  $\sim 300$ – $500$  nm: This range of moderate increase in photoconversion efficiency with increasing film thickness is dominated by the surface band gap of  $WO_3$  and its rapid decrease in the overall band gap with increasing film thickness.
- (3)  $\sim 500$ – $1400$  nm: This range of gradual increase in photoconversion efficiency with increasing film thickness is dominated by the bulk band gap of  $WO_3$  and its very slow decrease in the overall band gap with increasing film thickness.

The increase in photoconversion efficiency with increasing film thickness is attributed to the decrease in the optical indirect band gap and the improved light absorption of the films. A similar inflection at  $\sim 500$ – $530$  nm in the photocurrent as a function of film thickness for  $WO_3$  films was obtained by Miller et al. [45] for films of thickness 530–2830 nm. More generally, other studies [35,45,47,48] have shown more or less similar behaviour for  $WO_3$ , where the authors have commented that increasing film thickness can result in excessive charge carrier (electron) diffusion distance [35,48], increased film resistivity [35], increased charge carrier equilibration time [35], and/or increased volume of grain boundaries as electron–hole recombination sites [47].

As tabulated in Table 1, the photoconversion efficiency of film (e) (0.10 mol  $dm^{-3}$  tungsten for 30 min) is less than that of the film (b) (0.05 mol  $dm^{-3}$  tungsten for 60 min), even though it has a larger film thickness, suggesting that the porosity of the film deposited from 0.05 mol  $dm^{-3}$  tungsten played an important role in increasing the total surface area and allowing the permeation of electrolyte into the film.

As mentioned in Section 2.2, the photoelectrochemical performances of the films in the present work are not directly comparable with those of other researchers. There are several reasons for this, including the use of (1) light sources with different spectral outputs (tungsten–halogen versus xenon lamp) [49], (2) light sources with different radiant intensities (30  $mW cm^{-2}$  in the present work versus typically 100  $mW cm^{-2}$  for xenon [18,20,45,50–54]), and (3) differing sample–light distances ( $\sim 45$  cm in the present work versus typically unstated distances). The highest photocurrent density under tungsten–halogen light at the benchmark of an applied potential of 0.70 V was measured to be  $\sim 0.05$   $mA cm^{-2}$  for film (f), as shown in Fig. 7. However, an approximation of this

maximal photocurrent density, comparable to that under xenon light, can be obtained. That is, the ratio of the integrated light intensities of tungsten–halogen to xenon light sources [49] up to the cut-off region of the band gap (2.6 eV or 477 nm) was calculated to be 1:50. Assuming a linear photoelectrochemical response of the films to the light intensities [53], the photocurrent density can be multiplied by 50 in order to approximate an equivalent value under xenon light of  $\sim 2.5 \text{ mA cm}^{-2}$ , which is mid-range for values of  $\sim 1\text{--}5 \text{ mA cm}^{-2}$  for state-of-the-art  $\text{WO}_3$  films produced by both traditional wet-chemical methods (e.g., anodisation, solvothermal, sol-gel) and advanced physical vapour deposition methods (e.g., reactive sputtering) [9,18,20,45,50–57].

#### 4. Conclusions

The mineralogical, microstructural, morphological, optical, and photoelectrochemical properties of  $\text{WO}_3$  thin films with grain size in the range 78–122 nm and thickness 258–1394 nm have been studied. Films were prepared by electrodeposition using aqueous solutions of peroxotungstic acid of tungsten concentration 0.05–0.20 mol dm<sup>-3</sup>. The growth kinetics of the films depend largely on impingement/percolation and film thickness during grain growth, which themselves depend largely on the tungsten concentration. The size of the equiaxed  $\text{WO}_3$  grain and the true porosity are dominated by the tungsten concentration but not the deposition time. However, the film thickness is dominated by both tungsten concentration and deposition time. The observation of preferred orientation in monoclinic  $\text{WO}_3$  suggests differential growth rates that are dependent upon the tungsten concentration and deposition time. The mechanisms by which this occurs are considered to derive from stress from impingement/percolation, the effect of a mirror plane on the atomic deposition, and the effect of differential packing densities of different crystallographic planes.

Optical measurements show that the light absorption increased substantially and the optical indirect band gap decreased significantly from 3.05 eV to 2.60 eV with increasing film thickness. The trend in the latter is not linear and this is attributed to differential contributions from the surface and bulk band gap components. This suggests that the overall band gap can be tailored by controlling the film thickness. A further key contribution to this effect is considered to result from the generation of compressive stress within the film. Plotting the square of the photocurrent density against the applied potential (Butler's equation) reveals the formation of a Schottky depletion layer and a flat-band potential of +0.2 V to +0.3 V, which indicates that external bias is required for photolysis.

While the photoconversion efficiencies were commensurate with the use of a tungsten–halogen light source, they increased with increasing film thicknesses. This increase is attributed to the decrease in the optical indirect band gap and the increased light absorption of the thicker films. The shape of the curve is due to the relative contributions of the surface and bulk band gap components, where the surface component is dominant at low film thickness ( $\leq 500 \text{ nm}$ ) and the bulk component at higher film thickness. There is evidence of photolysis in the absence of an external applied potential and this is considered to result from alteration of the flat-band potential owing to change in the pH as a function of particle size at the photoanode/electrolyte interface.

#### Acknowledgments

This work was supported in part by a project funded by the Australian Research Council (ARC). The authors are grateful for the characterisation facilities from the Australian Microscopy & Microanalysis Research Facilities (AMMRF) node at the University of

New South Wales (UNSW). W.L. Kwong acknowledges with thanks receipt of a UNSW International Postgraduate Award.

#### References

- [1] C.A. Grimes, O.K. Varghese, S. Ranjan, Light, Water, Hydrogen The Solar Generation of Hydrogen by Water Photoelectrolysis, Springer Science + Business Media, LLC, New York, 2008.
- [2] T. Wallner, J. Eng, Gas Turbines Power 133 (2011) 082801.
- [3] E.L. Miller, in: L. Vayssieres (Ed.), On Solar Hydrogen and Nanotechnology, John Wiley and Sons, Singapore, 2009 (Chapter 1).
- [4] J. Nowotny, C.C. Sorrell, L.R. Sheppard, T. Bak, International Journal of Hydrogen Energy 30 (2005) 521.
- [5] T. Bak, J. Nowotny, M. Rekas, C.C. Sorrell, International Journal of Hydrogen Energy 27 (2002) 991.
- [6] Y. Li, J.Z. Zhang, Laser Photonics Review 4 (2010) 517.
- [7] J.A. Glasscock, P.R.F. Barnes, I.C. Plumb, N. Savvides, Journal of Physical Chemistry C 111 (2007) 16477.
- [8] F. Di Quarto, A. Di Paola, S. Piazza, C. Sunseri, Solar Energy Materials 11 (1985) 419.
- [9] A. Watcharenwong, W. Chanmanee, N.R. de Tacconi, C.R. Chenthamarakshan, P. Kajitvichyanukul, K. Rajeshwar, Journal of Electroanalytical Chemistry 612 (2008) 112.
- [10] X. Shen, G. Wang, D. Wexler, Sensors and Actuators B 143 (2009) 325.
- [11] Z. Deng, Y. Gong, Y. Luo, Y. Tian, Biosensors and Bioelectronics 24 (2009) 2465.
- [12] H.M.A. Soliman, A.B. Kashyout, M.S. El Nouby, A.M. Abosehly, Journal of Materials Science—Materials in Electronics 21 (2010) 1313.
- [13] D.A.H. Hanaor, G. Triani, C.C. Sorrell, Surface and Coatings Technology 205 (2011) 3658.
- [14] G. Hodes, D. Cahen, J. Manassen, Nature 260 (1976) 312.
- [15] M.A. Butler, Journal of Applied Physics 48 (1977) 1914.
- [16] J.J. Kelly, D. Vanrnaekelbergh, in: G. Hodes (Ed.), Electrochemistry of Nanomaterials, Wiley-VCH, Weinheim, 2001 (Chapter 4).
- [17] C. Santato, M. Ulmann, J. Augustynski, Advanced Materials 13 (2001) 511.
- [18] R. Solarska, B.D. Alexander, A. Braun, R. Jurczakowski, G. Fortunato, M. Stiefel, T. Graule, J. Augustynski, Electrochimica Acta 55 (2010) 7780.
- [19] C. Ng, C. Ye, Y.H. Ng, R. Amal, Crystal Growth and Design 10 (2010) 3794.
- [20] W. Li, J. Li, X. Wang, S. Luo, J. Xiao, Q. Chen, Electrochimica Acta 56 (2010) 620.
- [21] S.H. Baeck, T. Jaramillo, G.D. Stucky, E.W. McFarland, Nano Letters 2 (2002) 831.
- [22] B. Yang, H. Li, M. Blackford, V. Luca, Current Applied Physics 6 (2006) 436.
- [23] H. Kim, K. Senthil, K. Yong, Materials Chemistry and Physics 120 (2010) 452.
- [24] G. Leftheriotis, P. Yianoulis, Solid State Ionics 179 (2008) 2192.
- [25] M. Deepa, A.K. Srivastava, T.K. Saxena, S.A. Agnihotry, Applied Surface Science 252 (2005) 1568.
- [26] J. Augustynski, R. Solarska, H. Hagemann, C. Santato, Proceedings of SPIE 6340 (2006) 63400J.
- [27] P.K. Shen, A.C.C. Tseung, Journal of Materials Chemistry 2 (1992) 1141.
- [28] W.D. Kingery, Introduction to Ceramics, John Wiley and Sons, New York, 1960.
- [29] X. Pang, I. Zhitomirsky, M. Niewczas, Surface and Coatings Technology 195 (2005) 138.
- [30] P.M. Woodward, A.W. Sleight, T. Vogt, Journal of Physics and Chemistry of Solids 56 (1995) 1305.
- [31] J.N. Lalena, D.A. Cleary, E. Carpenter, N.F. Dean, Inorganic Materials Synthesis and Fabrication, John Wiley and Sons, New Jersey, 2008.
- [32] R.M. Cornell, U. Schwertmann, The Iron Oxides: Structure, Properties, Reactions, Occurrences, and Uses, Wiley-VCH, Weinheim, 2003.
- [33] J. Tauc, Materials Research Bulletin 3 (1968) 37.
- [34] L. Weinhardt, M. Blum, M. Bär, C. Heske, B. Cole, B. Marsen, E.L. Miller, Journal of Physical Chemistry C 112 (2008) 3078.
- [35] B. Yang, P.R.F. Barnes, W. Bertrama, V. Luca, Journal of Materials Chemistry 17 (2007) 2722.
- [36] Y. Sun, C.J. Murphy, K.R. Reyes-Gil, E.A. Reyes-Garcia, J.M. Thornton, N.A. Morris, D. Raftery, International Journal of Hydrogen Energy 34 (2009) 8476.
- [37] Y. Sun, S.E. Thompson, T. Nishida, Strain Effect in Semiconductors: Theory and Device Applications, Springer Science + Business Media, New York, 2010.
- [38] B.C. Mohanty, Y.H. Jo, D.H. Yeon, I.J. Choi, Y.S. Cho, Applied Physics Letters 95 (2009) 062103.
- [39] W.W. Gärtner, Physical Review 116 (1959) 84.
- [40] M. Radecka, P. Sobas, M. Wierzbicka, M. Rekas, Physica B 364 (2005) 85.
- [41] N. Sato, Electrochemistry at Metal and Semiconductor Electrodes, Elsevier Science, Amsterdam, 1998.
- [42] R.E. Stevens, M.K. Carron, American Mineralogist 33 (1948) 31.
- [43] W.H. Grant, Clays and Clay Minerals 17 (1969) 151.
- [44] Y. Guo, X. Quan, N. Lu, H. Zhao, S. Chen, Environmental Science and Technology 41 (2007) 4422.
- [45] E.L. Miller, B. Marsen, B. Cole, M. Lum, Electrochemical and Solid-State Letters 9 (2006) G248.
- [46] S.R. Visi-Iwakarma, J.P. Upadhyay, H.C. Prasad, Thin Solid Films 176 (1989) 99.
- [47] S.J. Hong, H. Jun, J.S. Lee, Scripta Materialia 63 (2010) 757.
- [48] V.S. Vidyarthi, M. Hofmann, A. Savan, K. Sliozberg, D. König, R. Beranek, W. Schuhmann, A. Ludwig, International Journal of Hydrogen Energy 36 (2011) 4724.
- [49] W.S. Yoo, K. Kang, Nuclear Instruments and Methods in Physics Research Section B 237 (2005) 12.
- [50] J. Su, X. Feng, J.D. Sloppy, L. Guo, C.A. Grimes, Nano Letters 11 (2011) 203.

- [51] V. Chakrapani, J. Thangala, M.K. Sunkara, *International Journal of Hydrogen Energy* 34 (2009) 9050.
- [52] S.J. Hong, S. Lee, J.S. Jang, J.S. Lee, *Energy and Environmental Science* 4 (2011) 1781.
- [53] B. Marsen, B. Cole, E.L. Miller, *Solar Energy Materials and Solar Cells* 91 (2007) 1954.
- [54] B. Cole, B. Marsen, E. Miller, Y. Yan, B. To, K. Jones, M. Al-Jassim, *Journal of Physical Chemistry C* 112 (2008) 5213.
- [55] L. Meda, G. Tozzola, A. Tacca, G. Marra, S. Caramori, V. Cristino, C.A. Bignozzi, *Solar Energy Materials and Solar Cells* 94 (2010) 788.
- [56] W. Lee, D. Kim, K. Lee, P. Roy, P. Schmuki, *Electrochimica Acta* 56 (2010) 828.
- [57] N.R. de Tacconi, C.R. Chenthamarakshan, G. Yogeeswaran, A. Watcharenwong, R.S. de Zoysa, N.A. Basit, K. Rajeshwar, *Journal of Physical Chemistry B* 110 (2006) 25347.

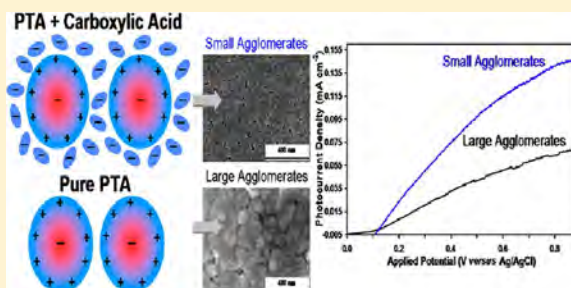
**APPENDIX 8: TUNABLE PHOTOELECTROCHEMICAL PROPERTIES BY NANOSTRUCTURAL CONTROL IN WO<sub>3</sub> THIN FILMS PREPARED BY CARBOXYLIC ACID-ASSISTED ELECTRODEPOSITION, *J. PHYS. CHEM. C* 117 (2013) 17766-17776.**

# Tunable Photoelectrochemical Properties by Nanostructural Control in WO<sub>3</sub> Thin Films Prepared by Carboxylic Acid-Assisted Electrodeposition

Wai Ling Kwong, Auppatham Nakaruk, Pramod Koshy, and Charles C. Sorrell\*

School of Materials Science and Engineering, University of New South Wales, Sydney, NSW 2052 Australia

**ABSTRACT:** The present work reports the synthesis of transparent (~60–80% transmission) WO<sub>3</sub> thin films by electrodeposition using peroxotungstic acid (PTA) solutions containing different carboxylic acids (formic, oxalic, and citric) of varying concentrations. The effects of these acids on the deposition kinetics and the morphological, mineralogical, optical, and photoelectrochemical properties of the films were investigated using scanning electron microscopy, X-ray diffraction, UV–vis spectrophotometry, and photoelectrochemical measurements. The deposited film thickness was dependent on the availability of hydronium ions (for hydrogen bonding with PTA ions) and molecular drag in the electrolytes, both of which were controlled through the use of carboxylic acids of different concentrations, degrees of dissociation, molecular weights, and associated sizes of the conjugate bases. The films consisted of agglomerates/particles (42–132 nm), the sizes of which decreased and the true porosities (<6%) of which increased with the amounts and sizes of the conjugate bases. These observations were considered to result from the separation of the PTA ions according to the amounts and sizes of the conjugate bases, the effects of which consequently changed the mechanisms of nucleation and grain growth. A nonlinear relationship between the grain sizes and the photoelectrochemical performances of the films was obtained where a maximum in the photocurrent density was observed for the film consisting of small agglomerates of ~93 nm (deposited with 0.03 mol L<sup>-1</sup> oxalic acid). This was considered to result from the positive balance of (i) surface reaction and recombination sites and (ii) the hole and electron transports in the film.



## 1. INTRODUCTION

Metal oxides have been proven to be suitable for photoelectrochemical applications owing to their high stability in aqueous solutions.<sup>1</sup> WO<sub>3</sub> is an *n*-type semiconductor that has found widespread applications in photocatalysis,<sup>2</sup> gas sensing,<sup>3,4</sup> electrochromism,<sup>5</sup> and electrodes for lithium ion batteries.<sup>6</sup> It is widely considered to be a popular candidate for photoelectrodes for photoelectrochemical cells owing to its high stability against both corrosion and photocorrosion and its relatively smaller optical indirect band gap (compared to TiO<sub>2</sub>),<sup>7</sup> which permits limited light absorption in the visible range.<sup>1</sup>

In recent years, there has been an increasing number of studies on photoelectrodes of metal oxide nanomaterials because their advantageous properties,<sup>8</sup> compared to those of their bulk counterparts,<sup>9,10</sup> include large specific surface areas, ease of material synthesis, enhanced photoelectrochemical properties due to suppressed photogenerated electron–hole recombination, and enhanced light absorption.<sup>11</sup> However, reducing the sizes of nanomaterials also may come with adverse effects on their crystallinity and electrical transport properties as a result of the increased grain boundary area and the associated increase in the number of surface defects.<sup>12,13</sup> Thus, it is important to optimize the grain size of WO<sub>3</sub> nanocrystalline

thin-film photoelectrodes by controlling the synthesis parameters in order to achieve a compromise between the microstructural parameters and the resultant optical and photoelectrochemical properties, thereby yielding optimal photoelectrochemical performance.

The size-controlled synthesis of WO<sub>3</sub> nanostructures has been reported using various techniques such as hydrothermal,<sup>13</sup> sol–gel,<sup>12,14,15</sup> hot-wire chemical vapor deposition,<sup>16</sup> arc discharge deposition,<sup>4</sup> and radio frequency magnetron sputtering.<sup>17,18</sup> Although some of these techniques require expensive instruments and/or vacuum systems, the sizes of the nanostructures have been controlled principally by thermal treatments at high temperatures (400–950 °C). An alternative to these techniques is organic-compound-assisted wet chemical synthesis. This technique combines the benefits of ecofriendly organic compounds with uncomplicated, economical, and large-area deposition methods. Sun et al. used colloidal processing at high oxalic acid concentrations with tungstic acid to produce smaller grain sizes and lower crystallinities in WO<sub>3</sub> thin films.<sup>19</sup> Meda et al. reported the size tuning of WO<sub>3</sub> grains prepared by

Received: December 16, 2012

Revised: July 26, 2013

Published: July 26, 2013

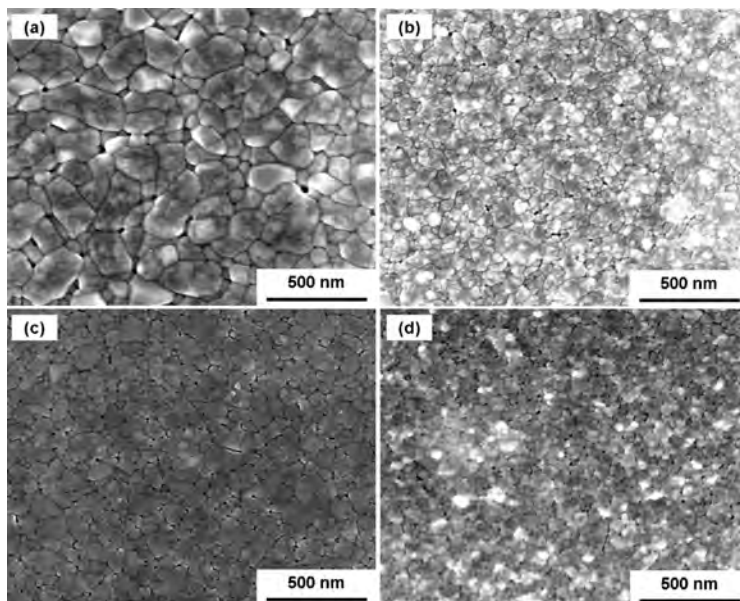


**Figure 1.** SEM images of  $\text{WO}_3$  thin films deposited from (a) pure PTA, (b) PTA with  $0.03 \text{ mol L}^{-1}$  formic acid, (c) PTA with  $0.03 \text{ mol L}^{-1}$  oxalic acid, and (d) PTA with  $0.03 \text{ mol L}^{-1}$  citric acid.

a proton exchange resin method through the addition of various organic dispersants, including ethylene glycol, poly(ethylene glycol), Igepal, Brij, and sugars, where the grain sizes decreased with increasing dispersant molecular weight.<sup>20</sup> Naseri et al. used poly(ethylene glycol) to control the topologies of  $\text{WO}_3$  nanocrystalline thin films prepared by a sol-gel method.<sup>21</sup>

There is a limited number of investigations on the size-controlled wet chemical synthesis of  $\text{WO}_3$  thin films using organic compounds, and the understanding of the mechanisms associated with the growth of the nanoparticles remains tentative. The present work reports the electrodeposition of  $\text{WO}_3$  thin films using peroxotungstic acid (PTA) containing different carboxylic acids of various concentrations in order to investigate the effectiveness of tailoring the grain sizes. The effects of these acids on the electrodeposition kinetics of  $\text{WO}_3$  thin films and the resultant morphological, mineralogical, and optical properties were investigated. The correlation and optimization of these properties for photoelectrochemical applications of the films are discussed.

## 2. EXPERIMENTAL SECTION

**2.1. Chemicals.** The chemicals used to prepare PTA solutions were tungsten foils (99.99%, Shanghai Leading Metal, China), 30% w/w hydrogen peroxide (analytical reagent, Univar), and propan-2-ol (99.5% analytical reagent, Univar). The carboxylic acids used were formic acid (99% analytical reagent, Asia Pacific Specialty Chemicals), oxalic acid dihydrate (oxalic acid, 99.5% Merck), and citric acid monohydrate (citric acid, 99–102% ACS reagent, Sigma-Aldrich).

**2.2.  $\text{WO}_3$  Thin Film Preparation.** Detailed preparation procedures for PTA solutions have been reported elsewhere.<sup>22</sup> In brief, solutions of PTA with  $0.2 \text{ mol L}^{-1}$  tungsten containing  $0.03 \text{ mol L}^{-1}$  carboxylic acid (i.e., formic, oxalic, and citric acids individually) were used as the electrolytes for film deposition. Because optimal results were obtained with the addition of

oxalic acid, its effect was studied in detail using concentrations in the range of  $0.01$  to  $0.10 \text{ mol L}^{-1}$ . All films were deposited at room temperature using a three-electrode electrochemical system with fluorine-doped tin oxide on glass (FTO; Wuhan Ge'ao Scientific Education Instrument, China;  $15 \Omega \text{ sq}^{-1}$ ;  $3.0 \text{ cm} \times 2.5 \text{ cm}$ ), platinum foil, and Ag/AgCl as the working, counter, and reference electrodes, respectively. All potentials reported refer to the reference electrode. The depositions were done at an applied potential of  $-0.4 \text{ V}$  for  $5$ – $30 \text{ min}$ .<sup>22</sup> The as-deposited films were flushed immediately with distilled water, dried in air for  $\sim 30 \text{ min}$ , placed on an aluminosilicate brick, and annealed at  $450 \text{ }^\circ\text{C}$  in air for  $2 \text{ h}$  (heating and initial cooling rate of  $5 \text{ }^\circ\text{C min}^{-1}$ ).

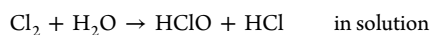
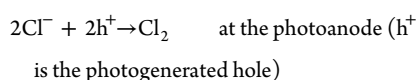
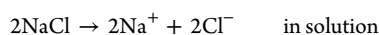
**2.3. Characterization.** The microstructures of the films were examined using scanning electron microscopy (SEM, FEI Nova NanoSEM) and atomic force microscopy (AFM, Bruker Dimension Icon). The film thicknesses were determined by sectioning the films using single-beam focused ion beam milling (FEI XP200). The true porosities of the films were determined using image analysis (*ImageJ* software, National Institutes of Health). The phase compositions of the films were determined by in situ X-ray powder diffraction (XRD, Philips X'pert Materials Powder Diffractometer) of the films. Light transmission of the films was measured using a dual-beam UV–vis spectrophotometer (Perkin-Elmer Lambda 35).

The photoelectrochemical properties of the films were measured at room temperature using the same electrochemical system as described above but using  $\text{WO}_3$  thin films on FTO substrates as the working electrodes. The PTA solutions were replaced with  $0.5 \text{ M NaCl}$  aqueous solutions (pH 6.27) as the supporting electrolyte for water photolysis.<sup>23</sup> Localized acidification by the formation of hypochlorous acid (HClO) during photoelectrolysis establishes a pH of  $\sim 2$  in the vicinity of the  $\text{WO}_3$  photoanode,<sup>23</sup> and thus it was not necessary to acidify the electrolyte. Therefore, an electrolyte pH approaching neutral can be used. The relevant reactions are

**Table 1. Analytical Data Obtained from the Different Tests on the Films Deposited for 30 min from Pure PTA and PTA Containing 0.03 mol L<sup>-1</sup> Carboxylic Acids**

electrolyte composition	electrolyte pH	electrolyte conductivity (mS cm <sup>-1</sup> )	deposition time (min)	film thickness (nm)	microstructure	grain size (nm) <sup>a</sup>	true porosity (%)
PTA	1.71	2.900	30	653	large agglomerates	131	0.87
PTA + formic acid	1.70	3.120	30	700	small agglomerates	94	1.21
PTA + oxalic acid	1.41	6.570	30	1039	small agglomerates	83	1.91
PTA + citric acid	1.84	0.009	30	319	individual particles	45	3.78

<sup>a</sup>Measured using the line-intercept method (300 000× SEM images; 10 lines).



The intensity of the incident light source (50 W tungsten-halogen lamp, chopped at a frequency of 0.05 Hz) used for exposure was measured with a light meter (Digitech QM1587) to be  $\sim 100 \text{ mW cm}^{-2}$  (light source to film distance  $\sim 25 \text{ cm}$ ). Linear potentiodynamic photocurrent measurements were made at a scan rate of  $5 \text{ mV s}^{-1}$  and a step size of  $1 \text{ mV}$ .

### 3. RESULTS AND DISCUSSION

**3.1. Effect of Types of Carboxylic Acid.** Figure 1 shows the representative surface morphologies of the films deposited from pure PTA and PTA containing different carboxylic acids at constant concentrations. It is clear that there are three types of microstructures, viz., individual particles, small agglomerates, and large agglomerates, as summarized in Table 1. The individual particles consist of discrete grains with possible subgrains whereas the agglomerates are polycrystalline, containing multiple particles. The grain (agglomerate or particle) size effect is considered to result from a process similar to the deflocculation and dispersion of colloidal particles described by Sun et al. for  $\text{WO}_3$  films prepared by oxalic acid-assisted colloid chemistry.<sup>19,24</sup> Carboxylic acids dissociate in aqueous solutions to form conjugate bases and hydronium ions.<sup>25</sup> These hydronium ions form hydrogen bonds with the highly electronegative oxygen atoms of PTA ions, thereby resulting in net positively charged states developed around the PTA ions, as shown in Figure 2. The interpretations of the effects of conjugate bases and hydronium ions bonded to the PTA ions (PTA–hydronium ion complexes) on the microstructures of the films are illustrated in Figure 3 and are as follows: (1) Pure PTA: large agglomerates of size  $\sim 131 \text{ nm}$  ( $\sim 500 \text{ nm max}$ ). In pure PTA, the absence of a separation effect by a deflocculation mechanism resulted in solute clustering and consequent rapid grain growth during annealing since the proximity of the ion complexes minimized the diffusion distances. (2) PTA containing  $0.03 \text{ mol L}^{-1}$  formic (oxalic) acid: small agglomerates of size  $\sim 94 \text{ nm}$  ( $\sim 83 \text{ nm}$ ). In PTA containing carboxylic acids whose conjugate bases have molecular weights of  $45 \text{ g mol}^{-1}$  (formate) and  $125 \text{ g mol}^{-1}$  (oxalate), (i) the hydronium ions caused deflocculation and (ii) the volumes occupied by the conjugate bases in solution contributed to some extent to increasing the degree of separation of the ion complexes. (3) PTA containing  $0.03$

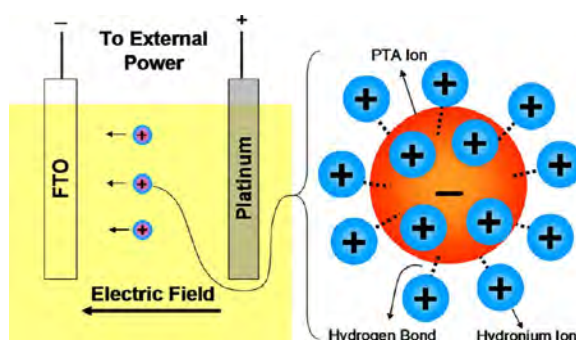


**Figure 2.** Schematic diagram of the effect of hydronium ions on positive charge imposition and consequent cathodic deposition.

$\text{mol L}^{-1}$  citric acid: individual particles of size  $\sim 45 \text{ nm}$ . In PTA containing citric acid, with a conjugate base of molecular weight  $209 \text{ g mol}^{-1}$ , deflocculation occurred, but the larger volume occupied by the citrate ions in solution effectively separated the ion complexes and increased the diffusion distance to the extent that little grain growth took place during annealing.

In summary, it can be seen that the use of carboxylic acids is inevitably effective in facilitating deflocculation and suppressing solute clustering immediately before electrodeposition. The microstructures of the annealed films can be manipulated by using carboxylic acids of different molecular weights and associated sizes of conjugate bases, where the sizes of the conjugate bases control the distribution density of the  $\text{WO}_3$  nuclei, their proximity, the corresponding diffusion distances, the tendency to undergo grain growth during annealing, and hence their susceptibility to forming solid agglomerates. Therefore, it is possible to obtain individual particles provided the conjugate bases are sufficiently large. It may be noted that the conjugate bases and hydronium ions were oxidized and effectively removed from the films upon annealing.

$\text{WO}_3$  exhibits an orthorhombic  $\rightarrow$  monoclinic phase transformation upon cooling from  $\sim 330 \text{ }^\circ\text{C}$ , and this is associated with an extremely high thermal contraction of  $\sim 13 \times 10^{-6} \text{ }^\circ\text{C}^{-1}$  from this temperature to room temperature, measured both directly and calculated from the lattice parameters.<sup>26,27</sup> Although the high thermal contraction and the phase transformation experienced during cooling from  $450 \text{ }^\circ\text{C}$  could be expected to facilitate delaminations between agglomerates, this is not supported by the observation that the film deposited from pure PTA (with the largest agglomerates) did not exhibit such delaminations. It is well known that agglomerates shrink independently during heating, so this also represents a possible mechanism of delamination.<sup>28</sup> Again, the

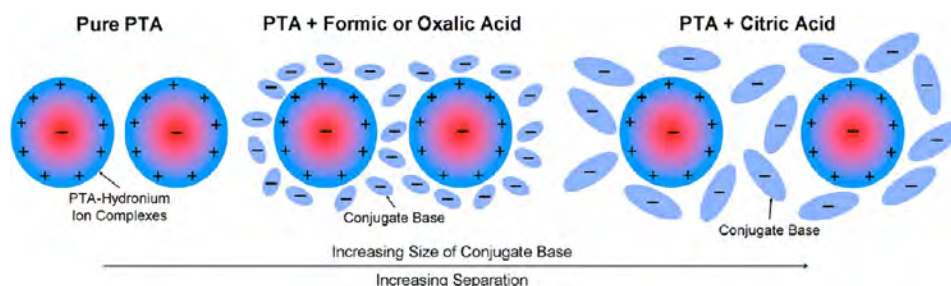


**Figure 3.** Illustration of the solute deflocculation effect from the hydronium ions and the separation effect from the conjugate bases for the different electrolyte compositions.

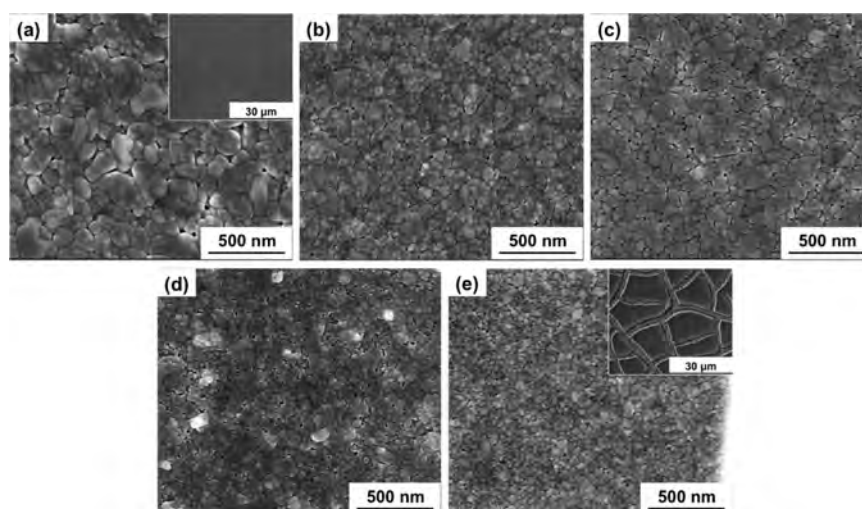


**Figure 4.** SEM images of  $\text{WO}_3$  thin films deposited from (a) pure PTA and PTA containing oxalic acid at concentrations of (b) 0.01, (c) 0.03, (d) 0.05, and (e) 0.10  $\text{mol L}^{-1}$ . Insets in a and e are at lower magnification.

SEM images in Figure 1 show that the largest agglomerates, which are in the film deposited from pure PTA, would be expected to show the largest annealing shrinkage, but no delaminations were observed.

These two observations support the conclusion of the importance of the separation effect by the conjugate bases. That is, for the film deposited from pure PTA, the absence of the conjugate bases allowed the close proximity of all particles, thereby facilitating effective intergranular bonding within and between agglomerates. For the films deposited from PTA containing formic or oxalic acid, the separation effect was such that effective bonding occurred within the agglomerates but thermal contraction and annealing shrinkage were sufficient to overcome the bonding between agglomerates. For the film deposited from PTA containing citric acid, the separation effect prevented agglomeration in the first place.

An examination of the true porosity data in Table 1 also supports the preceding conclusions. The film deposited from pure PTA had the lowest porosity, which consists of closed pores only. Despite the large agglomerate size, delaminations between agglomerates did not occur owing to the strong bonding between tightly packed agglomerates. In the films deposited with carboxylic acids, the porosities were increased by delaminations, which occurred owing to the separation effect of the conjugate bases. Hence, the porosity is a reflection of the separation effect: This separation effect on PTA containing

formic acid (stronger bonding, fewer delaminations) was less than that on PTA containing oxalic acid (weaker bonding, more delaminations). With PTA containing citric acid, the largest conjugate base, the separation between individual particles was the greatest, so the porosity followed accordingly. In this case, delaminations were not apparent because the stress was evenly distributed throughout the particle network rather than along the agglomerate boundaries.

A comparison of the thicknesses of the films in Table 1, which were deposited for 30 min from pure PTA and PTA containing different carboxylic acids, shows that the deposition thicknesses increased, remained almost constant, and decreased (with respect to pure PTA) for the depositions done in PTA containing oxalic, formic, and citric acids, respectively. The same and reverse orders are seen in the respective case for the electrolyte conductivities and pH values. These observations suggest that the deposition thickness is a function of these two variables.

According to the  $\text{p}K_{a1}$  values (logarithm of the first proton acid dissociation constant) of the acids,<sup>29–31</sup> the degree of dissociation follows the order oxalic > citric > formic acid. The partial dissociation of formic acid produces a small number of hydronium ions and therefore minimally changed the electrolyte pH compared to that of pure PTA. The increase in the pH of PTA containing citric acid suggests that the pH was affected by hydrogen bonding between the highly electronegative

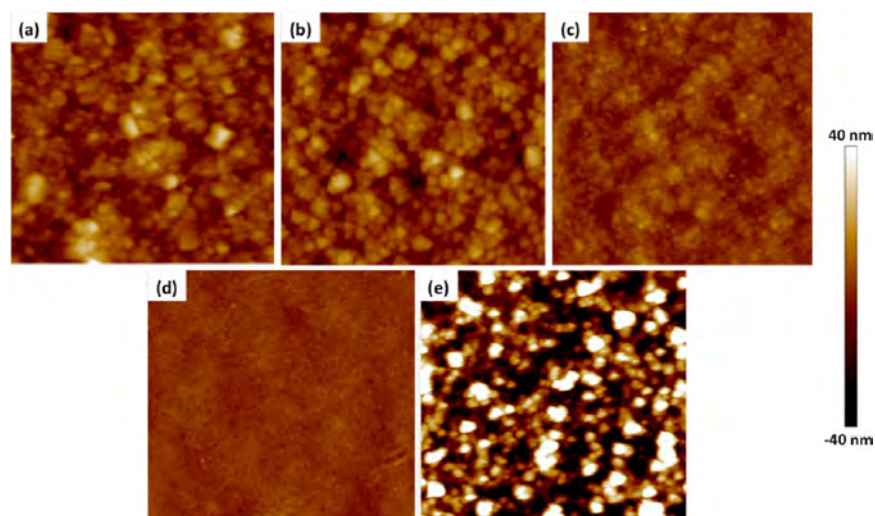


Figure 5. AFM images of  $\text{WO}_3$  thin films deposited from (a) pure PTA and PTA containing oxalic acid at concentrations of (b) 0.01, (c) 0.03, (d) 0.05, and (e) 0.10  $\text{mol L}^{-1}$ .

Table 2. Analytical Data Obtained from the Different Tests on the Films Deposited from Pure PTA and PTA Containing Oxalic Acid at Different Concentrations

film	oxalic acid concentration ( $\text{mol L}^{-1}$ )	electrolyte pH	electrolyte conductivity ( $\text{mS cm}^{-1}$ )	microstructure	grain size ( $\text{nm}$ ) <sup>a</sup>	crystallite size ( $\text{nm}$ ) <sup>b</sup>	true porosity (%)	(002) peak area	(020) peak area	(200) peak area	optical indirect band gap (eV)
A	0.00	1.71	2.90	large agglomerates	132	35	0.75	8052	1708	8885	2.90
B	0.01	1.49	5.06	small agglomerates	101	35	1.68	7997	1745	8071	2.90
C	0.03	1.41	6.57	small agglomerates	93	34	1.88	7177	1756	7780	2.95
D	0.05	1.35	8.35	small agglomerates	58	33	3.23	5281	1706	6566	3.05
E	0.10	1.25	12.50	individual particles	42	29	5.66	2700	1239	4066	3.30

<sup>a</sup>Measured using the line-intercept method ( $160,000\times$  SEM images; 10 lines). <sup>b</sup>Measured using the Debye–Scherrer's equation by averaging (002), (020), and (200) crystallite sizes.

oxygen atoms of citrates and hydronium ions, thereby reducing the availability of hydronium ions. However, the dissociation of oxalic acid produces a large number of hydronium ions, as confirmed by the decreased electrolyte pH. This created highly net positively charged PTA ions resulting from the hydrogen bonding with the hydronium ions. Under cathodically biased conditions, the PTA ions were driven by the electric field to the working electrode, where they were reduced to form tungsten oxides, hence resulting in thicker films deposited in PTA containing oxalic acid.

Furthermore, it is clear that the molecular weights and associated sizes of the conjugate bases adversely affected the deposition thickness through molecular drag in the solutions. In this case, the order is citrate > oxalate > formate (molecular weights of the ions  $209 > 125 > 45 \text{ g mol}^{-1}$ ). Since the effects of  $\text{p}K_{\text{a}1}$  values and molecular weights of the carboxylic acids show different trends with the electrolyte conductivity and pH, it is clear that they represent interdependent variables. The enhanced deposition thickness in PTA containing oxalic acid demonstrates that oxalic acid has the highest conductivity, the lowest pH, and the lowest  $\text{p}K_{\text{a}1}$  value, but its conjugate base does not have the lowest molecular weight. Therefore, it is concluded that the effect of the carboxylic acid is predominantly

electrochemical and not physical, where the electrochemical factors are the  $\text{p}K_{\text{a}1}$  values of the acids and the resultant electrolyte conductivities and pH, whereas the physical factors are the molecular weights of the acids.

**3.2. Effect of Concentrations of Oxalic Acid.** Further studies on the effect of varying the oxalic acid concentrations were carried out by considering the advantages to a synthesis process yielding an enhanced deposition thickness from PTA containing oxalic acid. Higher concentrations of oxalic acid in PTA also resulted in increasing deposition thicknesses, which are attributed to the increasing availability of hydronium ions to form hydrogen bonds with the PTA ions. However, the initial trials revealed that longer deposition times resulted in cracked and poorly adhered thick films. To avoid this, films of similar thicknesses ( $400 \pm 20 \text{ nm}$ ) were prepared where shorter deposition times ( $\leq 20 \text{ min}$ ) were applied to PTA containing higher oxalic acid concentrations. The films are named A–E according to their depositions from pure PTA and PTA containing 0.01, 0.03, 0.05, and 0.10  $\text{mol L}^{-1}$  oxalic acid, respectively.

Figures 4 and 5 present the surface morphologies of the films deposited from pure PTA and PTA containing oxalic acid of different concentrations, as examined by SEM and AFM,

respectively. The scanned areas of the AFM images were  $3 \mu\text{m} \times 3 \mu\text{m}$ . The films consist of agglomerates/particles with sizes in the range of 42–132 nm, where the size decreases with increasing oxalic acid concentration (Table 2). Varying the oxalic acid concentration reveals that the separation effect of the conjugate bases is not only size-dependent but also depends on the amount present in the PTA electrolytes. Figure 4a,e shows insets at lower magnifications, illustrating the two characteristic types of larger-scale microstructures that were observed. The microstructure in Figure 4a is relatively homogeneous in terms of the grain size distribution and true porosity. Although this image is for the film A, it is similar to the images for films B–D. In contrast, Figure 4e shows a completely different microstructure of film E, consisting of isolated islands of unagglomerated particles that were generated by excessive shrinkage of the high-surface-area/energy particles ( $\sim 39 \text{ nm}$ ) during annealing. The shrinkage appeared to have been so extreme that the microstructures of the islands are highly disrupted, with uneven steps and concavities. This is in contrast to the other agglomerated films, which consist of coarser particles of lower surface area/energy.<sup>28</sup>

Bruker NanoScope Analysis v1.4 software was used to analyze the AFM images of films A–E for information on the root-mean-square (rms) surface roughness and the surface area ratio (3D surface area/2D projected surface area).<sup>21,32</sup> The results have been plotted as a function of the grain size, as illustrated in Figure 6. Interestingly, the data for both the

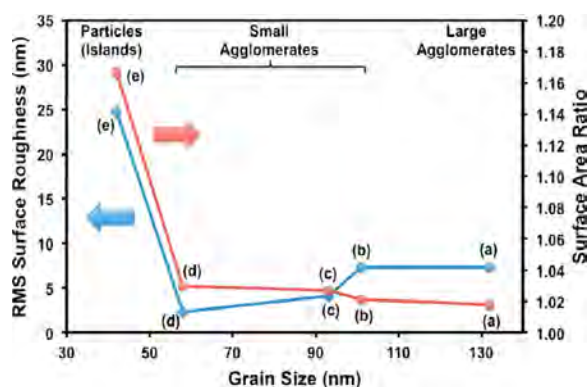


**Figure 6.** Root-mean-square surface roughnesses (blue  $\blacklozenge$ ) and surface area ratios (red  $\blacksquare$ ) as a function of the grain size of  $\text{WO}_3$  thin films deposited from (a) pure PTA and PTA containing oxalic acid at concentrations of (b) 0.01, (c) 0.03, (d) 0.05, and (e)  $0.10 \text{ mol L}^{-1}$ .

surface area ratios and the rms surface roughness are bimodal. An abrupt increase in the specific surface area with decreasing grain size is observed at the transition from small agglomerates to particles, owing to the islandlike microstructure in Film E, as explained subsequently. A small grain is an advantage in terms of the specific surface area for photoelectrochemical applications, which depend on, inter alia, the number of reaction sites for water photolysis.<sup>11</sup>

At lower oxalic acid concentrations ( $\leq 0.05 \text{ mol L}^{-1}$ ), the rms surface roughness decreases from  $\sim 7$  to  $\sim 2 \text{ nm}$  with decreasing agglomerate size, as expected. In contrast, film E, which was deposited from PTA containing the highest oxalic acid concentration ( $0.10 \text{ mol L}^{-1}$ ) and consisting of small particles rather than fine agglomerates, gives an unexpectedly high roughness of  $\sim 24.80 \text{ nm}$ . This results from the islandlike

microstructure shown in Figure 4e, which caused the AFM tip to register the uneven steps and concavities created by the annealing shrinkage. For agglomerated films A–D, which were deposited from PTA containing  $\leq 0.05 \text{ mol L}^{-1}$  oxalic acid, the trend in the rms surface roughnesses is consistent with the work of other researchers with respect to  $\text{WO}_3$  thin films synthesized by various methods and coarsened and agglomerated by annealing at  $400\text{--}950 \text{ }^\circ\text{C}$ .<sup>13,15,20,21,33</sup>

Figure 7 shows the raw XRD results of the films deposited from pure PTA and PTA containing oxalic acid at different

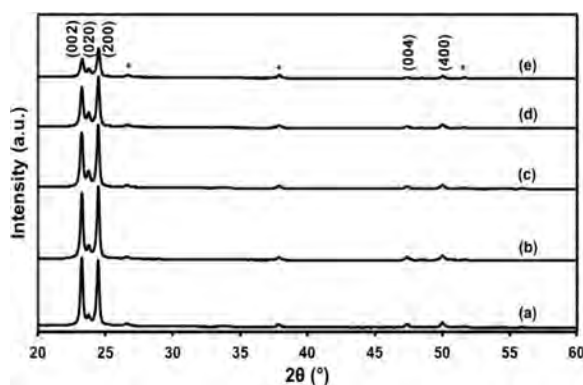


**Figure 7.** XRD spectra of monoclinic  $\text{WO}_3$  thin films deposited from (a) pure PTA and PTA containing oxalic acid at concentrations of (b) 0.01, (c) 0.03, (d) 0.05, and (e)  $0.10 \text{ mol L}^{-1}$  (\* FTO peaks).

concentrations, with major peaks at  $23.3$ ,  $23.7$ , and  $24.4^\circ 2\theta$ , which correspond to the (002), (020), and (200) planes of monoclinic  $\text{WO}_3$ ,<sup>34</sup> respectively. The contributions of the FTO (positions, intensities, and full-widths at half-maxima) are approximately equivalent for all films, so a direct comparison of  $\text{WO}_3$  films of variable thicknesses is facilitated. Compared to film A, films B–E show weaker and broader peaks with increasing oxalic acid concentrations. These data are consistent with the SEM images in Figure 4 and the data in Table 2. That is, true porosity controlled the peak intensities because it decreased the solid material area scanned by the X-ray beam. The grain size of  $< 0.5 \mu\text{m}$  is much smaller than the beam diameter of  $6.4\text{--}24 \text{ mm}$ . The areas under the three main peaks scale in inverse proportion to the true porosities, as shown in Table 2.

In contrast, for colloidal  $\text{WO}_3$  particles, Sun et al. observed that the particle size, degree of aggregation, and crystallinity decreased with increasing concentration of oxalic acid in the colloid suspension.<sup>19</sup> The first two observations were consistent with the role of the separation effect of the conjugate bases. The effect on crystallinity probably was not comparable because Sun et al. did not mention annealing their samples.<sup>19</sup>

The crystallite (subgrains comprising discrete grains) sizes of  $\text{WO}_3$ , as shown in Table 2, were estimated using the Debye–Scherrer equation by averaging those of the three major XRD reflections (002), (020), and (200).<sup>35</sup> The crystallite sizes are found to decrease from  $35$  to  $29 \text{ nm}$  with increasing oxalic acid concentration. The grain sizes, as suggested in Figure 4, show the same trend where they decrease from  $132$  to  $42 \text{ nm}$  for the same oxalic acid concentrations. These data show that the grains consist of multiple crystallites per grain ( $\sim 3.8$  crystallites/grain) in the absence of oxalic acid and approach

unity ( $\sim 1.4$  crystallites/grain) at the highest oxalic acid concentration.

Figure 8 shows the optical transmittance spectra of the films deposited from pure PTA and PTA containing oxalic acid at

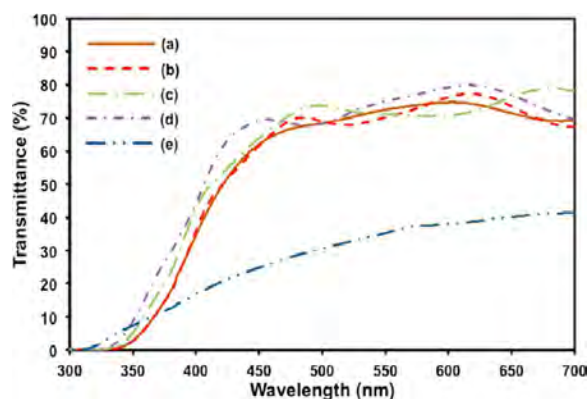


**Figure 8.** Transmittance spectra of  $\text{WO}_3$  thin films deposited from (a) pure PTA and PTA containing oxalic acid at concentrations of (b) 0.01, (c) 0.03, (d) 0.05, and (e) 0.10 mol  $\text{L}^{-1}$ .

different concentrations. In general, films A–D, which were deposited from PTA containing  $\leq 0.05$  mol  $\text{L}^{-1}$  oxalic acid, absorb light in the near-UV region ( $< 350$  nm). Their optical absorption edges fall in the wavelength range of 350–450 nm. Relatively high transmittances ( $\sim 60$ – $80\%$ ) in the wavelength range of  $> 450$  nm are observed, and these are consistent for all of the films except for film E, which shows an indistinct optical absorption edge and very low transmittance owing to the scattering losses from its having the highest rms surface roughness and porosity resulting from the channels between the islands, uneven steps, and concavities.

Blue shifts of  $< 20$  nm in the optical absorption edge, relative to film A, are observed in films B–D. The shifts follow the alphabetical order of the films, where film D shows the largest shift. This suggests that the optical band gaps of the films are dependent on the agglomerate/particle sizes. Tauc plots were used to obtain the optical indirect band gaps of the films, and the results are shown in Table 2.<sup>36</sup> The band gaps of the fabricated films vary in the range of 2.90–3.30 eV (wavelength range 376–428 nm). These values are significantly higher than the expected (theoretical) value of 2.60 eV for pure  $\text{WO}_3$ .<sup>37</sup> The principal reason for this is that the band gaps of thin films are dependent on their mineralogical and morphological characteristics, which in turn depend on the synthesis techniques employed. For electrodeposited  $\text{WO}_3$  films with thickness in the range of  $\sim 250$ – $1400$  nm, the reported band gap values were 2.60–3.30 eV, with lower band gaps being measured for thicker films.<sup>22,38,39</sup> Similar trends between the band gap and film thickness also have been reported for  $\text{WO}_3$  films synthesized using other techniques.<sup>40–42</sup> Films with band gaps close to the theoretical value have been reported to have typical thicknesses of several micrometers.<sup>43–45</sup> The main reason for these variations lies in the effect of residual stress on the thin films owing to thermal expansion mismatch between film and substrate as well as grain impingement in the film. Although these residual stresses give rise to structural imperfections and defects, which are known to affect the band gap,<sup>22,46–50</sup> these stresses decrease as the distance from

the substrate to the film surface increases in thicker films, thus lowering the band gap. More generally, the relevant effects, including macrostructural and microstructural, on the band gap are as follows:

**Bulk chemistry:** All of the films had the same bulk composition, so this effect should not be relevant.

**Defect chemistry:** It is known that dopants affect the optical band gaps of materials.<sup>51–53</sup> Although no dopants were added, it was possible that contamination from Sn, F, Na, Ca, and/or Si might have occurred owing to diffusion from the FTO substrates during annealing. However, because all of the films were subjected to the same annealing conditions, this effect should be minimal or absent.

**Mineralogy:** There are five known atmospheric-pressure polymorphs of  $\text{WO}_3$ ,<sup>27</sup> two of which are stable at room temperature ( $15$ – $25$  °C) and one of which could be quenched from the annealing temperature ( $450$  °C). However, the X-ray diffraction data show that only the monoclinic polymorph is present, so this effect should not be relevant.

**Macrostructure:** The variations in structure, composition, and grain-impingement-induced compressive stress as a function of film thickness are known to affect the band gaps of materials.<sup>22,46–50</sup> However, because the film thicknesses are similar ( $400 \pm 20$  nm), this effect should not be significant.

**Microstructure:** The films consist of interconnected networks of grains in which the grain boundary areas (within the bulk and at the exposed surface) increase with decreasing grain size and increasing porosity. The increase in these grain boundary areas, which represent terminating structural and bonding regions and discontinuities in the lattice order, is known to increase the band gaps of materials.<sup>12,18,24,54</sup> Table 2 shows that the true porosity and the grain size vary with the amount of oxalic acid present in PTA. The associated variation in grain boundary areas would be expected to be relevant because these affect the proportion of defects.

In light of the preceding brief survey, it is probable that the principal factor affecting the band gap is the density of the defects associated with grain boundary areas.

**3.3. Photoelectrochemical Tuning by Microstructural Control.** The linear potentiodynamic photocurrent density measurements of the films deposited from pure PTA and PTA containing oxalic acid at different concentrations are shown in Figure 9. Effective photocurrents were measured as the

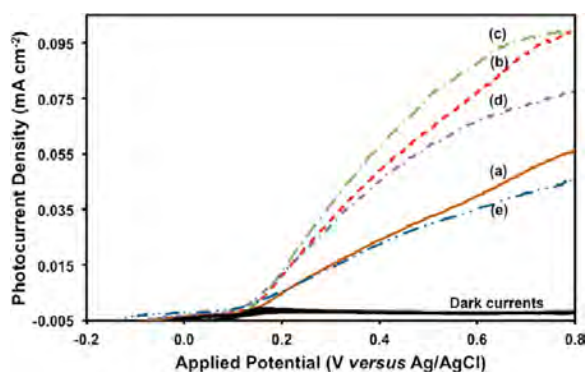


**Figure 9.** Linear potentiodynamic photocurrent densities of  $\text{WO}_3$  thin films deposited from (a) pure PTA and PTA containing oxalic acid at concentrations of (b) 0.01, (c) 0.03, (d) 0.05, and (e) 0.10 mol  $\text{L}^{-1}$ ; dark currents (measured without illumination) also are shown.

difference between photocurrents (with illumination) and dark currents (without illumination). It has been shown that the use of sodium chloride can stabilize the photoelectrochemical performance of  $\text{WO}_3$  photoanodes by avoiding the formation of a passivating layer of peroxy (O–O) species on the surface of the photoanodes, which is favored when commonly used acids are employed as supporting electrolytes to lower the electrolyte pH.<sup>23,55,56</sup> It may be noted that up to ~20% of the dark currents may be provided by chlorine gas formation (“...about 20% of the current efficiency.”)<sup>23</sup> Also, because Xe light sources, which normally are used, and tungsten-halogen light sources produce significantly different spectral outputs, it is relevant to note that the integrated intensities of these two sources over the wavelengths absorbed below the minimal band gap of  $\text{WO}_3$  film of ~2.90 eV (~428 nm) differ by a factor of approximately 50.<sup>57</sup> That is, the reported photocurrent densities were underestimated 50-fold (relative to the standard AM1.5G using a Xe light). Gaussian-shaped peaks, which correspond to electrochromic reactions of  $\text{WO}_3$  films, are barely visible in the potentiodynamic scans in the present work owing to (i) the starting potential of –0.2 V versus Ag/AgCl, which is close to the peak potentials that occur in the typical range of ~–0.2 V to –0.1 V versus Ag/AgCl,<sup>32,58–60</sup> and (ii) the relatively low scan rate of 5 mV s<sup>–1</sup>, which is much lower than the typical rate of >50 mV s<sup>–1</sup> reported in the literature.<sup>61–64</sup>

There were various microstructural (and structural) variables that influenced the photoelectrochemical results of the films, as summarized in Table 3. Decreasing grain sizes are beneficial in

**Table 3. Effect of Decreasing Grain Size on Photoelectrochemical (PEC) Performance Factors and Associated Photocurrent Densities of  $\text{WO}_3$  Thin Films**

microstructural variable	PEC performance factor	effect of decreasing grain size on	
		PEC performance factor	photocurrent density
specific surface area	number of reaction sites	increase	increase
	number of recombination sites	increase	decrease
grain radius	hole transport	increase	increase
grain boundary distribution density	number of electron transport barriers	increase	decrease

(i) providing large specific surface areas and the associated number of reaction sites (oxygen vacancies)<sup>65</sup> for water photolysis and (ii) improving hole transport because the holes photogenerated in the outermost grains travel a shorter distance to the photoanode/electrolyte interface and oxidize water before they can recombine with the photogenerated electrons.<sup>11</sup> Vacancy filling by oxidation may degrade the photoelectrochemical activity owing to the reduced number of reaction sites.<sup>66</sup> The hole transport is moderated by the hopping distance, where long distances require more energy than short ones.<sup>67</sup> However, the large specific surface area also is associated with a high fraction of dangling bonds owing to the terminations of the crystal continuity.<sup>68</sup> These dangling bonds introduce deep localized levels in the energy band gap, which can trap photogenerated electron–hole pairs, thereby increasing their probabilities of surface recombination.<sup>69,70</sup> These undesirable dangling bonds may be removed by surface

passivation.<sup>69</sup> For photogenerated electrons, the grain boundaries also act as weak links that hinder electron transport to the substrate.<sup>71</sup> It is well known that high-angle grain boundaries are associated with greater lattice mismatch and higher interfacial energies than low-angle grain boundaries.<sup>28</sup> Consequently, the greater the grain boundary angle, the weaker the link for electron transport.<sup>72</sup> The present work shows that these variables, which act concurrently, and their consequent influences on the photoelectrochemical performance of the films can be manipulated through grain size variation. The explanation of these data is as follows:

Pure PTA: Film A has the largest agglomerates (~132 nm average; ~500 nm maximum) and hence a relatively long hole diffusion distance and a limited specific surface area for both reaction and recombination sites. Across the film thickness of ~400 nm, the number of agglomerates is ~3, thus requiring the electrons to cross this relatively low number of transport barriers. This facilitates electron transport.

PTA containing 0.01–0.05 mol L<sup>–1</sup> oxalic acid: Films B–D have small agglomerates (~58–101 nm), so the hole diffusion distances are decreased. These small agglomerates also are associated with large specific surface areas for reaction sites. Nonetheless, these specific surface areas also are associated with a relatively high fraction of dangling bonds as recombination sites. The number of agglomerates in the cross section is ~4–7, so the electrons must cross a greater number of transport barriers, which hinders electron transport.

PTA containing 0.10 mol L<sup>–1</sup> oxalic acid: Film E has individual particles of ~42 nm. The large specific surface area is associated with a high fraction of dangling bonds. This disadvantage is dominant over the advantages of a large number of reaction sites and a short hole diffusion distance. The intersection density of ~10 agglomerates requires the electrons to cross a great number of transport barriers, thereby minimizing the electron transport.

The concept that condenses the main principles in terms of the size effect and the corresponding microstructural features that result in a maximum in the photocurrents is summarized schematically in Figure 10. Because the nuclei that precede crystallization are amorphous, they show negligible photocurrents,<sup>54</sup> and because single crystals have a minimal specific surface area, they show minimal photocurrents.<sup>10</sup> Therefore, it is clear that in microstructures that range from individual particles to small agglomerates to large agglomerates there must be a maximum in the photocurrent density. Hence, the observed maximum at a small agglomerate size of ~90 nm corresponds to a balance between (i) the surface reaction and recombination sites and (ii) the hole and electron transports.

Similar bell-shaped relationships also have been observed by Li et al. and Hong et al.<sup>12,13</sup> Both observed optimal photoelectrochemical performance in  $\text{WO}_3$  films consisting of what appeared to be small agglomerates of ~60 nm size. The difference in the optimal size value could be the result of the different processing techniques employed in the synthesis of  $\text{WO}_3$  films. These studies illustrated that the microstructures of these materials must be tuned so that the combination of the preceding four main photoelectrochemical performance factors can be optimized for maximal photoelectrochemical performance.

#### 4. CONCLUSIONS

$\text{WO}_3$  thin films with controlled grain sizes (42–132 nm) were electrodeposited from PTA containing different carboxylic acids

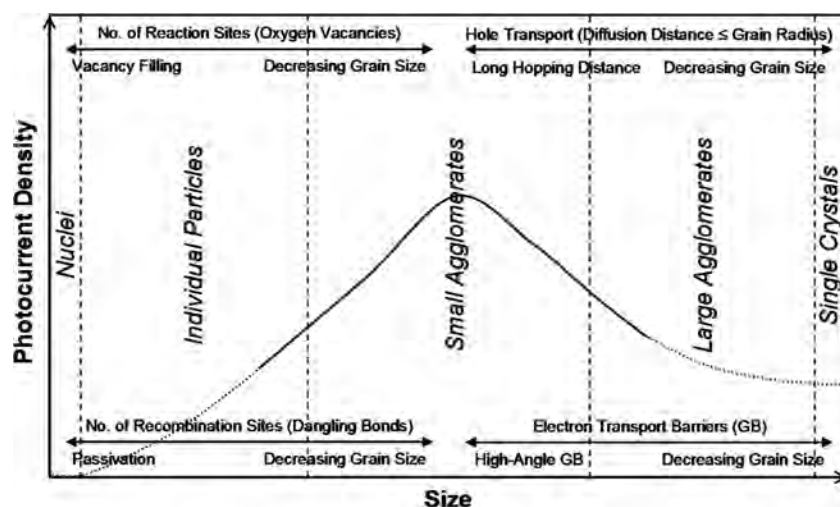


**Figure 10.** Schematic of the trend in the size effect on photocurrent density, where arrows indicate the effect of the fundamental microstructural feature (below arrows) on the photoelectrochemical performance factor (above arrows) ( $\rightarrow$  indicates an increase in the performance factor;  $\leftarrow$  indicates a decrease in the performance factor). The solid line (—) indicates experimental data, the dotted line (⋯) indicates extrapolation, and GB indicates grain boundaries.

(formic, oxalic, and citric). The electrodeposition of the films from PTA containing oxalic acid of different concentrations also was investigated. The deposition thickness was dependent on the electrolyte pH and electrical conductivity, both of which were dependent on the amount, degree of dissociation, molecular weight, and associated sizes of the acids. These influenced the availability of hydronium ions (for hydrogen bonding with PTA ions) and molecular drag in the electrolytes.

The morphological, mineralogical, optical, and photoelectrochemical properties of these films have been investigated. These data can be correlated through microstructural effects, viz., grain sizes and true porosities of the films. These effects were tunable through the use of carboxylic acids with different concentrations and sizes of conjugate bases, which contributed to the separation of the PTA ions, the distribution density of the  $\text{WO}_3$  nuclei, their proximity, the corresponding diffusion distances, the tendency to undergo grain growth during annealing, and hence their susceptibility to forming agglomerates. The grain sizes decreased whereas the true porosities of the films increased with the increasing concentrations and sizes of the conjugate bases. These observations were consistent with the mineralogical data and were supported by the optical data in that the films consisting of smaller agglomerates/particles showed lower transmissions. These were consistent with the larger density of delaminations between particles and the greater amount of true porosity, which would scatter light maximally.

The nonlinear relationship between the grain sizes and the photoelectrochemical performance of  $\text{WO}_3$  thin films suggested that the optimal photoelectrochemical performance of a film was a result of the tuning of (i) surface reaction and recombination sites and (ii) the hole and electron transports. The positive balance of the preceding photoelectrochemical performance factors resulted in a maximal photocurrent density at an agglomerate size of  $\sim 90$  nm, which was deposited from PTA containing  $0.03 \text{ mol L}^{-1}$  oxalic acid. Although it usually is assumed that nanomaterials with large specific surface areas are beneficial owing to the associated number of reaction sites, the

present work shows that the optimization of the concurrent factors that affect the photoelectrochemical properties requires a more nuanced approach to processing. That is, small agglomerates appeared to offer a means of controlling the effective grain boundary area, which needs to be tuned between extremes.

## AUTHOR INFORMATION

### Corresponding Author

\*E-mail: c.sorrell@unsw.edu.au. Tel: (+61-2) 9385-4421. Fax: (+61-2) 9385-6565.

### Notes

The authors declare no competing financial interest.

## ACKNOWLEDGMENTS

This work was supported in part by a project funded by the Australian Research Council (ARC). We are grateful for the characterization facilities from the Australian Microscopy & Microanalysis Research Facilities (AMMRF) node at the University of New South Wales (UNSW). W.L.K. gratefully acknowledges the receipt of a UNSW International Postgraduate Award to undertake this research degree.

## REFERENCES

- (1) Hodes, G.; Cahen, D.; Manassen, J. Tungsten Trioxide as a Photoanode for a Photoelectrochemical Cell (PEC). *Nature* **1976**, *260*, 312–313.
- (2) Watcharenwong, A.; Chanmanee, W.; de Tacconi, N. R.; Chenthamarakshan, C. R.; Kajitvichyanukul, P.; Rajeshwar, K. Anodic Growth of Nanoporous  $\text{WO}_3$  Films: Morphology, Photoelectrochemical Response and Photocatalytic Activity for Methylene Blue and Hexavalent Chrome Conversion. *J. Electroanal. Chem.* **2008**, *612*, 112–120.
- (3) Shen, X. P.; Wang, G. X.; Wexler, D. Large-Scale Synthesis and Gas Sensing Application of Vertically Aligned and Double-Sided Tungsten Oxide Nanorod Arrays. *Sens. Actuators, B* **2009**, *143*, 325–332.
- (4) Fang, F.; Kennedy, J.; Futter, J.; Hopf, T.; Markwitz, A.; Manikandan, E.; Henshaw, G. Size-Controlled Synthesis and Gas

Sensing Application of Tungsten Oxide Nanostructures Produced by Arc Discharge. *Nanotechnology* **2011**, *22*, 335702.

(5) Soliman, H. M. A.; Kashyout, A. B.; El Nouby, M. S.; Abosehly, A. M. Preparation and Characterizations of Tungsten Oxide Electrochromic Nanomaterials. *J. Mater. Sci.: Mater. Electron.* **2010**, *21*, 1313–1321.

(6) Li, W. J.; Fu, Z. W. Nanostructured WO<sub>3</sub> Thin Film as a New Anode Material for Lithium-Ion Batteries. *Appl. Surf. Sci.* **2010**, *256*, 2447–2452.

(7) Hanaor, D. A. H.; Triani, G.; Sorrell, C. C. Morphology and Photocatalytic Activity of Highly Oriented Mixed Phase Titanium Dioxide Thin Films. *Surf. Coat. Technol.* **2011**, *205*, 3658–3664.

(8) Liu, X.; Wang, F.; Wang, Q. Nanostructure-Based WO<sub>3</sub> Photoanodes for Photoelectrochemical Water Splitting. *Phys. Chem. Chem. Phys.* **2012**, *14*, 7894–7911.

(9) Li, Y.; Zhang, J. Z. Hydrogen Generation from Photoelectrochemical Water Splitting Based on Nanomaterials. *Laser Photonics Rev.* **2010**, *4*, 517–528.

(10) Santato, C.; Ulmann, M.; Augustynski, J. Enhanced Visible Light Conversion Efficiency Using Nanocrystalline WO<sub>3</sub> Films. *Adv. Mater.* **2001**, *13*, 511–514.

(11) Kelly, J. J.; Vanmaekelbergh, D. Porous-Etched Semiconductors: Formation and Characterization. In *Electrochemistry of Nanomaterials*; Hodes, G., Ed.; Wiley-VCH: Weinheim, Germany, 2001; pp 103–139.

(12) Li, W.; Li, J.; Wang, X.; Ma, J.; Chen, Q. Photoelectrochemical and Physical Properties of WO<sub>3</sub> Films Obtained by the Polymeric Precursor Method. *Int. J. Hydrogen Energy* **2010**, *35*, 13137–13145.

(13) Hong, S. J.; Jun, H.; Borse, P. H.; Lee, J. S. Size Effects of WO<sub>3</sub> Nanocrystals for Photooxidation of Water in Particulate Suspension and Photoelectrochemical Film Systems. *Int. J. Hydrogen Energy* **2009**, *34*, 3234–3242.

(14) Sun, X. L.; Cao, H. T.; Liu, Z. M.; Li, J. Z. Influence of Annealing Temperature on Microstructure and Optical Properties of Sol-Gel Derived Tungsten Oxide Films. *Appl. Surf. Sci.* **2009**, *255*, 8629–8633.

(15) Su, P. G.; Pan, T. T. Fabrication of a Room-Temperature NO<sub>2</sub> Gas Sensor Based on WO<sub>3</sub> Films and WO<sub>3</sub>/MWCNT Nanocomposite Films by Combining Polyol Process with Metal Organic Decomposition Method. *Mater. Chem. Phys.* **2011**, *125*, 351–357.

(16) White, C. M.; Jang, J. S.; Lee, S. H.; Pankow, J.; Dillon, A. C. Photocatalytic Activity and Photoelectrochemical Property of Nano-WO<sub>3</sub> Powders Made by Hot-Wire Chemical Vapor Deposition. *Electrochem. Solid-State Lett.* **2010**, *13*, B120–B122.

(17) Vemuri, R. S.; Bharathi, K. K.; Gullapalli, S. K.; Ramana, C. V. Effect of Structure and Size on the Electrical Properties of Nanocrystalline WO<sub>3</sub> Films. *ACS Appl. Mater. Interfaces* **2010**, *2*, 2623–2628.

(18) Gullapalli, S. K.; Vemuri, R. S.; Ramana, C. V. Structural Transformation Induced Changes in the Optical Properties of Nanocrystalline Tungsten Oxide Thin Films. *Appl. Phys. Lett.* **2010**, *96*, 171903.

(19) Sun, M.; Xu, N.; Cao, Y. W.; Yao, J. N.; Wang, E. G. Preparation, Microstructure and Photochromism of a New Nanocrystalline WO<sub>3</sub> Film. *J. Mater. Sci. Lett.* **2000**, *19*, 1407–1409.

(20) Meda, L.; Tozzola, G.; Tacca, A.; Marra, G.; Caramori, S.; Cristino, V.; Bignozzi, C. A. Photo-Electrochemical Properties of Nanostructured WO<sub>3</sub> Prepared with Different Organic Dispersing Agents. *Sol. Energy Mater. Sol. Cells* **2010**, *94*, 788–796.

(21) Naseri, N.; Yousefzadeh, S.; Daryaei, E.; Moshfegh, A. Z. Photoresponse and H<sub>2</sub> Production of Topographically Controlled PEG Assisted Sol-Gel WO<sub>3</sub> Nanocrystalline Thin Films. *Int. J. Hydrogen Energy* **2011**, *36*, 13461–13472.

(22) Kwong, W. L.; Savvides, N.; Sorrell, C. C. Electrodeposited Nanostructured WO<sub>3</sub> Thin Films for Photoelectrochemical Applications. *Electrochim. Acta* **2012**, *75*, 371–380.

(23) Augustynski, J.; Solarska, R.; Hagemann, H.; Santato, C. Nanostructured Thin-Film Tungsten Trioxide Photoanodes for Solar Water and Sea-Water Splitting. *Proc. SPIE* **2006**, *6340*, 63400J.

(24) Sun, M.; Xu, N.; Cao, Y. W.; Yao, J. N.; Wang, E. G. Nanocrystalline Tungsten Oxide Thin Film: Preparation, Microstructure, and Photochromic Behavior. *J. Mater. Res.* **2000**, *15*, 927–933.

(25) Kotz, J. C.; Treichel, P. M.; Townsend, J. R. *Chemistry and Chemical Reactivity*; Brooks/Cole: Belmont, CA, 2010.

(26) Sawada, S.; Ando, R.; Nomura, S. Thermal Expansion and Specific Heat of Tungsten Oxide at High Temperatures. *Phys. Rev.* **1951**, *84*, 1054–1055.

(27) Lassner, E.; Schubert, W. D. *Tungsten: Properties, Chemistry, Technology of the Element, Alloys, and Chemical Compounds*; Kluwer Academic/Plenum Publishers: New York, 1999.

(28) Kingery, W. D.; Bowen, H. K.; Uhlmann, D. R. *Introduction to Ceramics*; John Wiley and Sons: New York, 1976.

(29) Barile, F. A. *Principles of Toxicology Testing*; CRC Press: Boca Raton, FL, 2008.

(30) Bettelheim, F. A.; Brown, W. H.; Campbell, M. K.; Farrell, S. O. *Introduction to Organic and Biochemistry*; Brooks/Cole: Belmont, CA, 2010.

(31) Armstrong, J. *General, Organic, and Biochemistry: An Applied Approach*; Brooks/Cole: Belmont, CA, 2012.

(32) Vernardou, D.; Drosos, H.; Spanakis, E.; Koudoumas, E.; Savvakisab, C.; Katsarakis, N. Electrochemical and Photocatalytic Properties of WO<sub>3</sub> Coatings Grown at Low Temperatures. *J. Mater. Chem.* **2011**, *21*, 513–517.

(33) Xin, G.; Guo, W.; Ma, T. Effect of Annealing Temperature on the Photocatalytic Activity of WO<sub>3</sub> for O<sub>2</sub> Evolution. *Appl. Surf. Sci.* **2009**, *256*, 165–169.

(34) Woodward, P. M.; Sleight, A. W.; Vogt, T. Structure Refinement of Triclinic Tungsten Trioxide. *J. Phys. Chem. Solids* **1995**, *56*, 1305–1315.

(35) Waseda, Y.; Matsubara, E.; Shinoda, K. *X-ray Diffraction Crystallography: Introduction, Examples and Solved Problems*; Springer: New York, 2011.

(36) Tauc, J. Optical Properties and Electronic Structure of Amorphous Ge and Si. *Mater. Res. Bull.* **1968**, *3*, 37–46.

(37) Koffyberg, F. P.; Dwight, K.; Wold, A. Interband Transitions of Semiconducting Oxides Determined from Photoelectrolysis Spectra. *Solid State Commun.* **1979**, *30*, 433–437.

(38) Hechavarria, L.; Hu, H.; Miranda, M.; Nicho, M. E. Electrochromic Responses of Low-Temperature-Annealed Tungsten Oxide Thin Films in Contact with a Liquid and a Polymeric Gel Electrolyte. *J. Solid State Electrochem.* **2009**, *13*, 687–695.

(39) Monllor-Satoca, D.; Borja, L.; Rodes, A.; Gómez, R.; Salvador, P. Photoelectrochemical Behavior of Nanostructured WO<sub>3</sub> Thin-Film Electrodes: The Oxidation of Formic Acid. *ChemPhysChem* **2006**, *7*, 2540–2551.

(40) Azimrad, R.; Akhavan, O.; Moshfegh, A. Z. Influence of Coloring Voltage and Thickness on Electrochromical Properties of E-Beam Evaporated WO<sub>3</sub> Thin Films. *J. Electrochem. Soc.* **2006**, *153*, E11–E16.

(41) Johansson, M. B.; Baldissera, G.; Valyukh, I.; Persson, C.; Arwin, H.; Niklasson, G. A.; Osterlund, L. Electronic and Optical Properties of Nanocrystalline WO<sub>3</sub> Thin Films Studied by Optical Spectroscopy and Density Functional Calculations. *J. Phys.: Condens. Matter* **2013**, *25*, 205502.

(42) Kalagi, S. S.; Mali, S. S.; Dalavi, D. S.; Inamdar, A. I.; Im, H.; Patil, P. S. Transmission Attenuation and Chromic Contrast Characterization of R.F. Sputtered WO<sub>3</sub> Thin Films for Electrochromic Device Applications. *Electrochim. Acta* **2012**, *85*, 501–508.

(43) Su, J.; Feng, X.; Sloppy, J. D.; Guo, L.; Grimes, C. A. Vertically Aligned WO<sub>3</sub> Nanowire Arrays Grown Directly on Transparent Conducting Oxide Coated Glass: Synthesis and Photoelectrochemical Properties. *Nano Lett.* **2011**, *11*, 203–208.

(44) Qin, D. D.; Tao, C. L.; Friesen, S. A.; Wang, T. H.; Varghese, O. K.; Bao, N. Z.; Yang, Z. Y.; Mallouk, T. E.; Grimes, C. A. Dense Layers of Vertically Oriented WO<sub>3</sub> Crystals as Anodes for Photoelectrochemical Water Oxidation. *Chem. Commun.* **2012**, *48*, 729–731.

- (45) Ng, C.; Ye, C. H.; Ng, Y. H.; Amal, R. Flower-Shaped Tungsten Oxide with Inorganic Fullerene-Like Structure: Synthesis and Characterization. *Cryst. Growth Des.* **2010**, *10*, 3794–3801.
- (46) Mohanty, B. C.; Jo, Y. H.; Yeon, D. H.; Choi, I. J.; Cho, Y. S. Stress-Induced Anomalous Shift of Optical Band Gap in ZnO:Al Thin Films. *Appl. Phys. Lett.* **2009**, *95*, 062103.
- (47) Marotti, R. E.; Guerra, D. N.; Bello, C.; Machado, G.; Dalchiale, E. A. Bandgap Energy Tuning of Electrochemically Grown ZnO Thin Films by Thickness and Electrodeposition Potential. *Sol. Energy Mater. Sol. Cells* **2004**, *82*, 85–103.
- (48) Pandiaraman, M.; Soundararajan, N.; Vijayan, C. Effect of Thickness on the Optical Band Gap of Silver Telluride Thin Films. *J. Ovonic Res.* **2011**, *7*, 21–27.
- (49) Goh, E. S. M.; Chen, T. P.; Sun, C. Q.; Liu, Y. C. Thickness Effect on the Band Gap and Optical Properties of Germanium Thin Films. *J. Appl. Phys.* **2010**, *107*, 024305.
- (50) Weinhardt, L.; Blum, M.; Bar, M.; Heske, C.; Cole, B.; Marsen, B.; Miller, E. L. Electronic Surface Level Positions of WO<sub>3</sub> Thin Films for Photoelectrochemical Hydrogen Production. *J. Phys. Chem. C* **2008**, *112*, 3078–3082.
- (51) Cole, B.; Marsen, B.; Miller, E.; Yan, Y. F.; To, B.; Jones, K.; Al-Jassim, M. Evaluation of Nitrogen Doping of Tungsten Oxide for Photoelectrochemical Water Splitting. *J. Phys. Chem. C* **2008**, *112*, 5213–5220.
- (52) Tang, J.; Wang, D.; Zou, Z.; Ye, J. Modification of Photophysical Properties of WO<sub>3</sub> by Doping Different Metals. *Mater. Sci. Forum* **2003**, *423–425*, 163–166.
- (53) Sun, Y.; Murphy, C. J.; Reyes-Gil, K. R.; Reyes-Garcia, E. A.; Thornton, J. M.; Morris, N. A.; Raftery, D. Photoelectrochemical and Structural Characterization of Carbon-Doped WO<sub>3</sub> Films Prepared via Spray Pyrolysis. *Int. J. Hydrogen Energy* **2009**, *34*, 8476–8484.
- (54) Diqarto, F.; Dipaola, A.; Piazza, S.; Sunseri, C. Influence of Thermal-Treatment on the Photoelectrochemical Behavior of WO<sub>3</sub> Photoanodes Electrochemically Grown. *Sol. Energy Mater.* **1985**, *11*, 419–433.
- (55) Alexander, B. D.; Augustynski, J. Nanostructured Thin-Film WO<sub>3</sub> Photoanodes for Solar Water and Sea-Water Splitting. In *On Solar Hydrogen and Nanotechnology*; Vayssieres, L., Ed.; John Wiley and Sons: Singapore, 2009; pp 342–345.
- (56) Ulmann, M.; Detacconi, N. R.; Augustynski, J. Behavior of Surface Peroxo Species in the Photoreactions at TiO<sub>2</sub>. *J. Phys. Chem.* **1986**, *90*, 6523–6530.
- (57) Yoo, W. S.; Kang, K. Electrical Activation of Ultra-Shallow B and BF<sub>2</sub> Implanted Silicon by Flash Anneal. *Nucl. Instrum. Methods Phys. Res., Sect. B* **2005**, *237*, 12–17.
- (58) Deepa, M.; Kar, M.; Singh, D. P.; Srivastava, A. K.; Ahmad, S. Influence of Polyethylene Glycol Template on Microstructure and Electrochromic Properties of Tungsten Oxide. *Sol. Energy Mater. Sol. Cells* **2008**, *92*, 170–178.
- (59) Ahn, K. S.; Lee, S. H.; Dillon, A. C.; Tracy, C. E.; Pitts, R. The Effect of Thermal Annealing on Photoelectrochemical Responses of WO<sub>3</sub> Thin Films. *J. Appl. Phys.* **2007**, *101*, 093524.
- (60) Liao, C. C.; Chen, F. R.; Kai, J. J. Electrochromic Properties of Nanocomposite WO<sub>3</sub> Films. *Sol. Energy Mater. Sol. Cells* **2007**, *91*, 1282–1288.
- (61) García-Cañadas, J.; Mora-Seró, I.; Fabregat-Santiago, F.; Bisquert, J.; Garcia-Belmonte, G. Analysis of Cyclic Voltammograms of Electrochromic α-WO<sub>3</sub> Films from Voltage-Dependent Equilibrium Capacitance Measurements. *J. Electroanal. Chem.* **2004**, *565*, 329–334.
- (62) Shiyonovskaya, I.; Hepel, M.; Tewksbury, E. Electrochromism in Electrodeposited Nanocrystalline WO<sub>3</sub> Films I. Electrochemical and Optical Properties. *J. New Mater. Electrochem. Syst.* **2000**, *3*, 241–247.
- (63) Kim, D. H. Effects of Phase and Morphology on the Electrochromic Performance of Tungsten Oxide Nano-Urchins. *Sol. Energy Mater. Sol. Cells* **2012**, *107*, 81–86.
- (64) Zhang, J.; Wang, X. L.; Xia, X. H.; Gu, C. D.; Tu, J. P. Electrochromic Behavior of WO<sub>3</sub> Nanotree Films Prepared by Hydrothermal Oxidation. *Sol. Energy Mater. Sol. Cells* **2011**, *95*, 2107–2112.
- (65) Wendt, S.; Vang, R. T.; Besenbacher, F. Fundamental Reactions on Rutile TiO<sub>2</sub> (110) Model Photocatalysts Studied by High-Resolution Scanning Tunneling Microscopy. In *On Solar Hydrogen and Nanotechnology*; Vayssieres, L., Ed.; John Wiley and Sons: Singapore, 2009.
- (66) Wang, S.; Verma, A.; Yang, Y. L.; Jacobson, A. J.; Abeles, B. The Effect of the Magnitude of the Oxygen Partial Pressure Change in Electrical Conductivity Relaxation Measurements: Oxygen Transport Kinetics in La<sub>0.5</sub>Sr<sub>0.5</sub>CoO<sub>3-δ</sub>. *Solid State Ionics* **2001**, *140*, 125–133.
- (67) Feng, D.; Jin, G. *Introduction to Condensed Matter Physics*; World Scientific Publishing: Singapore, 2005.
- (68) Pai, M. R.; Banerjee, A. M.; Tripathi, A. K.; Bharadwaj, S. R. *Functional Materials: Preparation, Processing and Applications*; Elsevier: Waltham, MA, 2012.
- (69) Yacobi, B. G. *Semiconductor Materials: An Introduction to Basic Principles*; Kluwer Academic/Plenum Publishers: New York, 2003.
- (70) Mendis, B. G.; Bowen, L.; Jiang, Q. Z. A Contactless Method for Measuring the Recombination Velocity of an Individual Grain Boundary in Thin-Film Photovoltaics. *Appl. Phys. Lett.* **2010**, *97*, 092112.
- (71) Deutscher, G. Origin of Weak-Link Behavior of Grain Boundaries in Superconducting Cuprates and Pnictides. *Appl. Phys. Lett.* **2010**, *96*, 122502.
- (72) Yau, J. K. F.; Sorrell, C. C. High-J<sub>c</sub> (Bi,Pb)<sub>2</sub>Sr<sub>2</sub>Ca<sub>2</sub>Cu<sub>3</sub>O<sub>10+x</sub> Tapes Fabricated by Electrophoretic Deposition. *Physica C* **1997**, *282–287*, 2563–2564.

**APPENDIX 9: PHOTOELECTROCHEMICAL PROPERTIES OF WO<sub>3</sub> NANOPARTICULATE THIN FILMS PREPARED BY CARBOXYLIC ACID-ASSISTED ELECTRODEPOSITION, *THIN SOLID FILMS* 544 (2013) 191-196.**



# Photoelectrochemical properties of WO<sub>3</sub> nanoparticulate thin films prepared by carboxylic acid-assisted electrodeposition

W.L. Kwong<sup>a,\*</sup>, A. Nakaruk<sup>a,b</sup>, P. Koshy<sup>a</sup>, C.C. Sorrell<sup>a</sup>

<sup>a</sup> School of Materials Science and Engineering, University of New South Wales, Sydney, NSW 2052, Australia

<sup>b</sup> Department of Industrial Engineering, Faculty of Engineering, Naresuan University, Phitsanulok 65000, Thailand

## ARTICLE INFO

Available online 9 April 2013

### Keywords:

WO<sub>3</sub> thin films  
Electrodeposition  
PTA  
Photocurrent  
Carboxylic acids

## ABSTRACT

Optimisation of particle sizes of WO<sub>3</sub> films is important for photoelectrochemical applications. However, most of the developed size-controlled synthesis techniques involve complicated instruments or vacuum systems. The present work presents an alternative method using carboxylic acid-assisted electrodeposition where WO<sub>3</sub> thin films were deposited from peroxotungstic acid (PTA) solution containing different carboxylic acids (formic, oxalic, citric). The effects of carboxylic acids on the electrodeposition and the resultant morphological, mineralogical, optical, and photoelectrochemical properties of the WO<sub>3</sub> films were investigated. The analysis showed that the films consisted of equiaxed nanoparticulate monoclinic WO<sub>3</sub>. The deposition thicknesses and the average grain (individual particle and agglomerate) sizes of the films were dependent on the amount of hydronium ions and the molecular weight and associated sizes of the conjugate bases released upon the dissociation of carboxylic acids in the PTA solutions, which result in hydrogen bond formation and molecular dispersion. The photocurrent densities of the films deposited with carboxylic acids were greater than that of the film deposited from pure PTA. These differences were attributed to improvements in (1) grain size, which controls photogenerated electron-hole transport, and (2) effective grain boundary area, which controls the numbers of active reaction sites and electron-hole recombination sites.

© 2013 Elsevier B.V. All rights reserved.

## 1. Introduction

Photoelectrochemical (PEC) hydrogen production is one of the most attractive and environmentally sustainable methods to harvest and convert solar energy to chemical energy, which is stored in the form of H<sub>2</sub> fuel. WO<sub>3</sub> is an *n*-type semiconductor, which has been investigated for various applications such as photocatalysis [1], gas sensing [2,3], electrochromism [4], electrodes for lithium ion batteries [5], and PEC water splitting [6]. WO<sub>3</sub> has great potential for photoelectrochemical applications owing to its high stability against both corrosion and photocorrosion and its relatively small optical indirect band gap [7,8], which permits limited light absorption in the visible range.

Compared to their bulk counterparts [9], nanomaterials as photoelectrodes for PEC cells are advantageous owing to their superior physical properties, including (1) higher surface area to volume ratio, which increases the number of reaction sites for water photolysis; (2) suppressed charge carrier recombination rates, since photo-generated holes are more likely to diffuse to the photoanode/electrolyte interfaces before recombination in nanomaterials with sizes smaller than their hole diffusion lengths [10] (the hole diffusion length of WO<sub>3</sub> is ~150 nm [11]); and (3) enhanced optical absorption, which

results from increased optical path length by incident light scattering, caused by the change of refractive indices at the boundaries of grains of different orientations [9,10]. However, grain boundaries also act as transportation barriers to photogenerated electron-hole pairs and so it is essential to optimise the sizes of the nanomaterials by varying the synthesis parameters in order to obtain optimal photoelectrochemical performance.

Controlling the size of WO<sub>3</sub> nanostructures has been done using techniques such as hydrothermal [12], sol-gel [13], hot-wire chemical vapor deposition [14], arc discharge deposition [3], radio-frequency magnetron sputtering [15], and organic compound-assisted wet chemical techniques [16–18]. The latter have shown considerable promise as economical and uncomplicated routes for size-controlled synthesis of WO<sub>3</sub> nanostructures. Sun et al. [16] used colloidal processing at high oxalic acid concentrations in tungstic acid to produce smaller grain sizes and lower crystallinities of WO<sub>3</sub> thin films. Meda et al. [18] reported the size-tuning of WO<sub>3</sub> grains prepared by a proton exchange resin method through the addition of various organic dispersants, including ethylene glycol, polyethylene glycol, Igepal®, Brij®, and sugars, where the grain sizes decreased with increasing molecular weight of the dispersant.

To date, the number of investigations on the size-controlled wet chemical synthesis of WO<sub>3</sub> thin films using organic compounds is limited and so the mechanisms related to the growth of nanoparticles have not been explained clearly. The present work reports the

\* Corresponding author. Tel.: +61 2 9385 4421; fax: +61 2 9385 6565.  
E-mail address: [w.l.kwong@student.unsw.edu.au](mailto:w.l.kwong@student.unsw.edu.au) (W.L. Kwong).

electrodeposition of  $\text{WO}_3$  thin films with varied grain sizes using peroxotungstic acid solutions containing different carboxylic acids. The effects of carboxylic acids on the electrodeposition and the resultant morphological, mineralogical (phase composition), optical, and photoelectrochemical properties of  $\text{WO}_3$  thin films were investigated.

## 2. Experimental details

Tungsten foils (99.99%, Shanghai Leading Metal, China), 30% w/w hydrogen peroxide (analytical reagent, Univar), and propan-2-ol (99.5% analytical reagent, Univar) were used to prepare peroxotungstic acid (PTA) solutions. The carboxylic acids used were formic acid (99% analytical reagent, Asia Pacific Specialty Chemicals), oxalic acid dihydrate (99.5% Merck), and citric acid monohydrate ( $\geq 99\%$  ACS reagent, Sigma-Aldrich).

Detailed preparation procedures of PTA solutions have been reported elsewhere [19]. In brief, 0.03 M carboxylic acids (*viz.*, formic, oxalic, or citric acid) were added to PTA solutions with 0.2 M tungsten and these PTA solutions were used as the electrolytes for film deposition. The films were deposited at room temperature using a three-electrode electrochemical system with fluorine-doped tin oxide on glass (FTO), platinum foil, and Ag/AgCl as the working, counter, and reference electrodes, respectively. All potentials reported refer to the reference electrode. A potential of  $-0.4$  V was applied for times ranging from 15 to 60 min in order to deposit films of varying thicknesses. This deposition potential value was chosen owing to the reduction peak obtained in the linear potential sweeps prior to the deposition process. The as-deposited samples were flushed immediately with distilled water, dried in air, placed on an aluminosilicate brick, and annealed at  $450$  °C in air for 2 h (heating and initial cooling rates of  $5$  °C  $\text{min}^{-1}$ ).

The film thicknesses were determined using focused ion beam milling (FIB; FEI XP200). The microstructures were examined using scanning electron microscopy (SEM; FEI Nova NanoSEM; operating voltage 5 kV). True porosities of the films were investigated using image analysis (*ImageJ*, National Institute of Health). The mineralogies of the unaltered films were determined by X-ray powder diffraction (XRD; Philips X'pert Materials Powder Diffractometer; Cu  $K\alpha$  radiation; 45 kV; 40 mA). Light transmissions were measured using a dual-beam UV–VIS spectrophotometer (Pelkin-Elmer Lambda 35).

The photoelectrochemical properties of the samples were measured at room temperature using the same electrochemical system as described above but using  $\text{WO}_3$  thin films on FTO substrates as the working electrodes. The PTA electrolyte solutions were replaced with 0.5 M NaCl aqueous solutions (pH = 6.27). The intensity of incident light (50 W tungsten-halogen lamp, chopped at a frequency of 0.05 Hz) was measured with a light meter (Digitech QM1587) to be  $\sim 100$   $\text{mW}/\text{cm}^2$  (light source to sample distance  $\sim 25$  cm). Transient potentiostatic photocurrent measurements were done at a bias potential of 0.7 V. In order to measure the relaxation time of the open-circuit photopotential, the films were pre-treated by biasing at 0.7 V for 1 min under illumination so as to achieve an equilibrium state (as shown by achievement of stable photocurrents) and then left to reach a stationary potential under open-circuit (without bias) and dark conditions. Subsequently, illumination was switched on for the photopotential to reach a stationary value and then off again to measure the time taken for it to decay.

## 3. Results and discussion

Fig. 1 shows the film thickness variation as a function of deposition times for depositions done in pure PTA and PTA containing carboxylic acids solutions. The film thicknesses were measured from the cross-sections of the films, which were milled by FIB. All films adhered well to the substrates (as shown by the resistance to robust handling) except for those deposited for times longer than 30 min in pure PTA,

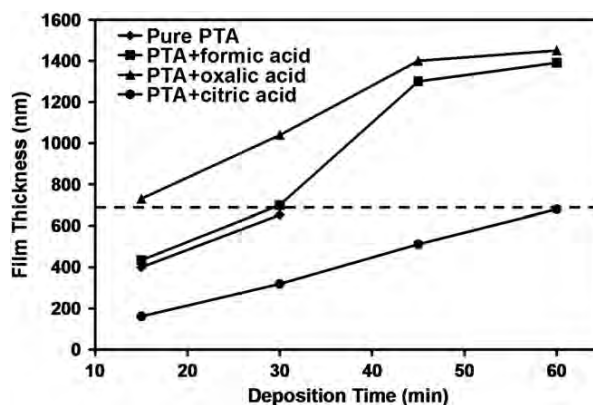


Fig. 1. Thicknesses of  $\text{WO}_3$  thin films as a function of deposition times. Dashed line indicates film thickness  $\sim 700$  nm.

which cracked owing to drying stresses. Compared to pure PTA, the deposition thicknesses increased, remained constant, and decreased when the depositions were done from PTA containing oxalic, formic, and citric acids, respectively. Table 1 shows that the same order and the reverse order were seen for the electrolyte conductivities and pH values, respectively. These observations suggest that the deposition thickness is a function of these two variables, which are determined by the hydronium ions and conjugate bases produced upon the dissociation of the acids in aqueous solutions [20].

According to the logarithm of the first proton acid dissociation constant ( $\text{p}K_{a1}$ ), the dissociation of the acids follows in the order oxalic > citric > formic. The small change in the pH of the PTA containing formic acid was caused by the limited dissociation of the acid, which produced a minimal amount of hydronium ions. In contrast, the increase in pH of PTA containing citric acid suggests that the pH was controlled by hydrogen bonding between the relatively large number of highly electronegative oxygen atoms in the citrate ion and the hydronium ions, thereby reducing the availability of hydronium ions. In further contrast, the decrease in pH in PTA containing oxalic acid confirmed the release of a large amount of hydronium ions upon the dissociation of the acid, thereby resulting in high availability of the hydronium ions in the PTA electrolyte despite their formations of hydrogen bonds with the electronegative oxygen atoms in the small oxalate ion. As a consequence of the formation of hydrogen bonds between the hydronium and PTA ions (PTA–hydronium complex ions), a net positive charge developed around the PTA ions, as shown in Fig. 2. This aided the deposition process by driving the PTA–hydronium complex ions to the cathodically biased working electrode, thereby resulting in thicker films deposited from PTA containing oxalic acid. On the other hand, the electrolyte conductivity can be affected by the  $\text{p}K_{a1}$  values of the acids, which determine the amounts of ions formed in the electrolytes and the molecular weights and associated sizes of the conjugate bases of the acids (in this case the order is citrate > oxalate > formate), which determine the molecular drag in the electrolyte.

The preceding observations show that the relationships between the controlling variables such as  $\text{p}K_{a1}$ , molecular weight of the conjugate bases, electrolyte pH, and electrolyte conductivity are complex and that the electrodeposition parameter of film thickness cannot be associated independently with them.

Fig. 1 also shows that there was an apparent decrease in the deposition rates at longer times. The main reasons for this were assumed to be the decreasing PTA concentrations during deposition [21,22] and the decreasing electrical conductivities of the films with increasing thicknesses [23].

Since the film thickness is known to influence photoelectrochemical performance [18,19],  $\text{WO}_3$  films of similar thicknesses ( $\sim 700$  nm),

**Table 1**

Analytical data obtained for all the samples from the different tests.

Electrolyte composition	Electrolyte pH	$\kappa$ (mS cm <sup>-1</sup> )	$t$ (min)	Grain size* (nm)	Crystallite size^ (nm)	Film strain^ ( $\times 10^{-4}$ )	(002) peak area	(200) peak area	True porosity (%)	$E_g$ (eV)
0.2 M PTA	1.71	2.900	30	131 $\pm$ 16	107	7	9384	10067	0.87	2.55
0.2 M PTA + 0.03 M formic acid	1.70	3.120	30	94 $\pm$ 12	82	4	7150	4252	1.21	2.70
0.2 M PTA + 0.03 M oxalic acid	1.41	6.570	15	83 $\pm$ 10	92	6	3640	1760	1.91	2.65
0.2 M PTA + 0.03 M citric acid	1.84	0.009	60	45 $\pm$ 4	43	4	6478	9588	2.12	2.63

, electrolyte conductivity;  $t$ , deposition time;  $E_g$ , optical indirect band gap; \* measured from SEM images; ^ measured from Williamson–Hall plots.

deposited for various times from different electrolyte compositions, were characterised further using SEM analysis, XRD analysis, UV–VIS spectrophotometry, and photoelectrochemical measurements.

Fig. 3 shows the surface morphologies of the films. The average sizes of the WO<sub>3</sub> grains (individual particles or agglomerates), measured by the line-intercept method (300,000 $\times$  photographs, 10 lines, 5–10 grains per line), were smaller for the films deposited from PTA containing carboxylic acids compared to that of the film deposited from pure PTA. This was considered to result from the deflocculation and dispersion mechanism of electrosteric stabilisation [24] shown in Fig. 2. The effectiveness of the separation of PTA ions was controlled by the relative availability of hydronium ions for hydrogen bonding with the electronegative oxygen atoms of the PTA ions and the molecular weight and associated sizes of the conjugate bases that occupied the volume of the electrolyte as follows:

- Pure PTA* – Large agglomerates of size ~131 nm (~500 nm maximum); In pure PTA, the absence of particle separation by any deflocculation mechanism caused solute agglomeration, rapid grain growth, and consequent agglomeration during annealing since the proximity of the ion complexes minimised the diffusion distance.
- PTA containing formic acid* – Small agglomerates of size ~94 nm and *PTA containing oxalic acid* – Small agglomerates of size ~83 nm; In PTA containing carboxylic acids, with conjugate bases of molecular weights 45 g mol<sup>-1</sup> (formate) and 125 g mol<sup>-1</sup> (oxalate), the hydronium ions provided a basic deflocculation mechanism of electrosteric stabilisation [24] and the volumes occupied by the conjugate bases in solutions contributed to an increase in the degree of separation of the PTA ions and the resultant diffusion distance.
- PTA containing citric acid* – Individual particles of size ~45 nm; In PTA containing citric acid, with conjugate base of molecular weight 209 g mol<sup>-1</sup>, deflocculation by electrosteric stabilisation occurred but the larger volume occupied by the citrate ions in the solution separated the PTA ions and increased the diffusion distance such that little grain growth took place during annealing.

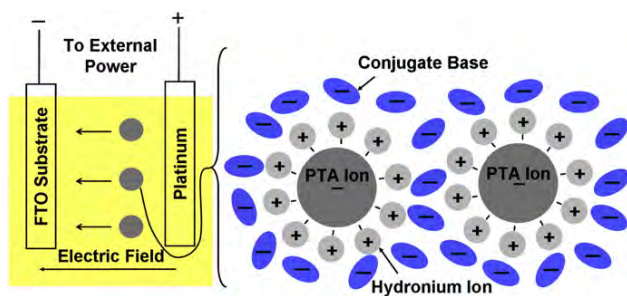


Fig. 2. Schematic diagram of the effects of hydronium ions and conjugate bases on deflocculation and dispersion of PTA ions.

In summary, it can be seen that the use of carboxylic acids is effective in facilitating deflocculation and suppressing solute clustering before electrodeposition. Therefore, the microstructures of the annealed films can be manipulated by using carboxylic acids of different molecular weights and associated sizes of conjugate bases since the sizes of the conjugate bases control the distribution density of the WO<sub>3</sub> nuclei, their proximity, the corresponding diffusion distances, the resultant tendency to undergo grain growth during annealing, and hence their susceptibility to form solid agglomerates.

The true porosity data, which were determined by image analysis, in Table 1 support the preceding conclusions. The film deposited from pure PTA had the lowest true porosity (closed pores only). Even though the agglomerate size was large, delaminations between agglomerates were avoided owing to the strong bonding between the tightly packed agglomerates. In contrast, the films deposited with carboxylic acids exhibited porosities that had been enhanced by delaminations between agglomerates, which resulted from the separation effect of the conjugate bases. Therefore, the true porosity reflects the effect of separation. That is, with PTA containing citric acid (the largest conjugate base), the separation between individual particles was the greatest and so the true porosity also was the greatest. However, delaminations were not visible because the thermal contraction stresses were distributed more evenly across the homogeneous particle array rather than concentrating along inhomogeneously distributed agglomerate boundaries.

Fig. 4 shows the XRD results of the WO<sub>3</sub> thin films. The major peaks for monoclinic WO<sub>3</sub> were present at 23.3°, 23.7°, and 24.4° 2 $\theta$ , which correspond to the (002), (020), and (200) planes [25], respectively. The XRD peaks of the films deposited with carboxylic acids were weaker (lower intensities and smaller areas) and broader compared to the film deposited from pure PTA, despite their being of similar thicknesses (the small FTO peaks served as *in situ* normalising standard). The explanations are as follows:

- XRD peak areas*; As shown in Table 1, the XRD peak areas of the films deposited from pure PTA and from PTA containing formic and oxalic acids showed inverse trend with the true porosities and parallel trend with the grain sizes of the films. This was consistent with the beam intensity reduction effect of true porosity (which reduced the area of scanned solid) and the scattering from the agglomerates (which reduced the planarity of the surface profile). Consequently, the XRD peaks of the film deposited from PTA containing citric acid showed anomalously high intensities because, as shown in Table 1 and the preceding text, the true porosity was the highest and agglomerates were absent.
- XRD peak breadths*; The XRD peak breadths of the films depend on the perfection of crystallinity of the individual grains and the randomness of the grain orientations. The Williamson–Hall approach [26] usually is used to determine the crystallite (subgrain) size and this involves measurement of the breadth of the peak at half-height. Table 1 shows that the crystallite sizes and grain sizes were similar, which indicates that the individual grains were single crystals (*i.e.*, no subgrains) and that the image analysis was relatively accurate. The strain values of the films, which

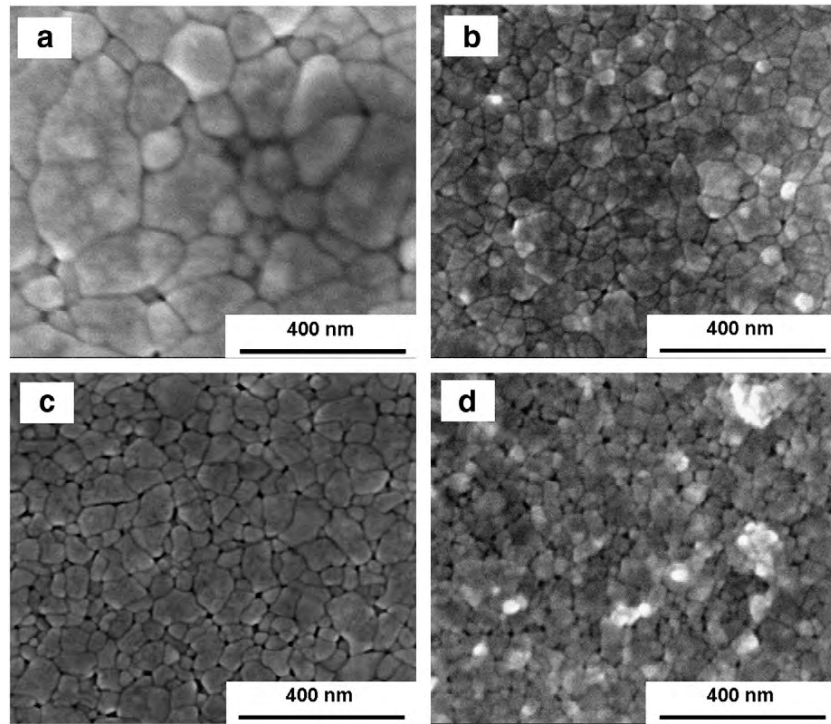


Fig. 3. SEM images of  $\text{WO}_3$  thin films deposited from (a) pure peroxotungstic acid (PTA) and (b) PTA with formic acid, (c) PTA with oxalic acid, and (d) PTA with citric acid.

were estimated from the Williamson–Hall plot (not shown), were negligibly small and thus the broadening of the XRD peaks was unlikely to be caused by the strain in the film [26].

Fig. 5 shows the optical transmittance spectra of the films. The transmittance of the films differed marginally in the near-UV (<400 nm) and visible (400–800 nm) regions. The main differences were a small blue-shift (<15 nm) in the optical absorption edge of the films deposited with carboxylic acids (differentiation between these films was ambiguous) and slightly lower optical transmittance of the film deposited with PTA containing citric acid in the visible region. The blue shift was attributed to microstructural defects, as described subsequently. The lower transmittance was attributed to scattering losses resulting from the high true porosity of the film deposited with PTA containing citric acid, as shown in Table 1.

Tauc plots were used to obtain the optical indirect band gaps of the films and the results are shown in Table 1. The optical indirect band gaps of the films varied in the range 2.55–2.70 eV, which is in good

agreement with previous works [27–29]. Since the films showed variations in true porosity (small variation) and grain size (large variation), the associated variation in surface areas would be expected to affect the proportion of surface defects, an increase in which is known to increase the optical band gaps of materials [6,17]. However, the variation between the band gaps, which were determined by a graphical technique involving extrapolation, was too small to differentiate between films.

When a photoanode is in contact with an electrolyte in a dark environment, energy band bending occurs at the photoanode/electrolyte interface in order to achieve thermal equilibrium [30]. On illumination, electron-hole pairs are generated at the photoanode, with the electrons' being excited to the conduction band and the holes' reaching the photoanode/electrolyte interface. This in turn decreases the band bending, where the amount of decrease corresponds to the photopotential [31]. When the illumination is switched off, the photopotential diminishes as the energy band bending is re-established. The relaxation time of the photopotential determines the recombination rate of the photogenerated electron-hole pairs [18].

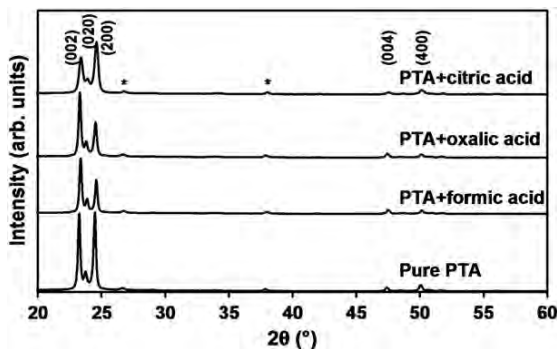


Fig. 4. XRD patterns of  $\text{WO}_3$  thin films deposited from different electrolyte compositions. The film thicknesses were  $\sim 700$  nm for all samples. \* marks the FTO peaks.

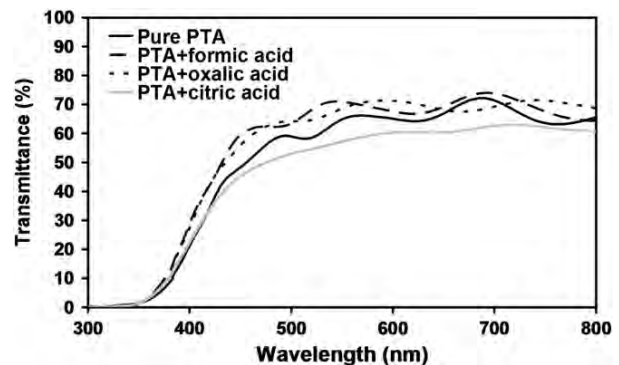


Fig. 5. Optical transmittance spectra of  $\text{WO}_3$  thin films deposited from different electrolyte compositions. The film thicknesses were  $\sim 700$  nm for all samples.

The transient open-circuit photopotential measurements of the films are shown in Fig. 6. The stable potentials attained in the dark were  $\sim 0.15$  V. Once illumination was switched on, the photopotentials developed immediately and then commenced the approach to steady values. The times taken for the photopotentials to decay to their initial value of  $\sim 0.15$  V after the illumination was turned off were  $\sim 110$  s, 160 s, 150 s, and 120 s for the films deposited from pure PTA and PTA with formic acid, oxalic acid, and citric acid, respectively. The relatively long photopotential relaxation times ( $\sim 150$ – $160$  s) of the films consisting of small agglomerates ( $\sim 83$ – $94$  nm), which were deposited from PTA containing formic or oxalic acid, suggest that the recombination rates of the photogenerated electron-hole pairs were slow. This was attributed to the relatively short hole diffusion distance to the photoanode/electrolyte interface owing to the small agglomerate sizes. Therefore the photogenerated holes had a higher probability of oxidising water before they could recombine with the photogenerated electrons. The relatively high specific surface area associated with the small agglomerate sizes also may have contributed to the long photopotential relaxation time since this provided a large number of reaction sites for water oxidation. For the film consisting of individual particles, which was deposited from PTA containing citric acid, the large grain boundary area associated with the small particle sizes resulted in a high fraction of surface defects (*viz.*, dangling bonds), which acted as electron-hole recombination sites [32]. In addition, the grain boundaries also act as weak links that hindered electron transport to the back contact (substrate) [33], thereby increasing the recombination rate.

Fig. 7 shows the transient photocurrent densities of the films measured under a tungsten-halogen lamp at an applied potential of 0.7 V. The trend of the photocurrent densities was in the same order as the photopotential relaxation times. This suggests that, as expected, the photocurrent density measurements were dominated by the photogenerated electron-hole separation rate, which depended on the electron transport, the hole transport, the number of reaction sites for water oxidation, and the number of electron-hole recombination sites. The maximal photocurrent density, which was measured in the film consisting of small agglomerates (deposited from PTA containing oxalic acid), was an outcome of a positive balance of these preceding factors.

The measurement for 2 h of the transient photocurrent densities of the films deposited from pure PTA (lowest photocurrent density) and PTA containing oxalic acid (highest photocurrent density) is shown in Fig. 8. The photocurrent density of the film deposited from pure PTA remained stable at  $\sim 0.06$  mA cm $^{-2}$  throughout the measurement. The film deposited from PTA containing oxalic acid showed a decrease in the photocurrent density from  $\sim 0.135$  mA cm $^{-2}$  to  $\sim 0.110$  mA cm $^{-2}$  ( $\sim 19\%$ ) after an hour of measurement and remained stable for the rest

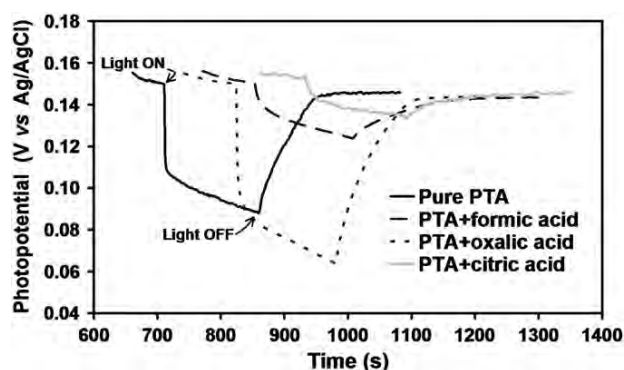


Fig. 6. Transient open-circuit photopotential measurements of  $\text{WO}_3$  thin films deposited from different electrolyte compositions. The film thicknesses were  $\sim 700$  nm for all samples.

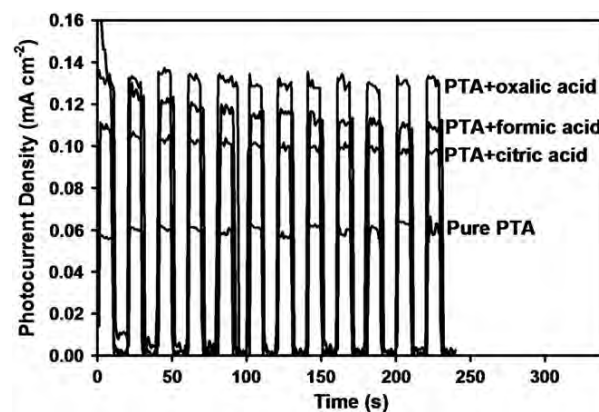


Fig. 7. Transient photocurrent measurement of  $\text{WO}_3$  thin films deposited from different electrolyte compositions. The film thicknesses were  $\sim 700$  nm for all samples.

of the measurement. Overall the films demonstrated stability as photoanodes for photoelectrochemical cells.

It may be noted that, as observed before [34,35], the photocurrent densities increased linearly with increasing light intensity, which was varied in the range 30–100 mW cm $^{-2}$  (data not shown). It is well known that photon absorption; which depends on the light intensity, absorption edge, transmission, and reflection; results in the generation of electron-hole pairs, which dominates the photoelectrochemical performance [34,35].

Hong et al. [12] and Li et al. [36] reported grain size control ( $\sim 25$ – $500$  nm) of  $\text{WO}_3$  films using post-deposition thermal treatment methods, where the maximal photoelectrochemical performances were observed in the films consisting of apparently small agglomerates of  $\sim 60$  nm. They obtained maximal photocurrent densities of 0.4–0.8 mA cm $^{-2}$  at an applied potential of  $\sim 0.7$  V vs. Ag/AgCl, by using a xenon lamp (100 mW cm $^{-2}$ ) as a light source. Also, other researchers [1,37] had observed photocurrent densities of  $\text{WO}_3$  nanoporous films in the range  $\sim 3$ – $6$  mA cm $^{-2}$  under identical measurement conditions.

It should be noted that the photocurrent densities in the present work are not directly comparable with those using other light sources, such as a xenon lamp, since different light sources produce different spectral outputs [38]. However, the results from different light sources can be converted approximately using an integrated intensity-wavelength conversion [19]. Using this, the equivalent photocurrent densities for the present samples were in the range  $\sim 3.0$ – $6.5$  mA cm $^{-2}$ .

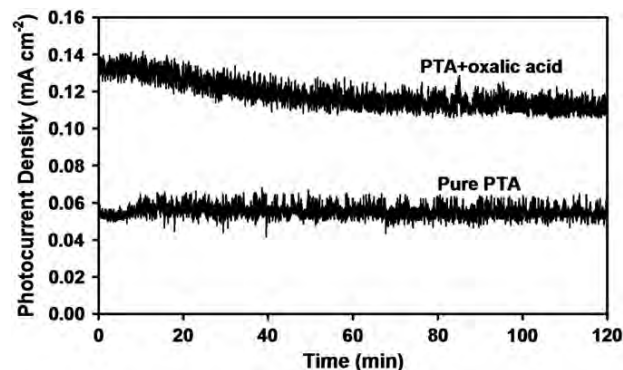


Fig. 8. Transient photocurrent measurement of  $\text{WO}_3$  thin films deposited from pure PTA and PTA containing oxalic acid. The film thicknesses were  $\sim 700$  nm for both samples.

The present work and that of others [12,36] show that small agglomerates appear to offer a means of optimising the concurrent factors that affect the photoelectrochemical properties of the films.

#### 4. Conclusions

WO<sub>3</sub> thin films can be electrodeposited from PTA electrolyte solutions in the absence and presence of carboxylic acids. The film deposition thicknesses were influenced by the PTA electrolyte pH and conductivity, which were influenced by the amount of hydronium ions and the size of the conjugate bases of the dissociated carboxylic acids. The pK<sub>a1</sub> values determined the degrees of acid dissociation while the sizes of the conjugate bases determined the molecular drag in the electrolyte. However, the relationships between the controlling variables such as pK<sub>a1</sub>, molecular weight of the conjugate bases, electrolyte pH, and electrolyte conductivity were complex and so the film thickness cannot be associated independently with them. The average grain sizes of the films deposited from pure PTA and PTA containing formic, oxalic, and citric acids were 131 nm (large agglomerates), 94 nm (small agglomerates), 83 nm (small agglomerates), and 45 nm (individual particles), respectively. The grain sizes of the films were attributed to the separation of the PTA ions by the conjugate bases and the corresponding diffusion distance. The photocurrent densities of the films deposited with carboxylic acids were greater than that of the film deposited from pure PTA. These differences were attributed to improvements in (1) grain size, which controls photogenerated electron-hole transport, and (2) effective grain boundary area, which controls the numbers of active reaction sites and electron-hole recombination sites.

#### Acknowledgments

This work was supported in part by a project funded by the Australian Research Council (ARC). The authors are grateful for the characterisation facilities from the Australian Microscopy & Microanalysis Research Facilities (AMMRF) node at the University of New South Wales (UNSW). W.L. Kwong gratefully acknowledges the receipt of UNSW International Postgraduate Award and Postgraduate Research Support Scheme.

#### References

- [1] A. Watcharenwong, W. Chanmanee, N.R. de Tacconi, C.R. Chenthamarakshan, P. Kajitvichyanukul, K. Rajeshwar, *J. Electroanal. Chem.* 612 (1) (2008) 112.
- [2] X.P. Shen, G.X. Wang, D. Wexler, *Sensors Actuators B* 143 (1) (2009) 325.
- [3] F. Fang, J. Kennedy, J. Futter, T. Hopf, A. Markwitz, E. Manikandan, G. Henshaw, *Nanotechnology* 22 (33) (2011) 335702.
- [4] H.M.A. Soliman, A.B. Kashyout, M.S. El Nouby, A.M. Abosehly, *J. Mater. Sci. Mater. Electron.* 21 (12) (2010) 1313.
- [5] W.J. Li, Z.W. Fu, *Appl. Surf. Sci.* 256 (8) (2010) 2447.
- [6] F. Diquarto, A. Dipaola, S. Piazza, C. Sunseri, *Sol. Energy Mater.* 11 (5–6) (1985) 419.
- [7] G. Hodes, D. Cahen, J. Manassen, *Nature* 260 (5549) (1976) 312.
- [8] D.A.H. Hanaor, G. Triani, C.C. Sorrell, *Surf. Coat. Technol.* 205 (12) (2011) 3658.
- [9] Y. Li, J.Z. Zhang, *Laser Photonics Rev.* 4 (4) (2010) 517.
- [10] J.J. Kelly, D. Vanmaekelbergh, *Electrochemistry of Nanomaterials*, Wiley-VCH, Weinheim, 2001.
- [11] M.A. Butler, *J. Appl. Phys.* 48 (5) (1977) 1914.
- [12] S.J. Hong, H. Jun, P.H. Borse, J.S. Lee, *Int. J. Hydrogen Energy* 34 (8) (2009) 3234.
- [13] X.L. Sun, H.T. Cao, Z.M. Liu, J.Z. Li, *Appl. Surf. Sci.* 255 (20) (2009) 8629.
- [14] C.M. White, J.S. Jang, S.H. Lee, J. Pankow, A.C. Dillon, *Electrochem. Solid-State Lett.* 13 (11) (2010) B120.
- [15] R.S. Vemuri, K.K. Bharathi, S.K. Gullapalli, C.V. Ramana, *ACS Appl. Mater. Interfaces* 2 (9) (2010) 2623.
- [16] M. Sun, N. Xu, Y.W. Cao, J.N. Yao, E.G. Wang, *J. Mater. Sci. Lett.* 19 (16) (2000) 1407.
- [17] M. Sun, N. Xu, Y.W. Cao, J.N. Yao, E.G. Wang, *J. Mater. Res.* 15 (4) (2000) 927.
- [18] L. Meda, G. Tozzola, A. Tacca, G. Marra, S. Caramori, V. Cristino, C.A. Bignozzi, *Sol. Energy Mater. Sol. Cells* 94 (5) (2010) 788.
- [19] W.L. Kwong, N. Savvides, C.C. Sorrell, *Electrochim. Acta* 75 (2012) 371.
- [20] J.C. Kotz, P.M. Treichel, J.R. Townsend, *Chemistry and Chemical Reactivity*, Brooks/Cole, Belmont, 2010.
- [21] I. Zhitomirsky, L. Galor, A. Kohn, H.W. Henniske, *J. Mater. Sci. Lett.* 14 (11) (1995) 807.
- [22] I. Zhitomirsky, L. Galor, *Mater. Lett.* 31 (1–2) (1997) 155.
- [23] S. Bijani, L. Martinez, M. Gabas, E.A. Dalchiale, J.-R. Ramos-Barrado, *J. Phys. Chem. C* 113 (2009) 19482.
- [24] C.C. Sorrell, H. Taib, T.C. Palmer, F. Peng, Z. Xia, M. Wei, in: S. Zhang (Ed.), *Biological and Biomedical Coatings Handbook: Processing and Characterization*, vol. 1, CRC Press, Boca Raton, 2011, p. 81.
- [25] P.M. Woodward, A.W. Sleight, T. Vogt, *J. Phys. Chem. Solids* 56 (10) (1995) 1305.
- [26] S.T. Tan, B.J. Chen, X.W. Sun, W.J. Fan, H.S. Kwok, X.H. Zhang, S.J. Chua, *J. Appl. Phys.* 98 (2005) 013505.
- [27] L. Weinhardt, M. Blum, M. Bar, C. Heske, B. Cole, B. Marsen, E.L. Miller, *J. Phys. Chem. C* 112 (8) (2008) 3078.
- [28] B. Yang, P.R.F. Barnes, W. Bertram, V. Luca, *J. Mater. Chem.* 17 (26) (2007) 2722.
- [29] Y. Sun, C.J. Murphy, K.R. Reyes-Gil, E.A. Reyes-Garcia, J.M. Thornton, N.A. Morris, D. Raftery, *Int. J. Hydrogen Energy* 34 (20) (2009) 8476.
- [30] E.L. Miller, *On Solar Hydrogen and Nanotechnology*, John Wiley & Sons, Singapore, 2009.
- [31] C.A. Grimes, O.K. Varghese, S. Ranjan, *Light, Water, Hydrogen. The Solar Generation of Hydrogen by Water Photoelectrolysis*, Springer Science+Business Media, New York, 2008.
- [32] B.G. Yacobi, *Semiconductor Materials: An Introduction to Basic Principles*, Kluwer Academic/Plenum, New York, 2003.
- [33] J.K.F. Yau, C.C. Sorrell, *Physica C* 282–287 (1997) 2563.
- [34] H. Wang, T. Lindgren, J. He, A. Hagfeldt, S.E. Lindquist, *J. Phys. Chem. B* 104 (2000) 5686.
- [35] N. Naseri, S. Yousefzadeh, E. Daryaei, A.Z. Moshfegh, *Int. J. Hydrogen Energy* 36 (2011) 13461.
- [36] W. Li, J. Li, X. Wang, J. Ma, Q. Chen, *Int. J. Hydrogen Energy* 35 (2010) 13137.
- [37] N.R. de Tacconi, C.R. Chenthamarakshan, G. Yogeewaran, A. Watcharenwong, R.S. de Zoysa, N.A. Basit, K. Rajeshwar, *J. Phys. Chem. B* 110 (50) (2006) 25347.
- [38] W.S. Yoo, K. Kang, *Nucl. Inst. Methods Phys. Res. Sect. B* 237 (1–2) (2005) 12.